

Proceedings of IX Congress

# NATIONAL GROUP OF MECHANICAL AND THERMAL MEASUREMENTS

Ancona, 11-13 september 2014

<http://www.diism.univpm.it/mmt2014>



e-book (PDF)  
ISBN 978-88-97683-68-1

---

With the sponsorship of:



**MILANO SYSTEMS**

**SIEMENS**  **Spectra S.r.l.**

2014, Universitas Studiorum S.r.l. - Casa Editrice  
via Sottoriva, 9 - 46100 Mantova (MN)  
tel. 0376 1810639; e-mail: [info@universitas-studiorum.it](mailto:info@universitas-studiorum.it)  
<http://www.universitas-studiorum.it>  
P. IVA 02346110204

Prima edizione 2014

ISBN 978-88-97683-68-1 (e-book, formato PDF)

## INDEX

<i>R. Vallascas, M. Usai</i> FEM Model for the Miscuffing Errors Verification	5
<i>R. Montanini, T. Scimone, S. De Caro, A. Testa</i> Multiple time-delayed acquisition method for acquisition of very fast thermal transients using a standard infrared camera	12
<i>E. Schena, P. Saccomandi, G. Allegretti, C. Massaroni, S. Silvestri</i> MR-Thermometry Applied to Pancreas during Laser Ablation: Sensitivity Analysis of Two T1-Weighted Sequences	19
<i>M. Lancini, I. Bodini, D. Vetturi, S. Pasinetti, A. Mazzù, L. Solazzi, C. Petrogalli, M. Faccoli</i> Vibration measurements for contact topology assessment in a rolling contact fatigue bench	25
<i>I. Bodini, G. Baronio, G. Bonomi, A. Donzella, F. Fallavollita, M. Lancini, S. Pasinetti, D. Vetturi, P. Vitulo, A. Zenoni, G. Zumerle</i> Monte Carlo simulations of a stability monitoring system based on tracking cosmic rays	33
<i>I. Bodini, A. Borboni, M. Lancini, S. Pandini, S. Pasinetti, D. Vetturi</i> Measurement of forces exerted by a polymeric shape-memory stent for biomedical applications	43
<i>M. Pertile, S. Chiodini, S. Debei, E. Lorenzini</i> Laboratory calibration and comparison of three visual odometry systems	48
<i>A. Scorza, G. Lupi, L. Battista, J. Galo, S. A. Sciuto</i> Influence of transducer position on quality assurance measurements in B-mode Ultrasound: a case study	56
<i>D. Scaccabarozzi, B. Saggin, D. Baruffaldi</i> Contactless temperature measurement of thin wires: methods comparison	63
<i>M. Tarabini, B. Saggin</i> Measurement of the heat removed by devices for skin tags treatment	70
<i>G. D'Emilia, A. Gaspari, E. Natale</i> Calibration Uncertainty of Three-Axis Low Frequency Accelerometers: Test Rig and Procedure Aspects	75
<i>M. Becchetti, R. Marsili, F. Cannella, A. Garinei</i> A system based on light scattering to measure pressure distribution on the finger	82

<i>G. M. Revel, M. Arnesano, F. Pietroni</i> A method to employ low-cost IR sensors for the indoor thermal comfort measurement	87
<i>A. Cavuto, M. Martarelli, G. Pandarese, G. M. Revel, E. P. Tomasini</i> Laser Ultrasonics for Train Wheel and Axle Diagnostics	95
<i>G. Dinardo, G. Vacca</i> Cross Correlation Method Enhancement for FBG Demodulation	103
<i>G. Dinardo, L. Fabbiano, G. Vacca</i> Proposal of a Simpler Procedure for Flow Rate Estimation in Square Cross Section Ducts	111
<i>A. Ancillao, F. Patanè, S. Rossi, A. Pacilli, P. Cappa</i> Lower limb strength measurements by Hand Held Dynamometer assisted by optoelectronic system	119
<i>G. Genta, A. Germak</i> Metrological Characterization of an Hexapod-Shaped Multicomponent Force Transducer	121



# FEM Model for the Miscuffing Errors Verification

R. Vallasca\* M. Usai\*\*

\* Department of Mechanical Chemistry and Materials Engineering, University of Cagliari, Cagliari, Italy

\*\* Department of Electrical and Electronics Engineering University of Cagliari, Cagliari, Italy

## Abstract

*The aim of the work is focused on the generation of FEM model by Ansys code, able to effectively evaluate the miscuffing errors. For this purpose it was measured the circumferential distribution of the pressure produced by the cuff on the arm during the inflation and deflation phases, concerning bladders of longitudinal dimensions comprised between 60% and 100% of the circumference of the experimental arm. The model parameters have been identified by searching vessel-occluded conditions at the subject systolic blood pressure for the bladder/arm ratio equal to 80%. The Young's modulus is fixed to 40 kPa and the Poisson's ratio to 0,44. The measured pressure distributions for the 60%, 70%, 90% and 100% ratios have allowed to verify miscuffing errors reported in bibliography by the constructed FEM model.*

## 1. Introduction

For the last two decades the authors have been involved into blood pressure measurements, with the development of phenomenological simulators, Vallasca (2005) [21], and also with the proposal of an innovative application of oscillometric method, Vallasca (2012) [22]. This work falls within the topics of interest and it was focused on the implementation of a finite elements model, which is able to highlight miscuffing errors and provide capable information in order to use, and eventually redesign, the cuff.

It is well known that the most common mistakes during brachial and radial blood pressure measurements, come from the adoption of not proportionate cuff to the arm circumference<sup>1</sup>. This kind of problem is very common into the pediatric field, where the patient's arm size has even wider

range, of possible values, than on the adult population.

The inner bladder is the most significant metrological factor, which must be constrained to comply the correct longitudinal and transverse dimensions.

This bibliography field is quite large and articulated, mainly including clinical measurements, recommendations of regulatory Bodies and researches about modeling and simulation. Alexander et al. (1977) [1], indicate the cuff's selection criteria, until they create a new pediatric cuff design. In Reid and Chantler (1982) [18], have been reported the corrections made by Maxwell, who was one of the first to suggest in 80% the optimum ratio between the bladder and the arm circumference, and to define the functional link between measurement errors and the quoted ratio in a quantitative way.

Several authors have highlighted the reading difference that it is possible to obtain comparing cuffs of different sizes. These results are reported in relative terms and don't care about errors in absolute terms. Iyriboz et al. (1994) [10], have quantified the reading differences obtained using 12/23 and 15/33 cuffs. Bakx et al. (1997) [3], have determined the effects using cuffs having different width and height bladder. Marks and Gronch (2000) [13], come to the conclusion, based on the comparison between the auscultatory and direct pressure measurements, that the measurement error can be minimized by using a bladder having width equal to 46% of the arm circumference. Jilek and Stork (2010) [12], had analyzed the influence of the bladder's width during the use of the radial site.

The American Heart Association (AHA) (2005) [16], sets four cuffs standard sizes, moreover it established that "the ideal cuffs should have a bladder length of 80%, and a width of at least 40% of the arm circumference". A length/width ratio of 2:1 appear to be optimal, especially regarding the insertion problem around the arm that smaller ratios might entail.

<sup>1</sup> The phenomenon of miscuffing occurs when the size of the bladder, in relation to the arm's circumference is or too small, undercuffing, or too large, overcuffing.

The European Society of Hypertension (ESH) (2003) [15], recommend the three cuffs mentioned by the British Hypertension Society (BHS) and refers to the dimensions standardized by the AHA. The numerical modeling works are mostly oriented to deepen issues related to the oscillometric method. For instance, Foster and Turney (1986) [9], Baker et al. (1977) [4], and Jeon et al. (2007) [11], based their model on the static pressure-volume relation, Ursino e Cristalli (1996) [19], propose a whole model with lumped parameters, Wang et al. (2001) [23], focus their proposal on fuzzy logic, Pinheiro (2008) [17], analyzes the signal transduction related issues, while Mersich and Jobbagy (2009) [14], had developed a set-up in order to determinate the cuffs pressure-volume transfer function, also analyzing the compression conditions (tight, loose and canvas) of themselves on the support, and quantifying the measurement errors.

The authors, Usai and Vallascas (2011) [20], had confirmed in a previous memory, by using a preliminary and simplified EF mathematical model, the data reported by Reid an Chantler (2002) [18], for the 12/23 cuff. Furthermore, referring to the ratio between transversal and longitudinal dimension, they found that the error introduced can be considered constant and negligible over the 25% of this ratio. The models proposed, so far to interpret and simulate phenomena of blood pressure measurement, even if they have the theoretical formulation, sufficiently comprehensive and rigorous in the assumptions and interpretation of phenomena, are often supported by experimental validation of a low level.

In the present paper the authors have focused their attention on the adoption of a method of measurement and the development of a computational model suitable for the evaluation of the errors resulting from the miscuffing and from the positioning of the cuff. In this analysis they will use pressure distributions on the real human arm, previously obtained experimentally. This feature requires the availability of a suitable measurement set-up and of a 3D "sectorialised" model. That permits the application of punctual loads on the outer contours of the arm. It appears that oriented researches in this direction has not ever been proposed in the literature. The modern knowledge about the distribution of cuff's pressure on the arm are qualitative, and imply a uniform distribution equal to the amount of pressure inside the cuff. An exception is reported by Cristalli, Neuman and Ursino (1994) [7], which have conducted pressure measurements on the

interface between the cuff and the arm, but limited to a few points without characterizing the distribution on the complete circumference. Usually it is ignored the possibility that the cuff can be set lobes up onto the cuff, in order to locally load the arm, generating non-uniformity of pressure.

## 2. Setup

In order to determinate the pressure distribution exerted by the cuff on the lateral surface of the arm, it was necessary acquiring a suitable set of sensors. After it was experimented with a variety of available sensors on the market, it was decided to use a more reliable set of self-made sensors.

The sensor is built, Figure 1, with a silicon duct with an internal diameter equal to 4 mm, and a length equal to  $35 \pm 1$  mm, it is connected to a pressure transducer<sup>2</sup> by a smaller diameter rigid tube. The transmission fluid is made of distilled and degassed water. All the sensors are calibrated daily before each measurement cycle. During the calibration process are removed the offsets and it is calculated the gain, through a comparing procedure with an aneroid manometer that derives the traceability by a mercury differential U manometer.

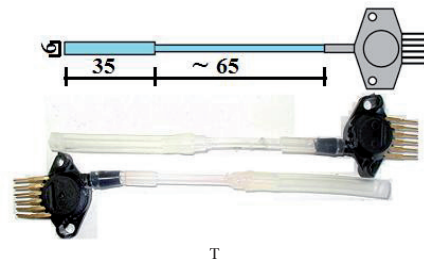


**Figure 1. Constructive diagram and picture of the sensors**

In order to insert the sensors on the measurement spot, they have been assembled on a flexible cloth, keeping a constant gap one each other; in this way they have been able to cover the entire arm circumference.

For not modify the physical distribution of the pressures and to contain the sensors, an equivalent rigidity material fills the empty space between them. During the operational stage the cloth is wrapped around the arm, under the cuff, Figure 2. The signals have been acquired by a board, using NI USB 6251 and Labview 2012 software.

<sup>2</sup> Motorola MPX 5050.

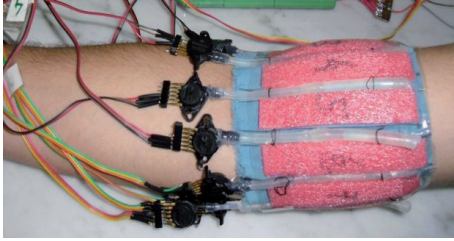


**Figure 2. Operational setup**

The maximum uncertainty of the single measurement was estimated to be less than 1 mmHg.

### 3. Measurements

During the miscuffing analysis it was used a cuff 12/29, whose bladder, Figure 3, can be extracted and one of its ends can be folded back on itself to the size of interest, to allow the partializing, through the forced insertion of a C aluminium profile.



**Figure 3. Bladder used for the partializing of the cuff**

Cuff/arm ratios (CC/AC) between 60% and 100%, with step equal to 10%, have been analysed. The arm circumference, on which the measurement were conducted, was measured equal to  $260 \pm 5$  mm on the cuff insertion site.

In order to verify the repeatability of the phenomenon, the measurements have been repeated after the cuff insertion on the arm for each configuration. The repeatability, also in consideration of the fact that deflation was conducted manually, was contained within 5 mmHg in all the measuring points, Figure 4. The picture present on the abscissa the time, expressed in seconds and on the ordinate axis the corresponding value of the pressure, expressed in

mmHg. The yellow curve in the center refers to the cuff internal pressure during the phases of inflation and deflation.

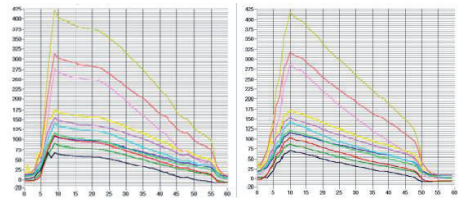


**Figure 4. Example of pressure monitoring**

The Figure 5 shows the diagrams relating to the circular distribution of the pressures measured by 10 sensors for the analyzed configurations. It is evident the lack of axial-symmetric distribution in all cases. This effect was observed both in measurements conducted on human arm than on rigid cylinders, with the difference that human limb pressure distribution does not undergo appreciable variation turning the headset within  $\pm 20^\circ$ , while on a rigid support, of course, the diagram follows the rotation. From the diagrams were derived circumferential pressures, used to load the model.

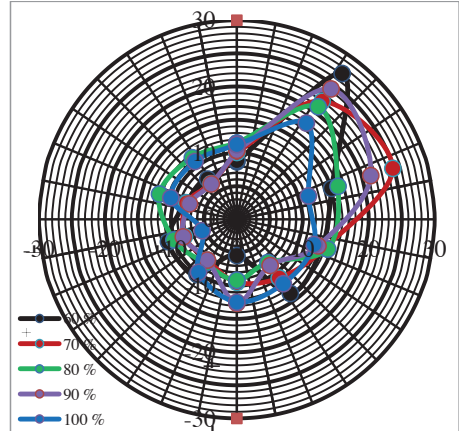


**Figure 5. Diagram of pressure distributions [kPa] around the arm**

### 4. Fem model

The arm simulation model was developed by using Ansys code. It is considered a half of the total volume, assuming the model symmetry to the YZ plan (cross-section). The software Ansys, allows the rebuilding of the sizes distributions of

the field, on the whole volume, through post-processing operations.

The arm's tissue has been assumed homogeneous and elastic, this because, after the "pressurization" accomplished by the cardiac pump, the arm is able to resume to the initial configuration. It is also wanted to keep the presence of the basilica vein inside of the tissue for a better correspondence to a real situation.

#### 4.1 Parameters characterizing the materials

In reference to the cross-sections, quoted in Eycleshymer and Schoemaker [8], it has been assumed a configuration built with a tissue with a circular section, placed in a uniform way around the bone and containing the brachial artery and the basilica vein, along the same diameter.

The external bone diameter has been assumed equal to 28 mm, the external arm diameter has been assumed equal to 108 mm, the artery inner diameter has been assumed equal to 4 mm with a thickness of 0.6 mm, while the inner diameter of the vein has been assumed equal to 7 mm with thickness equal to zero.

In order to further reduce the number of the nodes and of the elements, it was considered only the bone outer surface, removing the whole volume.

The rigidity has been imposed to the bone outer surface through the CERIG Ansys command. The numerical model consists of a total of 38 volumes, 194 areas, 309 lines, 158 key points, 58284 nodes and 39138 solid elements, 92 plus 1 elements, Target170 for the pilot node. The processing time was reduced to about 8 minutes.

The overall arm tissue was modelled as forming a set composed of skin, muscle, nerves and fat, all to be homogeneous, elastic and isotropic, at this set was assigned a modulus of elasticity  $E = 40$  kPa. The Young's modulus was chosen, through a process of calibration of the model, on the basis of experimental values of cuff pressure corresponding to the closure of the artery. The Young's modulus, is of the same order of magnitude than those determined by Zheng on the forearm (1999) [24], and that might even be overestimated considering the values found for a bovine muscle by Whereas Chen (1996) [6]. are lower of an order of magnitude.

The venous vessels' presence has been preserved in order to constitute a possible preferential breakdown point to facilitate the artery collapse. The arterial was considered isotropic and characterized by an elastic modulus  $E = 440$  kPa and a Poisson's ratio  $\nu = 0.45$ .

The elastic modulus values are in agreement with the results reported in Avolio (1980) [2], and Bank (1996) [5].

#### 4.2 Constraints and boundary conditions

As mentioned, the analysed structure concerns half of the entire volume of the arm, and it were applied to it the following constraints and loads.

It was imposed a uniform pressure of 100 Pa to the discharge zone of the arm, and the pressure determined by the experimental distributions to the loaded area in correspondence of the cuff.

It is supposed a pressure of 0.2 kPa within the vein, and a diastolic pressure equal to 10.66 kPa into the artery.

The condition of symmetry is applied on the transverse surface, which contains the cuff, while all the points of the cross section, on the shoulder side, were left without constraints.

It was made the static analysis for small deformations. Various tests have been made, and it was verified that using the mesh recommended level value, equal to 6, the numerical method allows to converge to the results in a range between 5 and 8 minutes of computation, using a 2 GHz portable PC with 4 GB of RAM and 220 GB of hard drive.

#### 4.3 Validation

Since there is an almost unanimous acceptance in considering equal to zero the measurement error induced by the cuff, when the ratio bladder/arm (CC/AC) is around 80%, for the model validation is simply verified that with the actual distribution of the pressures, determined experimentally, the cross section of the artery was occluded, Figure 6.

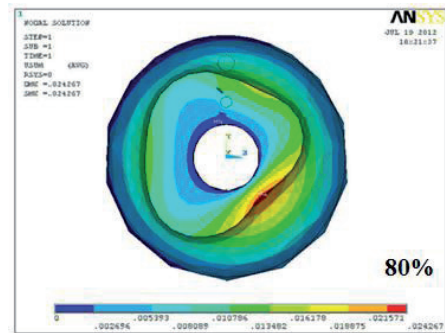


Figure 6. Displacements diagram for CC/AC = 80%

For this assessment, given the three-dimensional nature of the displacements, it was decided to identify the achievement of the occluded vessel conditions by means of a visual estimation of the diagrams obtained by the numerical program.

## 5. Results

It has been analysed cuff/arm ratios between 60% and 100% with step 10%.

Figures 7 and 8 represent the vertical displacements diagrams of the structure, relative to ratios equal to 60% and 100%, during the working stage.

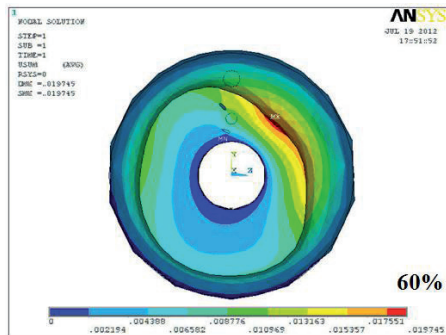


Figure 7. Displacements diagrams for CC/AC equal to 60%

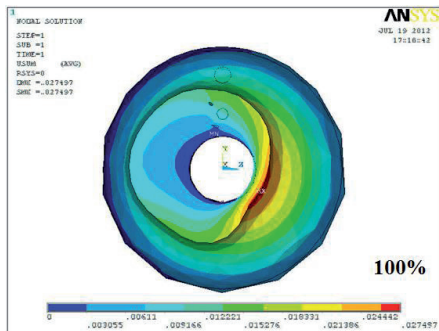


Figure 8. Displacements diagram for CC/AC equal to 100%

Figure 9 represents the summary of the results obtained by the FEM model, compared to the errors in measuring the systolic pressure, derived from the work [16] the results are strictly related to the selected 12/29 cuff that is suitable to cover 100% of the test arm.

For each the examined situations, the deviation are always smaller than 2%, if compared to the 15/30 cuff.

The results are, in the opinion of the authors, widely acceptable, also considering the uncertainty related to the errors that are recruited as a reference and which cannot be estimated less than a 100 Pa.

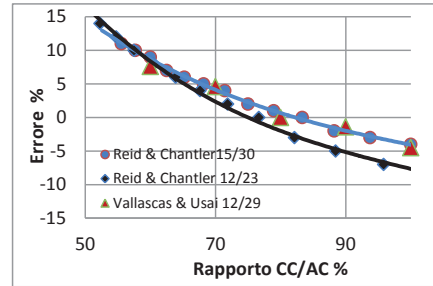


Figure 9: Measurements errors by the EF model

The same FEM model has been applied to both the determination of the influence of cuff rotation and the evaluation of the changes made by forcing the cuff on the arm.

For these experiments were used a commercial cuff with bladder 10/24 positioned on the same instrumented arm. The outer circumference was of 290 mm (CC/AC = 82%).

In the first case are analyzed rotation angles comprised between  $-20^\circ$  and  $+20^\circ$  in steps of  $10^\circ$ . The differences fall within  $\pm 500$  Pa.

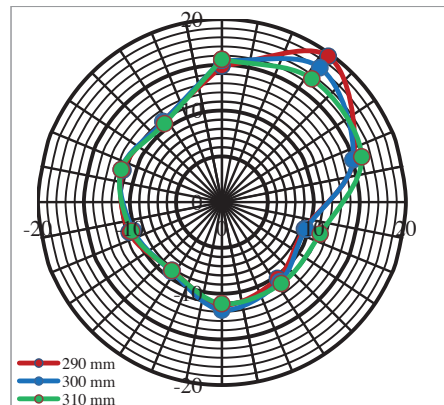


Figure 10. Pressure [kPa] around the arm as a function of the cuff length

In the second analysis, not having a dynamometer for measuring the cuff's force on the arm, were



taken into consideration three configurations: cuff close with as much force as possible, loose cuff of 10 mm and loose cuff of 20 mm. The related circular diagrams are shown in Figure 10. The outer curve (length equal to 290 mm) corresponds to the maximum forcing, the inner curve (310 mm) corresponds to the minimum. The model showed no appreciable differences in the situations concerned.

## 6. Conclusions

A FEM model, implemented by commercial software Ansys and validated by a static analysis for small deformations, has been presented. This model introduces the possibility of applying pressure loads distributed non-uniformly on the outer contour of the arm. For the determination of the pressure distribution in the interface arm-cuff to use as load on the FEM model has been prepared an original set up that uses a cuff with a bladder-height invariant and variable length obtained through an original solution which plans to fold back a 'end to the desired length.

A further test of the model validation was carried out to evaluate the error resulting from the use of badly dimensioned bladder, in order to quantify the phenomenon of miscuffing.

The results derived from the model developed, loaded with the experimental pressure distributions, have confirmed, for all the examined situations, the diagrams derived from the work of Reid & Chantler.

The FEM model was then applied both to the determination of the influence of the rotations of the cuff with respect to the location of the artery and to the evaluation of the changes made by the forcing of the cuff on the arm.

In the first case were analyzed rotation angles comprised between  $-20^\circ$  and  $+20^\circ$  with step  $10^\circ$ , and were found differences in the evaluation of the systolic pressure contained within  $\pm 500$  Pa.

In the second analysis, were taken into account three different configurations: cuff close with the maximum force as possible, cuff loose of 10 mm and cuff loose of 20 mm.

The results showed no appreciable differences for all situations considered. The model and the method proposed have allowed to highlight and confirm knowledge commonly accepted in the practice of blood pressure measurement concerning a) the optimum dimensional relationships, b) the correct positioning of the cuff, c) its forcing on the arm and d) the errors introduced by the less considered phenomenon of miscuffing. In the light of the obtained results the

authors believe that the level reached by the simulation model can afford both to more effectively analyze aspects related to the measurement of blood pressure and to perform test operations of the innovative cuffs that can be designed to provide greater flexibility and lower measurement errors.

Therefore the model was validated with experimental tests in laboratory. Through validation were chosen the most suitable parameters to characterize the biological materials of the model (blood, bone, artery, vein).

In the model was performed static structural analysis, referring to the condition of equilibrium fluid-dynamic that occurs when the artery is occluded.

Therefore if we consider the real nature of multi-physics of the problem examined, this work constitutes a valid starting point to get also more accurate results, applying the FEM multi-physics model with a structural analysis that taking account of the fluid-dynamic of the real model before it occurs artery occlusion.

## Bibliography

- [1] Alexander H., Cohen M.L., Steinfeld L., "Criteria in the choice of an occluding cuff for the indirect measurement of blood pressure", *Medical & Biological Engineering & Computing* January 1977, pagg 1-10
- [2] Avolio A.P., "Multi-branched model of the human arterial system", *Med. & Biol. Eng. & Comput.*, 1980, 18, pagg 709-718
- [3] Bakx C., Oerlemans G., van den Hoogen H, van Weel C., Thien T., "The influence of cuff size on blood pressure measurement", *Journal of Human Hypertension* 1997 11, pagg 439-445
- [4] Baker P.D., Westenskow D.R., Kuck K., "Theoretical analysis of non-invasive oscillometric maximum amplitude algorithm for estimating mean blood pressure", *Medical & Biological Engineering and Computing*: May 1997, pagg 271-278
- [5] Bank A. J., Wang H., Holte J. E, Mullen K, Shammass R., Kubo S H., "Contribution of Collagen, Elastin, and Smooth Muscle to In Vivo Human Brachial Artery Wall Stress and Elastic Modulus", *Circulation*. 1996; 94, pagg 3263-3270. © 1996 American Heart Association, Inc.
- [6] Chen E.J., Novakofski J., Jenkins W.K., O'Brien W. D. Jr., "Young's modulus measurements of soft tissues with application to elasticity imaging", 0885-3010/96 IEEE, pagg 191-194
- [7] Cristalli C., Neuman M.R., Ursino M., "Studies on soft tissue pressure distribution

- in the arm during non invasive blood pressure measurement", 0-7803-2050-6/94 IEEE, pagg 41-42
- 8] Eycleshymer A.C., Schoemaker D.M., "A cross section anatomy", processed by Reviewer, [www.rrlivingston.com](http://www.rrlivingston.com)
  - 9] Forster F.K., Turney D., "Oscillometric determination of diastolic, mean and systolic blood pressure – A numerical model", *J. of Biomechanical Engineering*, November 1986 Vol. 108, pagg 359-364.
  - 10] Iyriboz Y., Hearon C.M., Edwards K., "Agreement between large and small cuffs in sphygmomanometry: a quantitative assessment", *Journal of Clinical Monit.* Vol 10 N°2, March 1994, pagg 127-133
  - 11] Jeon G.R., Jung J.H., Kim I.C., Jeon A.Y., Yoon, S.H., Son J.M., Kim J.H., Ye S.Y., Ro J.H., Kim D.H., Kim C.H., "A Simulation for Estimation of the Blood Pressure using Arterial Pressure-volume Model", *World Academy of Science*, 2007, *Engineering and Technology*, 30, pagg 366-371
  - 12] Jilek J., Stork M., "Cuff width alters the amplitude envelope of wrist cuff pressure pulse waveforms", *Physiol Meas*, 31 2010: pagg N43-N49
  - 13] Marks L.A., Gronch A., "Optimizing cuff width for noninvasive measurement of blood pressure", *Blood Press. Monit.* 5, pagg 153-156
  - 14] Mersich A., Jobbagy A., "Identification of the cuff transfer function increases indirect blood pressure measurement accuracy", *Physiol. Meas.* 2009, 30, pagg 323-333
  - 15] O'Brien E. et al., "European Society of Hypertension recommendations for conventional, ambulatory and home blood pressure measurement", *Journ. of Hypertension* 2003, Vol 21 (5 ), pagg 821-848
  - 16] Pickering T.G. et al., "Recommendations for Blood Pressure Measurement in Human and Experimental Animals; Part 1: Blood Pressure Measurement in Humans: A statement for professionals from the subcommittee of professional and public education of the AHA council on high blood pressure research", *Hypertension*. January 2005, pagg 142-161
  - 17] Pinheiro E.C., "Oscillometric blood pressure monitor modeling", 30th Annual International IEEE EMBS conference Vancouver, British Columbia, Canada August 20-24 2008, pagg 303-306
  - 18] Reid C., Chantler C., "Systemic hypertension 2° ed", RH Anderson et al Churchill Livingstone Londra 2002, pagg 1809-1844
  - 19] Ursino M., Cristalli C., "A mathematical study of some biomechanical factors affecting the oscillometric blood pressure measurement", *IEEE transactions on biomedical engineering*: August 1996, 43, (8), pagg 761-778
  - [20] Usai M, Vallasca R., "Un nuovo modello FEM per la verifica degli errori di misurazione della pressione arteriosa", *X Giornata di Studio Bioingegneria Catania*, 2011
  - [21] Vallasca R., "Riferibilità dei simulatori nella verifica delle prestazioni dei monitor NIBP", *VII Giornata di Studio materiali innovativi in biomeccanica Messina*, 1 luglio 2005:
  - [22] Vallasca R., "L'applicazione del metodo oscillometrico per la misurazione della pressione arteriosa nell'uomo", *Informazione Ordine degli ingegneri della provincia di Cagliari* Anno XXXIII (119) gennaio 2012, pagg 34-37
  - [23] Wang J.J., Liu S.H., Lin C.T., Hsieh J.H., "Modeling the arterial unloaded situation in oscillometric blood pressure waveform measurement using fuzzy logic control", *J. of medical And biological Engineering*: 2001, 21(2), pagg 93-104
  - [24] Zheng Y., Mak A.F.T., Lue B., "Objective assessment of limb tissue elasticity: Development of a manual indentation procedure", *JRRD* Vol. 36 (2), April 1999

# Multiple time-delayed acquisition method for measurement of very fast thermal transients using a standard infrared camera

R. Montanini\*, T. Scimone\*, S. De Caro\* and A. Testa\*

\* Univ. Messina, C.da di Dio, I-98166 Messina, Italy, {rmontanini, tscimone, sdecaro, atesta}@unime.it

## Abstract

The paper presents a method for mapping the temperature distribution of very fast transient events (i.e., having a bandwidth of 10 kHz or more) by means of a standard infrared camera working at 25 Hz frame rate with 320×256 pixels full frame. The proposed method is based on triggering multiple time-delayed acquisitions (MTDA) of the observed thermal phenomenon, which has to be reproducible, by means of a very precise and stable programmable digital micro-controller and by reconstructing the time domain IR sequence using the frames acquired at each trigger event. The method could find application in assessing the reliability of power electronic devices and, in particular, to measure dynamically the temperature distribution over the source metal of Power MOSFETs or IGBTs, which feature very fast thermal transients, even in the hundreds of microsecond scale and might develop local hot spots as a consequence of aging or failures.

## 1. Introduction

Measurement of temperature distributions which are characterized by very fast transients, below the millisecond scale, has always been a difficult problem to be addressed and, only in the recent past, few experimental techniques have been proposed to deal with this challenging task.

One typical application field, in which recording of fast thermal transients is needed, is the characterization of power electronics equipment [1]. "Operating" temperature has, in fact, important consequences for the performance and reliability of semiconductor devices. For instance, the speed, or maximum operating frequency, of a microprocessor typically decreases as the temperature increases, and the gain or transconductance of a transistor may either increase or decrease with increasing temperature, depending upon the device type and operating conditions. It is also commonly assumed that the safety margin or reliability of a semiconductor

device decreases as the temperature increases [2-3]. It is not surprising, then, that a significant amount of effort goes into accurately measuring the temperature at which devices operate [4-6].

Often designers are more interested in achieving the complete 2D temperature distribution across a well-defined region of the device rather than inferring the average temperature of the device itself [7]. While in this last case electrical methods exploiting the temperature sensitivity of specific properties of semiconductor devices can be used (e.g., the forward voltage of a pn-junction at a constant current is known to vary with temperature in a predictable way), detection of temperature distribution either requires a single-point x-y raster scanning system or the usage of an infrared camera. Moreover, whereas electrical methods make use of electrical connections which are already available for normal device operation and are the only type that can be made on fully packaged devices [7], measurement of the temperature distribution by means of contact or non-contact methods always requires a physical or optical access to the device surface, which therefore must be preliminary opened.

The thermal excursions that power devices undergo in the transient regime can be very large and fast. In addition, significant thermal gradients can arise on the device surface because of non-homogeneous current density distribution, which in turn can cause thermal instabilities and device failure. Hence, in order to get the map of temperature distribution, a measurement method with both broad bandwidth and proper spatial resolution is needed. The fulfillment of these requirements is not trivial.

Castellazzi *et al* [1] have presented an experimental method based on a polycrystalline IR-fibre which conveys the thermal radiation emitted by the heated surface within the spectral range from 8 to 12  $\mu\text{m}$  onto a photo-detector. The system is able to perform single-point transient temperature measurements well down to the microsecond-range with an estimated spatial resolution of about 700  $\mu\text{m}$ , but both the detector and the amplification circuitry needed to be



immersed in liquid nitrogen (77 K) in order to increase the signal-to-noise ratio of the equipment. In addition, a spray coating consisting of a diluted carbon-based paint was used to uniform the emissivity of the MOSFET surface.

An improved method was developed by the research group of Breglio *et al* [2, 8-9], who present an experimental set-up based on a radiometric microscope with a cooled InSb single-point sensor. The 2D scanning of the measured surface is obtained by means of an x-y motorized stage. In this way, by considering the microscope spot-size, it was possible to achieve a spatial resolution of less than 10  $\mu\text{m}$  over an extended area of 25  $\times$  25 mm<sup>2</sup>, with quite good time resolution (less than 10 ms).

The same research group also developed a second system based on thermoreflectance mapping, which exploits the thermo-optic effect to measure the superficial temperature with a time resolution in the order of tenths of nanosecond and a temperature resolution of some kelvin, along with a much better spatial resolution with respect to the previous method [8].

An experimental approach similar to that used by Breglio *et al* [2,8] was adopted at the University of Messina to develop a reliability model for power MOSFETs working in avalanche mode [10-11].

All the systems described so far rely on single-point measurements and hence require a proper scanning system in order to reconstruct the temperature distribution map over the region of interest. Modern infrared cameras with fast focal plane array (FPA) would in principle present definite advantages compared to single-point x-y raster scanning systems. Unfortunately, these devices have a common limitation regarding the maximum sampling rate at full frame, which is usually limited to some tens of hertz. Higher frame rates are sometimes possible at the expense of a reduced number of pixels.

Recently, Riccio *et al* [12] used the equivalent time sampling (ETS) concept to measure transient temperatures with an equivalent bandwidth of 100 kHz by means of a standard IR camera, thus allowing to overcome the limitations associated with single-point measurements as far as the observed phenomenon can be repeated periodically (as it is the case for power electronic devices heated by pulsed currents).

Here we exploit the same concept to propose an improved method that, in addition of allowing full frame measurements of replicable transient events with high bandwidth (limited only by the integration time of the IR camera) and good spatial resolution (depending on the optical lens

used in the experimental set-up), also provides automatic compensation of the background temperature, thus eliminating systematic errors caused by ambient temperature shifts at each trigger event. The proposed method makes use of a precise and stable programmable digital micro-controller used to trigger multiple time-delayed acquisitions (MTDA), allowing the time domain infrared sequence to be reconstructed based on the time-delayed frames acquired.

To prove the effectiveness of the proposed MTDA method, experimental tests have been carried out on a planar resistor heated with repeated pulsed currents. A practical application dealing with a dynamical analysis of the temperature distribution over the source metal of an IGBT power device is finally presented.

## 2. The MTDA method

A standard cooled IR camera (FLIR SC7000) equipped with a 320 $\times$ 256 pixels InSb FPA sensor was used for the experiments. The IR camera has a maximum frame rate at full resolution of about 100 Hz, while the integration time can be set between 10  $\mu\text{s}$  and 20.000  $\mu\text{s}$ , with steps of 1  $\mu\text{s}$ . The integration time ( $\tau$ ) used for acquiring the infrared images actually determines the maximum equivalent sampling frequency ( $f_{e,max}$ ) that can be reached by the MTDA method, being:

$$f_{e,max} = \frac{1}{\tau} \quad \text{Eq. 1}$$

The measurement principle of MTDA is schematically illustrated in Fig.1.

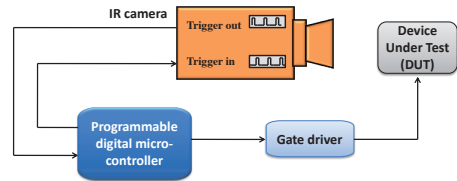


Fig. 1: Schematic illustration of the MTDA method.

Signals used for IR image acquisition are generated by means of three digital ports of an ATmega328 programmable digital micro-controller. The trigger output port of the IR camera (trigger OUT) generates a time base constituted by a train of impulsive signals having a period equal to the sampling time of the IR camera. When a rising edge occurs in the trigger output, a signal is generated by the

microcontroller and sent to the trigger input port (trigger IN) of the IR camera, starting the acquisition. A second signal is sent to the power device throughout a gate driver to start the heating event. These two signals are synchronized using the time base of the IR camera, thus providing an effective matching between the images acquisition and the transient event.

To account for possible variation of the ambient temperature during the test (actually the number of cycles required for the reconstruction of the thermal transient can be quite high, depending on the dynamics of the event), a further single frame acquisition is triggered at the end of each cooling period and used for ambient temperature compensation. Hence, temperature increments over the initial temperature ( $\Delta T$ ) before the start of each heating cycle were considered. All the frames acquired at each trigger event are used at the end of the measurement procedure to reconstruct the time and space behavior of the temperature over the device.

The timing sequence is schematically illustrated in Fig. 2, in which a) represents the switching time of the device under test, b) the timing of images acquisition and c) the trigger signals used for synchronization.

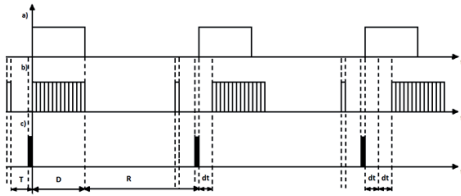


**Fig. 2: MTDA for slow transient events (not in scale): a) switching time of the device under test, b) timing of IR images acquisition and c) trigger signals used for synchronization.  $D$  = heating time,  $R$  = repetition rate (cooling time),  $dt$  = time delay,  $T$  = pre-trigger used for ambient temperature compensation.**

If  $FR$  is the frame rate of the camera, at each iteration  $N$  infrared images will be acquired (note that, due to the time delay, sometimes one image lies outside the duration of the event and can't be utilized for the reconstruction):

$$N = D \times FR \quad Eq. 2$$

where  $D$  represents the time duration of the transient event. The number of iterations depends on the time delay, and hence on the required equivalent sampling frequency. If  $f_e$  is the equivalent sampling frequency and  $dt$  the time

delay (i.e., the equivalent sampling time), then the number of iterations will be:

$$M = \frac{f_e}{FR} = \frac{1}{dt \times FR} \quad Eq. 3$$

Each iteration is shifted of  $dt$  allowing the complete reconstruction of the transient event that must be replicated  $M$  times. This holds as long as  $D$  is greater than the frame rate (i.e., for slow transient events).

For fast transient event (i.e., when  $D$  is smaller than the frame rate of the IR camera), the MTDA method can be still used by acquiring, at each iteration, only a single image instead of  $N$  images (Fig. 3). In this figure the shaded rectangle actually represents the IR camera integration time, which, according to (1), must be smaller than the time duration of the event. Of course, in this case the duration of the reconstruction process will be much longer.

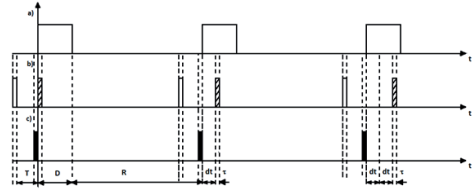


**Fig. 3: MTDA for fast transient events (not in scale): a) switching time of the device under test, b) timing of IR images acquisition and c) trigger signals used for synchronization.  $D$  = heating time,  $R$  = repetition rate (cooling time),  $dt$  = time delay,  $T$  = pre-trigger used for ambient temperature compensation,  $\tau$  = integration time.**

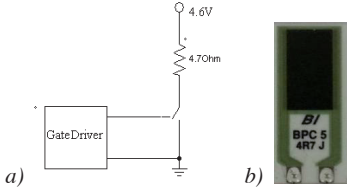
### 3. Validation of the proposed method

To validate the MTDA method, a laser-cut planar resistor was chosen as reference target. The test circuit employed to carry out the experimental tests is schematically illustrated in Fig. 4a. The resistor (Fig. 4b) was heated cyclically from ambient temperature up to about 37 °C by means of pulsed currents of  $D = 1600$  ms duration. No paint was applied onto the resistor to uniform the target area emissivity, which was estimated to be about 0.95 by separate tests. The repetition rate of the trigger pulse ( $R$ ) has been chosen to be 1 min in order to allow the device to dissipate the excess temperature increase before a new trigger pulse is applied. A further single frame acquisition is triggered at the end of each cooling period and used for ambient temperature compensation, as already explained in the previous section. The

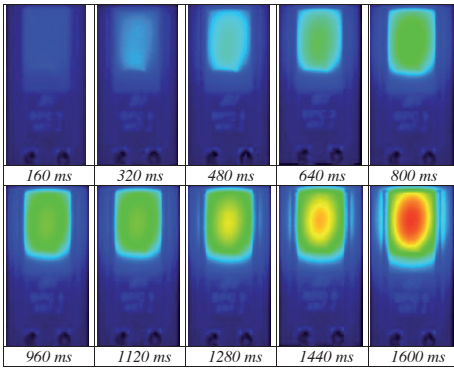
relatively slow dynamics of resistor's heating allows images acquisition to be performed also in normal operation mode (i.e., without time delay). All computations were carried out using Matlab™.

Fig. 5 shows selected infrared images taken at 25 Hz frame rate during one heating cycle (the complete sequence includes 40 images). These images were taken without introducing any time delay (i.e.,  $dt = 0$  ms) and served as reference for verifying the effectiveness of the proposed method and assessing the uncertainty of the reconstruction process.

As expected, it can be observed that heat is generated suddenly as the current flows into the resistor, and eventually spread across the whole area of highly conductive material, with the hottest elliptically-shaped region located in the inner part of the resistive element. It can also be highlighted that the two conductive films used to drive current to the resistor element do not dissipate power significantly, because of their low resistance. In addition, this part of the resistor has a lower emissivity coefficient with respect to the black target area.



**Fig. 4: a) Test circuit for slow dynamics analysis and b) reference planar resistor used to carry out the experimental tests.**



**Fig. 5: Current-driven heating of the planar resistor (one cycle).**

The next figure (Fig. 6) reports normalized temperature profiles ( $\Delta T$  increments) of the

hottest point of the resistor measured throughout five cycles, with no time delay. From this plot it can be realized that the repeatability of the observed event is quite good, being the average standard deviation (21 mK) comparable to the NETD value of the used IR camera.

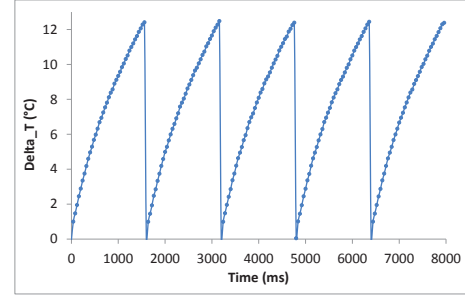


**Fig. 6: Normalized temperature profiles of hottest point of planar resistor (five cycles,  $dt = 0$  ms).**

The next experimental tests were carried out by using the MTDA method to capture the current-driven heating of the resistor with an equivalent sampling rate of 200 Hz ( $dt = 5$  ms) and 1000 Hz ( $dt = 1$  ms), respectively. In the first case, the complete sequence includes 320 infrared images, while in the second one the number of infrared images captured is 1600. Each test was repeated five times and average heating profiles of selected points of the target area were computed. Fig. 7 compares the reconstructed average heating profiles of the middle point (hot spot) of the target area with that obtained by using the infrared camera in normal operation mode (at 25 Hz frame rate). It can be observed a very good agreement among the three profiles.

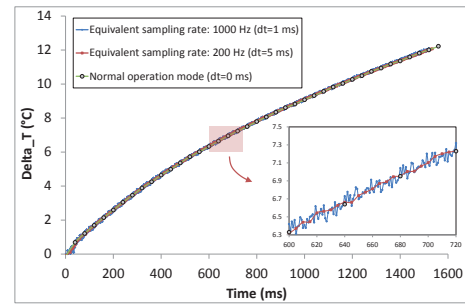


**Fig. 7: Reconstructed heating profiles of hottest point of target area, resampled at 200 Hz ( $dt = 5$  ms) and 1000 Hz ( $dt = 1$  ms). Values were measured by means of a cooled infrared camera operating at 25 Hz frame rate. The circles show temperatures recorded in normal operation mode.**

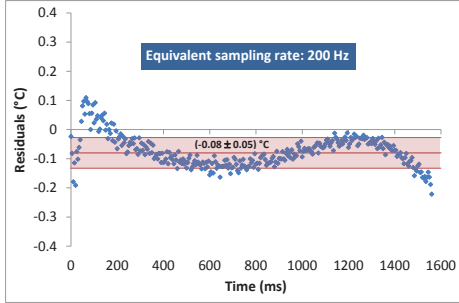


**Fig. 8: Statistical deviation between average values of the heating profile of the hottest point of the target area sampled at 200 Hz and third order polynomial fitting of the heating profile measured in normal operation mode.**

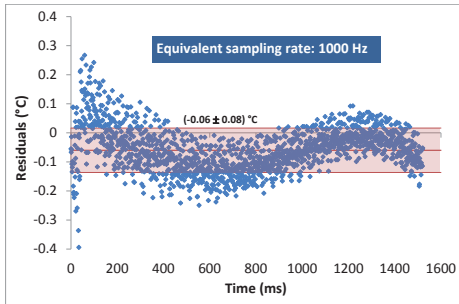


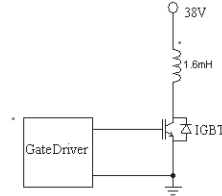
**Fig. 9: Statistical deviation between average values of the heating profile of the hottest point of the target area sampled at 1 kHz and third order polynomial fitting of the heating profile measured in normal operation mode.**

In order to assess the measurement accuracy of the reconstruction process, the statistical residuals between the average values of the heating profiles obtained by MTDA and the third order polynomial fitting of the heating profile measured in normal operation mode were evaluated. Results are shown for an equivalent sampling rate of 200 Hz and 1000 Hz in Figs. 8 and 9, respectively. An average error of  $(-0.08 \pm 0.05) ^\circ\text{C}$  and  $(-0.06 \pm 0.08) ^\circ\text{C}$  was obtained, with no evidence of systematic effects related to the increasing of the equivalent sampling rate.

#### 4. Application to reliability assessment of IGBT power device

The on-state voltage of power electronic devices tasked to perform several billions of repetitive

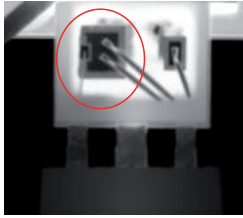
switching operations during their life is subject to modifications caused by the progressive ageing of semiconductor and metal layers. Endurance tests are the traditional way to monitor these changes in order to assess device reliability. However, they are very time expensive, requiring even months of uninterrupted laboratory tests. An interesting alternative is to assess the reliability through a suitable mathematical model. Specifically, coupling the results of a very fast thermodynamic analysis with a reliability model based on the Coffin–Manson law, device degradation over time can be estimated and the level of reliability evaluated [10]. The proposed MTDA method was applied to investigate the temperature distribution over the source metal surface of an IGBT power device during a switching cycle. According to the test circuit of Fig. 10, in each switching cycle the device is turned on for 6 ms to generate a fast heating, and then turned off for 60 s, a time sufficient to allow the device to reach again the initial temperature. The time delay was set to  $100 \mu\text{s}$  (corresponding to  $f_c = 10 \text{ kHz}$ ), therefore it was necessary to carry out 60 iterations to completely reconstruct the heating event. A 1.6 mH inductor is exploited to limit the device current during the switching cycle. The device under test (DUT) was previously subjected to a suitable accelerated ageing procedure, then, the package molding was chemically removed to expose the source metal surface, as shown in Fig. 11.



**Fig. 10: Test circuit for IGBT fast dynamics analysis.**

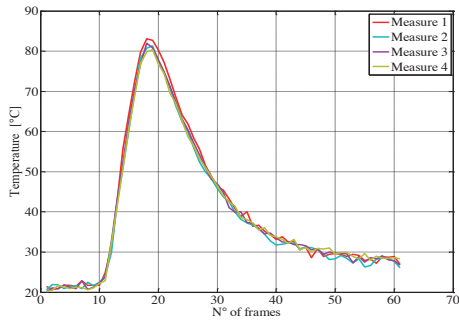
Since the exposed surface encompasses regions made of different materials (aluminum, oxides, passivation etc.), a suitable emissivity map is needed to obtain the true temperature mapping. This was done by passively heating the device at constant temperatures. Moreover, in order to focus the investigation exclusively on the region of interest, captured images were post-processed by applying a mask exploiting the different emissivity of the target area with respect to the outer part of the device, which is made of silicon oxide. Before further computation, each infrared image was masked and corrected for the actual emissivity. No microscope lens was used for this

test, hence the spatial resolution is poor because of the small dimension of the device.



**Fig. 11: Live IR image of DUT**

Fig. 12 reports the reconstructed normalized temperature profiles measured in avalanche mode on one point of the DUT surface. Typically, a maximum deviation of about 1.1 °C was observed at the peak point. This value is comparable to the measurement accuracy of the IR camera ( $\pm 1\%$  or  $\pm 1^\circ\text{C}$ ) as stated by the manufacturer.



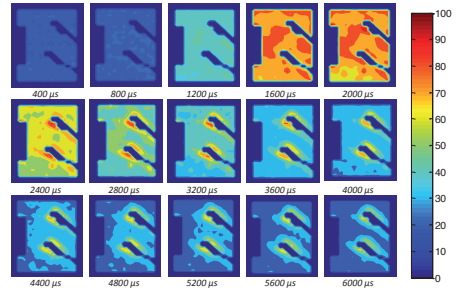
**Fig. 12: Normalized temperature profiles measured in avalanche mode on one point of the DUT surface (four cycles,  $dt = 100 \mu\text{s}$ ).**

Fig. 13 shows reconstructed temperature distribution maps of the DUT surface (in the figure, only images taken every 400  $\mu\text{s}$  are shown).

Though the spatial resolution of the images is rather low because of the lens system (50 mm, F/2) used to perform these preliminary tests, nevertheless, the obtained results reveal the potentiality of MTDA method in mapping thermal transient events at full frame with outstanding time resolution.

As far as the specific application is concerned, the ability to track the thermal evolution of IGBT power device allows important information to be obtained. For example, hot spots due to aging or failures as well as non-homogeneous current

density distributions and thermal instabilities can be easily detected.



**Fig. 13: Reconstructed temperature distribution maps of the DUT surface, sampled at 10 kHz equivalent frame rate ( $dt = 100 \mu\text{s}$ ).**

## 5. Conclusions

A novel method able to extend the area of application of standard infrared systems to the investigation of very fast replicable heating/cooling transient events has been presented. The method basically relies on triggering multiple time-delayed acquisitions (MTDA) of the observed thermal phenomenon, by means of a very precise and stable programmable digital micro-controller and by reconstructing the time domain IR sequence using the frames acquired at each trigger event. As a result, the time resolution of full frame IR sequences is increased by two order of magnitude or more with respect to that of a standard infrared camera. Preliminary results obtained on a power electronics device with the molding package removed are very promising. The presented method, originally developed to assess the reliability of power devices, could find application in other areas as well.

## References

- [1] Castellazzi A., Honsberg-Riedl M. and Wachutka G., "Thermal characterization of power devices during transient operation", *Microelectronics Journal*, vol. 37, pp. 145–151, 2006.
- [2] Irace A., Breglio G., Spirito P., R. Letor, S. Russo, "Reliability enhancement with the aid of transient infrared thermal analysis of smart Power MOSFETs during

short circuit operation", *Microelectronics Reliability*, vol. 45, pp. 1706–1710, 2005.

[3] Yin C.Y., Lu H., Musallam M., Bailey C. and Johnson C.M., "In-service reliability assessment of solder interconnect in power electronics modules", *Proceedings of Prognostics & Systems Health Management Conference*, paper MU3095, Macau, 5 pp., 2010.

[4] Breglio G., Rinaldi N., Spirito P., "Thermal mapping and 3D numerical simulation of new cellular power MOS affected by electro-thermal instability", *Microelectronics Journal*, vol. 31, pp. 741–746, 2000.

[5] Breitenstein O., Langenkamp M., "Lock-in contact thermography investigation of lateral electronic inhomogeneities in semiconductor devices", *Sensors and Actuators A*, vol. 71, pp. 46-50, 1998.

[6] Riccio M., Rossi L., Irace A., Napoli E., Breglio G., Spirito P., Tagami R., Mizuno Y., "Analysis of large area Trench-IGBT current distribution under UIS test with the aid of lock-in thermography", *Microelectronics Reliability*, vol. 50, pp. 1725-1730, 2010.

[7] Blackburn D.L., "Temperature measurements of semiconductor devices - A review", in *Proceedings of the 20th Annual IEEE Symposium on Semiconductor Thermal Measurement and Management*, San Jose, California, pp. 70–80, 2004.

[8] Rossi L., Breglio G., Irace A., Spirito P., "Thermal transient mapping systems for integrated semiconductor devices and circuits", in *Proceedings of 8th Quantitative InfraRed Thermography conference*, paper QIRT2006-022 Padua(Italy), 2006.

[9] Breglio G., Spirito P., "Experimental detection of time dependent temperature maps in power bipolar transistors", *Microelectronics Journal*, vol. 31, pp. 735–739, 2000.

[10] Testa A., De Caro S., Russo S., "A Reliability Model for Power MOSFETs Working in Avalanche Mode Based on an Experimental Temperature Distribution

Analysis". *IEEE Transaction on Power Electronics*, vol. 27, pp. 3093 – 3100, 2012.

[11] Testa A., De Caro S., Panarello S., Patanè S., Russo S., Patti D., Poma S., Letor R., "Reliability of planar, Super-Junction and trench low voltage power MOSFETs". *Microelectronics Reliability*, vol. 50, pp. 1789 - 1795, 2010.

[12] Riccio M., Breglio G., Irace A. and Spirito P., "An equivalent time temperature mapping system with a full-frame sampling rate", *Rev. Sci. Instrum.*, vol 78, n.10, pp. 106106, 2007.



# **MR-Thermometry Applied to Pancreas during Laser Ablation: Sensitivity Analysis of Two $T_1$ -Weighted Sequences**

E. SCHENA\*, P. SACCOMANDI\*, G. ALLEGRETTI\*, C. MASSARONI\*, and S. SILVESTRI\*

\* Università Campus Bio-Medico di Roma

## **Abstract**

*Magnetic Resonance Imaging (MRI) thermometry is a non-invasive technique appropriate for temperature distribution monitoring in tissues. This technique, through a multidirectional scan without use of ionizing radiation, estimates the temperature variation thanks to the thermal dependence of several MRI parameters (i.e.,  $T_1$  and  $T_2$  relaxation times, proton resonance frequency shift and others). The use of  $T_1$  shows some advantages, such as: low sensitivity to patient motion, high thermal sensitivity and linearity; on the other hand, the thermal sensitivity strongly depends on the organ tissue.*

*The aim of this study is to assess the sensitivity of MRI thermometry using two  $T_1$ -weighted sequences (i.e., IRTF and SRTF) and an 1.5-T MR scanner on healthy swine pancreases undergoing Laser Ablation (LA). The effect of temperature variation on the signal intensity was analyzed. The reference temperature was measured by MRI-compatible fiber optic sensors (fiber Bragg grating sensors). The sensitivity of the proposed techniques were estimated and compared. The IRTF sequence provides higher temperature sensitivity than the SRTF one ( $1.8 \pm 0.2$   $^{\circ}\text{C}^{-1}$  vs  $1.4 \pm 0.1$   $^{\circ}\text{C}^{-1}$ ) but the correlation between signal intensity and temperature variation is lower ( $R = -0.66$  vs  $-0.97$ ). Results show that the proposed technique may be adequate for temperature monitoring during LA.*

## **1. Introduction**

Laser Ablation (LA) is a minimally invasive procedure employed to treat tumor. Its safety and efficacy could be improved by performing a real-time temperature monitoring, hence several techniques have been investigated during the last thirty years. These techniques are usually divided in non-invasive approaches and invasive ones [1]. The interest on non-invasive approaches is motivated by the advantages related to the non-invasiveness and to the ability of these techniques

to provide a tridimensional map of tissue temperature. The most investigated non-invasive approaches are: 1) MRI thermometry, which is based on the sensitivity of several MRI parameters on temperature [2]; 2) CT-based thermometry, which is based on the influence of temperature on images obtained by Computed Tomography scans [3,4]; and 3) ultrasound-based thermometry, which is based on the dependence of several ultrasound parameters on temperature [5].

MRI thermometry shows some advantages, such as high thermal sensitivity, low sensitivity to motion, good linearity and it does not employ ionizing radiations [2].

The first investigation about the influence of temperature on MR parameters was conducted by Bloembergen et al. [6] in 1948, and Jolesz and coauthors developed the technique of MRI-guided LA [7]. Since the study of Jolesz (1988), a big research effort has been dedicated to assess the feasibility of MRI thermometry for temperature monitoring during LA, and among the several MR parameters,  $T_1$  relaxation time and proton resonance frequency (PRF) have been considered the most attractive [8].

The aim of this work is twofold: the sensitivity analysis of MRI thermometry for temperature monitoring of pancreatic tissues during LA; the comparison between the characteristics of MRI thermometry using two  $T_1$ -weighted sequences. The reference temperature for MRI thermometry characterization has been measured by MRI-compatible temperature sensors (i.e., fiber Bragg grating, FBG, sensors). To the best of our knowledge, this study represents the first investigation of MRI thermometry on pancreatic tissue, and this is important because of the influence of the tissue histological characteristics on  $T_1$  thermal sensitivity. A further novelty of this work is related to the use of new settings for the two employed  $T_1$ -based sequences.

## 2. Theoretical background

A number of MR parameters depend on temperature [2]: proton density,  $T_1$  and  $T_2$  relaxation time, magnetization transfer and proton resonance frequency (PRF) among others.

As is well known, after the transmission and the successive interruption of a radio frequency signal to the medium, proton spin reacquires the initial position and direction. The mechanisms of relaxation of the spin proton to recover the equilibrium status are described by two temporal parameters, i.e., spin-lattice relaxation time  $T_1$  and the transversal relaxation time  $T_2$ . Therefore, they provide information about the structure of the tissue. For application in temperature mapping the time  $T_2$  is not attractive because its thermal sensitivity is lower than the one of  $T_1$  [9] and because it can be masked by other factors [10]. Similarly, variations in the proton density can be influenced not only by temperature but also by other parameters, such as  $T_1$ . Therefore, mostly used parameters are  $T_1$  and PRF, because of their good sensitivity to temperature variation. The main limitation of the first parameter (i.e.,  $T_1$ ) is the sensitivity dependence on tissue; on the other hand, the negligible sensitivity to movement is its main advantage. PRF is not tissue-dependent and has a linear dependence from temperature in ranges wider than those of  $T_1$ ; however, PRF shows high sensitivity to movement, which can be an issue during *in vivo* applications [2].

We report in detail only the principles of  $T_1$ -based MRI thermometry because we used  $T_1$ -weighted sequences during experiments, as described in Section 3.

$T_1$  of water protons is a measurement of the time required to protons to return to the initial equilibrium conditions, after the interruption of the radio frequency signal, thanks to the transfer of energy to the surrounding micro-environment. Spin relaxation results from the interaction of the dipoles with the lattice, which is due to their translational and rotational motion. The temperature (T) dependence of this motion causes the  $T_1$  increase with T, which can be expressed as follows [2]:

$$T_1 \propto \exp\left(-\frac{E_a(T_1)}{k \cdot T}\right) \quad \text{Eq. 1}$$

where  $E_a(T_1)$  is the activation energy of the relaxation process,  $k$  is the Boltzmann constant, and  $T$  is the absolute temperature.

This relationship can be linearized in a wide temperature range (e.g., from 30 °C up to 70 °C):

$$T_1 - T_{1ref} = m \cdot (T - T_{ref}) \quad \text{Eq. 2}$$

where  $T_{ref}$  is the reference temperature,  $m$  is the thermal coefficient, empirically determined for

each tissue [11], and  $T_{1ref}$  is the  $T_1$  value at a temperature  $T_{ref}$ . Non-linear effects can occur if the tissue properties change, for instance they can change because of the tissue coagulation during LA. Furthermore, the thermal sensitivity of  $T_1$  depends on the tissue type (e.g., 1–2%·°C<sup>-1</sup> in liver, 1.4%·°C<sup>-1</sup> in bovine muscle, and 0.97%·°C<sup>-1</sup> in fat), therefore the previous knowledge of the thermal coefficient of each tissue is essential to obtain a temperature map. The research group headed by TJ Vogl is performing a deep analysis of  $T_1$  weighted images during LA of liver metastasis, and of liver-mimicking acrylamide gel phantom [12,13].

In order to monitor the tissue temperature during LA and during MRI scans, we employed fiber Bragg grating (FBG) sensors, which do not present artifacts because of their immunity from electromagnetic interferences and their MRI-compatibility [14]. They consist of a periodic variation in the reflective index of the fiber core. The grating is characterized by its spatial period,  $\Lambda$ , and the effective reflective index,  $n_{eff}$ . When interrogated with a broadband radiation, a narrow range of wavelengths is reflected, the other ones are transmitted. The reflected wavelengths range is centered around a specific value, i.e., the Bragg wavelength ( $\lambda_B$ ), expressed as follows:

$$\lambda_B = 2 \cdot \Lambda \cdot n_{eff} \quad \text{Eq. 3}$$

The  $\lambda_B$  variation ( $\Delta\lambda_B$ ) depends on the variation of temperature,  $\Delta T$ , and on mechanical strain,  $\epsilon$ . During LA, considering negligible the strain, the  $\Delta\lambda_B$  can be considered only dependent on the temperature increments and therefore it provides an indirect measurement of temperature increase during the treatment.

## 3. Experimental setup, data acquisition and processing

LA was performed on swine pancreases by a Nd:YAG laser ( $\lambda=1064$  nm) that conveyed the radiation into a fiber applicator. Each organ was placed into an MRI-compatible box (10x10x2 cm) composed of (poly)dimethylsiloxane (PDMS), necessary to insert the applicator and FBGs and to control their relative distances during LA. Figure 1a shows a 3-D view of the box and the positions of the laser applicator and the four fibers F1, F2, F3, F4, each of them equipped with 3 FBG sensors. The FBG sensors have a sensing element with 1 mm of length. The laser applicator was inserted into the tissue at a depth of 2 mm and at the center of the box.

Three FBGs (i.e., G1, G2 and G3) housed in each optical fiber, are placed at a distance of 2 mm each other; considering that the x-y plane of



the applicator is perpendicular to the plane of the optical fibers, the central FBG -i.e., G2- is placed at the same quote of the applicator (fig. 1b). The four fibers were placed at the same four positions in all the tests; these positions correspond to the center of the four Region of Interests (ROIs) which were selected to analyze the images.

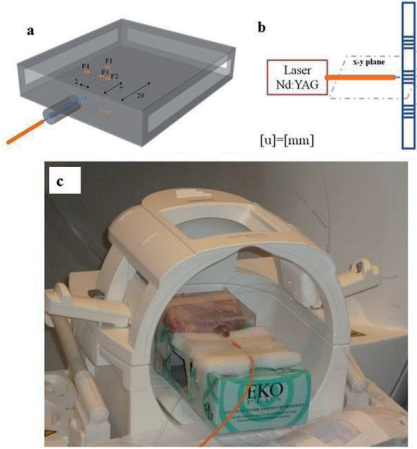


**Fig. 1:** a) polymeric box used to control distances between laser applicator and optical fibers F1, F2, F3, F4; b) arrangement of FBGs (G1, G2, G3) inside each fiber; c) pancreatic tissue inside the box placed within MR coils.

The heating process was monitored by an 1.5-T MR scanner (Siemens Magnetom Avanto, 1.5 T), using two  $T_1$ -weighted sequences: inversion recovery turbo flash (IRTF) and saturation recovery turbo flash (SRTF), fig. 1c. The variation of  $T_1$ , due to the increase of temperature (Eq. 2), causes the changes of image signal intensity,  $\Delta S$ , in  $T_1$ -weighted images. In order to obtain the thermal dependence of  $\Delta S$ , images were analysed in ROIs centered in correspondence of the FBG sensors. The FBGs output (Bragg wavelength,  $\lambda_B$ ) has been recorded by an optical spectrum analyzer, OSA (Optical Sensing Interrogator, sm125, Micron Optics). The OSA records the wavelength shift due to the temperature variation. The temperature increment during laser ablation is estimated by the calibration curve of the FBG sensors, which were calibrated in a wide range of measurement (i.e., from 18 °C up to 100 °C).

#### 4. Results and Discussion

In order to obtain the relationship between  $\Delta S$ , and the temperature increase,  $\Delta T$ , the averaged intensity of each ROI was synchronized and

correlated with the temperature values monitored by the FBGs.

First of all the noise of the images obtained using the two sequences has been analysed. We considered the standard deviation, std, of the pixels intensity in a ROI with no nuclear MR signal. The std was calculated considering a ROI with about 5000 pixels in two images, the first one obtained using SRTF and the second one using IRTF. The STRF image showed lower noise (std=0.67) than the IRTF image (std=1.2).

Regarding the analysis of pixel intensity (S) in the image representing the tissue, it must be considered that the std increases because of the tissue dishomogeneity. A typical histogram obtained considering a ROI of about 5000 pixels representing a pancreas is shown in fig. 2 for the two sequences.

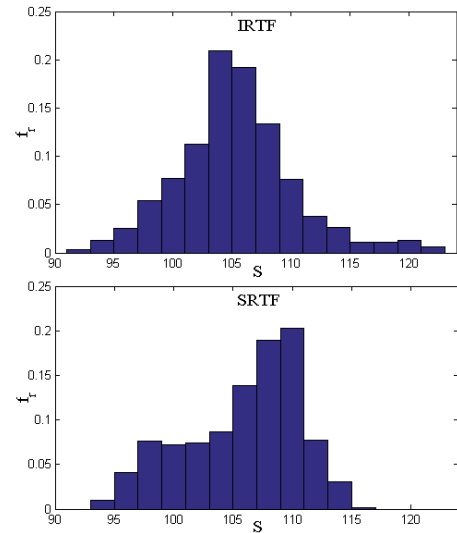


**Fig. 2:** histograms of the signal intensity of a ROI representing a pancreas obtained using the two sequences.

The std values of the image obtained by SRTF is slightly lower than the one obtained by IRTF (i.e., 4.8 and 5.1 for SRTF and IRTF, respectively). The tissue dishomogeneity should influence the performances of the MRI-thermometry.

After this preliminary analysis has been investigate the changes of signal intensity during the treatment, caused by the temperature increase. In particular, the value of  $\Delta S$ , which is the ROI value difference between the current and the reference image acquired at the beginning of the trial, has been calculated for all the MRI scans performed during the procedure. Figure 3 shows  $\Delta S$  as a function of  $\Delta T$ .

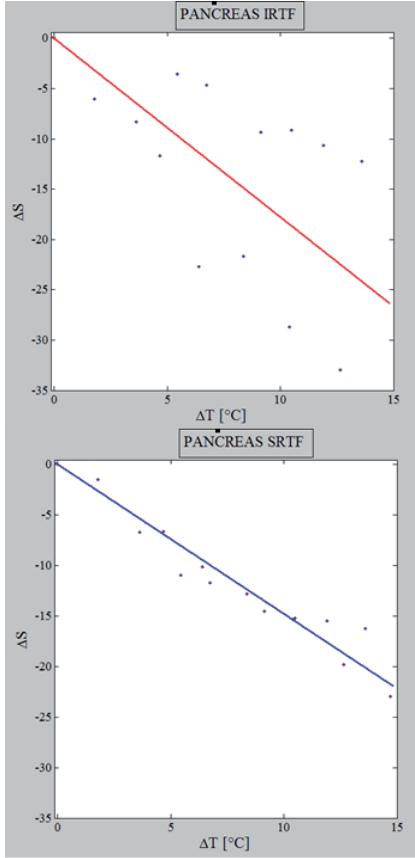


**Fig. 3: Signal intensity vs temperature for the two sequences. The best fitting lines are also shown.**

Figure 3 shows that the use of IRTF allows increasing the sensitivity: the slope of the best fitting line, which represents the thermal sensitivity, is  $1.8 \pm 0.2$   $^{\circ}\text{C}^{-1}$  using IRTF and  $1.4 \pm 0.1$   $^{\circ}\text{C}^{-1}$  using SRTF. On the other hand the correlation with  $\Delta T$  improves using SRTF, as shown in fig. 3 and confirmed by the values of correlation coefficient, R (i.e., -0.97 and -0.66 for SRTF and IRTF, respectively).

The  $\Delta T$  has been calculated by the calibration curve of the FBG sensors. All the FBG sensors were calibrated using an experimental set up composed of: *i*) an optical spectrum analyzer (Bragg Fiber Sensing, FS2200 8 CH, Sequoia Technology Group Ltd), which records the output ( $\lambda_B$ ) of the FBGs, *ii*) a PC to record the output data from the analyzer, *iii*) an oven to control the temperature, *iv*) a module to acquire and record the signal provided by four K-type thermocouples (FX106-4-2, YOKOGAWA®), *v*) a PC to process data.

The calibration was performed between 18  $^{\circ}\text{C}$  and 100  $^{\circ}\text{C}$ . The mean value of the measures obtained by the four thermocouples was used as reference for the FBGs calibration. The change of the Bragg wavelength ( $\Delta\lambda_B$ ) for each sensor during the whole process was recorded and synchronized with the temperature provided by the thermocouples in order to obtain the calibration curves of the FBGs by fitting the  $\Delta\lambda_B$  with T.

The curves have been obtained by a linear regression of the data. A typical curve was:

$$\Delta\lambda_B = 0.010 \cdot T - 0.25 \quad \text{Eq. 4}$$

Therefore the sensitivity of the FBGs was about  $0.010 \text{ nm}^{\circ}\text{C}^{-1}$ .

Figure 4 shows a comparison between the temperature increases measured by FBGs ( $T_{\text{ref}}$ ) and the ones estimated by the two sequences ( $T_{\text{IRTF}}$  and  $T_{\text{SRTF}}$ ) obtained by considering the two best fitting lines reported in fig. 3.

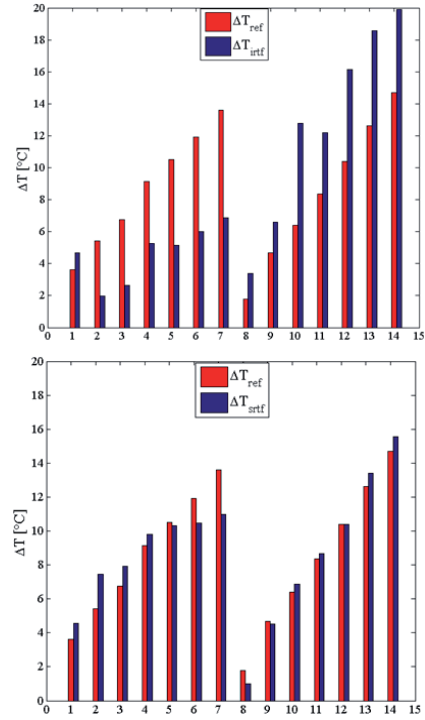


**Fig. 4: comparison between the temperature increases measured by FBG and by the two sequences. For both the sequences data obtained during the LA performed on two pancreases are reported.**

Data reported in Fig. 4 show that for the 14 scans performed during LA of two pancreases the

differences between the  $\Delta T$  estimated by SRTF sequence and the  $\Delta T$  estimated by FBGs are lower than the ones between the  $\Delta T$  estimated by IRTF sequence and the  $\Delta T$  estimated by FBGs. Considering the high accuracy of FBG measurement (i.e.,  $\approx 0.1$  °C), the T estimations performed by SRTF sequence have a smaller measurement error than the ones measured by IRTF. This consideration is also confirmed by the Root Mean Squared Error for the two sequences calculated as:

$$RMSE_{IRTF} = \sqrt{\frac{\sum_{i=1}^N (\Delta T_{ref} - \Delta T_{IRTF})^2}{N}} \quad Eq. 5$$

and

$$RMSE_{SRTF} = \sqrt{\frac{\sum_{i=1}^N (\Delta T_{ref} - \Delta T_{SRTF})^2}{N}} \quad Eq. 6$$

In fact the value of  $RMSE_{IRTF}$  resulted bigger than the one of  $RMSE_{SRTF}$  (i.e.,  $8.3$  °C vs  $1.8$  °C)

The improvement obtained by performing the estimation by SRTF has also confirmed by the Bland Altman analysis: the narrow range defined by the limit of agreements (LOAs) for SRTF (i.e., from  $-2.3$  °C to  $2.1$  °C) confirms the better precision of these measures than the ones obtained by IRTF (i.e., from  $-9.4$  °C to  $9.1$  °C); also the mean of differences (MODs) show a low value (i.e.,  $0.1$  °C for both the sequences).

## 5. Conclusion

Summing up, the sensitivity during LA on healthy porcine pancreas of two  $T_1$ -weighted sequences has been evaluated by comparing the  $\Delta S$  with the  $\Delta T$  measured by MRi compatible sensors based on fiber Bragg technology. The SRTF sequence has shown lower sensitivity than the IRTF one; on the other hand it shows a better precision than IRTF.

In conclusion, we have investigated the feasibility of MR-based thermometry for monitoring pancreatic tissue temperature during LA, and the two  $T_1$ -weighted sequences can be assessed positively considering the MOD and LOA values especially for the pancreas SRTF sequence:  $MOD_{SRTF} = -0.1$  °C and  $LOA_{SRTF} = [-2.3; 2.1]$  °C. Moreover, SRTF and IRTF are standard sequences, therefore commonly used in clinical practice for the traditional analysis.

Real time MR-based thermometry could represent a valuable tool to lead the physician in

the optimal laser settings during thermal ablation procedure. This technique is particularly attractive for LA due to the laser MR-compatibility.

## Reference

- [1] P Saccomandi et al. "Techniques for temperature monitoring during laser induced thermotherapy: An overview" *Int J Hyperthermia*, 2013, 609-619, DOI: 10.3109/02656736.2013.832411.
- [2] V Reike, et al. "MR Thermometry" *J Magn Reson Imaging*, 2008, 376-390, DOI: 10.1002/jmri.21265.
- [3] E Schena et al., "Experimental assessment of CT-based thermometry during laser ablation of porcine pancreas" *Phys Med Biol*, 2013, 5705-16, DOI: 10.1088/0031-9155/58/16/5705.
- [4] F Fani et al. "CT-based thermometry: an overview" *Int J Hyperthermia*, 2014, In press, DOI:10.3109/02656736.2014.922221.
- [5] KW van Dongen et al., "A feasibility study for non-invasive thermometry using non-linear ultrasound" *Int J Hyperthermia*, 2011, 612-24, DOI: 10.3109/02656736.2011.599357.
- [6] N Bloembergen et al., "Relaxation effects in nuclear magnetic resonance absorption" *Phys Rev* 1948,679-712, DOI: <http://dx.doi.org/10.1103/PhysRev.73.679>
- [7] FA Jolesz FA et al. "MR imaging of laser-tissue interactions" *Radiology* 1988, 249-53.
- [8] McDannold N. "Quantitative MRI-based temperature mapping based on the proton resonant frequency shift: Review of validation studies". *Int J Hyperthermia* 2005, 533-46, DOI:10.1080/02656730500096073
- [9] Parker DL. "Applications of NMR imaging in hyperthermia: An evaluation of the potential for localized tissue heating and noninvasive temperature monitoring". *IEEE Trans Biomed Eng* 1984,161-7.
- [10] SJ Graham et al. "Time and temperature dependence of MR parameters during thermal coagulation of ex vivo rabbit muscle". *Magn Reson Med* 1998,198-203, DOI:10.1002/mrm.1910390206
- [11] HE Cline et al., "Magnetic resonance-guided thermal surgery" *Magn Reson Med*, 1993, 98 106, DOI: 10.1002/mrm.1910300115
- [12] Vogl TJ et al. "MR-guided laser-induced thermotherapy (LITT) of liver tumours: Experimental and clinical data" *Int J Hyperthermia* 2004;20: 713-24, DOI:10.1080/02656730400007212
- [13] Bazrafshan B et al. "Temperature imaging of laser-induced thermotherapy (LITT) by MRI: Evaluation of different sequences in phantom" *Lasers Med Sci*, 2014,173-83, DOI:10.1007/s10103-013-1306-5

- [14] Taffoni F et al. "Optical fiber-based MR compatible sensors for medical applications: an overview." *Sensors*, 2013: 14105-14120, DOI:10.3390/s131014105

# Vibration measurements for contact topology assessment in a rolling contact fatigue bench

Lancini M., Bodini I., Vetturi D., Pasinetti S., Mazzù A., Solazzi L., Petrogalli C., Faccoli M.

Department of Mechanical and Industrial Engineering – University of Brescia - Italy

## Abstract

*Rolling contact fatigue (RCF) plays a critical role in railway components, and the characterization of materials used, in terms of RCF life, is still an open task, made complex by the interactions of different phenomena, such as wear, cyclic contact, and ratcheting.*

*The presented case study regards a bi-disk test bench, used to evaluate the RCF behaviour of wheel and rail steels. In the test, a wheel steel specimen rotates against a rail steel specimen, while pressed, the one against the other, by a constant force.*

*A numerical simulation, based on a multiple source damage model and on parameters obtained from direct measurements during the test, is then used to determine properties of the material.*

*The contact surface, in particular, plays a key role in determining the evolution of an RCF life test, since it has a direct impact on the pressure exerted and can change during the test, due to wear.*

*The procedure proposed aims at using vibrations of a test bench during RCF-life tests to identify the contact topology, specifically understanding when damage phenomena cooperate to cause a quick flattening of the surface, and when this process is complete.*

## 1. Introduction

Characterization of RCF life of materials is critical in railway applications due to the fact that cyclic, localized stresses lead to rolling contact fatigue (RCF) phenomena, which can cause severe damage and sudden failure of a component.

Wear, also, is a common phenomenon occurring on both rail and wheels, but its interaction with RCF is not always detrimental: in specific conditions (uniformity, low rate, stability), it could optimize contact geometry, increasing RCF life, while, in non-optimal conditions, it could reduce RCF life. Moreover, the high shear stress has to be taken into account, leading to a complex combination of concurring damage phenomena [1,2]. Models describing cyclic plasticity are available in

literature, although their results are not reliable if material parameters are obtained by laboratory tests in standard stress condition [3,4], especially due to a different propagation mechanism [5].

A reliable procedure to analyse RCF-wear interaction would be to carry on accelerated RCF tests on controlled slip ratio conditions with multiple specimens, interrupting the test at different times and performing destructive analysis on the specimen, which is costly and time consuming.

The alternative proposed it to perform a single RCF test, monitoring different mechanical quantities to detect changes in the process.

## 2. Materials

The proposed procedure was applied to a pair of wheel and rail materials (ER8 EN13262 and UIC 900A respectively), as a case study.

The wheel specimens were 60-mm wide and 10-mm thick cylindrical disks, while the rail specimens were 59.5 mm in diameter, a 10 mm thickness and had a crowning radius of 200 mm, to prevent any border effect on the contact surface.

The mechanical properties of wheel rims and rail heads of the manufacturer are reported in Table 1.

Steel	ER8	900A
Ultimate tensile stress [MPa]	940	930
Monotonic yield stress [MPa]	590	470
Cyclic yield stress [MPa]	470	390
Necking [%]	54	26
Elongation [%]	17	14
Brinell hardness [HB]	230-255	296

Table 1. Mechanical properties of the steel used

Three different contact pressure levels were tested, in two different sliding ratio conditions, for a total of 6 different rolling/sliding parameter

combination, here reported in Table 2. Vibration recordings from those with highest sliding ratio ( $S=3\%$ ) and with the highest nominal pressure ( $P=1500$  MPa) were also examined using the proposed procedure.

ID	L Contact load [N]	R Rolling speed [r.p.m.]	S Sliding ratio [%]	P Nominal contact pressure [MPa]
A	1,500	516.0 (R) 492.5 (W)	3	1,100
B	2,490	516.0 (R) 492.5 (W)	3	1,300
C	3,830	516.0 (R) 492.5 (W)	3	1,500
D	3,830	511.0 (R) 497.5 (W)	1	1,500
E	2,490	511.0 (R) 497.5 (W)	1	1,300
F	1,500	511.0 (R) 497.5 (W)	1	1,100

Table 2. Test parameters (W=wheel, R=rail)

### 3. Methods

#### 3.1. Measurement system

The test bench used is a bi-disk machine dedicated to study interactions between two components subjected to cyclic contact in different load conditions, already presented in previous works by the authors [6], and whose general layout could be found in Figure 1.

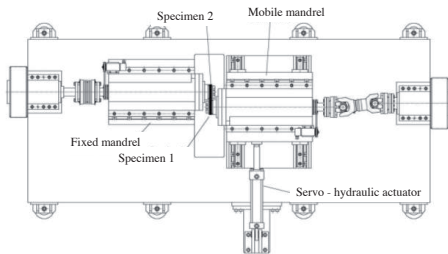


Figure 1: Test bench layout

The contact load, up to 70 kN, is maintained thanks to a servo-hydraulic actuator enabling the sliding of one of the mandrels, while two independent 33 kW engines provide the specimens rotation. Both engines and the actuator are controlled to perform tests at given slip ratio, rotating speed, contact force and engine torque.

On both mandrel supports, piezo-accelerometers were positioned, one in the vertical and one in the horizontal plane, both normal to the rotation axis and having a sensitivity of  $0.98 \text{ V/(m/s}^2\text{)}$  and a linear bandwidth in the 5-20 kHz range.

The signals from the two accelerometers, as well as those from a torque sensor, positioned on the sliding mandrel, were acquired by means of a configurable data acquisition system at a 5 kHz synchronous sampling frequency.

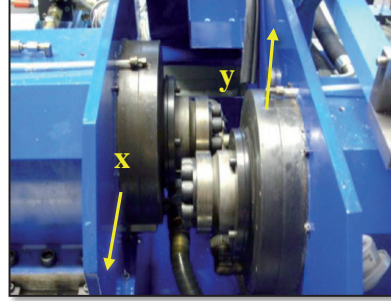


Figure 2: specimens mounted on mandrels. The accelerometers measuring axes are highlighted

An L101b-2k BASLER linear array camera, in a setup leading to a resolution of  $1 \mu\text{m}$  on the specimen mid surface, in sync with the bench rotation, was also used to monitor contact surface conditions of both specimens, but, due to lubrication, it was only used at regular intervals while the test was on halt.

Every  $2 \times 10^5$  cycles the test was halted to perform weighing with a precision scale (0.01 g resolution), to evaluate weight loss due to wear.

At the end of each test samples were cut in mid-thickness, polished and etched (using 2% Nital) and inspected using an optical microscope to measure the plastic flow.

Following this, RCF crack paths were also sought using a LEO EVO-40XVP scanning electron microscope with a microprobe, and  $HV_{10}$  micro-hardness was measured at different depths on the cross-section of each sample.

#### 3.2. Mechanical Model

While vibration analysis is commonly used to detect faults on gears and bearing components [7-10], its use in material characterization is limited, as this is usually carried on with standardized methods, generally involving destructive testing or evaluation at the end of test.

In previous works [11] a damage indicator, estimated from vibrations and correlated to surface cracks was proposed. Following the same approach the two specimen interactions are synthesized, as it



is common in a modal analysis, using frequency transfer functions (FRF) between torque  $T$  and accelerations in the  $x$  and  $y$  directions, as depicted in Figure 3.

The idea behind this approach is that any variation in the material or geometry of the samples would be reflected by a simultaneous change in the FRFs values, helping identifying when crowing gets flattened and the process duration.

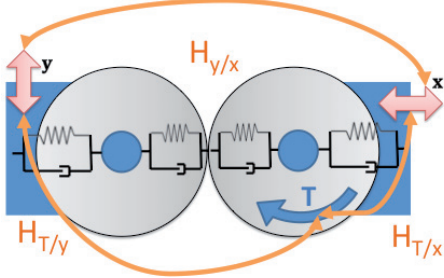


Figure 3: Simplified FRF based model

FRFs were numerically computed as the  $H_{a/b}$  cross-spectrum between a signal  $a$  and a signal  $b$ , divided by the autospectrum of signal  $b$ . In particular, the quantities monitored were the transmissibility  $H_{y/x}$ , between the  $y$  acceleration on the fixed mandrel support along the vertical axis and the  $x$  acceleration of the moving mandrel support along the pneumatic actuator axis, as well as the rotating inertances  $H_{x/T}$  and  $H_{y/T}$  between the  $x$  and  $y$  accelerations and the torque  $T$  measured on the rotating axis of the sliding mandrel. To provide a complete set of transfer function indicators, the reciprocals to those three quantities were also computed, resulting in the computation of  $H_{x/y}$ ,  $H_{T/x}$  and  $H_{T/y}$ .

Though all these quantities are related to properties of the system, such as masses and stiffnesses, their connection to any proper mechanical parameter would require an overly complex multiple degree of freedom model, which would exceed the scope of this research. Therefore their absolute values are not considered meaningful *per se*, and only their variation from their initial value of each test has been taken into account.

### 3.3. Preliminary tests

Preliminary tests were carried on to select which quantity to monitor and the frequency range in which the changes sought have a higher impact.

To avoid misreadings due to external or uncorrelated sources of vibrations, the test bench was monitored while running in jog mode, as well as in full operational mode, but without any load

applied between the samples. A power spectral density analysis of  $x$ ,  $y$  and  $T$  signals, recorded for about 100 s, and averaged using a 1 Hz spectral resolution, revealed that their frequency content was located below 400 Hz, while the same analysis performed in the final phases of standardized RCF tests revealed vibrational phenomena up to 1,000 Hz.

An experimental modal analysis of the pneumatic actuator, also, pointed out a resonance frequency lower than 100 Hz, therefore, the spectral quantities monitored were treated using a band-pass filter between 400 and 1,000 Hz.

A comparison between the quantities monitored during a full test of an unrelated rail/wheel couple [11], here reported in Figure 4, pointed out how the FRF between torque and acceleration along the linear actuator axis, and its reciprocal, displayed a sensible change, coherent with other damage indicators, and a behaviour less affected by spikes associated with accidental impacts or other impulsive events due to the uncontrolled environment in which the bench operates.

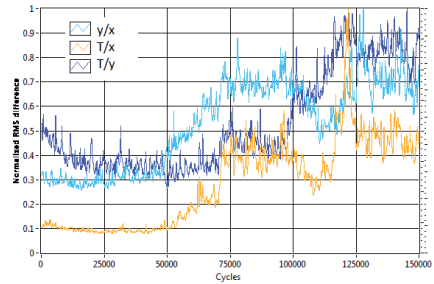


Figure 4: comparison between  $H_{y/x}$ ,  $H_{T/x}$  and  $H_{T/y}$ , other indicators pointed out a wear rate change after 60,000 and 100,000 cycles [11]

### 3.4. Vibration analysis

Using the acquired data, the transfer function  $H_{T/x}(\omega)$  between torque and acceleration was computed averaging 5 windows of 1 s, thus producing a spectrum of 1 000 lines every 5 s.

The initial modal properties of the system made up by the test bench and the intact specimens were assessed by averaging the  $H_{T/y}(\omega)$  values of the first 2500 cycles, thus assumed as a set of reference values  $H_{T/x}^{ref}(\omega)$ .

To point out changes in the system, the difference  $d_{T/x}(\omega)$  between the current status and the reference value, for each frequency resolution  $\omega_i$ , has been computed, then the synthetic index  $D_i$  has been evaluated as the root mean square (RMS) summation for all frequencies, as shown in Equation 1.

$$D_{T/x} = \frac{1}{n} \sqrt{\sum_{i=1}^n (H_{T/x}(\omega_i) - H_{T/x}^{ref}(\omega_i))(H_{T/x}(\omega_i) - H_{T/x}^{ref}(\omega_i))^*} \quad (1)$$

To further smooth the resulting signal, given the relative slow process, the RMS value was averaged on a 30 s window. The same procedure, here illustrated in Figure 5, was performed for the reciprocal  $H_{x/T}$ , leading to an indicator  $D_{x/T}$ , which was also monitored during the RCF tests.

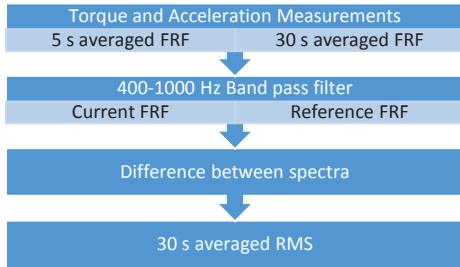


Figure 5: Signal processing procedure's step

## 4. Results

### 4.1. Vibrations

The values of  $D_{x/T}$  for the four tests under scrutiny are reported in Figure 6. All three tests with a high

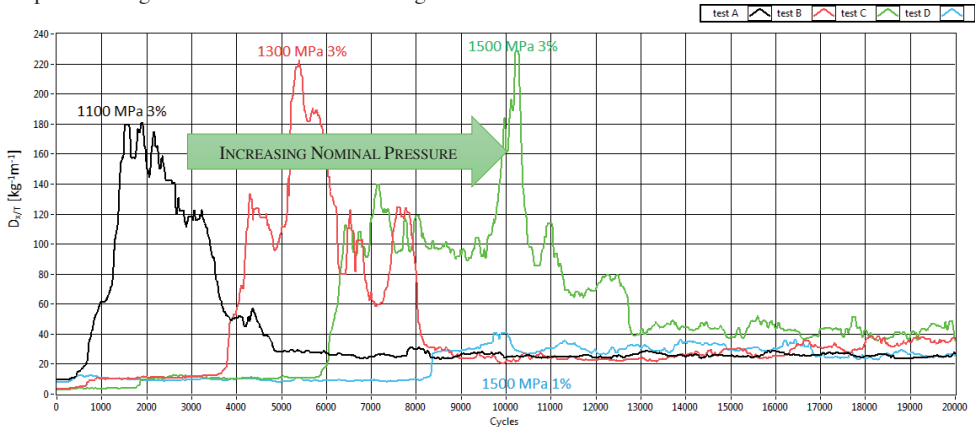


Figure 6:  $D_{x/T}$  indicators for tests A (black), B (red), C (green) and D (cyan)

### 4.2. Weight loss

The **wear rate**, in terms of weight loss as a function of cycle number, with varying nominal contact pressure  $P$ , is shown in Figure 7 and Figure 8 for sliding ratios  $s = 1\%$  and  $s = 3\%$  respectively. Given the substantially linear relationship between weight loss and cycle number in the steady state period of the wear curves, the wear rates were calculated from the linear best fit of the

sliding ratio level (3%) report a steep increase in value (from 10 to more than  $100 \text{ kg}^{-1} \text{ m}^{-1}$ ), after few thousand cycles, followed by an abrupt decrease after a variable amount of cycles, then settling around a stationary level ( $30 \text{ kg}^{-1} \text{ m}^{-1}$ ).

The last test, with a 1% sliding ratio, displayed only a slight increase after 8,000 cycles to a stationary level ( $20 \text{ kg}^{-1} \text{ m}^{-1}$ ).

Such behaviour could be used to identify a time frame, characterized by higher  $D_{y/T}$  levels, during which the damage process is clearly different than the initial or stationary stages: the approximate onset and duration of these periods are reported in Table 1.

ID	Onset	Offset	Duration	
	[cycles]	[cycles]	[cycles]	[s]
A	700	4,700	4,000	480
B	3,800	8,500	4,700	560
C	6,000	12,700	6,700	800
D	-n/a-	8,200	-n/a-	-n/a-

Table 1: onset and duration of high  $D_{y/T}$  levels

experimental points. Their values increased as nominal contact pressure and sliding ratio increased. The wear rate in general was higher for the rail steel samples, despite the surface damage was more severe for the wheel steel ones: this means that wear mitigates the effect of surface pitting by removing damaged layers. This linear wear rate behavior suggests a stationary contact geometry already achieved before the first measurement (after 200,000 cycles), while the difference between 3% and 1% sliding ratio tests



points out a decreased wear rate associated with the lower sliding condition.

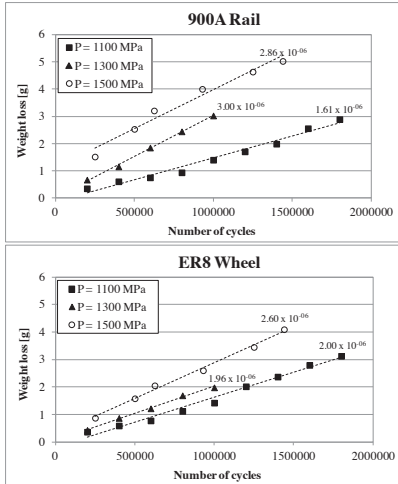


Figure 7: 1% sliding test weight loss for rail (upper) and wheel (lower)

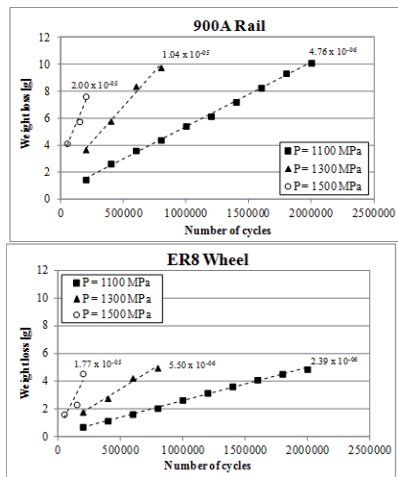


Figure 8: 3% sliding test weight loss for rail (upper) and wheel (lower)

### 4.3. Surface images

Shape changes due to wear and RCF were assessed by measuring the worn portion of the wheel specimen as shown on images recorded by the linear camera before test and after 200,000 cycles, here displayed in Figure 9 to Figure 12.

The worn portion was identified by manually selecting the image area of the specimen surface where linear patterns, due to the specimen machining during production, were not present, or were only partially visible. The process was

repeated on 20 images per sample and then the ratio between damaged and visible area was averaged and multiplied by the nominal thickness of the specimen. When no clear traces of the original surface of the wheel specimen was identified in the image, the whole surface (10.0 mm) was considered as damaged.

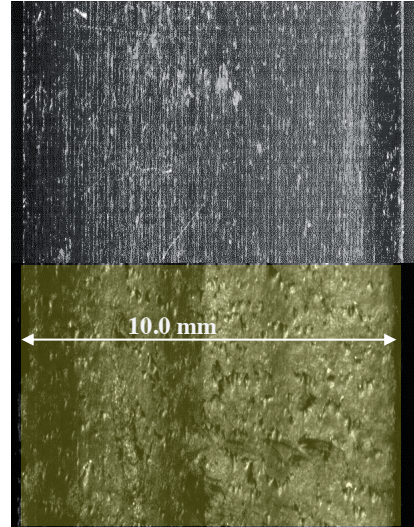


Figure 9: wheel contact surfaces before and after the first 200,000 cycles for test A  
Area worn by contact is highlighted.

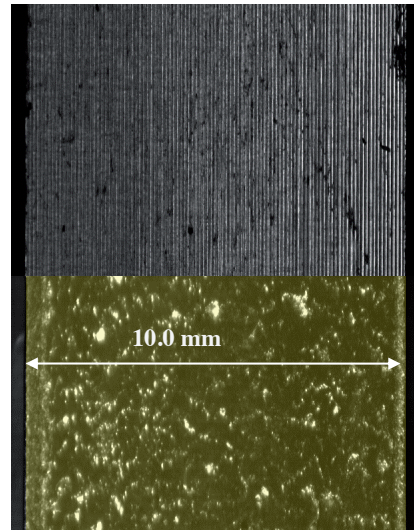


Figure 10: wheel contact surfaces before and after the first 150,000 cycles for test B  
Area worn by contact is highlighted.

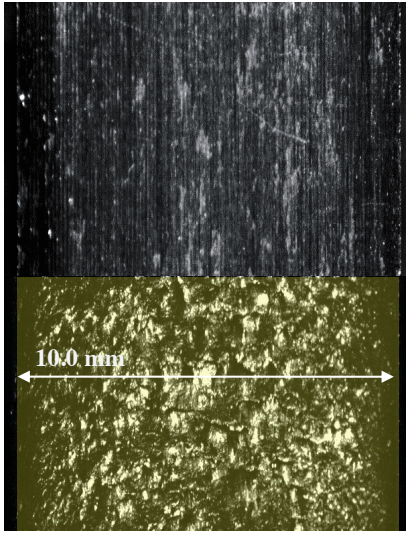


Figure 11: Wheel contact surfaces before and after the first 200,000 cycles for test C  
The area worn by contact is highlighted

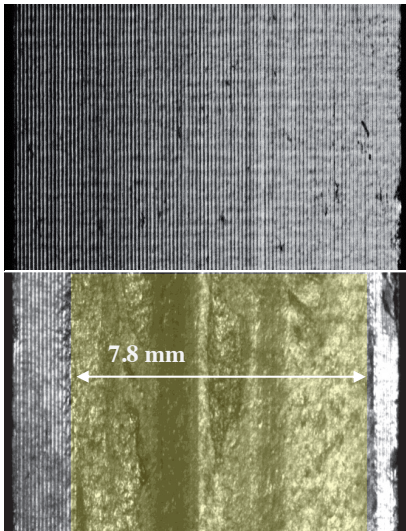


Figure 12: Wheel contact surfaces before and after the first 200,000 cycles for test D  
The area worn by contact is highlighted.

#### 4.4. Scanning Electron Microscope

The inspection of specimen sections pointed out that the main damage mechanism, in both rail and wheel steels sample, was ratcheting, initiating cracks which propagate to cause RCF failure.

Figure 13 shows the RCF crack path for various test conditions: the rail steel samples (a and c) were

always less damaged than the wheel steel ones (b and d) in all tested conditions, and presented only surface cracks. In addition, the wheel steel sample also presented subsurface cracks.

All surface and subsurface cracks analyzed display a shallow angle to the surface and follow the plastically deformed material during their growth.

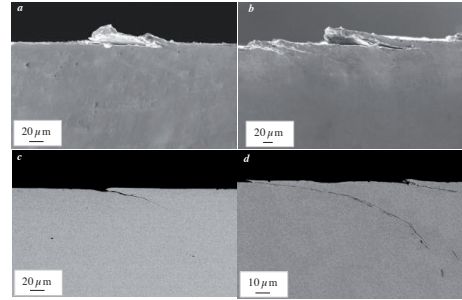


Figure 13: RCF crack path in: a) rail steel sample tested at  $s = 1\%$  and  $P = 1,500$  MPa; b) wheel steel sample tested at  $s = 1\%$  and  $P = 1,500$  MPa; c) rail steel sample tested at  $s = 3\%$  and  $P = 1,300$  MPa; d) wheel steel sample tested at  $s = 3\%$  and  $P = 1,300$  MPa

#### 4.5. Micro-hardness

After tests were completed, micro-hardness measurements were taken at different depths for each specimen. The resulting hardness profiles are shown in Figure 14.

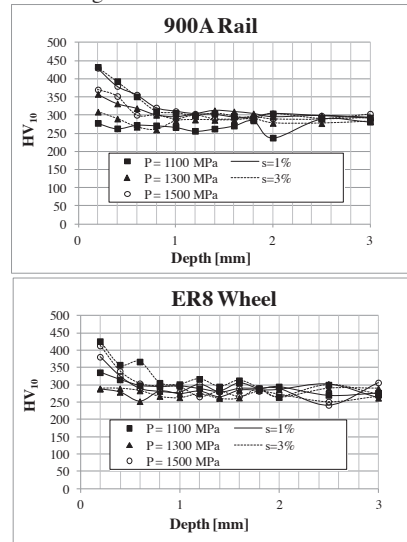


Figure 14: Micro-hardness profiles on the cross-section of rail and wheel steel samples

A higher hardening was observed in tests with higher sliding ratios and contact pressures, involving layers between 0.4 to 0.8 mm.

## 5. Discussion

The plastic behaviour was numerically simulated using a formulation by Mazzù for rolling contact [13], to predict plasticization in a two-dimensional plane-strain half-space subjected to contact pressure and friction, also taking into account wear as a concurring phenomenon removing layers from the surface.

The micro-hardness profiles pointed out a behaviour associated with isotropic hardening, which allowed for a model simplification, supposing a linear relationship between yield stress and hardness increase [14].

The images taken after the first 200,000 cycles, displayed in Figure 9 to Figure 12, allowed to prove that wear flattened the rail specimen, thus increasing the contact surface and reducing the actual contact pressure exerted.

Vibrations analysis, in particular of the first 20,000 cycles reported in Figure 6, identified a timeframe in which the flattening process was occurring.

Time and extent of the flattening allowed to replace the standard point Hertz contact in the model with a line contact surface, with a track width of 10 mm (8 mm for the 1% sliding ratio), occurring at the very beginning of the RCF simulations, as shown in Table 2.

ID	Nominal contact width	Contact width used	Width reported since
	[mm]	[mm]	[cycles]
A	1.785	10	4,700
B	2.113	10	8,500
C	2.440	10	12,700
D	2.440	8	8,200

**Table 2: onset and duration of high Dy/T levels**

The material properties needed for the simulation were calibrated by iteratively repeating simulation until the predicted displacements of material points due to plastic flow were in agreement with the experimental ones.

The superposition of the calculated displacements on the observed grain boundaries, for two different test conditions, is presented in Figure 15. A good agreement between the two is evident.

The simulation correctly predicted that the cracks and plasticized layers cannot be deeper than 40-50  $\mu\text{m}$ , even though the ratchetting never stops, because wear removes plasticized and cracked

layers from the surface, preventing deep crack propagation.

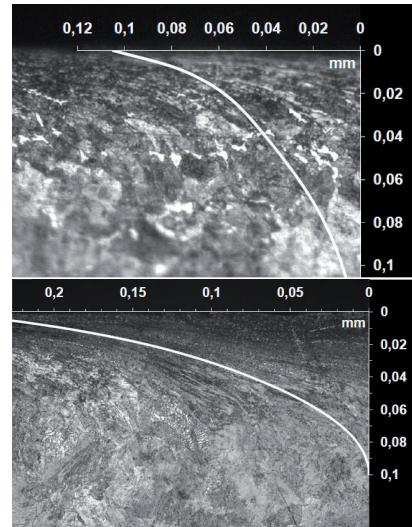


**Figure 15: Superposition of calculated and observed plastic strain bands in tests with  $s = 1\%$  and  $P = 1,100 \text{ MPa}$  (left), and  $s = 1\%$  and  $P = 1,300 \text{ MPa}$  (right), after 2,000,000 cycles**

## 6. Conclusions

A procedure to assess the presence, onset and duration of collaborative RCF and wear phenomena leading to contact shape alteration was proposed. The approach was applied to a wheel and rail steels characterisation procedure based both on rolling-sliding contact tests, on disk specimens, and numerical simulation.

The advantage of the proposed method rests in its non-destructive and in-line nature, therefore allowing for a continuous assessment without halting tests or interfering with the specimens.

This procedure completes the described full RCF failure life test, and allows to correct numerical models required to characterize the materials. It points out phenomena whose duration is too short to be taken into account by the same numerical model describing, for the whole RCF life of the specimen, the different damage phenomena and their interactions in a complex case as cyclic contact.

## Acknowledgements

The authors are grateful to Silvio Bonometti and Valentina Ferrari for their support in the experimental activities, and to Franco Docchio for careful reading and revision.

## References

1. Zerbst U., Beretta S., "Failure and damage tolerance aspects of railway components", *Engineering Failure Analysis*, 2011, 18 pp. 534-542
2. Donzella G. et al. "Progressive damage assessment in the near-surface layer of railway wheel – rail couple under cyclic contact", *Wear*, 2011, 271(1-2), pp. 408-416
3. Fedele R., Filippini M., Maier G., "Constitutive model calibration for railway wheel steel through tension-torsion tests", *Computers & Structures*, 2005, 83(12-13), pp. 1005-1020.
4. Liu Y., Stratman B., Mahadevan S., "Fatigue crack initiation life prediction of railroad wheels", *International Journal of Fatigue*, 2005, 28, pp. 747-756.
5. Liu Y., Liu L., Mahadevan S., "Analysis of subsurface crack propagation under rolling contact loading in railroad wheels using FEM", *Engineering Fracture Mechanics*, 2007, 74, pp. 2659-2674.
6. Solazzi L. et al. "Rolling contact fatigue damage detected by correlation between experimental and numerical analyses", *Structural Durability and Health Monitoring*, 2012 8(4), pp 329-340
7. Nohál, L., et al., "An experimental investigation of rolling contact fatigue of steels using acoustic emission method." *Insight: Non-Destructive Testing and Condition Monitoring*, 2013. 55(12): p. 665-669.
8. Byington, C.S., et al., "Shaft coupling model-based prognostics enhanced by vibration diagnostics." *Insight: Non-Destructive Testing and Condition Monitoring*, 2009. 51(8): p. 420-425.
9. Roemer, M.J., C.S. Byington, and J. Sheldon, "Advanced vibration analysis to support prognosis of rotating machinery components." *International Journal of COMADEM*, 2008. 11(2): p. 2-11.
10. Sakanaka, N., et al. "Development of ultrasonic torsional fatigue tester to evaluate rolling bearing steels." 2012.
11. Solazzi, L., C. Petrogalli, and M. Lancini. "Vibration based diagnostics on rolling contact fatigue test bench." *Procedia Engineering* 2011, 10 p 3465–3470.
12. Mazzù A., et al. "Una procedura sperimentale e di calcolo per l'analisi del danneggiamento in materiali innovativi per ruote ferroviarie", *AIAS* 2014, 402
13. Mazzù A., "Surface plastic strain in contact problems; prediction by a simplified non-linear kinematic hardening model", *Journal of Strain Analysis*, 2009, 44(3) pp. 187-199
14. Lai M.O., Lim K.B. "On the prediction of tensile properties from hardness tests", *Journal of Material Science*, 1991, 26, pp. 2031-2036



# Monte Carlo simulations of a stability monitoring system based on tracking cosmic rays

Ileana Bodini\*, Gabriele Baronio\*, Germano Bonomi\*, Antonietta Donzella\*, Francesco Fallavollita\*\*, Matteo Lancini\*, Simone Pasinetti\*, David Vetturi\*, Paolo Vitulo\*\*, Aldo Zenoni\*, Gianni Zumerle\*\*\*

\* Department of Mechanical and Industrial Engineering, University of Brescia

\*\* Department of Physics, University of Pavia

\*\*\* Department of Physics and Astronomy, University of Padua

## Abstract

*This paper describes the results of preliminary Monte Carlo simulations to investigate feasibility, performances and limitations of an original application of cosmic ray tracking to monitor static stability of civil structures, in particular historical buildings, where conservation constraints are severe and the time evolution of eventual deformation phenomena may be of the order of months or years. The simulated system consists of three or more particle detectors vertically aligned and linked together with the considered building. When a cosmic ray crosses all the measuring detectors, its track can be reconstructed and the reciprocal position of detectors can be determined. Continuous measurements allow to ascertain possible variations in detector positions related to deformations of the studied building.*

## 1. Introduction

At the sea level, cosmic ray radiation is mostly composed of high energy muons that continuously hit the Earth's surface at a rate of 10000 muon/(m<sup>2</sup>·min). Their energy distribution has a mean value of 3 GeV with a long tail at high energies and their angular distribution has its maximum value around the zenith direction [1].

Cosmic rays are largely exploited in nuclear and elementary particle physics for detector testing and calibration, and for the alignment of detectors in the very complex apparatuses used in this field [2]. Recently, cosmic ray muons are being increasingly considered as a source of natural, free, ubiquitous, high-penetration radiation of potential use for a number of applications: from monitoring in geology [3, 4, 5] to iron and steel industry [6], from security purposes [7, 8, 9, 10, 11, 12] to monitoring alignment and stability of large mechanical and civil structures [13, 14, 15].

The present study regards preliminary Monte Carlo simulations to investigate the feasibility,

performances and possible limitations of a system based on cosmic ray muon tracking, that monitors stability of the “Palazzo della Loggia”, shown in Fig. 1, an historical civil building, seat of the municipal hall in the town of Brescia, in Italy. The top beam of its vaulted wooden roof has undergone a progressive deflection of 1 mm per year [16]. In particular, the standard measurement uncertainty, as a function of time, has been assessed, and the results have been discussed in comparison with a conventional monitoring system. Moreover, possible developments of the proposed technique have been considered and discussed, in order to improve the performances of the measurement system.



Fig. 1: A picture of the Palazzo della Loggia, located in Brescia, Italy.

## 2. The case study: the Palazzo della Loggia

### 2.1. Overview of the case study

The Palazzo della Loggia in the city of Brescia, Italy, presently hosting the Municipal Hall, was completed in 1574. Since then, it has cumulated a long sequence of injuries, transformations,

repairing interventions, some of which have generated considerable problems of structural stability of the building. The wooden vaulted roof, in particular, was completely reconstructed in 1914: its maximum elevation is 16 m, and its shape is that of an upside-down ship, with planar rectangular sides of about 25 m and 50 m respectively.

The structural architecture of the vault consists of principal truss wooden arches and simple secondary arches; both are connected at the top by a truss-made wooden beam. Immediately after its construction, the structure underwent progressive deformation of the longitudinal top beam and of the key points of the connected arches. In particular, the progressive deflection of the top beam was measured to be 190 mm in 1923, 520 mm in 1945, 800 mm in 1980 [16].

## 2.2. The traditional monitoring approach

Keeping the wooden vaulted roof of the *Palazzo della Loggia* under control consists in measuring the possible displacements of several constituent elements with reference to a coordinate system fixed with the masonry structure of the building. The measurements should be taken at a frequency of days/weeks, for a total duration of several years.

The systematic campaign of investigation by traditional measurement systems has been continuously performed for more than ten years, from 1990 to 2001 [16]. On four, out of the seven principal arches, three couples of wires, 2.0 mm in diameter, one made of ordinary steel and the other made of invar, were stretched between symmetric points at three different levels: A1 - B1, at the point of connection of the arches with the building structure; A2 - B2 and A3 - B3, on the arch reins. These points are shown in Fig. 2.

The wire tension was maintained by means of a system of pulleys and balance weights. The relative displacements of two symmetric points were assessed by the differential elongation of the two wires and were continuously registered. The different thermal expansion coefficients of the two different materials made possible to factorize out the thermal deformation of the monitoring system itself, subject to considerable daily and seasonal thermal variations under the roof covered by lead plates. As a result, the vault deformation was shown to be of about 1 mm/yr [16].

The study described in [16] shows mutual displacements of the aforementioned points as a function of the monitoring time.

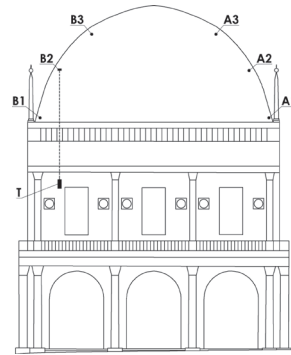


**Fig. 2: Positioning of the muon telescope (T) and muon targets (B1, B2, B3) on the building to be monitored**

It is worth remarking that the mechanical method actually adopted in [16] could only provide the measurement of the horizontal relative displacement of points of the wooden structure in opposite positions and not their absolute displacements with respect to a common reference system linked to the building structure.

## 3. The proposed monitoring system

### 3.1. Layout of the muon telescope

Highly penetrating cosmic ray muons rain continuously on the *Palazzo della Loggia* at a rate of  $210\,000\ \mu/\text{s}$ , corresponding to  $10\,000\ \mu/(\text{m}^2\cdot\text{min})$ . The proposed monitoring system based on cosmic ray detection, able to monitor roof deformations, has the following general geometrical structure. Three square muon hodoscope modules, of about  $(400\times 400)\text{ mm}^2$  area and 6.0 mm thickness, are positioned on an appropriate mechanical structure, axially aligned at a distance of 500 mm from each other. This set-up corresponds to the *muon telescope* T, shown Fig.3a, having a total height of about 1 000 mm. The number of modules has been chosen to allow for a minimum level of redundancy on the tracking information for the crossing muon.

The geometry of the sensitive volume of each hodoscope module is based on two orthogonal layers of 360 mm width, composed of 120 scintillating fibers with  $(3.0\times 3.0)\text{ mm}^2$  cross section and 400 mm length. The two layers are arranged along the  $x$  and  $y$  axes of a Cartesian reference system as shown in Fig.3b. The two layers provide the measurement of the crossing position of an incident muon in the  $x$  and  $y$  coordinates with a pitch of 3.0 mm. Considering a flat detection efficiency over the full surface of

the scintillating fiber, the spatial resolution on the coordinate of the impact is expected to be  $\sigma = (3.0 \text{ mm})/\sqrt{12} = 0.87 \text{ mm}$ .

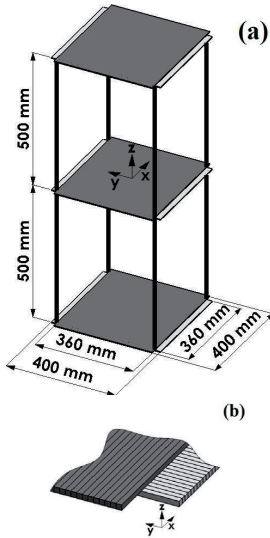


**Fig. 3: (a) Structure of the muon telescope formed of three muon odoscope modules axially aligned at a distance of about 50 cm each other, and (b) sensitive volume of the muon odoscope module formed of two orthogonal layers of 120 scintillating fibers with  $(3.0 \times 3.0) \text{ mm}^2$  cross section and 400 mm length.**

As shown in Fig. 2, the muon telescope T must be mechanically fixed to a structural element of the building, which is considered as the reference system for the measurement of the position of the building points to be monitored. A fourth muon hodoscope module, with the same geometry and structure as the others, must be positioned as *muon target* in each of the points to be monitored: in the considered case, point B1, B2 or B3 of the wooden arches of the roof in Fig. 2, corresponding to the ones monitored by means of the traditional system described above.

In this arrangement, cosmic ray muons that cross the full four-detectors system and the interposed structures of the buildings allow the continuous monitoring of the displacement of the muon target relative to the fixed muon telescope.

The overall accuracy of the position measurement depends on the system geometry, the interposed materials, and the data collection time. The recognition of the signals generated by the same cosmic ray muon crossing the four detectors against background accidental events generated by different cosmic ray muons may be efficiently insured by time coincidence of the four detector signals [2].

The direction and crossing point of any cosmic ray traversing the muon telescope can be measured with an accuracy that depends on telescope geometry and detector granularity. The measured cosmic ray trajectory can be extrapolated from the muon telescope to the plane of the muon target detector, in the hypothesis that the trajectory of the muon is a perfect straight line.

The distance between the muon telescope and the muon target can be deduced, with sufficient approximation, either from the building project drawings or from survey. Due to the geometry of the system, which limits the solid angle covered by cosmic ray muons traversing all four detectors, any uncertainty in the determination of this distance has negligible effects on the determination of the  $x$  and  $y$  coordinates of the extrapolated crossing point.

### 3.2. Sources of measurement uncertainties

The hypothesis that the muon trajectory is a perfect straight line is justified only in the absence of magnetic fields and in vacuum. The interaction between the terrestrial magnetic field and a typical  $3.0 \text{ GeV}/c$  cosmic ray muon causes a deflection of about  $5 \mu\text{m}/\text{m}$  in the direction perpendicular to both magnetic field and particle velocity. Since in cosmic ray flux there is an excess of positive muons with respect to negative ones, this could induce a systematic effect on the measurement. However, since the measured displacement is obtained considering differences between absolute measurements performed at different times, the effect of the terrestrial magnetic field can be neglected.

More relevant is the effect of materials interposed on the muon paths, which determines stochastic deviations of the muon trajectories due to multiple scattering with atomic nuclei [17, 18, 19]. The angular deviation is proportional to the density of the material, to its atomic number and to the total amount of crossed material, and inversely proportional to the square of the muon momentum.

The uncertainty in the prediction of the crossing point coordinates of the muon, in the muon target plane, starting from the measurement of its trajectory in the muon telescope, depends on several factors: (i) position resolution of the muon detectors, (ii) geometry of the muon telescope, (iii) distance of the muon target from the muon telescope, (iv) amount of multiple scattering angular deviations and displacement of the muon

trajectory, which depend on the amount of interposed materials and their positions.

Being these effects mainly of stochastic nature, statistical distributions of the difference between measured crossing point coordinates in the muon target and the predicted crossing point coordinates obtained by extrapolation from the muon telescope is necessary to reduce the stochastic effects by statistical inference methods. Using the methods developed in [15], efficient unbiased estimators of the systematic displacement can be extracted by means of a statistical analysis of the distributions. The expected resolution and performances of the proposed measurement system can be analyzed by Monte Carlo simulations.

Finally, it is worth noting that, depending on the solid angle covered by the muon telescope and on the position and distances of the building parts to be monitored, more than one muon target could be monitored simultaneously by the same muon telescope, with only some reduction of the acceptance of the system for the points more off-axis. In this way, a global and simultaneous stability monitoring of several parts of the building can be performed.

#### 4. Monte Carlo simulation of the proposed system

The features and expected performance of the proposed measurement system have been calculated by means of a Monte Carlo simulation, performed by GEANT4 [20], a C++ toolkit for the simulation of the passage of particles through matter largely used in the design of nuclear and particle physics experiments. In the simulation, the geometry and the relevant structural parts of the *Palazzo della Loggia* building were taken into account, and the structure and component materials of the muon telescope and muon target were modeled in detail.

In three separated simulations, the muon telescope was located in three different positions, 3.0 m below the ceiling of the large *Salone Vanvitelliano* at the first floor of the Palace, as shown in Fig. 2, on the vertical of each one of the three points of the wooden vaulted roof to be monitored: B1, B2 and B3. These points are positioned, respectively, 0.5 m, 5.8 m, and 10.0 m above the ceiling of the *Salone*. In these three points a muon target was located for each of the three separated simulations, on the vertical of the corresponding muon telescope. A realistic cosmic ray muon generator, based on experimental data, was implemented in the code to simulate the momentum, the angular distribution, and the

charge composition of the cosmic ray radiation at the sea level [21].

The ceiling of the *Salone* was modeled as a 150 mm thick wooden layer. No vertical structures of the Palace were modeled, to study the intrinsic limits of the monitoring system without adding any systematic effect, nor the wooden vaulted roof covered by lead plates, since this would have introduced only a negligible distortion of the incoming cosmic ray spectrum and angular distribution, without sensitive effects on the system performances.

A preliminary simulation was focused on the evaluation of the resolution of the muon telescope in the measurement of the direction of the cosmic ray crossing the muon telescope and in the prediction of the coordinates of the extrapolated muon crossing point on the plane of the upper detector module. To this aim a population of cosmic ray muons has been generated randomly on the surface of the upper detector module of the muon telescope.

In each detector module the passage of the muon is registered when an amount of energy is released by ionization energy loss in one scintillating fiber. The measured position of the muon crossing point in  $x$  and  $y$  coordinates is defined by the position of the axis of the crossed scintillating fiber, on the corresponding layer, in the coordinate system shown in Fig.3.

To simplify the analysis, only the muons providing a single hit in all the three scintillating fiber layers on the same coordinate are considered. For this sample of cosmic ray muons, the three measured points on the three layers for each coordinate are fitted by means of a linear regression. The direction of the reconstructed straight line is compared with the direction of the generated muon at the entrance of the muon telescope and the  $x$  and  $y$  coordinates of the crossing point of the straight line with the upper surface of the upper detector module are compared with the coordinates of the muon origin point randomly extracted.

Fig. 4a shows the distribution of the difference  $\Delta x$  between the  $x$  coordinates of a generated point and of the corresponding reconstructed one. Since the system is symmetrical, the distribution for the  $y$  coordinate is statistically the same as the  $x$  one. The distribution is obtained with a number of simulated events corresponding to a data taking time of 6 hours. The standard uncertainty in the determination of the muon crossing point is 0.77 mm, compatible with the intrinsic granularity of the muon detector modules, which is expected to be 0.87 mm, as already said in section 3.1.



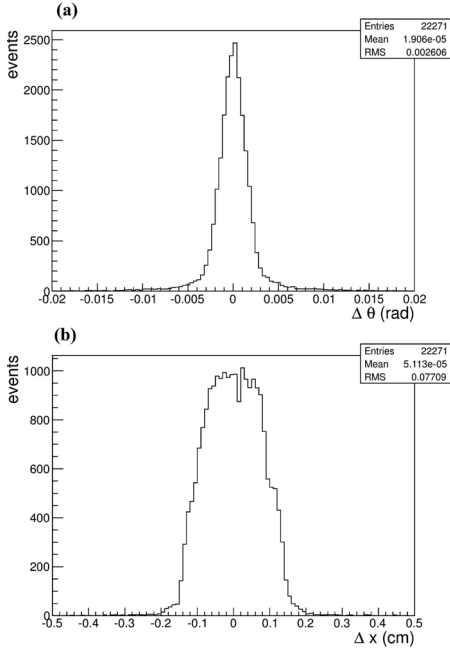


**Fig. 4: a) Distribution of the difference between the x coordinate of the point of generation of the cosmic ray on the surface of the upper detector module of the muon telescope and the same coordinate reconstructed by the straight line fit. b) Distribution of the difference between the projected angle on the x-z plane of the generated cosmic ray crossing the muon telescope and the same angle reconstructed with the straight line fit. The distributions are obtained with a statistic corresponding to a data taking time of 6 hours.**

Fig. 6b shows the distribution of the difference  $\Delta\theta$  between the projected angle on the x-z plane of the generated cosmic ray and the reconstructed one. The standard uncertainty in the determination of the muon projected direction is 2.6 mrad, compatible with the granularity and the geometry of the telescope, which suggests an uncertainty of about 3 mrad.

With such an accuracy in the determination of the direction of the cosmic ray muon, the expected contribution of the muon telescope uncertainty in the determination of the muon crossing point on the muon target plane positioned at 10 m distance is about 30 mm, that is, 3 mm/m.

## 5. Position measurement uncertainty of the monitoring system vs data taking time

With the proposed set-up, simulations of the tracking of cosmic ray muons through the measurement system were performed in the three configurations described above. For cosmic ray muons yielding a single hit in the four detector modules, the differences  $\Delta x$  and  $\Delta y$  between the crossing point coordinates measured in the muon target and the crossing point coordinates of the extrapolated muon trajectory measured by the muon telescope have been recorded. All relevant physical processed in the generation and tracking of the cosmic ray muons are taken into account in the simulation program.

Cosmic ray muons generating multiple hits in the same detector layer are rejected from the analysis. Multiple hits may be produced by the crossing of more than one scintillating fiber in one layer or, alternately, by showering of the cosmic rays muons and possible generation of delta rays. The number of cosmic ray muons producing multiple hits in the same detector is about 15% of the total number entering the measurement system geometrical acceptance.

Fig. 5 shows the distributions of the statistical variable  $\Delta x$  for the three configurations of the measurement system described above, for a data taking time of 15 days, corresponding to about  $31.7 \cdot 10^6$  cosmic ray muons crossing the muon target surface. The distributions of  $\Delta y$  are not shown, as they are statistically identical to the  $\Delta x$  ones. The number of events in each distribution is compatible with the number of expected cosmic ray muons entering the geometrical acceptance of the measurement system given by:

$$N_{acc} = \frac{d^2 N}{d\Omega_{xy} dA_1} \cdot \frac{A_2}{R^2} \cdot A_1 \cdot T \quad Eq. 1$$

where  $d^2 N/(d\Omega_{xy} dA_1) = 70 \mu/(m^2 \cdot s \cdot sr)$  is the muon rate per unit area and unit solid angle around the zenith direction [1],  $A_1$  is the surface of the muon target,  $A_2$  is the lowest surface of the telescope and  $R$  is their distance, and  $T$  is the elapsed time of the data taking in seconds.

As the muon target and the muon telescope are exactly coaxial in the simulation, the  $\Delta x$  distributions are symmetric and centered at zero. The shape of the distributions exhibits a central narrow peak with very long tails on both sides. This shape is due both to the intrinsic uncertainty of the muon telescope in measuring the direction of the cosmic ray muon, and to the multiple

scattering angular deviations of the muon trajectories traversing the interposed materials.

At fixed momentum and for little angles, these deviations follow a Gaussian law with a variance that depends on the inverse square of the muon momentum [19].

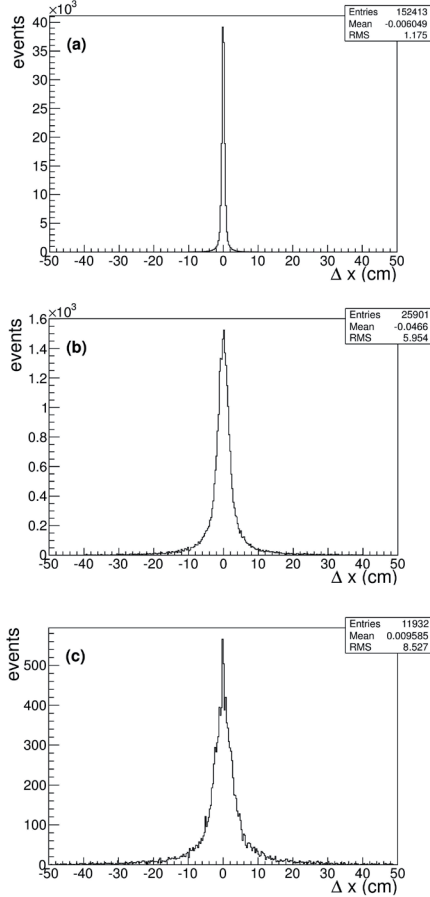


**Fig. 5:** a) Distribution of the difference  $\Delta x$  between the crossing point coordinates detected by the muon target at position B1 (a), B2 (b) and B3 (c), and the crossing point coordinates on the muon target of the extrapolated muon trajectory measured by the muon telescope. Simulated data taking time is 15 days.

The latter effect dominates for larger distances of the muon target from the muon telescope. The long tails of the distributions are due in part to low-momentum muons, suffering larger deviations, and, in part, to spurious events corresponding to emission of delta rays or cosmic ray showering, most of which can be discarded

with a more refined data analysis. At present, the only selection applied to these low-quality events is an arbitrary cut of both tails in the three distributions, discarding about 1.0% of the total events.

RMS values of the  $\Delta x$  distributions are 1.2 cm, 6.0 cm and 8.5 cm respectively for the three configurations examined. They correspond to an estimation of the standard deviation of the parent populations  $\sigma_{distr}$ , and represent the uncertainties in the prediction of the crossing coordinate of the cosmic ray muon on the muon target detector extrapolated by the muon trajectory measured with the muon telescope. This uncertainty depends mainly on the distance between muon target and muon telescope and on the amount and position of the interposed materials. The mean value of the sample distribution represents an unbiased estimator of the position of the muon target relative to the telescope axis. The uncertainty on the mean value of a sample distribution is given by the well-known relation [22]:

$$\sigma_{mean} = \sigma_{distr} / \sqrt{N_{ev}} \quad \text{Eq. 2}$$

where  $N_{ev}$  is the number of events in the distribution. In the three configurations considered and for a data taking time of 15 days, these standard uncertainties are respectively 0.030 mm, 0.37 mm, 0.78 mm.

Since in the same geometrical condition  $N_{ev}$  is simply proportional to the data taking time, the measurement standard uncertainty depends only on the inverse of the square root of the data taking time. In Fig 6 the relation of the position measurement standard uncertainty and the data taking time for the three examined conditions is plotted considering a data taking time up to one month. As time increases the measurement standard uncertainty decreases. By fitting the plots with the following general relation [15]:

$$\sigma_{mean} = C / \sqrt{t} \quad \text{Eq. 3}$$

where  $C$  is a constant depending on the geometry and materials interposed and  $t$  is the data taking time in days, the following values for the constant  $C$  were obtained in the three conditions considered:  $1.12 \text{ mm} \cdot \text{d}^{1/2}$ ,  $1.42 \text{ mm} \cdot \text{d}^{1/2}$ ,  $2.96 \text{ mm} \cdot \text{d}^{1/2}$ , with a standard uncertainty of the order of 1%.

As expected, the standard uncertainty of the measurement system depends on the geometrical configuration considered, since both the root mean square of the  $\Delta x$  distributions and the rate of useful events collected are strongly dependent on the geometry of the system and on the amount of materials interposed. Nevertheless, although requesting different data taking times, the

monitoring of the displacement of the three inspected points in the wooden vaulted roof of the *Palazzo della Loggia*, using a cosmic ray tracking system, could provide performances compatible with the requested accuracy and with the time scale characteristic of the deformation phenomenon. Typical time scales, in the case of *Palazzo della Loggia* and, in general, for historical buildings, may span over several years.

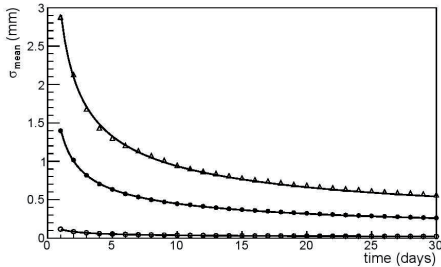


**Fig. 6: Standard measurement uncertainty as a function of data taking time**

In position B1, a measurement standard uncertainty of the order of 0.1 mm may be achieved in about one day of data taking, whereas a standard uncertainty of the order of 0.5 mm may be achieved in a week of data taking in position B2 and in one month of data taking in position B3, where muon target and muon telescope are positioned 13.0 m far apart.

## 6. Performances of the proposed system vs the traditional approach

To demonstrate how a monitoring system based on cosmic ray muon tracking may perform better than or well as more traditional systems, provided that the acquisition time is long enough, the results shown in Fig. 6 have been compared to those performed with the traditional monitoring system described in section 2.2 and presented in [16]. In [16] both the cyclic seasonal deformation of few millimeters for a position of the wooden vaulted roof structure of the *Palazzo della Loggia* and the general trend of displacement with a rate of deformation of the order of 1~mm/yr are shown.

A first result is that a monitoring system based on cosmic ray tracking would be largely sensitive enough to detect the progressive deflection of 1 mm/yr of the vaulted wooden roof of the *Palazzo della Loggia*. Indeed, looking at Fig. 6, it is possible to deduce that, in the worst studied case, the proposed simulated system reaches a standard measurement uncertainty of 1 mm after an elapsed time of about 10 days. This means that

the system is able to identify a displacement of 1 mm, with a 68.3% confidence interval, in 10 days.

Moreover, in [16], the measured seasonal displacement of the roof structure on a period of several years are reported. To investigate how a monitoring system based on cosmic ray muon tracking could follow cyclic seasonal deformations as well as systematic ones, a seasonal displacement of the three positions B1, B2 and B3 in Fig. 2 was reproduced in the simulation program as a function of time. The behavior of the structure in point B2 for the first year of data taking, experimentally measured thanks to the traditional mechanical monitoring system previously described, was adopted as a realistic model of the phenomenon. A cosmic ray data taking one year long was simulated to reproduce the measurement of the possible seasonal displacements of the roof structure in points B1, B2 and B3 by the proposed monitoring system.

In Fig. 7, the displacement with time corresponding to the supposed seasonal deformation (the same for the three points) is shown as a continuous line. The results of the simulated measurements using the sample mean of the position of the muon target, displaced following the assumed structural deformation, is shown, with sampling rate of one week, two weeks and one month respectively for points B1, B2 and B3.

The ability of the proposed measurement system to follow seasonal displacements of few millimeters and, even more so, also systematic ones is demonstrated.

## 7. Discussion and conclusion

The comparison between the numerical results of the proposed feasibility study, presented in Fig. 6, and the experimental results reported in [16], demonstrates that a measurement system based on cosmic ray muon tracking is suitable to monitor the static stability of historical buildings. In the particular case study considered, seasonal displacements can be identified, and systematic displacements that could affect building stability can be measured with a standard uncertainty equal to or even better than the one associated with traditional methods.

The assessment of the overall monitoring system standard uncertainty could be significantly improved both by modifying some geometrical parameters of the system and improving the data analysis:

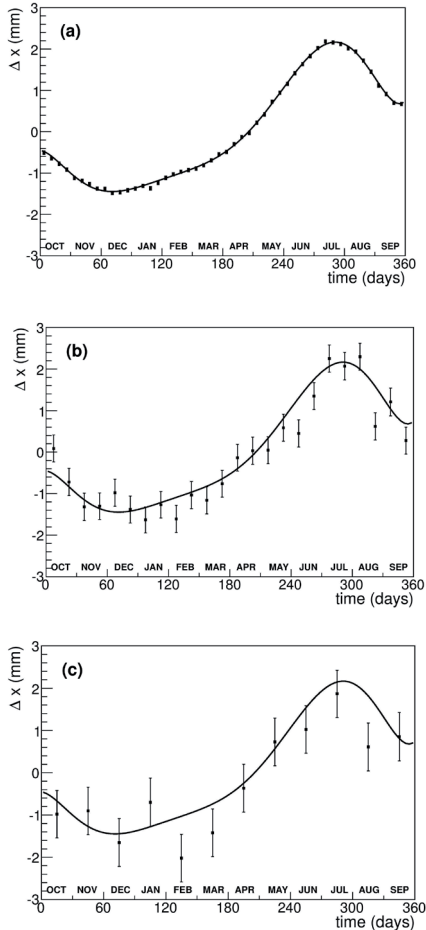


**Fig. 7: a) Seasonal deformation of few millimeters assumed for the point at position B1 Fig. 2. Dots indicate the simulated measurement of the position of the muon target with the muon stability monitoring system using the sample mean value, with sampling rate of one week. The measurement uncertainty is given by equation Eq.2. b) The same for the point in position B2, with sampling rate of two weeks. c) The same for point in position B3, with sampling rate of one month.**

1. In [15] it was demonstrated that a more efficient unbiased estimator of the position and possible displacement of the muon target detector can be obtained by fitting the parent population of the statistical variables  $\Delta x$  and  $\Delta y$  by an appropriate analytical function, and by determining their shape parameters using a best fit procedure. In this way, the standard uncertainty is expected to be improved by a factor of 2 to 3 [13].

2. The same work [15] points out that the low momentum muons can be discarded by the data sample by means of a muon absorber in the form of a thick iron plate positioned below the muon telescope and followed by a further plane scintillation counter in coincidence. By eliminating the low momentum muons, which suffer the largest multiple scattering deviations, and the possible electron showering that adds spurious events to the sample, the long tails of the  $\Delta x$  and  $\Delta y$  distribution can be reduced, thus reducing the root mean square  $\sigma_{distr}$  of the distributions.
3. A possible way to improve the accuracy of the monitoring system and to decrease data collection time involves both system parameters and data analysis. Instead of using only one detector module, the muon target could consist of a couple of particle detector modules assembled to form a telescope, allowing both the crossing position and the direction of the incident muon cosmic ray to be measured at the muon target point.

In this way, when the multiple scattering deviation is concentrated in only one main layer (an interposed floor for example), the deviation effect on the muon trajectories can be largely compensated and it was estimated by Monte Carlo simulation that the system measurement uncertainty previously reported may be reduced up to a factor 3.

When the building structures interposed between the muon telescope and the muon target are more complex (presence of more than one floor or vertical walls), a reconstruction algorithm based on a likelihood function and on Monte Carlo simulation of the muon statistical behavior, can be implemented to determine the more probable position of the muon target accounting for the known distribution of the interposed structures and composing materials.

4. Finally, an increment of 50% of the single module size corresponds to a reduction of a factor 2.2 of the data collection time needed to obtain the same standard uncertainty on the position measurement. This solution has to be compatible principally with the cost of suitable particle detectors and with the complexity of their control system.

In conclusion, cosmic ray muon detection techniques have been investigated for measurement applications in the field of civil engineering and have been demonstrated to be

particularly suitable for static monitoring of historical buildings, where the evolution of the deformation phenomena is of the order of months or years. Appealing features of the proposed monitoring system are: (i) the use of a natural and ubiquitous source of radiation avoiding any problem of radiation protection; (ii) its applicability also in presence of horizontal and/or vertical building structures interposed between the reference system and the parts to be monitored; (iii) the limited invasiveness, and the flexibility and ease of installation of the monitoring system devices; (iv) the possibility to design a global monitoring system, where the position of different points of the building may be simultaneously monitored relative to the same reference system; (v) the use of well-known physical principles and established technologies in the field of nuclear and particle physics to build up the cosmic ray muon detectors featuring the characteristics suitable to satisfy the requirements of any specific application.

### Acknowledgments

The authors gratefully acknowledge Prof. Ezio Giuriani of the Department of Civil, Architectural, Land and Environmental Engineering and Mathematics of the Brescia University and Prof. Alessandra Marini of the Engineering Department of the Bergamo University for the information provided on the long-lasting study performed of the *Palazzo della Loggia* and for the invaluable advice concerning the problem of historical building monitoring. The authors would also like to thank Prof. F. Docchio for his comments and his careful reading of the manuscript.

This work has been performed thanks to a special funding of the Department of Mechanical and Industrial Engineering of the University of Brescia.

### Bibliography

- [1] Beringer J. et al. (Particle Data Group), "The Review of Particle Physics", *Phys. Rev. D*, 2012, vol. 86
- [2] ALICE Collaboration 2010, "Alignment of the ALICE Inner Tracking System with cosmic-ray tracks", *Journal of Instrumentation*, 2010, vol. 5
- [3] Marteau J. et al., "Muons tomography applied to geosciences and volcanology", *Nucl. Instrum. Meth A*, 2012, vol. 695, pagg. 23-28
- [4] Barnaföldi G. et al., "Portable cosmic ray muon telescope for environmental applications", *Nucl. Instrum. Meth A*, 2012, vol. 689, pagg. 60-69
- [5] Ambrosi G. et al., "The MU-RAY project: Volcano radiography with cosmic-ray muons", *Nucl. Instrum. Meth A*, 2011, vol. 628, pagg. 120-123
- [6] Gilboy W. B. et al., "Industrial radiography with cosmic-ray muons: A progress report", *Nucl. Instrum. Meth A*, 2007, vol. 580, pagg. 785-787
- [7] Benettoni M. et al., "Noise reduction in muon tomography for detecting high density objects", *JINST*, 2013, vol. 8, pag. 12007
- [8] Perry J. et al., "Imaging a nuclear reactor using cosmic ray muons", *J. Appl. Phys.*, 2013, vol. 113, pag. 184909
- [9] Riggi S., "Muon tomography imaging algorithms for nuclear threat detection inside large volume containers with the Muon Portal detector", *Nucl. Instrum. Meth A*, 2013, vol. 728, pagg. 59-68
- [10] Jonkmans G. et al., "Nuclear waste imaging and spent fuel verification by muon tomography", *Ann. Nucl. Energy*, 2013, vol. 53, pagg. 267-273
- [11] Borozdin K. et al., "Cosmic ray radiography of the damaged cores of the Fukushima reactors", *Phys. Rev. Lett.*, 2012, vol. 109, pagg. 152501
- [12] Pesente S. et al., "First results on material identification and imaging with a large-volume muon tomography prototype", *Nucl. Instrum. Meth A*, 2009, vol. 604, pagg. 738-746
- [13] Zenoni A. et al., "Historical building stability monitoring by means of a cosmic ray tracking system", *arXiv:1403.1709*, 2014
- [14] Donzella A., "Stability monitoring of an historical building by means of cosmic ray tracking", *Il Nuovo Cimento C - Proceedings XCIX SIF National Congress (Trieste)*, 2014, in press
- [15] Bodini I. et al., "Cosmic ray detection based measurement systems: a preliminary study", *Meas. Sci. Technol.*, 2007, vol. 18, pagg. 3537-3546
- [16] Bellini A. et al., "Il palazzo della Loggia di Brescia - Indagini e progetti per la conservazione", 2000, Starrylink editrice, Brescia

- [17] Moliere G Z, "Theorie der Streuung schneller geladener Teilchen I - Einzelstreuung am abgeschirmten Coulomb-Feld", *Z. Naturforsch.*, 1947, vol. 2°, pagg. 133-145
- [18] Moliere G Z, "Theorie der Streuung schneller geladener Teilchen II - Mehrfach und Vielfachstreuung", *Z. Naturforsch.*, 1948, vol. 3a, pagg. 78-97
- [19] Bethe H A, "Moliere's theory of multiple scattering", *Phys. Rev.*, 1953, vol. 89, pagg. 1256-1266
- [20] Agostinelli S. et al., "Geant 4 – a simulation toolkit", *Nucl. Instr. Meth. A*, vol. 506, pp. 250-303, 2003
- [21] Bonechi L., "Development of ADAMO detector: test with cosmic rays at different zenith angles", *Proceedings of the 29th International Cosmic Ray Conference*, (Pune), vol. 00, pp. 101-104, 2005
- [22] Rotondi A et al., "Probabilità Statistica e Simulazione", 2001, Milan: Springer-Verlag Italia



# Measurement of forces exerted by a polymeric shape-memory stent for biomedical applications

Ileana Bodini, Alberto Borboni, Matteo Lancini,  
Stefano Pandini, Simone Pasinetti, David Vetturi

\* Department of Mechanical and Industrial Engineering, University of Brescia

## Abstract

*This paper aims at describing the dynamic behaviour of polymeric shape-memory stents. In particular, considering the recovering phase, measurements have been performed to find a relation between different configurations and forces, which the specimens exerts. Shape memory materials, in fact, can exert a force when recovering their permanent form.*

*An analytic model that describes the shape of an expanding specimen, based on a vision system, has been developed and experimentally calibrated.*

*A measurement device has been specially designed to measure forces, which the expanding specimen exerts. This device is based on six trolleys free to fall, frictionless, thanks to pneumostatic bearing, on an inclined rail. So entity of the force applied on a shape memory specimen, constant along the whole movement, is determined by the inclination of the guide.*

## 1. Introduction

With the name “shape-memory polymers” (SMPs) literature refers to a category of smart materials, which have the ability to be deformed from a “permanent” shape to a “temporary” one, and to revert back to the “permanent” shape once an external stimulus, usually a change in temperature, is applied.

Thanks to the peculiar characteristics of polymers, SMPs may offer various advantages against their metallic counterparts (shape memory alloys) [2, 3], such as being lightweight and easy to process, being capable of recovering large strains and a relatively easily tailoring of the temperature that triggers the shape-memory effect. Literature is investigating the possibilities to employ SMPs in realistic situations, and in particular in the fields of sensors, actuators, biomaterials and smart textiles [2, 4-11]. It is, however, to be remarked that shape memory polymers are typically not capable of exerting high levels of stress, so that the capabilities of these systems meet the requirements of what can

be considered a soft actuation, which could be employed for biomedical applications, due to the compliance of soft tissues.

This paper investigates the capability of polymer-based star-shaped specimens to behave as actuators. In particular, the relation between their shape changes during the recovering phase and the forces that they can exert.

The activity of measurement described in this paper regards two different mechanical quantities: force and deformation/opening level.

For the measure of force a specific device has been designed and realized, while for the assessment of the deformation/opening level an image-based method has been proposed.

## 2. Experimental kinematics

The objects of the experimental investigations were actuators of a semicrystalline crosslinked polymer, poly ( $\epsilon$ -caprolactone) (PCL), which were prepared with a tubular shape as the “permanent” one. The choice of PCL networks as shape memory systems for our analysis is based on the fact that this class of polymers may be of large interest for biomedical applications and since their transformation temperature can be finely tuned by means of a proper choice of the material crosslink density, as shown in previous papers [16, 17]. The crosslinked structure was obtained starting from hydroxyl-terminated poly( $\epsilon$ -caprolactone) (PCL), with a molecular weight of 7000 g mol<sup>-1</sup>, later suitably modified to obtain methacrylate-terminated PCL precursors and crosslinked by a free-radical thermally activated process in presence of dicumyl peroxide as radical initiator (at 105°C for 5 hours).

The tubular specimens were prepared by pouring the reactive mixture in silicon molds with a cavity having the shape of a tube (height = 40 mm, outer diameter = 25 mm, thickness = 1.5 mm). Special attention was taken to reduce the presence of air bubbles that may be trapped in the cross-linked materials, maintaining the melted methacrylate-terminated polymers under reduced pressure for several hours before the thermal curing; more

details concerning the preparation of these materials are reported in a companion paper [18].

Differential scanning calorimetry (DSC) tests carried out on the material obtained revealed the presence of a semicrystalline structure (crystallinity content: about 40%), with a melting temperature  $T_m = 53^\circ\text{C}$  and a crystallization temperature  $T_c = 18^\circ\text{C}$ .

The shape memory response of the material was tested by first setting the specimen to a “temporary” configuration. This step, typically called “programming”, was carried out by heating the cylinder at a about  $80^\circ\text{C}$  (i.e. above  $T_m$ ) and, by employing an ad-hoc designed crimping tool (Figure 1), which allowed to fold them in a six arms star shaped configuration.

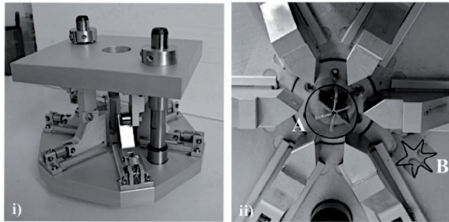


**Fig. 1: i) side-view of the crimping fixture; ii) top-view of the crimping fixture, without the top closure plate, and picture of an undeformed (A) and partially crimped (B) specimen.**

Once crimped, the specimen was cooled at about  $-17^\circ\text{C}$  (i.e. well below  $T_c$ ) for at least 10 minutes while maintaining the crimping arms blocked, so to fix this compact configuration. The folded specimens were then subjected to isothermal stress-free recovery test by immersion into a water bath, previously heated at various temperatures, chosen from room temperature ( $20^\circ\text{C}$ ) to above the material melting temperature ( $53^\circ\text{C}$ ). The recovery process was monitored as a function of time by means of a photocalera with a sampling frequency of 1 frame/s. In this case a color image (32 bit 4288x2848 pixel) is taken from by a Nikon D70 camera.

The star shaped actuator is monitored during a period of 17 seconds. A photograph of the opening stent is realized at the starting time and, as already said, every second during a transformation period. During this lapse of time the specimen receives thermal energy and realizes a conversion to mechanical energy through a shape change, as shown in Figure 2. In this experimental test, the heat transfer to the actuator is performed with a liquid media, where the actuator is completely immersed.

To describe the kinematics of the stent during its motion, an analytic model has been assumed and experimentally calibrated.



**Fig. 2: Transition from temporary shape to permanent shape**

In the initial instant, the shape could be described as a linear combination of rhodonea functions, and in the final instant as an annulus. The proposed model linearly combines these functions with parameters that are time-dependent. Figure 3 shows how the model (blue line) fits experimental data (red line), determined using an edge detection and filtering algorithm, specially developed.

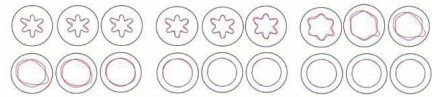


**Fig. 3: Comparison between the detected boundary (red line) and the model boundary (blue line)**

A complete description of the mathematical approach has been described in a dedicated paper presented by the authors [15].

The same approach has been used for the identification of the material opening level/deformation during the force controlled test, performed in order to find a relation between shape at a given opening level and the corresponding exerted force. During the force-deformation test the fluid media used for heating the polymer-based star-shaped specimens was the air at a controlled temperature.

For the opening level an evaluation of the uncertainty has been performed considering the results of the calibration of the kinematics mathematical model described in [15].

Analyzing the results of the model calibration and considering the resolution and the characteristic of the vision system used (HR digital camera) a value for the standard uncertainty, considered in further tests as “B” type, is 0.05 mm.

### 3. Force measuring device

A measuring device, shown in Figure 4, has been specifically developed to measure the radial force [12-14] that each specimen exerts during the transition from temporary to permanent shape. This transition takes place in air at a uniform and controlled trigger temperature. The device consists of six trolleys, in radial position with respect to the specimen. Each one is free to fall, frictionless thanks to pneumostatic bearing,

on an inclined rail. The angle ( $\theta$ ) of the rail can be modified, to vary the load ( $L$ ) applied to the specimen. The measuring device is based on null measurement method and the radial force ( $F_{stent}$ ) can be unequivocally determined when the component of the load of the trolley results equal to the component of the force which the opening specimen exerts, both components directed along the inclined rail. This is a static situation and the specimen keeps its shape unchanged.

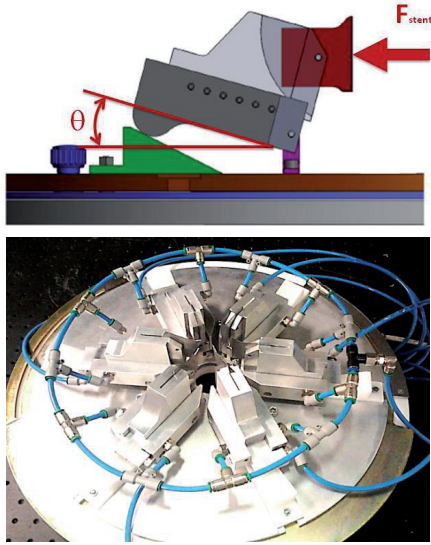


Fig. 4: measuring device

The simplest model for the evaluation of the  $F_{stent}$  can be expressed by the relation:

$$F_{stent} = m \cdot g \cdot \tan(\theta) + F_{friction} \quad Eq. 1$$

where  $m$  represents the value of the mass of a single trolley,  $g$  is the gravity acceleration,  $\theta$  is the angle of the rail and  $F_{friction}$  represents the residual part of friction between rail and trolley.

In the model of the measurement the friction force has been modelled as a statistical quantity with null average and standard deviation of 0.010 N. More investigation in that regard is needed and will be performed in later stages of this project using a comparison dynamometer.

From Eq. 1, a first evaluation of the measurement uncertainty (cat. B) can be calculated using the ISO13005 technique as shown in tables:

	x	u(x)	u%(x)	UM
m	228	5	2.2%	g
g	9.806	0.05	0.5%	m/s <sup>2</sup>
$\theta$	7.0	0.2	2.9%	°
$F_{friction}$	0	0.010	---	N

	u(x)	UM	ci	u(yi) <sup>2</sup>
m	0.005	kg	1.2040	3.62 10 <sup>-5</sup>
g	0.05	m/s <sup>2</sup>	0.0280	1.96 10 <sup>-6</sup>
$\theta$	0.0035	rad	2.2695	6.28 10 <sup>-5</sup>
$F_{friction}$	0.010	N	1.0000	1.00 10 <sup>-4</sup>

with:

$$F_{stent} = 0.275 \text{ N and } u(F_{stent}) = 0.014 \text{ N}$$

therefore the relative uncertainty is assessed at 5.2% and the main uncertainty contribution is the presence of friction between rail and trolley.

Similar results can also be obtained with other rail's inclination.

#### 4. Mechanical characterization

When the equilibrium between the aforementioned components is achieved,  $F_{stent}$  can be assessed using equations of static equilibrium of the system. Figure 5 shows some static configurations and the corresponding force exerted by the specimen.



Fig. 5: Each configuration of the expanding specimen corresponds to a radial force exerted by the specimen itself

The purpose of the experimental activity is to characterize mechanical behaviour of shape-memory materials, in particular to determine a possible relation between forces exerted by a specimen made of the considered material and its geometrical shape during the recovering phase, when the specimen is expanding. Forces are determined for different external load imposed and temperature conditions. In this way, it is possible to verify the actual usability of this kind of materials in biomedical applications.

The experimental activity allowed to characterize the main behaviour of the material.

The first indication is that the material has a variation of response in different examination as it is shown in next figure 6.

Figure 6 shows the level of opening of the specimen with a constant force level applied (rail-trolley inclination) in different testing. It is possible to observe that the first testing allows to the materials a greater level of expansion than the others tests. Each test in Figure 6 is performed in the same temperature and load conditions, using the same specimen. The variability between different test for the same specimen in the same condition testing (temperature, external load) is greater than uncertainty.

A different test has been also performed with a set of different specimens of the same material at their first test. For each experiment a different level of external load (rail-trolley inclination) has been applied.

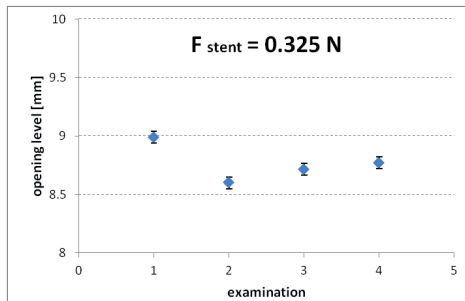


Fig. 6: repeatability

Results obtained show how the shape memory material works: when it is compressed to the non permanent shape (small entity of opening level) the force that the specimen can exert is the highest. During the expansion, this force decreases quickly and it became null at the maximum expansion.

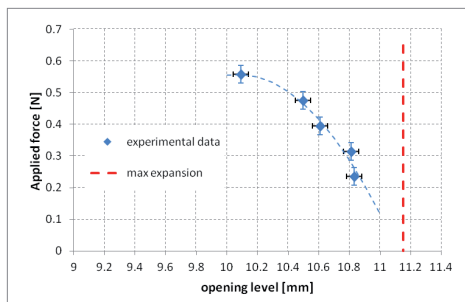


Fig. 7: mechanical behavior of the material

Many tests were conducted with various material compositions, different thicknesses and different

heights of specimens, in order to verify how the mechanical behavior of the devices is influenced by these variables.

## 5. Developments

Tests carried out have shown how the device developed for the force measurement allows to test only specimens of shape memory material capable of exercising limited forces up to 0.55 N. In order to increase the full scale of the force measuring instrument it will be necessary to install calibrated weights on the singular trolley for increase its mass.

A second activity, which must be further developed, is the direct metrological properties verification of the dynamometer proposed. In particular, the residual friction force entity should be assessed, also in relation to the increase in weight of the trolleys.

## 6. Conclusions

The present work concerns a methodology for the mechanical characterization of shape memory materials.

The proposed procedure requires the use of a vision system for assessing the level of shape changes (opening level). Forces exerted during the expansion of tested specimens were evaluated with a measuring tool specifically designed and developed.

The difficulty of the force measurement consists in the application of a load of very low intensity independently from its point of application. The solution adopted is the use of a trolley free to fall along an inclined rail with a pneumatic bearing.

Tests carried out have allowed to define a force-deformation curve that allows to evaluate material performances for its use as a stent in biomedical applications.

## Bibliography

- [1] A. Lendlein and S. Kelch., "Shape memory polymers", *Angew. Chem. Int. Ed.*, vol. 41(12), pp. 2034-2057, 2002
- [2] A. Lendlein and R. Langer, "Biodegradable, elastic shape-memory polymers for potential biomedical applications", *Science*, vol. 296(no. 5573), pp. 1673-1676, 2002
- [3] C.M. Yakacki, et al., "Strong, tailored biocompatible shape-memory polymer networks", *Adv. Funct. Mater.*, vol. 18, pp. 2428-2435, 2008
- [4] J. Leng, et al., "Shape memory polymers and their composites: stimulus method and applications", *Prog. Mater. Sci.*, vol. 56(7), pp. 1077-1135, 2011

- [5] A. Lendlein, et al., "Shape-memory polymers as a technology platform for biomedical applications", *Expert Rev. Med. Dev.*, vol. 7(3), pp. 357-379, 2010
- [6] X. Liang, et al., "Biodegradable shape-memory block co-polymers for fast self-expandable stents", *Biomaterials*, vol. 31, pp. 8132-8140, 2010
- [7] D. J. Maitland, et al., "Thermomechanical properties, collapse pressure, and expansion of shape memory polymer neurovascular stent prototypes", *J. Biomed. Mater. Res.*, Part B, vol. 90(1), pp. 421-429, 2009
- [8] G. M. Baer, et al., "Fabrication and in-vitro deployment of a laser-activated shape memory polymer vascular stent", *Biomed. Eng. Online*, vol. 6:43, 2007
- [9] V. J. Neiman and S. Varghese, *Smart Struct. Syst.*, vol. 7(3), pp. 185-198, 2011
- [10] L. Hines et al., *IEEE Trans. Robot.*, vol. 28(4), pp. 987-990, 2012
- [11] I. Bodini, D. Vetturi, et al., *Advanced in Science and Technology*, vol. 77, pp. 313-318, 2013.
- [12] M. A. Martínez, et al., *J. Mech. Behav. Biomed.*, vol. 10, pp. 166-175, 2012.
- [13] M. T. Voûte, et al., *J. Vasc. Interv. Radiol.*, vol. 22, pp. 661-666, 2011
- [14] F. H. Silver, et al, *Ann. Biomed. Eng.*, vol. 31, pp. 793-803, 2003
- [15] A. Borboni, et al., Experimental Kinematics of a Special Shape Actuator, 12th ASME Conference on Engineering Systems Design and Analysis ESDA2014, June 25-27, 2014, Copenhagen, Denmark
- [16] Messori, M., Degli Esposti, M., Paderni, K., Pandini, S., Passera, S., Riccò, T., and Toselli, M., 2013, "Chemical and Thermomechanical Tailoring of the Shape Memory Effect in Poly(E-Caprolactone)-Based Systems," *Journal of Materials Science*, 48(1), pp. 424-440.
- [17] Pandini, S., Passera, S., Ricco, T., Borboni, A., Bodini, I., Vetturi, D., Dassa, L., Cambiaghi, D., Paderni, K., Degli Esposti, M., Toselli, M., Pilati, F., and Messori, M., 2013, "Tailored One-Way and Two-Way Shape Memory Response of Poly(Epsilon-Caprolactone)-Based Systems for Biomedical Applications," *Adaptive, Active and Multifunctional Smart Materials Systems*, 77, pp. 313-318.
- [18] Xu, F., Hart, K., Flanagan, C. E., Nacker, J. C., Moftakhar, R., Aagaard-Kienitz, B., Consigny, D. W., Grinde, J. R., Crone, W. C., and Masters, K. S., 2009, "A Hybrid Coil/Polymer Device for Occlusion of Cerebral Aneurysms," *Journal of Medical Devices, Transactions of the ASME*, 3(4), pp.



# Laboratory calibration and comparison of three visual odometry systems

Marco Pertile, Sebastiano Chiodini, Stefano Debei, Enrico Lorenzini

\* CISAS G. Colombo, University of Padova, Italy  
marco.pertile@unipd.it

## Abstract

*In planetary exploration space missions, motion measurement of a vehicle on the surface of a planet is a very important task. The main contribution of this work is an experimental comparison among visual odometry systems using lenses with three different focal lengths (an ultra wide angle, a medium wide angle and a telephoto lens). For each focal length a complete calibration procedure is performed using a suitable reference instrument and taking into account different types of motion. The calibration procedure comprises a rigorous uncertainty analysis. Experimentally obtained uncertainties are compared, pointing out strengths and weaknesses of employing wide angle or telephoto lenses for motion measurement.*

## 1. Introduction

In planetary exploration, motion measurement of a vehicle on the surface of a planet should be very accurate in order to track the vehicle also for long paths. The odometric evaluation of vehicle position and attitude performed measuring the rotation of wheels has wide uncertainty due to slippage of wheels on a natural, often sandy or slippery, surface. Moreover, on extraterrestrial planets GPS-like positioning systems are not yet available and inertial navigation sensors exhibit unacceptable drifts. Thus, the need of a reliable and accurate motion instrument is particularly relevant. In this work a vision-based instrument for displacement and rotation measurement is calibrated using a high precision motor-driven rotary stage and a linear slide as reference instruments. To evaluate the measurement performance along paths longer than the reference linear slide, the visual odometry system is also mounted on a laboratory vehicle, which is driven along a closed path and the whole travelled trajectory is acquired by the stereo vision system.

The use of stereo systems for visual-odometry (VO) is well known, e.g. see [1]-[12], but is a still-open research subject, as proved by many recent papers, e.g. see [13]-[16]. An interesting

overview and an introducing tutorial on visual odometry can be found in [11] and [12]. In visual odometry, the displacement and rotation of a stereo vision system are measured through the images taken by the two cameras. Stereo-processing allows estimation of the three dimensional (3D) location of landmarks observed by a stereo-camera. If the same landmarks are acquired and detected by a moving stereo-system in two subsequent positions, the two 3D point clouds allow to evaluate the stereo camera movement (position and orientation) that took place between the acquisitions of the two stereo images. The whole trajectory is then calculated combining each motion step.

Particularly, reference [5] describes a method for visual odometry based on a stereo camera, providing experimental results gathered during development and flight phases of the NASA's twin Mars Exploration Rovers Spirit and Opportunity landed on the surface of Mars in January 2004. Reference [6], for the first time, analyzes the need of an anisotropic uncertainty modeling for 3D acquired landmarks. Reference [9] emphasizes the importance of a detailed and correct uncertainty evaluation, and describes a method for visual-odometry that allows to reduce the final measurement uncertainty. The methods described in [1] - [10] require that the same 3D landmarks are observed in two subsequent acquired stereo images; this requirement limits the maximum translation and, even more, the maximum rotation that can be measured in one step. To follow a whole trajectory, e.g. of a vehicle with the stereo system mounted, several incremental measurements are performed and combined together, with the warning that uncertainty may significantly increase with the number of steps, i.e. small errors in each measurement step can eventually cause large errors in the estimated trajectory. This drawback can be solved using more global approaches (e.g. Simultaneous Localization And Mapping, loop-closing, semi-global optimization). However, in the present work the attention is focused on comparing the measurement uncertainties



obtained by a visual odometry system using lenses with different focal lengths. The main purpose is to experimentally compare the metrological behavior obtained with different lenses, and not to find the best position measurement method based on a vision system. Thus, more global approaches are beyond the purpose of this work and are not taken into account.

The main aim of the presented comparison among different focal lengths and, thus, different values of field of view (FOV) is to yield useful advices to the problem of lens selection for the stereo camera of a visual odometry system. Reference [4] performed numerical simulations to evaluate which FOV yields the smallest long-range error of a visual odometry system. Authors analyzed several values of FOV between  $15^\circ$  and  $90^\circ$  using a numerical simulation procedure, and found that the optimal FOV is approximately  $35^\circ$ . In [4], the obtained numerical results are not validated by an experimental comparison. Despite the optimal values of FOV found in [4], reference [5] says that their visual odometry algorithm has been experimentally tested using the Jet Propulsion Laboratory's Rocky 8 rover, whose cameras have a horizontal FOV equal to  $80^\circ$  and  $64^\circ$  along vertical direction. Other tests were run on the MER Surface System Testbed Lite rover with a  $120^\circ$  FOV cameras and, of course, on the Mars rovers with a  $45^\circ$  FOV. However, in [5] there is not a rigorous comparison among experimental results obtained with these different FOV values. Moreover, different values of FOV are associated with different cameras and different rovers, thus, a direct comparison could not be meaningful, since FOV is not the only parameter that changes from one case to another one. Our contribution is a direct experimental comparison among visual odometry systems with three different focal lengths and FOV (an ultra wide angle, a medium wide angle and a telephoto lens), performed with all other influencing parameters kept constant (same cameras, same relative positions of cameras, same elevation angle of cameras, same imposed rotary and linear motions) and with a rigorous uncertainty analysis according to [17]-[18].

In [28], we applied about the same VO algorithm described in the present manuscript to the measurement of a vehicle trajectory. The vehicle was driven along a closed path and was brought to the initial position with a positioning uncertainty of about 1cm. The on-board mounted stereo camera acquired two video sequences with fixed frame rate during the motion. The optical encoders mounted on the wheels were not able to

acquire the trajectory with an uncertainty one order of magnitude better than the VO system. Thus, only the final position could be used to analyze the errors and the uncertainty achieved by the VO system. With reference to [28], the major contribution of the present manuscript is to describe the behavior of different VO systems using a complete new laboratory set-up, which allows to analyze the errors and uncertainties obtained by each VO system for all the acquired motion steps and not only at the end of the motion. With the new experimental set-up, we have the possibility to measure both linear displacements and rotations imposed to the stereo camera during all the motion steps with an uncertainty an order of magnitude better than that of the VO system. Thus a more detailed analysis can be performed than in [28].

In section 2, the paper describes a measurement method broadly based on the NASA rovers approach [4], [5] and slightly updated combining together subroutines and procedures more recent and advanced. Section 3 presents the performed uncertainty analysis, and section 4 discusses the experimental set-up and the obtained results.

## 2. Measurement algorithm

In this section, the procedure employed to perform the displacement and rotation measurement of the stereo system is described. In each motion step, the goal is to calculate the displacement and rotation of a calibrated stereo system using the images acquired in two subsequent positions. The whole trajectory of the vehicle is then evaluated combining each single motion step. Rotation is described by a sequence of Euler angles around axes X, Y, Z.

The procedure begins with the detection of image features (keypoints) which are the projections of physical landmarks in the two cameras. After the intrinsic and extrinsic parameters of a stereo system are carefully determined (the stereo camera is calibrated as described in [27]), one of the main uncertainty sources is the position on the image plane of the features detected and matched in corresponding images. Several feature detectors and descriptors were considered in the preliminary phases of this work, see [19]-[26]. Particularly, reference [23] compares several different detectors invariant to scale and affine transformations and finds out that the best results are obtained by the Hessian-Affine detector and the Maximally Stable Extremal Regions (MSER) approach. These methods are a good choice to find features even in presence of relatively wide scale and/or rotation variations

and of affine transformations between images. However, in our work we used two well known algorithms: the Harris detector [19] and the Scale Invariant Feature Transform (SIFT) detector [22], since two selected approaches are widely used and we do not need to cope with wide affine transformations when we apply the VO algorithm to subsequent images.

Reference [26] makes a comparison among different descriptors and concludes that the SIFT and the Gradient Location and Orientation Histogram GLOH descriptors are the best. For this reason, the SIFT descriptor is chosen to describe the image neighborhood of each detected feature and to reliably perform feature matching between stereo pairs and between corresponding features in subsequent vehicle movements. The SIFT descriptor is used for all features: those detected by SIFT detector and also those found by the Harris detector. This choice is one of the major difference between the employed algorithm and that of NASA rovers [4]-[5], which employ a Forstner or Harris operator as feature detector, and rely upon cross correlation along epipolar lines for feature matching. This is also a difference with our previous work [28]: in the present application we found out that the Hessian-Affine detector does not exhibit a significant advantage over the combination of Harris and SIFT detectors.

After the corresponding 2D features are detected, a triangulation phase allows to compute the 3D coordinates of the physical landmarks acquired by the cameras. The middle point algorithm is used for triangulation, as in [5], for more details see [10].

The uncertainties of 3D points (their 3x3 covariance matrix) are needed for the evaluation of stereo system displacement and rotation as described in subsection 2.1. Uncertainty evaluation for triangulated 3D points becomes an uncertainty propagation task, which is performed by the Kline-McClintock formula, see GUM [17]. This method is selected, instead of the Monte Carlo propagation approach, since the calculation is embedded in the algorithm that calculate the displacement and rotation of the stereo camera, and is performed for all detected features (see subsection 2.1). Thus, the use of a Monte Carlo simulation could lead to unacceptable time delays in the position and attitude evaluation of the stereo camera.

## 2.1. Stereo system displacement and rotation

When the stereo system is calibrated (intrinsic parameters of both cameras and the position and orientation of camera 2 with reference to camera 1 are known), the 3D points  ${}^{P1}\mathbf{X}$  can be calculated for all features detected by both cameras when the vision system is in an initial position P1. The notation  ${}^{P1}\mathbf{X}$  means that these points are expressed in the reference frame attached to the first camera, when the vision system is in the initial position P1. When the vision system is moved (cameras are rigidly connected) from the initial position P1 to a subsequent position P2, the same procedure can be used to compute the 3D vectors  ${}^{P2}\mathbf{X}$  of the same features detected by both cameras in the second position P2 and expressed in the new frame 1 attached to the first camera. For each feature that is detected by both cameras in both positions P1, P2, the following equation can be written:

$${}^{P1}\mathbf{X}_i = {}^{P1}\mathbf{R} \cdot {}^{P2}\mathbf{X}_i + {}^{P1}\mathbf{P}_{P2,P1} \quad Eq. 1$$

Where  ${}^{P1}\mathbf{R}$  is the rotation matrix from frame 1 in the second position P2 to frame 1 in the initial position P1;  ${}^{P1}\mathbf{P}_{P2,P1}$  is the origin of frame 1 in P2 with reference to the origin of frame 1 in P1 and expressed in P1;  $i = 1, \dots, n$ , with  $n$  being the number of common detected and matched features. Vector  ${}^{P1}\mathbf{P}_{P2,P1}$  and the Euler angles that

define matrix  ${}^{P1}\mathbf{R}$  are the numerical output values of the whole measurement procedure and, in this work are evaluated in two steps in a similar way as in [5]: first, a less accurate motion is estimated by least squares estimation embedded within a random sample consensus (RANSAC) process to remove outliers; then, a maximum likelihood motion estimation is performed minimizing a non linear problem. The main differences with [5] are: the feature detection and matching algorithms employed in this work are more advanced; the linear least squares approach is derived from [7]; the non linear minimization procedure comprises the Levenberg-Marquardt algorithm.

In the linear motion evaluation an error vector  $\mathbf{e}_i$  is defined for each couple of 3D points  ${}^{P1}\mathbf{X}$ ,  ${}^{P2}\mathbf{X}$  detected in both the first P1 and the second P2 position and then the cost function  $E$  to be minimized is calculated:

$$\mathbf{e}_i = {}^{P1}\mathbf{X}_i - {}^{P1}\mathbf{R} \cdot {}^{P2}\mathbf{X}_i - {}^{P1}\mathbf{P}_{P2,P1} \quad Eq. 2$$

$$E = \sum_{i=1}^n \|\mathbf{e}_i\|^2 \quad \text{Eq. 3}$$

In order to separate the evaluation of rotation and translation, the centers of the two point clouds are subtracted from the 3D points. Using the formulas explained in [7], first the rotation matrix is evaluated and then the translation  ${}^{P1}\mathbf{P}_{P2,P1}$  of the stereo system is calculated rearranging Eq.1.

In the non linear step also the covariance matrices of the 3D landmarks are taken into account. For the non linear analysis, the errors defined for each 3D feature in Eq.2 is weighted using the inverse of a combined covariance matrix. For each 3D point evaluated with the stereo system in the first position, the corresponding covariance matrix  ${}^{P1}\mathbf{C}_i$  is evaluated; then, this evaluation is repeated for the same feature in the second position to obtain the covariance matrix  ${}^{P2}\mathbf{C}_i$ .  ${}^{P1}\mathbf{C}_i$  and  ${}^{P2}\mathbf{C}_i$  of the same 3D landmark are combined together and the new cost function  $E_{nl}$  (minimized by the Levenberg-Marquardt algorithm) is:

$$\mathbf{C}_i = {}^{P1}\mathbf{C}_i + {}^{P1}\mathbf{R} \cdot {}^{P2}\mathbf{C}_i \cdot {}^{P1}\mathbf{R}^T \quad \text{Eq. 4}$$

$$E_{nl} = \sum_{i=1}^n \left( \mathbf{e}_i^T \cdot \mathbf{C}_i^{-1} \cdot \mathbf{e}_i \right) \quad \text{Eq. 5}$$

In this way each component of the error vector  $\mathbf{e}_i$  of the feature  $i$  can have a different weight that takes into account the uncertainty of feature  $i$  along the considered direction. This heteroscedastic modeling of uncertainty, i.e. inhomogeneous (it may be different from point to point) and anisotropic (it may be different in each direction) is particularly useful in stereo systems whose baseline (i.e. distance between cameras) is small and the uncertainty along a direction roughly parallel to the optical axes may be much greater than in the other directions. A properly tuned RANSAC algorithm used in the linear phase of motion estimation allows to identify and to exclude possible outlier landmarks. Thus, the non linear phase is performed taking into account only 3D points that passed RANSAC algorithm.

### 3. Uncertainty analysis

A detailed uncertainty analysis is carried out according to the metrological procedures described in [17] and [18]. The position and orientation uncertainty of the stereo camera is evaluated as in an indirect measurement by a Monte Carlo propagation approach. Along the imposed motion, the position and orientation of the stereo camera are obtained combining every

motion step and are treated as the output quantities of an indirect measurement. This uncertainty analysis can be performed off-line after the trajectory has been evaluated, thus, the aim is to evaluate uncertainties of position and attitude of the stereo system as precisely as possible, and not to calculate them in a fast way. Moreover, the whole measurement algorithm is highly non linear. Thus, a Monte Carlo simulation is employed for this off-line uncertainty analysis instead of the propagation formula embedded in the calculation algorithm as described in section 2 and that is an approximated method. In the new set-up, all the translations and/or rotations imposed to the stereo camera are known with an uncertainty at least one order of magnitude better than the measurements obtained by the VO system. Thus, the compatibility of the experimentally obtained errors (the difference between the values obtained by the VO system and those obtained by the reference instrumentation) with the uncertainties evaluated by the Monte Carlo method can be checked for all the positions and orientations imposed.

Several uncertainty sources are analyzed and evaluated using experimental tests. Particularly, the uncertainty associated with the following quantities are taken into account: intrinsic and extrinsic parameters of the stereo system, whose uncertainties are evaluated using the camera calibration procedure described in [27], and the positions of image features, whose uncertainty is affected by several contributions. In this paper two main contributions are evaluated for image features: the reading uncertainty (image noise) of the sensors, and the residual uncorrected optical distortions that the distortion model is not able to remove. According to [17] and [18], all uncertainty sources are expressed by a probability density function (PDF) and are then propagated to the output displacement of the stereo system using a Monte Carlo simulation. In this way, for each motion step the corresponding position and orientation uncertainties.

### 4. Experimental set-up and Results

In the calibration procedure of the visual odometry system, the stereo camera is mounted both on a high precision motor-driven rotary stage and on a linear slide. The rotary stage is driven by a stepper motor capable of a resolution equal to 1.125 arcseconds, while the linear slide is provided with a graduated scale, in order to compare the measurements obtained by the visual system respectively with known rotation angles and with known linear displacements. Fig.1

depicts the employed set-up comprising the stereo camera mounted on the rotary stage, which can translate along the linear slide.



Fig. 1: Experimental set-up

In [4], the simulated stereo camera had a fixed baseline equal to 10cm, a height from ground of 1.4 m and a downward tilt of  $30^\circ$ . The rover movement was simulated along a 500m path and with simulated measurement steps ranging between 30 and 70 cm. Reference [4] says that the optimal FOV remained between  $30^\circ$  and  $40^\circ$  also changing the length of measurement steps. In our laboratory set-up, we use a stereo camera having a baseline of 54 cm, a height from ground of 1.1 m and a downward tilt angle of  $0^\circ$ . Three lenses with different focal lengths are employed: 6mm, 10.4 mm, 50 mm. These nominal lengths, combined with the sensor size of the cameras, yield respectively the following FOV values:  $86^\circ \times 53^\circ$ ,  $57^\circ \times 32^\circ$ ,  $13^\circ \times 7^\circ$ . According to [4], we expect that the medium wide angle lens ( $57^\circ \times 32^\circ$  FOV) should be the best choice, while the ultra wide angle lens ( $86^\circ \times 53^\circ$  FOV), that exhibits the largest distance from the numerically evaluated optimal range ( $30^\circ$ - $40^\circ$ ), should be worst case.

In our lab, a translation test with a total travel of 1350mm using the linear slide and a rotation test from  $0^\circ$  to  $90^\circ$  using the rotary stage are performed. In the translation test, the stereo camera is incrementally translated along the linear slide with a motion step of 50 mm. After each step the motion is stopped and two images are acquired. Thus, two stereo images are available exactly every 50 mm. The same procedure is repeated in the rotation test using the rotary stage. In this case the stereo images are acquired every  $1^\circ$ .

The results obtained using the three lenses are summarized by the following figures. Fig. 2- Fig. 5 show results obtained in the linear translation test with the linear slide, while Fig. 6 – Fig. 9 deal

with the rotation test using the rotational stage. Fig. 2 shows the total displacement measured by the VO system vs. the one imposed along the linear slide. Fig. 3 illustrates the measured total errors for each motion step, which are the differences between the measured and the imposed total displacements.

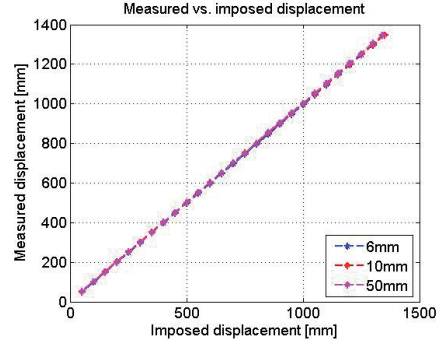


Fig. 2: Measured total displacement in the linear translation test

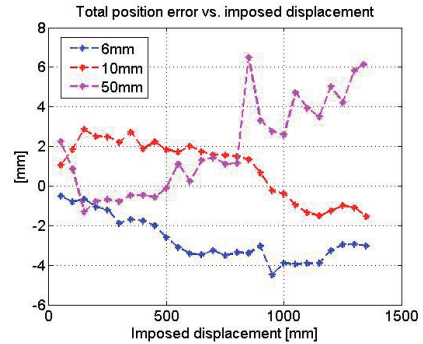


Fig. 3: Total displacement error in the linear translation test

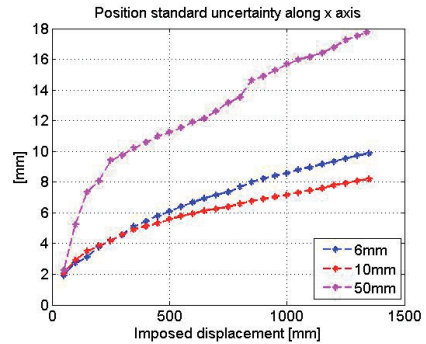


Fig. 4: Total position standard uncertainty along x axis in the linear translation test

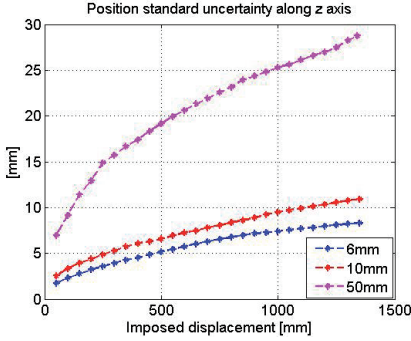


Fig. 5: Total position standard uncertainty along z axis in the linear translation test

Fig. 4 and Fig. 5 depict the standard uncertainties evaluated by the Monte Carlo approach for the total position along respectively the x and z axis (z axis is parallel to the linear slide, while the x axis is orthogonal). These uncertainties are obtained combining together all the single uncertainties of each motion step from the first one to the considered position.

Results slightly different from the expected ones emerge from the experimental tests. From Fig. 2 – Fig. 5, it is clear that all three lenses are able to measure the linear translation along a direction parallel to the optical axes of the stereo cameras. However, the worst case is the telephoto lens ( $f=50\text{mm}$ ) and not the ultra wide angle one ( $f=6\text{mm}$ ), as expected from [4]. In this linear test, the telephoto lens is always the worst case among the three lenses, but it behaves in a better way than during the tests described in [28].

In the translation test, both the two wide angle lenses perform very well, with similar results. In Fig. 3 the measurement errors obtained by medium wide angle ( $f=10\text{mm}$ ) are lower than those obtained by the ultra wide angle except than in the first part of the translation ( $<400\text{ mm}$ ). Looking at the evaluated uncertainties, the ultra wide angle lens achieves better values along the z axis than the medium wide one, and vice versa along the x axis.

Fig. 6 shows the total rotation measured by the VO system vs. the one imposed by the rotary stage in the rotation test. Fig. 7 illustrates the measured errors, which are the differences between the measured and the imposed total rotations in each position. Fig. 8 depicts the standard uncertainties evaluated by the Monte Carlo approach for the total rotation around the vertical axis y, while Fig. 9 shows the standard uncertainties evaluated for each rotational motion

step. The uncertainties of Fig. 8 are obtained combining together those depicted in Fig.9.

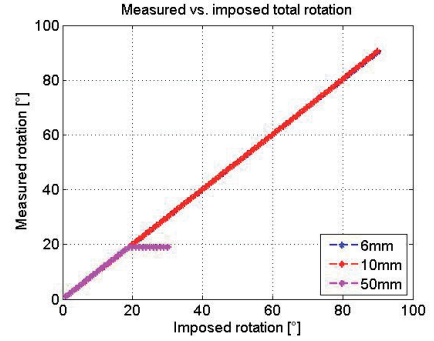


Fig. 6: Measured total rotation in the rotation test

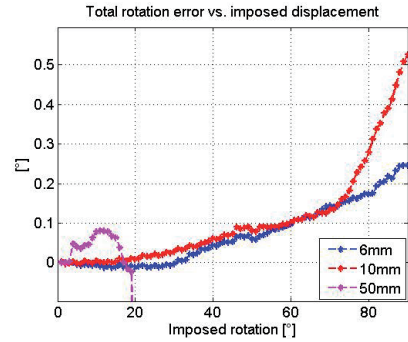


Fig. 7: Total rotation error in the rotation test

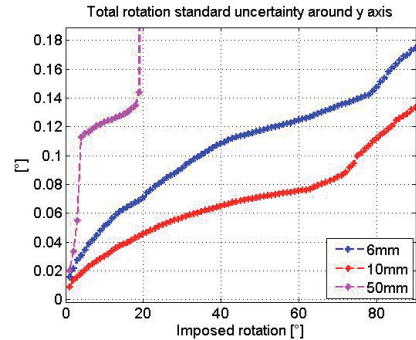
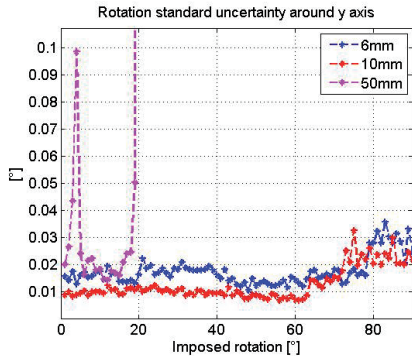


Fig. 8: Total rotation standard uncertainty around y axis in the rotation test

In the rotation test, the VO system equipped with the telephoto lens is able to measure the rotation up to an angle of about  $20^\circ$ . This behavior is due to the fact that the tests are performed in a rectangular room: when the rotation angle is about  $0^\circ$  the stereo camera optical axes are parallel to



the long walls of the room, while at 90° they are parallel to the short walls. Thus, the objects observed by the telephoto lenses at 0° are located at a distance of about 13m, but the rotation from 0° towards 90° makes the observed objects closer to the cameras, up to a distance of about 2-3 m. This shorter distance of the observed objects means the number of correctly matched features (3D points) decreases, until the VO algorithm is not able to evaluate the motion.



**Fig. 9: Rotation standard uncertainty (of each single motion step) around y axis in the rotation test**

Moreover, also for small total angles the evaluated uncertainties (Fig. 8 and 9) are higher for the telephoto lens than with the other two lenses. These results confirm that the telephoto is the less suitable lens for VO in a closed environment as observed in [28].

Possible reasons of the poor performance of the telephoto lens are:

- The intrinsic and extrinsic parameters evaluated by the Zhang approach [27] for the telephoto lenses are affected by wider uncertainties than those obtained for the other two focal lengths.
- A telephoto lens has a narrower depth of field than a wide angle lens.
- The number of acquired and correctly matched 3D points at each motion step is low due to the small (for a telephoto lens) distance of the observed objects

Also in the rotation test, the two wide angle lenses behave very well. The medium wide angle lens has a slight advantage up to an angle of 70°. At high rotation values, when the distance of observed objects approaches its minimum values, both the wide angle lenses begin to exhibit higher uncertainties. However, the medium wide angle lens (with a narrower field of view) sensibly worsens from about 70°, while the ultra wide angle starts later to increase its uncertainty, from

about 80° (see Fig. 9). This means that the advantage of the medium wide angle over the ultra wide one seems to disappear in narrow spaces. This effect is not present in the translation test, since in that case there is not a large reduction of the objects distance during the motion.

Possible reasons of the slight discrepancy between the simulations performed in [4] and the presented experimental results could be:

- the experimental tests are performed inside a closed environment. In this set-up the distance between the acquired objects (3D points) and the stereo cameras is necessarily limited by walls, the floor and ceil.
- the wide difference between the horizontal and vertical field of view.

## 5. Conclusions

A detailed experimental comparison among visual odometry systems using lenses with three different focal lengths (an ultra wide angle, a medium wide angle and a telephoto lens) was performed and described. The experimental results allow to point out that in a closed environment the two wide angle systems outperform the telephoto one and that the difference in the field of view can lead to slight different performances also between the ultra wide angle and the medium wide angle systems.

## References

- [1] Arun K. S., Huang T. S., Blostein S. D., "Least-squares fitting of two 3-d point sets", *IEEE Trans on PAMI*, Vol.9, No.5, 1987, pp. 698–700.
- [2] Eggert D., Lorusso A., Fisher R., "Estimating 3-d rigid body transformations: a comparison of four major algorithms", *Machine Vision and Applications*, Vol.9, No.5-6, 1997, pp.272–290.
- [3] Umeyama S., "Least-squares estimation of transformation parameters between two point patterns", *IEEE Trans on PAMI*, Vol. 13, No.4, 1991, pp. 376 – 380.
- [4] Olson C. F., Matthies L. H., Schoppers M., Maimone M. W., "Rover navigation using stereo ego-motion", *Robotics and Autonomous Systems*, Vol. 43, 2003, pp. 215–229.
- [5] Cheng Y., Maimone M. W., Matthies L., "Visual Odometry on the Mars Exploration Rovers", *IEEE Robotics & Automation Magazine*, 2006.



- [6] Matthies L, Shafer S A, "Error modeling in stereo navigation", IEEE Jou. of Robotics and Automation, Vol.3, No.3, June 1987, pp.239-248.
- [7] Horn B.K.P., Hilden H.M., Negahdaripour S., "Closed-form solution of absolute orientation using orthonormal matrices", Jou. of the Optical Soc. of Am., July 1988, Vol. 5, pp. 1127.
- [8] Ma Y., Soatto S., Kosecka J., Sastry S. S., "An invitation to 3-D Vision", Springer, 2004.
- [9] Dubbelman G., Groen F. C. A., "Bias Reduction for Stereo based Motion Estimation with Applications to Large Scale Visual Odometry", IEEE CVPR, 2009.
- [10] M Pertile, M Magnabosco, S Debei, "Calibration of a vision-based system for displacement measurement in planetary exploration space missions", Journal of Physics: Conference Series, Vol.238, doi:10.1088/1742-6596/238/1/012031, 2010.
- [11] Scaramuzza D, Fraundorfer F, "Visual Odometry Part I: the first 30 years and fundamentals", IEEE Robotics & Automation Mag., pp.80-92, Dec 2011.
- [12] Scaramuzza D, Fraundorfer F, "Visual Odometry Part II: matching, robustness, optimization, and applications", IEEE Robotics & Automation Mag., pp.78-90, Jun 2012.
- [13] Azartash H., Banai N., Nguyena T.Q., "An integrated stereo visual odometry for robotic navigation", Robotics and Autonomous Systems, Vol. 62, pp.414-421, 2014.
- [14] Fabian J., Clayton G.M., "Error Analysis for Visual Odometry on Indoor Wheeled Mobile Robots With 3-D Sensors", accepted, in press in IEEE/ASME Trans on Mechatronics, 2014.
- [15] Jiang Y., Xu Y., Liu Y., "Performance evaluation of feature detection and matching in stereo visual odometry", Neurocomputing, Vol. 120, pp380-390, 2013.
- [16] Wanga Z., Deng C., Pan C., Liu J., "A visual integrated navigation for precise position estimation", in press in Computers and Electrical Engineering, 2014.
- [17] BIPM, IEC, IFCC, ILAC, ISO, IUPAC, IUPAP, OIML, Evaluation of measurement data—Guide to the Expression of Uncertainty in Measurement, Geneva, Switzerland: International Organization for Standardization, 2008.
- [18] BIPM, IEC, IFCC, ILAC, ISO, IUPAC, IUPAP, OIML, Evaluation of measurement data—Supplement 1 to the Guide to the Expression of Uncertainty in Measurement—Propagation of distributions using a Monte Carlo method.
- [19] Harris C., Stephens M., "A Combined Corner and Edge Detector", Proc. Alvey Vision Conf., 1988, pp. 147-151.
- [20] Mikolajczyk K., Schmid C., "Indexing Based on Scale Invariant Interest Points", Proc. 8th Int. Conf. Computer Vision, 2001, pp. 525-531.
- [21] Lowe D., "Object Recognition from Local Scale-Invariant Features", Proc. 7th Int. Conf. Computer Vision, 1999, pp. 1150-1157.
- [22] Lowe D., "Distinctive Image Features from Scale-Invariant Keypoints", Int. J. Computer Vision, Vol. 2, No. 60, 2004, pp. 91-110.
- [23] Mikolajczyk K., Schmid C., "Scale and Affine Invariant Interest Point Detectors", Int. J. Computer Vision, Vol. 1, No. 60, 2004, pp. 63-86.
- [24] Mikolajczyk K., Tuytelaars T., Schmid C., Zisserman A., Matas J., Schaffalitzky F., Kadir, VanGool T., "A Comparison of Affine Region Detectors", Int. J. Computer Vision, No. 65, 2005, pp. 43-72.
- [25] Matas J., Chum O., Urban M., Pajdla T., "Robust wide-baseline stereo from maximally stable extremal regions", Image and Vision Computing, Vol. 22, 2004, pp.761-767.
- [26] Mikolajczyk K., Schmid C., "A Performance Evaluation of Local Descriptors", IEEE Trans On PAMI, Vol. 27, No. 10, 2005.
- [27] Zhang Z., "A Flexible New Technique for Camera Calibration", IEEE Trans on PAMI, vol. 22, n.11, 2000.
- [28] Pertile M., Chiodini S., Debei S., "Comparison of visual odometry systems suitable for planetary exploration", IEEE Int. Workshop on Metrology for Aerospace, 2014.

# ***Influence of transducer position on quality assurance measurements in B-mode Ultrasound: a case study.***

Andrea SCORZA<sup>1</sup>, Giulia LUPÍ<sup>1</sup>, Luigi BATTISTA<sup>2</sup>, Jan GALO<sup>3</sup>, Salvatore Andrea SCIUTO<sup>1</sup>

<sup>1</sup> Department of Engineering, Roma TRE University, Via della Vasca Navale 79/81, Roma, Italy

<sup>2</sup> Clinical Engineering Service, Religious General Hospital "F. Miulli", Acquaviva delle Fonti (BA), Italy

<sup>3</sup> Clinical Engineering Service, I.R.C.C.S. Children Hospital Bambino Gesù, P.zza S. Onofrio 4, Roma, Italy

## **Abstract**

*Image quality assurance tests on medical ultrasound systems are often performed by technicians using ultrasound phantoms and results depend on phantom features as well as scanner settings and operator experience. The aim of the present study is the evaluation of variations on some features of the B-mode image when the ultrasound probe is handled by the technician during a routine quality test: ultrasound images of two different ultrasound phantom are acquired and processed from two transducer to evaluate measurement dispersion in spatial resolution, penetration depth and accuracy in distance measurements when probe is handled by the operator. Results are then investigated and discussed.*

## **1. Introduction**

Image quality assurance tests in medical ultrasound system are usually based on measurements of specific parameters such as spatial resolution, low contrast penetration, accuracy in distance measurements and local dynamic range [1-7]: routine tests are often performed by technicians using ultrasound phantoms<sup>1</sup> and results depend on phantom features as well as scanner settings and operator manual skill and experience. In scientific literature the operator influence on tests precision seems not to be systematically evaluated and in particular effects of probe position on measurements of the above parameters: in this work the influence of probe position is estimated while the transducer is handled by the technician during the test.

<sup>1</sup> An Ultrasound Phantom is a volume of material behaving in essentially the same manner as tissue of the same dimensions, with respect to absorption and scattering of the ultrasound radiation in question, used for dosimetry or for the evaluation of sonographic images in diagnostic sonography.

## **2. Experimental set-up and methods**

The measurement setup is made of an ultrasound scanner Philips HD3, an array probe on the ultrasound phantom, and a notebook pc for data acquisition and processing. Tests are performed with two different models of array probe (convex and linear array) on two tissue mimicking phantoms<sup>2</sup> (see table 1 for specifications). In particular the study focuses on evaluation of the follow features: (a) accuracy in distance measurements (both vertical and horizontal directions) [3, 5], (b) high contrast spatial resolution (both lateral and axial resolution) [5] and (c) maximum depth of signal visualization [6-8].

*Table 1 – Ultrasound Phantoms characteristics*

Model	GAMMEX 405 GSX LE (phantom A)	GAMMEX 1425A (phantom B)
Dimensions	23.2×8.25×18.5 cm	40.7 × 22.9 × 35.6 cm
Weight	Approx. 2.8 kg	Approx. 10 kg
<i>Background Material</i>		
Speed of sound	1540±10 m/s	1540±10 m/s
Attenuation	0.7±0.05 dB/cm/MHz	0.5±0.05 dB/cm/MHz
<i>Pin targets</i>		
Diameter	0.1 mm	0.1 mm
Vertical spacing	2 cm at 2–16 cm deep	2 cm at 3–17 cm deep
Horizontal spacing	3 cm at 2–12 cm deep	3 cm at 3–13 cm deep

The ultrasound probe is applied on the phantom by hand and its position is manually adjusted to clearly display test objects in the US image, after that, a single image is acquired and then exported on a peripheral in a TIFF or DICOM format (lossless): for each phantom the whole procedure is repeated 16 times, so for a same test (see tab.2 for settings) 16 different ultrasound image are provided and processed in a Matlab environment

<sup>2</sup> tissue-mimicking material: material in which the propagation velocity (speed of sound), reflecting, scattering and attenuating properties are similar to those of soft tissue for ultrasound in the frequency range 0.5 MHz to 15 MHz.

[3, 5-9] to evaluate parameters (a), (b) and (c) variation due to probe manual application on the phantom surface.

*Table 2 – Measurements settings. Test 1, 2: Maximum Depth of Penetration, Accuracy in distance measurements (vertical and horizontal), High contrast spatial resolution (lateral and axial). Test 3, 4: Accuracy in distance measurements (vertical and horizontal), High contrast spatial resolution (lateral and axial). For each test and phantom 16 ultrasound images are acquired at a medium overall gain and a linear post processing.*

PROBE 1 (convex array)				
	Test 1	Test 2	Test 3	Test 4
Nominal Frequency range (MHz)	2-5	2-5	2-5	2-5
Field of View (mm)	180	180	110	110
Focus depth (mm)	70	70	70	70
Dynamic Range (dB)	Maximum	Medium	Maximum	Medium
Phantom	A, B	A, B	A, B	A, B

PROBE 2 (linear array)				
	Test 1	Test 2	Test 3	Test 4
Nominal Frequency range (MHz)	5-9	5-9	5-9	5-9
Field of View (mm)	75	75	50	50
Focus depth (mm)	20	20	20	20
Dynamic Range (dB)	Maximum	Medium	Maximum	Medium
Phantom	A, B	A, B	A, B	A, B

To better understand settings in table 2 and before showing measurements and related results, some definitions are reported below [5-8]:

- Nominal Frequency (of a transducer): acoustic working frequency of a transducer as quoted by the designer or manufacturer. In our study the ultrasound scanner does not provide a single value for nominal frequency but a range, i.e. 2-5 MHz for the convex array probe, 6-9MHz for the linear array probe.
- Field of View (FoV): area in the ultrasonic scan plane from which ultrasound information is acquired to produce one image frame. Since for each probe the size in pixel of the diagnostic image is quite constant a FoV variation produces a different scale factor (mm

to pixel ratio), influencing other image characteristics, i.e. spatial resolution.

- Focus Depth: nominal depth of the transmission focus in the ultrasound image. Transmission foci are usually marked on one side of the diagnostic image.
- Dynamic range (global): ratio of the maximum to the minimum echo-signal amplitude, even with changes of settings, that a scanner can process without distortion of the output signal.
- Local Dynamic Range: ratio, expressed in decibels, of the minimum echo amplitude that yields the maximum grey level in the digitized image to that of the echo that yields the lowest grey level at the same location in the image and the same settings. Local Dynamic Range influences image contrast and is setting dependent (i.e. through the dynamic range control on the ultrasound scanner).
- Gray Scale Mapping Function (GSMF): relationship between echo amplitudes and gray levels on the image. From GSMF the Local Dynamic Range can be estimated.

Settings have been chosen to display the maximum number of test object at the central frequency of the ultrasound probe (working frequency). Moreover all images are acquired within  $\pm 2^\circ$  tilt angle, at medium overall gain and linear post processing while persistence, edge enhancement and other image processing are set to minimum.

## 2.1 Accuracy in distance measurements

Wires embedded within the ultrasound phantoms are imaged with the sensitivity adjusted to make the displayed echoes as sharp as possible: horizontal and vertical distances are measured “from peak to peak” of wires sections and compared with their nominal values by software [3]. In particular, after the ultrasound image is acquired and processed in a workstation for setting the scale factor in the diagnostic area, the operator is asked to choice test object pairs: it is not necessary centering each target because the software developed automatically calculates its barycentric coordinates within a Region of Interest (ROI) and uses it for measuring the distance among each pair of wires, so errors due to operator’s visual acuity can be neglected. For each pair the measurement distance relative error  $e_{\%} = |d_{rk} - d_k| / d_{rk} \times 100$  between the nominal distance  $d_{rk}$  and the measured value  $d_k$  in the image is calculated for both horizontal and vertical distances.

## 2.2 High Contrast Spatial resolution

High-contrast resolution characteristics can be obtained by measuring dimensions of the point-spread function (PSF), which is the characteristic response of the imaging system to a high-contrast point target: PSF can be produced by imaging high reflection targets that are smaller than one wavelength, as nylon wires section in PSF phantoms of table 1. For ultrasound scanners the PSF is not singular, nor isotropic and has different axial and lateral size in the Field of View (FoV), depending on distance from the transducer emitting surface, so high contrast spatial resolution also changes with position and depth in the image. Thus, many different measurements of the axial and lateral diameter of displayed wires sections at different positions and depths have been performed by software for each settings in table 2 to obtain representative values of the system's axial and lateral resolution. In particular for each wire section  $k$  (point target) in the US image a threshold algorithm at Full Width Half Maximum is applied to evaluate both its maximum width  $PSF_{x_{max}}(k)$  and length  $PSF_{z_{max}}(k)$ :  $PSF_{x_{max}}(k)$  and  $PSF_{z_{max}}(k)$  values are assigned as high contrast axial and lateral resolution respectively

## 2.3 Maximum depth of signal visualization

Maximum Depth of Signal Visualization  $DSV_{max}$  is the maximum depth at which echo signals from scattering within a tissue-mimicking phantom can be detected [6-8]. In particular, as shown in fig. 1, for each image  $DSV_{max}$  is calculated from a depth profile (mean gray level vs depth) of gray levels within a  $ROI_{DP}$  of 30 pixel width, by means of a threshold at 2dB [8] above the mean value displayed in a  $ROI_n$  of  $10 \times 10$  pixels placed at the end of the Field of View (which is associated to the electronic noise level), applied to the US image. The +2dB threshold needs the relationship between gray level in the image and acoustical dB [8], so a Gray Scale Mapping Function is estimated by means of the procedure in [9] for each probe and dynamic range setting in table 2.

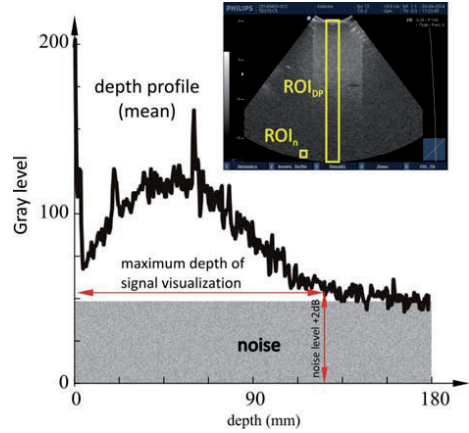


**Fig. 1: Maximum Depth of Signal Visualization:**  $DSV_{max}$  is evaluated from the depth profile of gray levels in  $ROI_{DP}$  at +2dB over the noise level. In  $ROI_n$  the mean gray level estimates the noise level.

## 3. Results and Discussion

For each of the above parameters results are classified for probe and phantom model. Since all measurements are done by means of an image analysis software that minimize errors due to operator's visual acuity and subjective judgment, principal causes of results dispersion can be related to small image variations due to manual probe position on the phantom surface. Therefore in our study influences of ultrasound transducer position on quality assurance measurements are estimated by means of expanded uncertainties, evaluated as measurement repeatability [10] with a coverage factor  $t = 2.13$  at 95 percent confidence level.

### 3.1 Accuracy in distance measurements

Accuracy in distance measurements has been evaluated for all the settings in table 2. In figure 2 results for the convex probe are shown: for both vertical and horizontal measurements no significant differences between tests have been observed, while for horizontal distances (fig. 2b and fig. 2d) discrepancies between phantoms can be noticed. Moreover, to evaluate test influences on measurement repeatability a Fisher test (F-test) has been performed for results at vertical-80mm and horizontal-60mm: while in vertical distance measurements no significant differences can be confirmed among variances, in horizontal ones homoscedasticity should be rejected (for both of phantoms), so we can suppose a variation in

measurement repeatability related to test settings. Measurements uncertainty ranges from: 0.3 to 0.7 percent for vertical distances, 0.2 to 1.3 percent for horizontal distances.

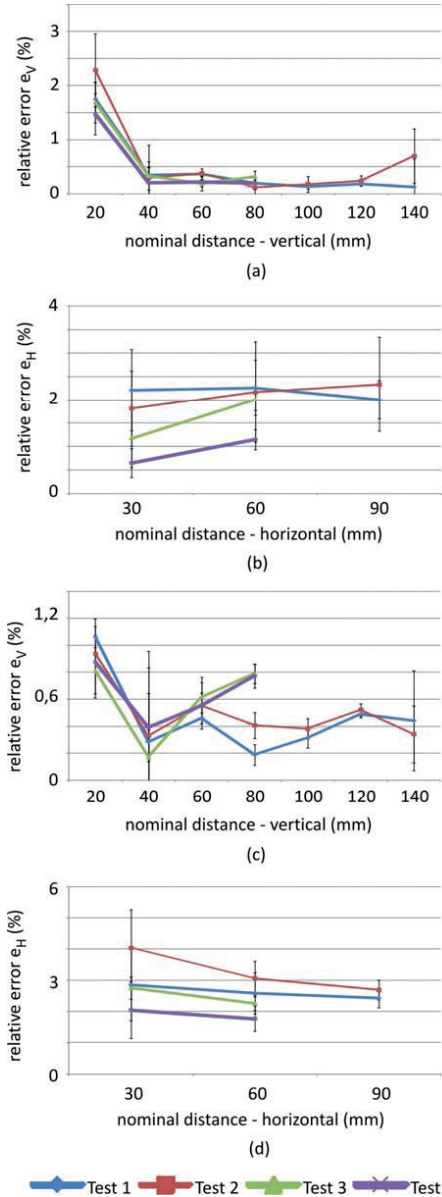


Fig. 2: Distance measurements for convex array probe. Phantom A: (a) vertical distances, (b) horizontal distances. Phantom B: (c) vertical distances, (d) horizontal distances.

In figure 3 results are shown for the linear array probe and no significant differences are observed

for most of the measurements, nevertheless the F-test indicates no equality of variances on vertical (20 mm, phantom A) and horizontal distances (30mm, both of phantoms). Measurements uncertainty ranges from: 0.1 to 5.5 percent for vertical distances, 0.1 to 0.6 percent for horizontal distances.

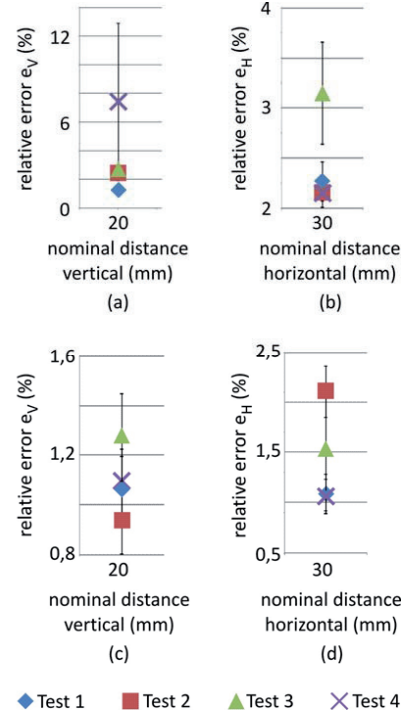


Fig. 3: Distance measurements for linear array probe. Phantom A: (a) vertical distances, (b) horizontal distances. Phantom B: (c) vertical distances, (d) horizontal distances.

For convex array transducer differences between test in horizontal distances (fig.2b and fig.2d) can be due to phantom tissue mimicking material (e.g. phantom A attenuation is 1.4 times greater than in phantom B so pin target imaging could be more smooth and less visible over the background speckle) and mostly to Field of View variation, because it influences mm to pixel ratio (scale factor) and the distortion of imaged nylon wires sections. In fact at lower FoVs, wires at 60mm are selected near image boundaries (at 20-30mm depth), where distortion artifacts are more intense and become more noticeable for higher contrasts, i.e. depending on the Dynamic Range settings. All of the causes above likely influence the measurement repeatability, enhancing slight differences in acquired images and their

processing by the analysis software. Similar considerations can be supposed for the linear array transducer, where the presence of high noise levels adds dispersion to results.

### 3.2 High Contrast Spatial resolution

Axial and lateral resolution at FWHM have been evaluated for all the settings in table 2. In figure 4 no significant variations between tests have been observed for most of axial and lateral measurements of the convex array probe, nevertheless some discrepancies between test can be noticed in phantom A. A Fisher test has been performed for results at 100 mm (both for axial and lateral resolution) and indicates that for results in fig.4c and fig.4d (phantom B) homoscedasticity should be rejected. Measurements uncertainty ranges from: 0.1 mm to 1.0 mm for axial resolution, 2.9 mm to 7.9 mm for lateral resolution.

In figure 5 spatial measurements are shown for the linear array probe and no significant differences are observed for most of the measurements, nevertheless the F-test indicates no equality of variances on both axial and lateral resolution values obtained with the phantom B. Measurements uncertainty ranges from: 0.1 mm to 0.4 mm for axial resolution, 0.1 mm to 1.4 mm for lateral resolution.

Differences between tests can be due to noise level, phantom tissue mimicking material and Field of View variation, because of its influence on mm to pixel ratio, and so both on scale factor and on pixelation error. As in distance evaluations, measurement repeatability likely depends on all of the causes above, because of the consequent enhancement of differences among acquired images.

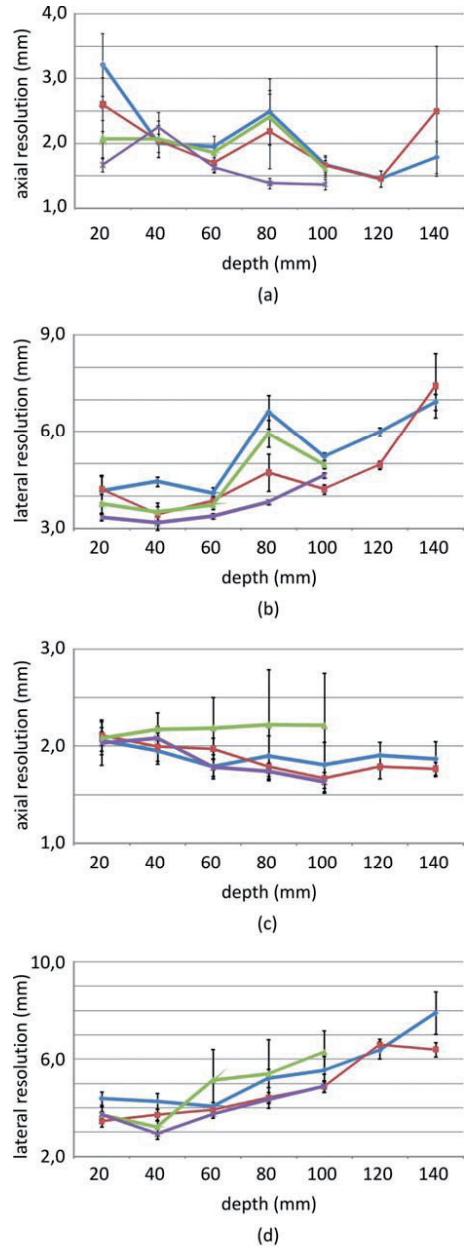


Fig. 4: High contrast spatial resolution measurements for convex array probe. Phantom A: (a) axial resolution (b) lateral resolution. Phantom B: (a) axial resolution (b) lateral resolution



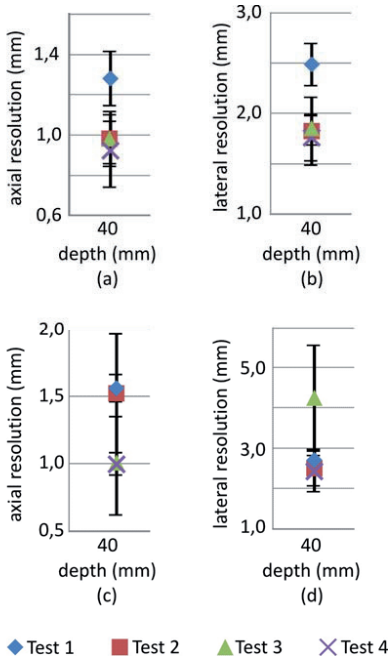


Fig. 5: High contrast spatial resolution measurements for linear array probe. Phantom A: (a) axial resolution (b) lateral resolution. Phantom B: (a) axial resolution (b) lateral resolution

### 3.3 Maximum depth of signal visualization

Maximum depth of signal visualization  $DSV_{max}$  has been evaluated for settings test 1 and test 2 in table 2. In figure 6 a significant discrepancy between phantom is observed for both of tests: higher depth values are related to phantom B. The F-test indicates that homoscedasticity should be rejected only for phantom B results. Measurements uncertainty ranges from 2 mm to 5 mm.

In figure 7 a significant difference in results between tests and phantom can be noticed: higher depth values are consistent to each other and related to settings of test 2 for both of the phantoms. Results from F-test denotes that variance should be considered non-homogeneous between tests for both of phantoms. Measurements uncertainty ranges from 1 mm to 10 mm.

In convex array analysis  $DSV_{max}$  seems to depend mostly on phantom model than test settings, it is likely due to different attenuation coefficient (phantom B attenuates less than phantom A). On the other hand, in linear array examinations

$DSV_{max}$  is more settings dependent while discrepancies between phantom are not significant: we suggest it can be due to excessive noise increasing with contrast (Dynamic Range variation). Variations in measurements repeatability could be due to phantom attenuation, e.g. higher attenuation provides less dependence on image tilting and consequent artifacts.

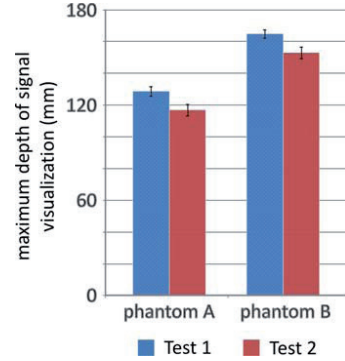


Fig. 6: Maximum depth of signal visualization for convex array probe

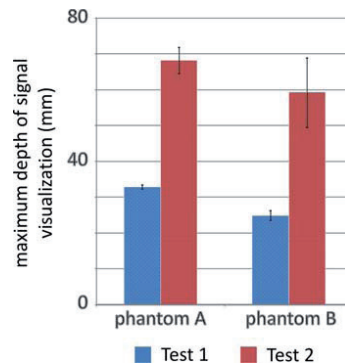


Fig. 7: Maximum depth of signal visualization for linear array probe

## 4. Conclusion

In the present study variations on some features of the B-mode image have been investigated when the ultrasound probe is handled by the technician during a routine quality test: ultrasound images of two different ultrasound phantom are acquired from two ultrasound transducer and processed by software to evaluate measurement dispersion in high contrast spatial resolution, penetration depth and accuracy in distance measurements.

Measurement uncertainties depend strongly on probe model and parameter investigated: they ranges from 0.1 to 5.5 percent in distance measurements error, from 0.1 to 7.9 mm in high contrast resolution and from 2 to 10 mm in maximum depth of signal visualization. Although numerical results are limited to the two examined probes some general consideration can be done: (a) measurements depend on settings as well on phantoms features, probes and parameters investigated (b) Field of View settings seems to be more important for measurement repeatability than Dynamic Range, (c) accuracy in distance measurements seems to be less dependent on settings and transducer position. However use of support stands and clamps is highly recommended during routine quality assurance tests in order to reduce uncertainty in ultrasound system performances estimation.

Other measurements are going to be collected on different ultrasound systems to perform an in-depth analysis of uncertainties in diagnostic ultrasound quality assurance by means of ultrasound phantoms and image analysis software.

## AKNOWLEDGMENT

The authors are grateful to Prof. Francesco Paolo Branca for his suggestions and support while writing this paper. The authors also wish to thank Enrico Ganduglia and Sandro Stefanelli of Philips Healthcare for helping us in hardware supply and assistance.

## REFERENCES

- [1] Dudley N, Russell S, Ward B and Hoskins P, BMUS QA working party, The BMUS guidelines for regular quality assurance testing of ultrasound scanners, *Ultrasound* 2014; 22: 6–7.
- [2] Kollman C, de Korte C, Dudley NJ, et al. Guideline for technical quality assurance (TQA) of ultrasound devices (B-Mode) – Version 1.0 (July 2012). *Ultraschall Med* 2012;33:544–9
- [3] Branca F P , Sciuto S A, Scorza A, Comparative evaluation of ultrasound scanner accuracy in distance measurement , (2012) *Review of Scientific Instruments* 83 (10)
- [4] Thijssen J M, Weijers G, De Korte C L, Objective performance testing and quality assurance of medical ultrasound equipment, *Ultrasound in Med. & Biol.*, Vol. 33, No. 3, pp. 460–471, 2007
- [5] IEC 61391-1:2006, *Ultrasonics - Pulse-echo scanners Part 1: Techniques for calibrating spatial measurement systems and measurement of system point-spread function response*.
- [6] IEC 61391-2:2010, *Ultrasonics - Pulse-echo scanners - Part 2: Measurement of maximum depth of penetration and local dynamic range*.
- [7] Lopez H et al., *Methods for measuring performance of Pulse-Echo Ultrasound Equipment-part II: digital methods (stage 1)*, American Institute of Ultrasound in Medicine, Laurel MD (1995)
- [8] Madsen E et al. , *AIUM Quality Assurance Manual for Gray-Scale Ultrasound Scanners (stage 2)*, American Institute of Ultrasound in Medicine, Laurel MD (1995)
- [9] Scorza A, A novel method for automatic evaluation of the effective dynamic range of medical ultrasound scanners, (2008) *IFMBE Proceedings* 22 PP. 1607 – 1611
- [10] ISO/IEC Guide 99:2007-12, *International vocabulary of metrology - Basic and general concepts and associated terms (VIM)*

# Contactless temperature measurement of thin wires: methods comparison.

Diego Scaccabarozzi\*, Bortolino Saggin\*, Davide Baruffaldi\*

\*Politecnico di Milano  
Polo Territoriale di Lecco  
Via G. Previati 1c  
Lecco

## Abstract

*This work describes the design of two contactless temperature measurement methods based on total radiance and two-colour pyrometry. The methods have been conceived to measure the temperature of a small brass coated steel wire during wire drawing. Usual contact sensors cannot be applied due to the wire movement and excessively large insertion errors in this critical condition. The pyrometers optical layouts have been analysed by means of numerical simulations in order to evidence their sensitivity to the wire oscillations. Performances of different infrared sensors have been compared on the basis of the achieved measurement uncertainty simulating background temperature variation, slope of the wire's emissivity and the effect of the atmosphere absorption.*

## 1. Introduction

Infrared thermometers allow temperature measurement without any contact between the sensor and an observed object. This is a clear advantage in case the object size is so small that even with the smallest contact thermometers (e.g. miniature thermocouples or RTDs) the loading effect due to the sensor cannot be accepted. Anyway, contactless temperature measurement is not an easy task since achievable accuracy relies directly on the knowledge of many quantities such as the object emissivity, the background temperature, the medium spectral transmissivity and on the condition that the emitting source fills completely the sensor Field of View (FOV) [1-5]. Emissivity is roughly known because depends on temperature and might change because of the local state of oxidation, cleanliness or roughness [2] of the observed surface. These criticalities affects the analysed case study, i.e. wire drawing, since the manufacturing process requires soaps and lubricant oils and the wire emissivity varies because of the material inhomogeneity or local oxidation, therefore the usage of common total radiance pyrometers can lead to large measurement errors. Moreover, the wire size (between 0.1 to 1

mm) is generally smaller than the measurement spot of any standard pyrometer or infrared camera [6]. This leads to measurement errors because beside the wire's emission some radiance from the background scene is measured as well, and averaged with the source one. Finally, significant transversal oscillations of the wire are present during the wire drawing and brass coating deposition process. In case of wire oscillations, radiative coupling between the source and the sensor changes with the wire position, causing the fluctuation of the measured temperature or in general, a SNR (Signal to Noise Ratio) worsening.

Thus, two contactless temperature measurement methods have been developed to overcome the drawbacks of the standard pyrometers and minimize the achievable uncertainty in measuring the temperature of small wires with large oscillations and emissivity changes. The expected improvements with respect to off the shelf instruments derive from purposely designed instruments optical layouts and the optimal choice of the detectors.

The paper is organized as follows: Section 2 summarizes the modelling of the two pyrometers whereas Section 3 describes the conceived optical layouts. Section 4 deals with the uncertainty and sensitivity analyses performed for the proposed instruments whereas Section 5 summarizes the numerical results. The obtained results are discussed in Section 6 and the manuscript is eventually concluded in Section 7.

## 2. Backgrounds and methods

According to the Planck law, the heat flux for unit wavelength at a given temperature is defined as:

$$E_{n\lambda} = \frac{C_1}{\lambda^5 * (e^{\frac{C_2}{\lambda T}} - 1)} \quad \text{Eq. 1}$$

where  $\lambda$  is the wavelength whereas  $C_1$  and  $C_2$  are known constants. In order to account for the emissivity of the source and the efficiency of the radiative exchange between two surfaces  $i$  and  $j$ , the radiative conductor ( $GR$ ) is defined as follows:

$$GR_{ij} = \varepsilon_i A_i GB_{ij} \quad \text{Eq. 2}$$

where  $A_i$  is the emitting surface area,  $\varepsilon_i$  is the surface emissivity and  $GB_{ij}$  is the Gebhart factor that expresses the fraction of power radiated from surface  $i$  and absorbed by surface  $j$ . The latter factor accounts for the multiple reflections of the wire radiance reaching the detector.

Finally, the detector output  $O$  for a source at a given temperature  $T$  is:

$$O(T) = \int_{\lambda_{min}}^{\lambda_{max}} R(\lambda) GR E_{n\lambda}(T) d\lambda \quad Eq. 3$$

where  $\lambda_{max}$  and  $\lambda_{min}$  are the extremes of the detector wavelengths range,  $R(\lambda)$  the detector sensitivity,  $E_{n\lambda}(T)$  the source spectral radiance.

Conversely, the two-colour pyrometer measurement method is based on the ratio between the heat fluxes at two different wavelengths; considering the two sensors outputs one can write:

$$\frac{O_1}{O_2} = \frac{GR_1 R_1(\lambda_1) \varepsilon(\lambda_1) \lambda_2^5 \left( e^{\frac{C_2}{\lambda_2 T}} - 1 \right)}{GR_2 R_2(\lambda_2) \varepsilon(\lambda_2) \lambda_1^5 \left( e^{\frac{C_2}{\lambda_1 T}} - 1 \right)} \quad Eq. 4.$$

The measured temperature can be derived from Equation 4 under the assumption that the source emissivity is a smooth function, and so, similar at the two adjacent wavelengths:

$$T = \frac{\left( \frac{1}{\lambda_2} - \frac{1}{\lambda_1} \right) C_2}{\ln \left( \frac{E_{n\lambda 1} \lambda_1^5}{E_{n\lambda 2} \lambda_2^5} \right)} \quad Eq. 5$$

Moreover, Equation 5 is valid under the hypothesis that the exponential term in Equation 4 is at least one order magnitude larger than one. The latter assumption is fully satisfied within the investigated wavelength range, i.e. between 0.5 and 5  $\mu\text{m}$ , and at the analysed temperatures (from 200°C to 800°C).

### 3. Optical layouts design

The radiative models of the pyrometers have been developed with ESATAN-TMS software. The model includes the infrared sensor active area, the mirrors, the wire and an enveloping box. Figure 1 shows the conceptual optical layouts. The first configuration for the total radiance pyrometer exploits one planar diffusive mirror to reflect the radiance emitted by the wire. The mirror is replaced in the two-colour pyrometer by parabolic reflectors. The internal surfaces of the optical cavity (mirrors and envelope box) aim to reflect the wire radiance that does not directly reach the sensor and therefore, materials with high infrared reflectivity have been used.

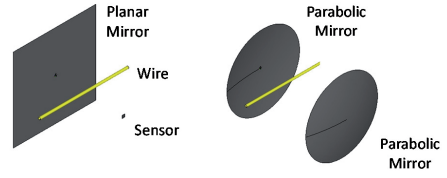


**Fig. 1: Pyrometers optical layouts; (left) total radiance configuration, (right) optical configuration for the two-colour pyrometer.**

The optical configurations have to be compared on the basis of the radiative efficiency and sensitivity to the wire oscillations.

Thus,  $GR$ s between wire and detector have been computed in nine different positions, as evidenced in Figure 2.

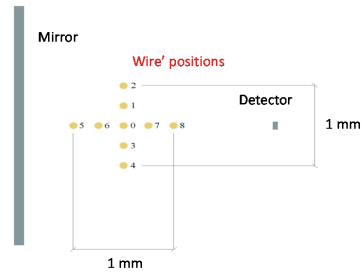


**Fig. 2: Source position with respect to the detector.**

The maximum distance from the reference position (position "0" in Figure 2) is 0.5 mm, value obtained from the measurement of the wire oscillation amplitudes in preliminary tests. The optical properties (emissivity, transmissivity and specular or diffusive reflectivities) of the materials are reported in Table 1. In particular, the coating for the total radiance pyrometer is sand blasted aluminium whereas gold is used in the two-colour configuration. The meshes of the optical elements in each configuration have been defined by preliminary analyses aiming to identify the maximum size for each component granting stability in the ray tracing analysis.

Material	$\varepsilon$	$\tau$	$\rho_{\text{specular}}$	$\rho_{\text{diffusive}}$
Brass	0.4	0	0	0.6
Sand blasted aluminium	0.15	0	0	0.85
Gold IR	0.03	0	0.9	0.07

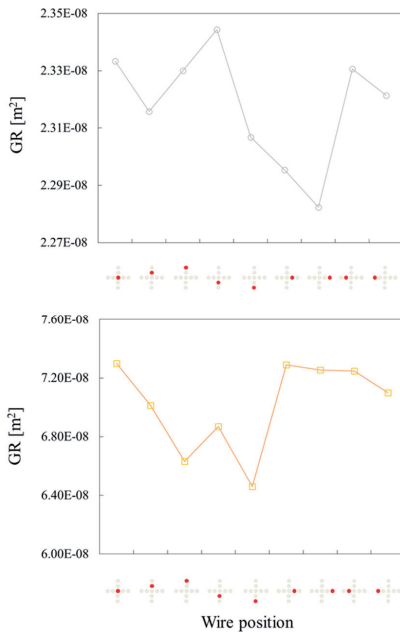
**Table 1 Materials optical properties**

Table 2 summarizes geometry and mesh for the analysed optical layouts.

Component	Mesh size	Model Size
Wire	30x30	32 mm, diameter 0.8 mm
Envelope Box	22x22x22	30x30x26 mm <sup>3</sup>
Planar Mirror	15x15	30x30 mm <sup>2</sup>
Parabolic Mirror 1	40x40	Diameter 30 mm, Focal length 36 mm;
Parabolic Mirror 2	40x40	Diameter 30 mm, Focal length 26 mm;
Detectors	1x1	1x1 mm <sup>2</sup>
Active area		

**Table 2 Models geometry and mesh size.**

The radiative analyses have been performed in each position of Figure 2 with the optical properties of Table 1. Figures 3 shows the computed *GRs*. Numerical simulations evidenced that for the total radiance pyrometer the planar mirror configuration with sand blasted aluminium coating allows reducing the sensitivity to the wire oscillations. In fact, the average *GR* computed among the different wire positions is about  $2.3 \cdot 10^{-8} \text{ m}^2$ , with a standard deviation 0.85% of the average value.



**Fig. 3: Computed *GRs* between wire and detector in the total radiance pyrometer (top) and in the two-colour configuration (bottom).**

Conversely, in the two-colour pyrometer, the configuration with two parabolic mirrors and gold coating achieves the highest *GR*, providing a maximum of about  $7.54 \cdot 10^{-8} \text{ m}^2$  but at the price of

a larger variability (about 4% with respect to the average value).

#### 4. Temperature uncertainty evaluation

In order to evaluate the expected uncertainty for the measured temperature, the first contribution comes from the detector noise [7], i.e. the photon noise. Typically, datasheets of commercial detectors provide the responses and the sensitivities of the detectors in terms of spectral detectivity  $D^*(\sigma)$ :

$$D(\sigma)^* = \frac{\sqrt{A_d \Delta f}}{NEP(\sigma)} \quad \text{Eq. (6)}$$

where  $A_d$  is the detector area,  $\Delta f$  is the sensor frequency bandwidth and  $NEP$  is the detector noise equivalent power. Both the  $D^*(\sigma)$  and the  $NEP$  depend on the wavenumber  $\sigma$ . In our case, once  $\Delta f$  has been set (i.e. 1 Hz), the  $NEP$  can be found reversing Equation 6. The ratio between the measured power and the  $NEP$  gives the achievable SNR.

Beside the uncertainty introduced by the photon noise, the radiance of the background leads to an overestimation of the source radiance. This effect has been evaluated in both pyrometers. Moreover, the variability of the total or spectral wire emissivity is expected to be of paramount importance to define the final measurement accuracy. Thus, some sensitivity analyses have been performed to identify the variability of the measured temperature due to a global emissivity change in the total radiance pyrometer, and a spectral emissivity slope for the two-colour configuration.

Three photoconductive infrared detectors have been analysed, i.e. Silicon (Si), Lead Sulfide (PbS) and Lead Selenide (PbSe), covering different wavelength ranges, responsivities and detectivities. The detectors characteristics are summarized in Table 3.

Type		Si	PbS	PbSe
Case		T0-18	T0-18	T0-18
$A_d$	mm <sup>2</sup>	1	1	1
Range	μm	0.4÷1.2	1÷2.8	1÷4.5
$D^*$	cm Hz <sup>0.5</sup> W <sup>-1</sup>	$4.4 \cdot 10^{12}$	$1 \cdot 10^{11}$	$5 \cdot 10^{10}$
NEP	W	$2.3 \cdot 10^{-14}$	$1 \cdot 10^{-12}$	$2 \cdot 10^{-12}$

**Table 3 Characteristics of the analysed detectors.**

The uncertainty and sensitivity analyses have been performed for the total radiance pyrometer with the following parameters:

- The nominal wire temperature has been set to 200, 400, 600 and 800 °C;
- Atmosphere spectral absorption at the different temperatures of the wire has been modelled [8];
- Worst case background emission has been simulated, with unitary emissivity and temperature ( $T_{BK}$ ) set at 30, 35 and 40 °C;
- A normal distribution of the total emissivity of the wire has been considered to account for the emissivity variation because of oils, soaps or oxidation in the manufacturing process. The mean emissivity has been set to 0.4 and the standard deviation to 10% of the average value.

The analyses in the two-colour pyrometer have been performed with the following additional parameters:

- The transmittance curves of commercially available infrared filters have been added to compute the measured power;
- A variable wire emissivity difference between the two reference wavelengths, up to 5%, has been simulated to take into account a possible variation of the source spectral emission; the simulated value is in agreement with literature data for brass, i.e. 20% change over 2.7  $\mu\text{m}$ , as shown in reference [9].

## 5. Analysis results

Hereafter the results of the performed simulations are described for both the analysed pyrometers.

### 5.1. Total radiance pyrometer

The SNRs for the selected sensors at the different temperatures are reported in Table 4 whereas Table 5 provides the expected temperature variability because of the wire oscillations.

T [K]	Si	PbS	PbSe
473	3.8	$2.6 \cdot 10^5$	$3.1 \cdot 10^6$
673	$2.1 \cdot 10^4$	$1.1 \cdot 10^7$	$3 \cdot 10^7$
873	$2.7 \cdot 10^6$	$9.1 \cdot 10^7$	$1.3 \cdot 10^8$
1073	$6.1 \cdot 10^7$	$3.8 \cdot 10^8$	$3.4 \cdot 10^8$

**Table 4 SNRs at different temperatures of the analysed detectors.**

The temperature error introduced by the background radiance is summarized in Figure 5 whereas, the temperature uncertainty related to the wire emissivity variability is highlighted in Table 6. In the latter case, the temperature uncertainty has

been derived using the numerical propagation as evidenced in reference [10].

T	$\sigma_{Si}$	$\sigma_{PbS}$	$\sigma_{PbSe}$
473	n.d.	0.047	0.12
673	0.067	0.13	0.13
873	0.087	0.16	0.16
1073	0.11	0.33	0.22

**Table 5 Variability of the measured temperature due to wire oscillation. Temperatures are in kelvin.**

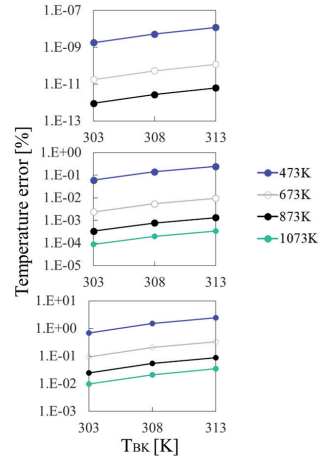


**Fig. 5 Expected temperature error due to background emission with the Si (top), PbS (middle) and PbSe (bottom) detectors.**

T [K]	Si	PbS	PbSe
473		0.69	1.06
673	0.49	1.14	1.69
873	0.61	1.38	1.96
1073	0.72	1.47	2.10

**Table 6 Relative uncertainty of the measured temperature because of the wire' emissivity distribution. The uncertainty is expressed as percentage.**



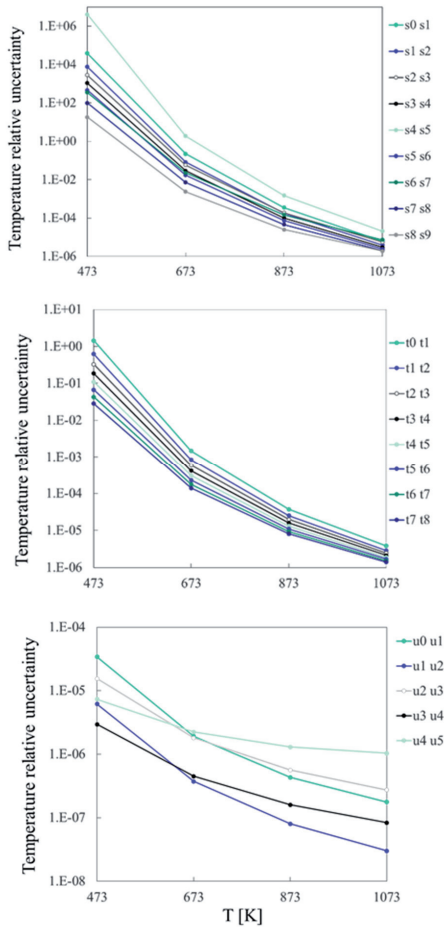


Fig. 6 Infrared filters comparison for Si (top), PbS (middle) and PbSe (bottom) detectors.

Filter pair	CWLs [nm]	T [K]			
		473	673	873	1073
s0-s1	730-766	0.36	0.49	0.62	0.74
s1-s2	766-800	0.42	0.59	0.75	0.91
s2-s3	800-830	0.59	0.88	1.19	1.53
s3-s4	830-852	0.74	1.03	1.30	1.56
s4-s5	852-855	70.60	24.38	14.43	11.53
s5-s6	855-880	0.70	0.98	1.25	1.51
s6-s7	880-905	0.95	1.50	2.17	3.02
s7-s8	905-940	0.62	0.90	1.19	1.49
<b>s8-s9</b>	<b>940-1064</b>	<b>0.26</b>	<b>0.42</b>	<b>0.63</b>	<b>0.93</b>

Table 6 Relative temperature error due to wire oscillation for different filter pairs, Si detector. Error is expressed as percentage.

Filter pair	CWLs [μm]	T [K]			
		473	673	873	1073
t0-t1	1.25-1.3	0.75	1.04	1.32	1.58
t1-t2	1.3-1.35	0.81	1.12	1.42	1.70
t2-t3	1.35-1.4	0.86	1.20	1.51	1.81
t3-t4	1.4-1.45	0.92	1.28	1.61	1.93
t4-t5	1.45-1.5	0.99	1.36	1.72	2.05
t5-t6	1.5-1.55	1.05	1.45	1.82	2.18
t6-t7	1.55-1.6	1.12	1.54	1.93	2.30
<b>t7-t8</b>	<b>1.6-1.65</b>	<b>1.18</b>	<b>1.63</b>	<b>2.04</b>	<b>2.43</b>

Table 7 Relative temperature error due to wire oscillation for different filter pairs, PbS detector. Error is expressed as percentage.

Filters pair	CWLs [μm]	T [K]			
		473	673	873	1073
u0-u1	2.7-2.95	0.77	1.11	1.44	1.77
<b>u1-u2</b>	<b>2.95-3.46</b>	<b>0.38</b>	<b>0.48</b>	<b>0.56</b>	<b>0.63</b>
u2-u3	3.46-3.6	1.98	2.95	3.79	4.56
u3-u4	3.6-4.26	0.57	0.76	0.95	1.13
u4-u5	4.26-4.67	1.37	2.44	3.69	5.24

Table 8 Relative temperature error due to wire oscillation for different filter pairs, PbSe detector. Error is expressed as percentage.

### 5.1. Two-colour pyrometer

Figure 6 compares the computed relative uncertainty in temperature measurement for some commercially available IR filters. The uncertainty has been computed propagating the uncertainty contributions of Equation 5. The uncertainty about the heat flux measured by each detector has been evaluated as the ratio between the detector' NEP and the measured radiance. The central wavelengths (CWLs) of the analysed filters range between 730 and 1064 nm for the Si detector, from 1250 to 1650 nm for the PbS and within 2700÷4670 nm for the PbSe.

The same filters have been used to highlight the pyrometer sensitivity against the wire oscillations. Results about the expected temperature variability are summarized in Table 7, Table 8 and Table 9.

The relative error caused by variations of the wire spectral emissivity within the IR band filters is evidenced in Figure 7. The error has been computed only considering the infrared filters selected for each detector (see the filters pairs in green bold in Tables 6, 7 and 8). Finally, the error due to background radiation is summarized in Figure 8.

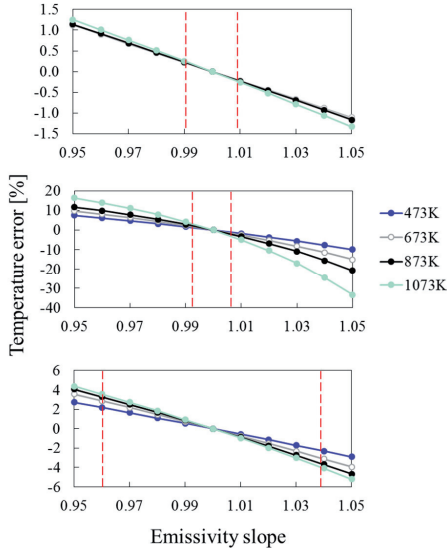


**Fig. 7 Temperature error due to spectral emissivity slope between the selected filters pairs for the Si (top), PbS (middle) and PbSe (bottom) detectors. Red dashed lines evidence the expected emissivity differences for the selected filters pairs for each detector.**

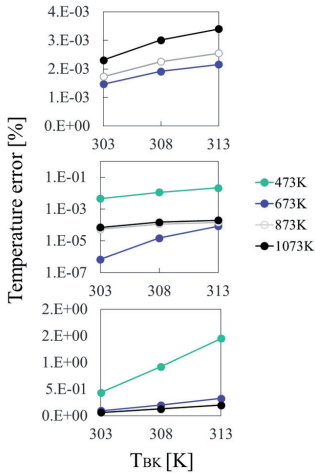


**Fig. 8 Temperature relative error due to the background emission for the Si (top), PbS (middle) and PbSe (bottom) detectors.**

## 6. Discussion

The computed SNRs for the analysed detectors in the total radiance pyrometer evidence that the best results are achieved with the PbSe but in general, high SNRs can be obtained as well for the other detectors. The Si provides a high SNR but only for

temperatures larger than 473 K (see Table 4). The result is somehow expected since increasing the temperature, the Plank curves shift towards the lower wavelengths, i.e. below the detector cut-off wavelength.

The wire oscillation in the total radiance configuration leads to small temperature errors for all detectors, as shown in Table 5. The maximum error is less than 0.5 K at the highest nominal wire temperature, i.e. 1073 K. This result is expected as well, since the optical layout was conceived to be inherently insensitive to wire oscillations, as can be verified by looking to the *GR* plots in Figure 3.

The effect of the background emission on the measured temperatures is shown in Figure 5: the largest temperature error is obtained at the lowest wire temperatures for all the detectors. Moreover, the computed temperature error is negligible for the Si and PbS detectors, which show maximum relative errors of about  $1.2 \cdot 10^{-8}$  and 0.25%. The error rises up to about 2.4% in case of the PbSe detector. This result is reasonable since the PbSe has a spectral range shifted to the high wavelengths (as shown in Fig. 4), therefore it is more sensitive to the background disturbance that deriving from low temperatures (in comparison to the wire) has most of its radiance in the in the mid infrared.

The simulation about the statistical variation of the wire emissivity highlighted a significant dependence of the expected temperature uncertainty on the total emissivity changes (as shown in Table 6); in fact, the temperature uncertainty varies between 7.7 K, maximum value for the Si detector, and 22.5 K, obtained with the PbSe. Moreover, for all the considered detectors, the uncertainty increases with the increase of the wire temperatures.

The analysis of some commercially available IR filters for the two-colour pyrometer led to the selection of the filter pairs s8-s9 for the Si detector, t7-t8 for the PbS and u1-u2 for the PbSe. These allow achieving the best SNRs (as shown in Figure 6) and minimizing the sensitivity to the wire oscillations (as evidenced in Table 6, Table 7 and Table 8). Starting from the selected filters, the sensitivities about the spectral emissivity variation and background emission have been investigated. The positive and negative slopes of the wire spectral emissivity leads to a temperature error that increases with the wire temperature increase. The maximum computed relative error has been found to be less than 0.26%, 5% and 4.2% for the Si, PbS and PbSe, respectively. These are highlighted by the red dashed lines shown in Figure 7.

The background emission is negligible for the Si and PbS but provides a maximum relative error of about 1.5%, at 200°C, for the PbSe. This error,

however, could be reduced if the temperature of the envelope box was stabilized, e.g. by using a thermoelectric cooler.

## 7. Conclusions

Two methods for the contactless temperature measurement of a thin wire during brass coating and drawing have been developed and optimized to overcome the shortcomings inherent to this measurement case i.e. the small wire size, emissivity changes, its velocity along the wire axis and transversal oscillations. The two methods, based on a total radiance and two-colour pyrometers, exploit commercially available infrared detectors and optical components. The instruments sensitivity to the wire oscillations, background emission and emissivity variation has been analysed through numerical modelling.

In the total radiance pyrometer, the PbSe detector evidences the best performances within the investigated temperature range, i.e. from 200 °C to 800 °C, providing the largest SNR and a temperature uncertainty between 1.8% and 2.5% considering the effect of emissivity variance.

In the two-colour pyrometer, the best results are obtained with the PbSe detector as well. The latter provides the highest SNR and the lowest measurement uncertainty, about 0.63%, using infrared filters with band centres positioned between about 3 and 3.5 µm. In both cases, the optics enclosure has been assumed to be thermally stabilized to avoid the large errors that have been evidenced for the background emission.

## References

- [1] Quinghai Ren, "Design of a dual channel thermometer for true temperature measurement", *International Journal of Infrared and Millimeters Waves*, 1996, pp. 1969-1975, Vol. 17, No. 11, doi: 10.1007/BF02069470.
- [2] Michael F. Modest, "Radiative Heat Transfer Third Edition", *Academic Press*, 2013, ISBN 978-0-12-386944-9.
- [3] Tairan Fu, Xiaofang Cheng, Xuiliang Fan and Jinlei Ding, "The analysis of optimization criteria for multi-band pyrometry", *Metrologia*, 2004, pp. 305-313, Vol. 41, doi:10.1088/0026-1394/41/4/012.
- [4] Krzysztof Chrzanowski and Marek Szulim, "Measure of the influence of detector noise on temperature-measurement accuracy for multiband infrared systems", *Applied Optics*, 1998, pp. 5051-5057, Vol. 37, No. 22, doi: 10.1364/AO.37.005051.
- [5] Krzysztof Chrzanowski and Marek Szulim, "Errors of temperature measurement with multiband infrared systems", *Applied Optics*, 1999, pp. 1998-2006, Vol. 39, No. 10, doi: 10.1364/AO.38.001998.
- [6] Diego Scaccabarozzi and Bortolino Saggin, "About the dynamic characterization of microbolometric infrared cameras", *Sensors and Actuators A : Physical*, July 2014, doi: 10.1016/j.sna.2014.06.018.
- [7] Davis, Sumner P., Mark C. Abrams, and James W. Brault, "Fourier transform spectrometry", *Academic Press*, 2001, ISBN: 978-0-12-042510-5.
- [8] Rothman, Laurence S., et al. "The HITRAN molecular database: Editions of 1991 and 1992." *Journal of Quantitative Spectroscopy and Radiative Transfer* 48.5 (1992): 469-507.
- [9] Sønnik Clausen, Axel Morgenstjerne and Ole Rathmann, "Measurement of surface temperature and emissivity by a multitemperature method for Fourier-transform infrared spectrometers", *Applied Optics*, 1999, pp. 5683-5691, 1996, Vol. 35, No. 28, doi: 10.1364/AO.35.005683.
- [10] JCGM 100:2008 Evaluation of measurement data - Guide to the expression of uncertainty in measurement (GUM).

# Measurement of the heat removed by devices for skin tags treatment

Marco Tarabini\*, Bortolino Saggin\*

\* Politecnico di Milano, Dipartimento di Meccanica, Via Prevati 1/C, 23900 Lecco

## Abstract

*This paper describes a method for the comparison of the cooling capability of over-the-counter devices for skin tags removal. The method is based on the principle of the heat flux-meter: the accuracy of temperature and heat flux measurements has been experimentally evaluated (lower than 6% for heat flux measurements and lower than 0.3 °C for temperature measurements). The instrument allowed comparing the thermal efficiency of nineteen Dimethyl ether and propane dispensers using different nozzles.*

## 1. Introduction

Dermatological cryotherapy is used to treat different skin problems, such as tags, verrucas, molluscum contagiosum, seborrheic and actinic keratosis. Cryotherapy, typically performed with liquid nitrogen, consists of freezing a small skin volume for a short time period. Up to ten years ago, it was not clear how the low temperature solved the skin problem [1]. The mechanisms of verrucas removal are nowadays clear and have been clearly explained by Nguyen and Burkhart [2]; when the tissue temperatures falls below -5°C to -15°C, extracellular ice crystals begin to form. The crystals mechanically disrupts cellular membranes and disturb fluid homeostasis, resulting in cellular dehydration and cell death. Vascular changes associated with circulatory failure become evident between the formation of extracellular and intracellular ice crystals, as tissue temperatures fall below -15°C. Microthrombi form within damaged vessels leading to ischemic necrosis.

The most effective cooling method is the topical application on lesions that one wishes to destroy of a cotton wool swab saturated by immersion in liquid nitrogen or other gases with low boiling temperatures. Nowadays, several over-the-counter (OTC) warts-freezing therapies are available. These devices use Dimethyl Ether and Propane instead of the liquid nitrogen and their efficiency is currently assessed by comparing their effects on patients, as in [3]. A very simple comparison

between over-the-counter wart preparations and liquid nitrogen is presented in reference [4]. The comparison was based on the evaluation of temperature measured by a thermometer in contact with the coolant. Given that the dynamic response of the thermometer was not compensated, results only evidenced the different temperatures obtained with liquid nitrogen and Dimethyl Ether therapies. Neither the comparison of effects on patients nor the measurement of temperature of the boiling fluid provide for quantitative parameter describing the heat that the cooling fluid removes from the skin. In addition, both methods prevent from performing a large number of tests in repeatability conditions.

In this paper, we describe a method for the measurement of the heat removed by different OTC devices for the skin tags removal, which are very similar to the ones used for verrucas treatment (same fluid, different spray nozzle). The measurement method, based on a heat flux meter, allows evaluating the heat flux produced by the OTC devices. As later explained, the heat flux can be used to estimate the skin temperature using the skin thermal resistance models available in the literature [5, 6].

## 2. Proposed Method

The thermal scheme of the interaction between the evaporating gas and the skin is shown in Fig. 1 a: the heat flux imposed by the medical device ( $J_{gas}$ ) is partially absorbed by the body ( $J_{skin}$ ) and partially from the environment ( $J_{leak}$ ).  $J_{leak}$  is generally small and depends on the OTC device characteristics. The skin temperature – one of the crucial parameters for treatment effectiveness – depends on the gas boiling temperature, on the skin thermal capacity and resistance and on the leak resistance. The comparison between different OTC devices can be performed by creating a skin simulator, i.e. a device that has a thermal resistance and a thermal capacity similar to that of the human skin. In this case, the comparison could be based on the cooled skin temperature or on any other parameter. An alternative approach (the one adopted in this paper) consists in the identification of the heat flux actually produced

by the boiling gas and the estimation of the skin temperature using one of the models existing in literature.

With the proposed measurement method, shown in Fig. 1 b, the human body is substituted by the heat flux meter, which derives the heat flux by dividing the temperature difference measured across a thermal resistance ( $\Delta T_{FM}$ ) by the resistance itself ( $R_{FM}$ ).

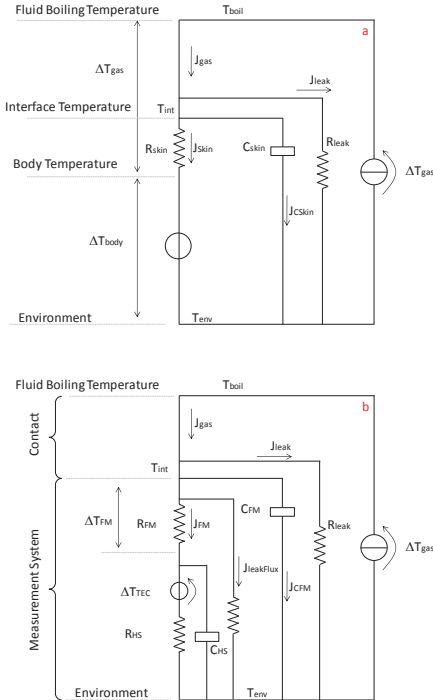


**Fig. 1 Thermal schemes of the interaction between the human body and the medical device for cryotherapy (a) and between the device and the measurement system (b)**

Also in this case, part of the flux generated by the evaporating gas is absorbed by the environment ( $J_{leak}$ ), but there are three main differences from Fig. 1 a:

- part of the heat flux entering the instrument leaks towards the environment without being measured;
- the heat flux, before being measured, crosses a capacitor ( $C_{FM}$ ) that modifies determines transient response of the measurement device; and
- a thermo electric cooler (TEC) has to be used in order to stabilize the temperature of the flux meter.

The heat flux useful for skin treatment purposes is  $J_{gas} - J_{leak}$ . In the scheme of Fig. 1 b this quantity equals  $J_{FM} + J_{leakflux} + J_{CFM}$ .  $J_{leakflux}$  has been numerically evaluated using the measurement model presented in ref. [5] and is shown in Fig. 2.

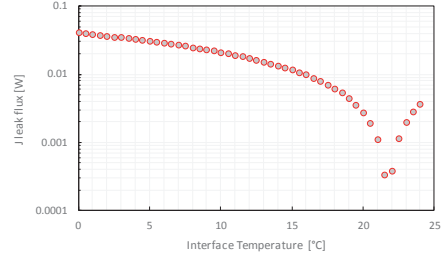


**Fig. 2 Heat flux dissipated by radiation and convection not measured by the flux-meter**

The lowest interface temperature reached in our tests was 5°C. Since the measured  $J_{FM}$  was 6 W, the flux not measured by the flowmeter was approximately 500 times lower than the measured one ( $J_{leakflux}$  equal to 0.03 W).

## 2.1. Measurement Uncertainty

According to the model in Fig. 1 b the difference between  $J_{gas}$  and  $J_{leak}$  equals the sum of  $J_{FM}$  and  $J_{leakflux}$  ( $C_{FM}$  only affects the dynamic response but the net flux on it is zero).  $J_{FM}$  has been computed as the ratio between  $\Delta T_{FM}$  and  $R_{FM}$ . The latter was measured using a differential thermocouple, calibrated versus Class 1 PT100 in a thermal bath.

$$J_{gas} - J_{leak} = \Delta T_{FM} / R_{FM} + J_{leakflux}(T_{int}) \quad (1)$$

The measurement uncertainty has been estimated by propagating the experimentally identified uncertainties in equation 1 using Monte Carlo simulations. Given that  $J_{leakflux}$  is negligible, the assumption of an adiabatic model does not increase the measurement uncertainty.

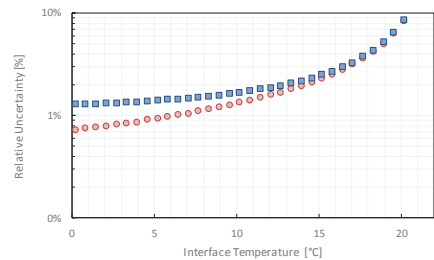


**Fig. 3 Relative measurement uncertainty of the adiabatic model (squares) and of the full**

**model (circles). Both curves are plotted with confidence interval 95%.**

Results evidenced that the measurement uncertainty is always lower than 10%. During our tests, the expected interface temperature is between 10 and 18 °C; consequently, the typical uncertainty values range between 2 and 6 % (confidence interval 95%).

Thermocouples were individually calibrated using a thermal bath; their standard measurement uncertainty was lower than 0.2 °C in the whole measurement range, as evidenced in ref. [5].

## 2.2. Dynamic response

As evidenced in the scheme of Fig. 1 b, the heat flux meter has two thermal capacitances,  $C_{FM}$  and  $C_{HS}$ . The two capacitances reflect in two different time constants  $\tau$ , whose values also depend on the resistances  $R_{FM}$  and  $R_{HS}$ . The calculated flux-meter capacity is 0.19 J/K. The expected flux-meter time constant is 1.25 s and is dominant during the cooling phase; given that the typical application time is in the order of 30 s, the value is satisfying. The second time constant is dominant during the heating phase and, as later explained, is different for devices with different heat flux time histories.

Although it is theoretically possible to compensate the flux-meter time constants (with the approach described in references [7, 8]), all the tests of interest were performed in quasi-static conditions, given that the cooling was much larger than the estimated time constant.

## 2.3. Tests description

Nineteen over-the-counter devices have been compared using  $J_{FM}$  and  $\Delta T_{FM}$  as figures of merit for the capacity of removing the heat from the skin. Three types of device were tested. With the “foam” type, the liquid dimethyl ether and propane mixture is released into a foam pad attached to the device. This foam pad is then held on the wart for approximately 20 s. With the “spray” devices, dimethyl ether and propane are pressurized in a can and are sprayed on the skin continuously. With the “dispenser” types, a fixed quantity of dimethyl ether and propane aerosol is sprayed on the skin at each push.



**Fig. 4 Some of the devices that underwent our tests. Dispenser type (first, third and fourth from the left), foam type (foam not shown, fifth from the left) and spray (second and last).**

Aim of the tests was the comparison of different nozzles for the dispenser devices. The nozzles differed mainly for the airflow passage section and location, which affect the evaporation time of the dimethyl ether and propane. Placing the evaporation holes close to the skin surface increases the cooling speed but may increase the fluid loss. Conversely, when the evaporation holes are far from the fluid, the cooling process is slower but the fluid leak is expected to be negligible. The different nozzles used in our tests are shown in Fig. 5.



**Fig. 5 Different nozzle specimens.**

For each measurement on a medical device, three repetitions were performed. Before each test, the interface temperature was restored to 22 °C using a thermo electric cooler (TEC, Fig. 1 b) with the cold side in contact with the heat sink. This prevented the progressive cooling of the instrument. The temperature data were acquired by an Agilent 34970A multiplexer with a scan rate of 1 sample/s for each channel. Data were acquired via serial interface by a fit-to-purpose LabVIEW virtual instrument. The heat flux and the interface temperature were stored on a PC and offline analysed.

## 3. Results

The  $T_{INT}$  and  $J_{FM}$  time histories of the medical device number 11 are shown in Fig. 6 and Fig. 7. The plots show that the cooling time is approximately 10 s, i.e. much larger than the flux-



meter time constant (1.25 s). The heating time, governed by the second time constant, is approximately 40 s. Since the three test are performed by actuating the device three times, the test repeatability is limited, as evidenced by the measurement standard deviation summarized in Table 1.

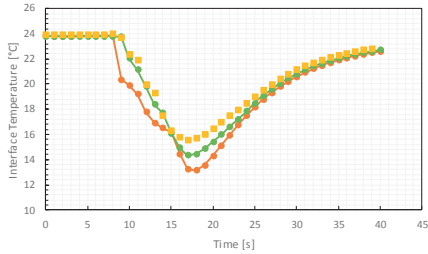


**Fig. 6 Time history of the interface temperature reached during the test of the device 11\_D1 (three repetitions).**

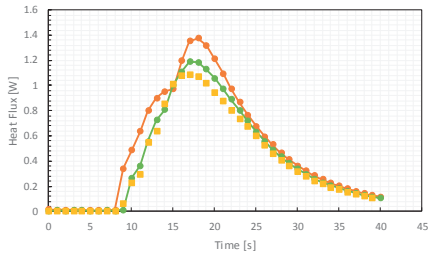


**Fig. 7 Time histories of the cooling power generated by the device 11\_D1 (three repetitions)**

The results of all the tests are summarized in Table 1. Results allow comparing the different solutions in terms of cooling capabilities as maximum flux and flux integral.

**Table 1 Summary of the tests results**

IdTest	Type	Delta T	SD	Jflux Integral	SD
0_O1	Foam	5.7	0.1	29.3	0.2
1_N1	Dispenser	6.2	0.2	19.8	0.5
2_M1	Spray	16.8	3.4	28.3	5.5
3_L1	Foam	5.8	0.5	19.5	2
4_H1	Spray	17.4	0.7	25.5	0.8
5_G1	Dispenser	6.1	0.8	12.4	1
6_F2	Dispenser	3.6	0.6	6.6	1.2
7_F1	Dispenser	6.5	0.8	12.4	0.9
8_E2	Dispenser	7.4	1.7	14.7	3.5
9_E1	Dispenser	5.9	1.8	13	0.7
10_D2	Dispenser	8.1	0.5	17.2	2.1
11_D1	Dispenser	9.5	1.2	18	2.2
12_C2	Dispenser	4.3	0.2	7.3	0.2
13_C1	Dispenser	4.4	0.3	7.6	0.3
14_B2	Dispenser	7.2	1.2	13.4	2.4
15_B1	Dispenser	6.5	0.7	12.6	3.2
16_A2	Dispenser	4.9	0.6	8.3	1.6
17_A1	Dispenser	7.1	1.4	12.5	1.7
18_P1	Dispenser	8	0.9	13.6	1.4
19_E3	Dispenser	4.4	0.4	6.1	0.5

Results show that the spray devices ensure the lowest interface temperatures (approximately 17 °C). The foam devices, thanks to the long evaporation time, have a very large flux integral in spite of the low  $\Delta T_{FM}$ . The “dispenser” devices are characterized by a  $\Delta T_{FM}$  between 3 and 10 °C. Given that devices with IDs from 5 to 19 have the same dispenser, the role of the nozzle is crucial. Best results were obtained with the dispenser 10 and 11, with 0.5 mm holes placed at 5 mm from the skin surface.

#### 4. Discussion and conclusions

In this paper, we have proposed a method for the comparison of different over-the-counter devices for skin tags treatment. Devices using different cooling methods (sprays, foam and dispenser) have been compared using a heat-flux meter originally designed for the measurement of the skin thermal resistance. The instrument uncertainty in heat flux measurement is lower than 6 % (C.I. 95 %) and the interface temperature uncertainty is lower than 0.3 °C.

The heat flux produced by 19 different OTC devices have been evaluated in controlled conditions. Results allowed the identification of the best nozzle geometry, which was the one that allowed reaching the largest  $\Delta T_{FM}$  (or, equivalently, the lowest interface temperature) and the largest heat flux.

#### 5. References

- [1] J. M. Plasencia, "Cutaneous warts: diagnosis and treatment," *Primary Care: Clinics in Office Practice*, vol. 27, pp. 423-434, 2000.

[2] N. V. Nguyen and C. G. Burkhart, "Cryosurgical treatment of warts: dimethyl ether and propane versus liquid nitrogen-case report and review of the literature," *J Drugs Dermatol*, vol. 10, pp. 1174-1176, 2011.

[3] D. R. Focht III, C. Spicer and M. P. Fairchok, "The efficacy of duct tape vs cryotherapy in the treatment of verruca vulgaris (the common wart)," *Arch. Pediatr. Adolesc. Med.*, vol. 156, pp. 971-974, 2002.

[4] C. G. Burkhart, I. Pchalek, M. Adler and C. N. Burkhart, "An in vitro study comparing temperatures of over-the-counter wart preparations with liquid nitrogen," *J. Am. Acad. Dermatol.*, vol. 57, pp. 1019-1020, 12, 2007.

[5] B. Saggin, M. Tarabini and G. Lanfranchi, "A device for the skin-contact thermal resistance measurement," *IEEE Transactions on Instrumentation and Measurement*, vol. 61, pp. 489-495, 2012.

[6] M. Tarabini, B. Saggin, D. Scaccabarozzi and G. Lanfranchi, "Estimation of the orthosis-limb contact pressure through thermal imaging," in *Instrumentation and Measurement Technology Conference (I2MTC), 2012 IEEE International*, 2012, pp. 2733-2737.

[7] M. Tarabini, B. Saggin, D. Scaccabarozzi and G. Moschioni, "The potential of micro-electro-mechanical accelerometers in human vibration measurements," *J. Sound Vibrat.*, vol. 331, pp. 487, 2012.

[8] G. Moschioni, B. Saggin and M. Tarabini, "3-D Sound Intensity Measurements: Accuracy Enhancements With Virtual-Instrument-Based Technology," *Instrumentation and Measurement, IEEE Transactions On*, vol. 57, pp. 1820-1829, 2008.

# **Calibration Uncertainty of Three-Axis Low Frequency Accelerometers: Test Rig and Procedure Aspects**

Giulio D'Emilia\*, Antonella Gaspari\*\*, Emanuela Natale\*

\* University of L'Aquila, Dipartimento di Ingegneria Industriale e dell'Informazione e di Economia,  
Via G. Gronchi, 18 – 67100 L'AQUILA (ITALY)

\*\* University of L'Aquila, Dipartimento di Ingegneria Industriale e dell'Informazione e di Economia,  
67100 L'AQUILA (ITALY), presently at Fraunhofer IPK, Pascalstraße 8-9, 10587 BERLIN (GERMANY)

## **Abstract**

*In this paper a methodology is described concerning the calibration of three-axis low-cost accelerometers in the 0 to 10 Hz frequency range, to be used for evaluation of existing civil infrastructures. Particular attention is paid to the evaluation of the calibration uncertainty with reference to both static and dynamic operating conditions and to the aspects specifically related to the test bench and to the calibration procedure. These aspects mainly concern the test bench behavior in realizing the requested motion law, the choosing of the reference for calibration and the data processing techniques.*

*The obtained results show that a great improvement of the low cost accelerometers' metrological characterization could be achieved according to the procedure described in this paper; furthermore, interesting considerations have been carried out with reference to the evaluation of main and cross sensitivity of accelerometers also in dynamic working conditions.*

## **1. Introduction**

Social resilience to disasters is now considered a topic of highest political and technical concern in advanced nations.

Social safety and building heritage along with sustainable urban development are important issues in setting guide lines which aim to improve this topic. For this purpose, evaluating the conditions and performance of existing civil infrastructures is a crucial aspect that allows the decision-makers to configure the best lines of activity in order to improve the quality of life [1].

To have integrated procedures involving geotechnical and structural aspects finalized to buildings' diagnostics, a distributed sensor network is needed, allowing us to operate in a selective manner and in the most critical situations. This implies the need of a greater

number of measuring sensors, for both the three-axis vibration as well as inclination measurements.

This innovation, together with the need of covering wide areas through this multi-sensors network in order to include different buildings, sets the requirement of lower-cost solutions that are nevertheless able to ensure the requested uncertainty of measurements.

Most of the above mentioned measurement and cost requirements could be satisfied by the well known micro-electro-mechanical systems (MEMS) technology and some examples of its use for these applications could be found in literature [2], even though careful attention should be paid to many possible causes of errors [3], especially when low-cost and low-precision MEMS accelerometers are considered. Due to these facts, many studies can be found in literature, referring to calibration of these sensors, using mechanical reference quantities [3], [4], or using fully electrical methods to estimate the sensitivity of capacitive MEMS accelerometers in batch fabrication [5].

Even if different aspects are studied, like bias correction and main and cross sensitivity evaluation, an exhaustive description of uncertainty causes can not be found, in particular with reference to the dynamic behavior in the low frequency range (0 to 10 Hz).

Market and literature solutions [2], [6], [7] and characteristics of the calibration test bench designed for this specific application [8], [9], [10], [11], [12] have been considered, but the provided solutions do not appear completely satisfactory if the right trade-off between uncertainty of calibration on one hand, and the cost of the test bench and the calibration procedure duration on the other hand are considered.

Furthermore, bearing in mind these considerations, the first aspect to be considered is the limit that could be achieved with reference to the uncertainty of sensors to be used for

acceleration and inclination, taking into account cost requirements as well.

This goal mainly involves sensor behavior, its power supply and conditioning, data acquisition technique, and initial and periodical calibration, especially in the low frequency range of vibrations (0 - 10 Hz).

This paper aims to investigate the main technical and procedural aspects to be considered for the definition of a calibration procedure modulated in function of the application, as well as the cost range of the sensors.

Particular attention is paid to the experiment design, the way through a mechanical reference acceleration is created and evaluated and how data processing techniques influence the variability of results, retrieving useful information without having to perform superfluous tests, according to the quality level of the sensors that are being selected.

It is to be pointed out that straight through the paper the acceleration will be measured in terms of  $g$ , acceleration of gravity; the authors are aware that is formally incorrect, but they prefer this solution for better understanding of results in the field of civil and seismic engineering.

## 2. Methodology

Scientific evaluations, experts' advice and market analysis led us to define the following ranges of interest for tests:

- frequency range: 0 - 40 Hz;
- maximum amplitude of vibration:  $\pm 2g$ .

In this paper the calibration in the frequency range 0 to 10 Hz will be studied. It is external to the best vibration frequency range of standard electro-dynamic shakers.

Calibration uncertainty of sensors will be evaluated with reference to the contribution of the effects tied to both the calibration test rig and the sensor characteristics.

The three-axis sensor will be calibrated both statically and dynamically. In fact, in field applications we are interested to use it as an inclinometer, the steady behavior, and as a three-axis accelerometer, involving the dynamic behavior.

For the general calibration of the accelerometer the following relationship between the input acceleration and the output signals can be set:

$$\begin{pmatrix} a_x \\ a_y \\ a_z \end{pmatrix} = \begin{pmatrix} S_{xx} & S_{xy} & S_{xz} \\ S_{yx} & S_{yy} & S_{yz} \\ S_{zx} & S_{zy} & S_{zz} \end{pmatrix} \begin{pmatrix} V_x \\ V_y \\ V_z \end{pmatrix} + \begin{pmatrix} q_x \\ q_y \\ q_z \end{pmatrix} \quad Eq. 1$$

being  $S_{xx}, S_{yy}, S_{zz}$  the main axis sensitivities; the other elements of the matrix are the transverse

(cross) sensitivities.  $\begin{pmatrix} a_x \\ a_y \\ a_z \end{pmatrix}$  are the measured

acceleration components,  $\begin{pmatrix} V_x \\ V_y \\ V_z \end{pmatrix}$  are the voltage

outputs of the sensor, and  $\begin{pmatrix} q_x \\ q_y \\ q_z \end{pmatrix}$  is the offset vector.

A total of 12 parameters have to be evaluated [3], [13], [14], [15].

For the static calibration a mechanical arm is used in order to adjust the sensor to different positions, through the gravity acceleration vector components along the three axes.

The minimum number of measurement orientations is 4, although more measurements may give a more robust calibration, using a linear Least Squares Optimization. In this article, the effect of the choice of the number of the angular positioning on the calibration uncertainty is investigated in order to provide useful information about the calibration procedure that is more suitable for the characteristics of the selected accelerometers.

The behavior of the main and transverse sensitivities in the frequency range 0 to 10 Hz is also a point of interest.

For the dynamic calibration a test bench based on a rotary device is used. It is driven by a brushless servomotor, controlled by a PLC by means of a high accuracy angular encoder, which allows us to realize different motion laws (sinusoidal, saw-tooth, ramp, etc..).

Being the rotation axis vertically placed, all the three axes will operate, measuring the acceleration of gravity  $g$  (or a component of it, depending on the position), the tangential acceleration,  $a_t$  (or a component of it, depending on the position), and the centrifugal acceleration,  $a_c$ , respectively. These acceleration values will be used as the reference accelerations [5], according to the following equations, where  $\omega$  is the angular velocity and  $r$  is the radius of sensor positioning:

$$a_t = \dot{\omega} \cdot r \quad Eq. 2$$

$$a_c = \omega^2 \cdot r \quad Eq. 3$$

It is to be pointed out that  $a_t$  is obtained through twice differentiation of angular encoder signal, which could cause high frequency noise problems. A high accuracy three-axis accelerometer will also be employed for further validation purposes, according also to literature indications [12].

The test bench is depicted in Fig. 1.

Furthermore, the accelerometer is placed so that X-Y or X-Z planes do not correspond to the horizontal one, as Fig. 2 shows: in this way all the measuring axes will be subjected to a variable acceleration at a frequency depending on the repetition rate of oscillations.

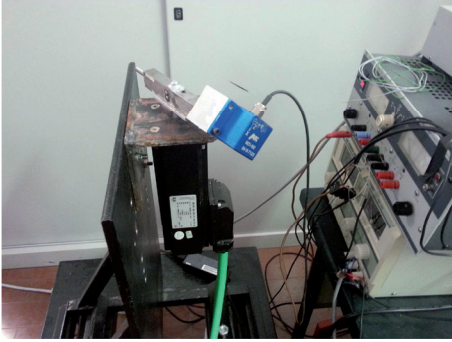


Fig. 1: The rotary table, driven by the brushless motor.

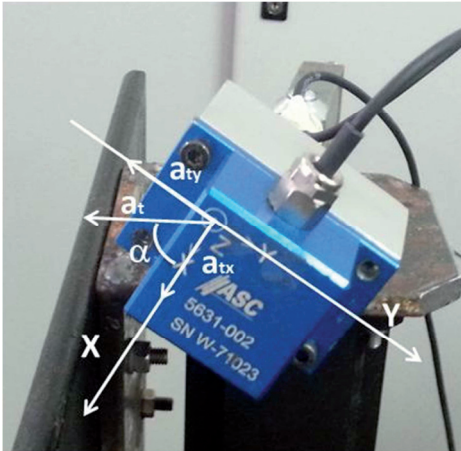


Fig. 2: Scheme of tangential acceleration components corresponding to a rotation angle  $\alpha$  of the plane X-Z with respect to the horizontal one.

In order to evaluate the effect of this parameter and to build the dynamic calibration matrix, the orientation of the accelerometer under investigation will be changed.

As to the uncertainty of radius, tests are carried out at different radial positioning of the sensors, to the purpose to reduce the whole uncertainty on the reference values of acceleration  $a_t$  and  $a_c$ . The radial positioning has been varied, inserting blocks of increasing and accurately measured thickness; the effective position of the rotation axis is estimated by a best fitting of the found tangential and radial accelerations at different radii, hypothesizing a linear behavior with the radius.

The effect of the actual motion law will also be analyzed, in relation to its theoretical setting, as well as the rotary device set-up. In particular the behavior of the calibration bench will be examined in case of both square wave and sinusoidal motion law for periodical oscillations.

As for uncertainty evaluation, the following assumptions have been made:

$$\frac{\sigma_{a_c}}{a_c} = \sqrt{\left(\frac{2\sigma_{\omega}}{\omega}\right)^2 + \left(\frac{\sigma_r}{r}\right)^2} \quad Eq. 4$$

$$\frac{\sigma_{a_t}}{a_t} = \sqrt{\left(\frac{\sigma_{\dot{\omega}}}{\dot{\omega}}\right)^2 + \left(\frac{\sigma_r}{r}\right)^2} \quad Eq. 5$$

where  $\sigma_r$  stands for the linearity standard deviation from the best fit line (a rectangular distribution has been assumed);  $r = 95.0$  mm,  $\sigma_r = 0.1$  mm;

The contributions to the whole uncertainty of  $a_c$  and of  $a_t$  deriving from the  $\omega$  and of the  $\dot{\omega}$  terms respectively, will be evaluated, taking into account the repeatability standard deviation of them, in correspondence of each angular position. Systematic effects on the angular position have been considered negligible.

For geometrical angles a standard deviation of  $1^\circ$  has been assumed.

Tests have been planned in order to consider the following aspects with reference to the uncertainty of  $a_c$  and of  $a_t$  (or a component of them depending on the position):

- motion laws;
- rotary device setting;
- choosing of the reference;
- number of points for calibration;
- data processing techniques.

Finally it is to be pointed out that the requested calibration procedure and the accuracy to be achieved should be able to fit the sensor characteristics, so that the performances of calibration rig and cost of calibration can be adequately reduced.

### 3. Results

#### 3.1. Static calibration

As a first step, a static calibration of a three-axis accelerometer has been done, according to the procedure based on Eq. 1.

A total of 10 different angular positions have been realized in order to fulfil the accuracy requirements described in [14].

The results are described in the following calibration matrix:

$$\begin{pmatrix} -0.994 & 0.000620 & 0.00404 \\ 0.0199 & -0.987 & 0.00347 \\ -0.0713 & -0.00310 & -0.994 \end{pmatrix} \left[ \frac{g}{V} \right]$$

and the offset vector:

$$\begin{pmatrix} 2.48 \\ 2.45 \\ 2.72 \end{pmatrix} [g]$$

A maximum relative deviation from the mean values of 2% has been evaluated for the coefficients of the main sensitivities, taking into account the angle uncertainty.

Anyway, measurements have been carried out after calibration in the range  $\pm g$  ( $\pm\pi/2$  as for the angle) for each axis: a maximum deviation of 0.01g has been evaluated. This result suggests that the sensitivity matrix should be evaluated on the whole, due to the compensation effect of the variability of the different matrix coefficients between each other.

#### 3.1. Dynamic calibration

##### 3.1.1 Identification of the motion law

In case of dynamic calibration of accelerometers, as a preliminary matter, the effect of the motion time law for oscillations on results accuracy has been investigated: in particular saw tooth and sinusoidal velocity profile of oscillations were considered.

At a preliminary evaluation saw tooth velocity profile, that means square wave profile for  $a_t$ , seemed interesting, having a plateau in  $a_t$ , being very simple to realize on the test bench and making able to investigate in the same test many frequencies (the odd harmonic components).

This motion law has been discarded, since experimental tests indicated that it is difficult to be realized not only practically but also theoretically, being necessary specific settings, which are meaningless from a physical point of view.

Furthermore, the graphs of Fig. 3 shows that strong oscillations in the test bench arise when  $a_t$  is changed, which is a problem also for sensors to be calibrated.

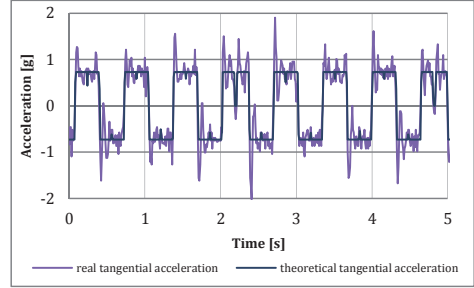


**Fig. 3: Comparison between real and theoretical tangential acceleration (saw-tooth motion law, fundamental component = 1.6 Hz).**

All the results hereinafter refer to tests driven with a sinusoidal motion law; the set-up of the rotary table for sinusoidal oscillations is remarkably more difficult from a programming point of view, since an electronic cam has to be realized. Tests have been carried out at a oscillation frequency of 0.5, 1.0 and 1.6 Hz; in particular indication will be stressed referring to 1.6 Hz oscillation, whose vibrations peaks are the highest.

##### 3.1.2 Identification of the reference

In a calibration procedure the definition of the reference is a fundamental issue.

The graphs of Fig. 4 show a comparison between real and theoretical time behavior of the acceleration components, with reference to the axes of the accelerometer. It is to be pointed out that the components of  $a_t$  act along the X and Y axes, while  $a_c$  acts along the Z one.

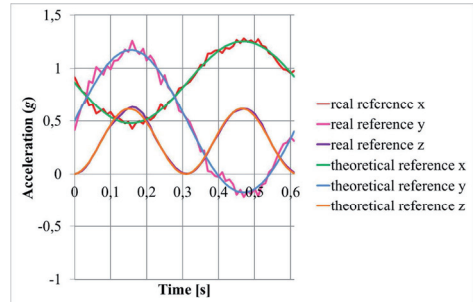


**Fig. 4: Comparison between real and theoretical time behavior of the acceleration components, with reference to the axes of the accelerometer.**



The mean square value of the difference between real  $a_{xt}(t)$ ,  $a_{yt}(t)$ ,  $a_{zt}(t)$  and theoretical values  $a_{xt}(t)$ ,  $a_{yt}(t)$ ,  $a_{zt}(t)$ , during the oscillation period, has been evaluated, being 0.029, 0.051, 0.012 g respectively.

The repeatability of  $a_{xt}(t)$ ,  $a_{yt}(t)$ ,  $a_{zt}(t)$  have been calculated during the oscillation period. The mean values are 0.051, 0.089, 0.016 g, respectively. The maximum values are 0.084, 0.15, 0.030 g, respectively.

Obviously, most of the oscillations found in  $a_{xt}(t)$  and  $a_{yt}(t)$  depends on numerical differentiation, even though higher order harmonics can be identified with respect to the theoretical behavior, due to effective oscillations at points where the motion is inverted.

Anyway, the relevance of these aspects is strongly reduced if the calibration of a three-axis accelerometer is considered.

### 3.1.3 Data processing techniques

In Tab. 1 and 2  $D_x$ ,  $D_y$ ,  $D_z$ , are evaluated, representing the mean square values of the differences between reference acceleration and corrected sensor data during the oscillation period. In Tab.1 reference data are those obtained by twice differentiation of angular encoder. In Tab. 2 the theoretical sinusoidal law is used as the reference. The effect of building calibration matrix with an increasing number of points,  $n$ , is also studied.

$n$	$D_x$	$D_y$	$D_z$
14	0.0877	0.114	0.0333
21	0.0883	0.112	0.0299
28	0.0829	0.109	0.0294
35	0.0790	0.105	0.0293
42	0.082	0.110	0.0298

Tab. 1:  $D_x$ ,  $D_y$ ,  $D_z$  using the dynamic calibration matrix as obtained from the real data.

$n$	$D_x$	$D_y$	$D_z$
14	0.0780	0.110	0.0452
21	0.0720	0.090	0.0360
28	0.0724	0.0940	0.0334
35	0.0707	0.0953	0.0327
42	0.0729	0.0966	0.0328

Tab. 2:  $D_x$ ,  $D_y$ ,  $D_z$  using the dynamic calibration matrix as obtained from the theoretical data.

The differences between the use of the dynamic calibration matrix as obtained from the real data with respect to the theoretical one are negligible.

Furthermore, provided that a sufficient number of points is considered, no effect of increasing it has been acknowledged.

On the contrary, the improvement of using dynamic calibration matrix with respect to the static one is clearly shown in diagrams of Fig. 5.a, 5.b, 5.c, where real encoder data, twice differentiated, used as the reference, sensor data corrected by static calibration matrix and data corrected by dynamic calibration matrix are compared.

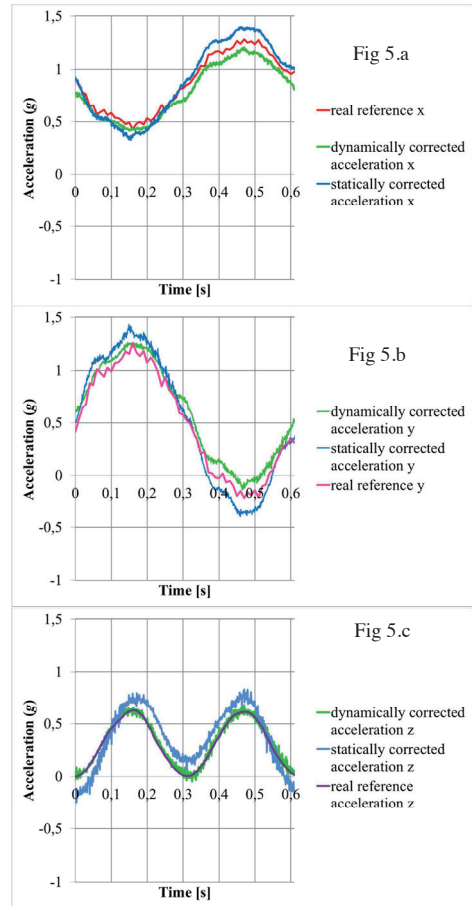


Fig. 5: Comparison among real encoder data, twice differentiated, used as the reference, sensor data corrected by static calibration matrix and data corrected by dynamic calibration matrix.

- a.  $a_x$  component (accelerometer X axis)
- b.  $a_y$  component (accelerometer Y axis)
- c.  $a_z$  acceleration (accelerometer Z axis)

### 3.1.4 System set up and number of points for calibration

The tests so far carried out also suggested some actions to be carried on to improve the calibration procedure performances by reducing calibration uncertainty, in particular of  $a_t$  and its components; this objective will be pursued by making more accurate and repeatable the real acceleration profile.

These actions on one hand require a mechanical improvement of the rotary table, allowing us to increase the transferability of the angular encoder information to the position of the accelerometer to be calibrated, on the other hand ask for a higher sampling rate of the angular encoder data.

It is to be pointed out that the used PLC allows us to use a task time of less than 1 ms, allowing a sampling rate of about 1 kHz.

Rather than increasing the number of points on which the matrix should be evaluated but provided that a sufficient number of points is considered, it seems more convenient to mix data measured changing the sensor orientation, also in dynamic calibration.

## 4. Conclusions

In this paper some aspects concerning the calibration uncertainty of three-axis low-cost accelerometers for diagnostics of civil buildings are considered. Both static conditions and dynamic behavior in the range 0 to 10 Hz as for vibrations have been examined.

A frequency varying three-axis field of acceleration has been realized by modulating both gravity acceleration, and tangential/radial acceleration components of a rotary motion created on a test bench driven by a brushless servomotor.

Reference values for  $a_x$  and  $a_t$  acceleration (or a component of it depending on position) have been deduced from the indications of a high precision rotary encoder used for axis control, in order to separate the effect on the whole uncertainty of calibration of the test bench characteristics and settings from the sensor performances.

The effects taken into account refer to :

- motion laws;
- rotary device setting;
- choosing of the reference;
- number of points for calibration;
- data processing techniques.

Experimental results, for both static and dynamic applications, show that both main and cross sensitivities of a three-axis capacitive accelerometer of good quality level from a

metrological point of view can be obtained; this allows to correct the effect of cross sensitivities also in dynamic applications, in order to remarkably improve the transducer accuracy for in field applications.

The work carried out it is to be considered as a first step of the whole research; in fact the experimental results have also suggested actions to be realized in order to improve the mechanical behavior of the test bench, the acquisition of the angular encoder data, the calibration procedure and the data processing techniques. Improving these aspects is expected to further reduce the calibration uncertainty.

## References

- [1] Wyss M and Rosset P "Mapping seismic risk: the current crisis" *Nat. Haz.* 68, 2013, pagg 49-52
- [2] Zhao M and Xiong X "A New MEMS Accelerometer Applied in Civil Engineering and its Calibration Test" *The Ninth International Conference on Electronic Measurement & Instruments*, 2009, ICEMI-2 122-125.
- [3] Ren Wei, Zhang Tao, Zhang Hai-yun, Wang Lei-gang, Zhou Yong-jie, Luan Meng-kai, Liu Hui-feng, Shi Jing-wei "A research on calibration of low-precision MEMS inertial sensors", *25<sup>th</sup> Chinese Conference on Control and Decision Conference (CCDC)*, 2013, pagg 3243 – 3247
- [4] Zanjani P N, Abraham A A, "A Method for Calibrating Micro Electro Mechanical Systems Accelerometer for Use as a Tilt and Seismograph Sensor" *12<sup>th</sup> International Conference on Computer Modelling and Simulation (UKSim)*, 2010, pagg 637 – 641
- [5] Dumas N, Azais F, Mailly F, Nouet P, "Study of the electrical set-up for capacitive MEMS accelerometer test and calibration", *Journal of Electronic Testing* 26, 2010, pagg 111-125.
- [6] Milligan D J, Homeijer B D and Walmsley R G "An ultra-low noise MEMS accelerometer for seismic imaging" *Sensors (IEEE)*, 2011, pagg 1281 - 1284.
- [7] Vallet F and Marcou J "A low-frequency optical accelerometer" *J. Opt.* 29, 1998, pagg 152-155.
- [8] Schiefer M I and Bono R "Improved low frequency accelerometer calibration" *XIX IMEKO World Congress Fundamental and Applied Metrology*, 2009
- [9] Choi K, Jang S and Kim Y "Calibration of Inertial Measurement Units Using Pendulum Motion" *Int. J. of Aeronautical &*

- Space Sci.* 11(3), 2010, pagg 234–239.
- [10] Zhu C, Qin X, Wu Z and Zheng L “Research on calibration for measuring vibration of low frequency” *International Conference on Mechanic Automation and Control Engineering*, 2010, pagg 3315 - 3318.
  - [11] Mohd-Yasin F, Nagel D J, Ong D S, Korman C E and Chuah H T “Low frequency noise measurement and analysis of capacitive micro-accelerometers” *Microelectronic Engineering* 84, 2007, pagg 1788-1791.
  - [12] Ohm W, Wu L, Hanes P and Wong G S K “Generation of low-frequency vibration using a cantilever beam for calibration of accelerometer” *Journal of Sound and Vibration* 289, 2006, pagg 192-209.
  - [13] Akira Umeda, Mike Onoe, Kohji Sakata, Takehiro Fukushima, Kouichi Kanari, Hiroshi Iioka, Toshiyuki Kobayashi “Calibration of three-axis accelerometers using a three-dimensional vibration generator and three laser interferometers” *Sensors and Actuators A: Physical* 114, 2004, pagg 93–101.
  - [14] Mark Pedley, “High Precision Calibration of a Three-Axis Accelerometer” *Freescale Semiconductor*, 2013
  - [15] Nakano A, Hirai Y, Sugano K, Tsuchiya T, Tabata O, Umeda A, “Rotational motion effect on sensitivity matrix of MEMS three-axis accelerometer for realization of concurrent calibration using vibration table”, *IEEE 26th International Conference on Micro Electro Mechanical Systems (MEMS)*, 2013, pagg 645 – 648

# A system based on light scattering to measure pressure distribution on the finger

M. Becchetti \*, R. Marsili \*, F. Cannella \*\*, A. Garinei \*\*\*

\*Dipartimento di Ingegneria, Università degli Studi di Perugia, Perugia, 06125, Italy

\*\*Istituto Italiano di Tecnologia, Genova, 16163, Italy

\*\*\* DMII, Università degli Studi Guglielmo Marconi, Roma, 00193, Italy

## Abstract

*The measurement of contact pressure of human fingers is very important to understand human perceptual mechanisms, that is the main goal of most of the neuroscientific studies. It may also lead to a correct development of tactile devices and haptic systems, as they are intended to convey controllable and effective stimuli.*

*In this work, an optical measurement system based on Frustrated Total Internal Reflection (FTIR) is proposed for the measurement of the pressure distribution on the contact area between a human finger and a flat surface. The feasibility study performed shows that the tested sensor can be effectively used for the measurement of the fingertip contact pressure both on static and dynamic conditions.*

**Keywords:** *Frustrated Total Internal Reflection (FTIR), fingertip contact pressure, biomechanics*

## 1. Introduction

The investigation of the mechanisms of human tactile perception represents a fundamental topic in haptics. The fingertip deformation is the basic mechanical action in the tactile perception, since tactile sensitivity depends on the tissue strain and hence on the contact area. Different models are available to predict the behavior of the fingertip in terms of contact area, deformation and pressure distribution [1,2]. Measurements are thus required both to determine the static fingertip area and force as input to the numerical models and to measure the area and the pressure necessary for numerical model validation. When measuring the contact pressure, the goal is to set up a measurement system with high sensitivity at low pressure, since, for specific applications, the typical pressure range is from 0 Pa to 50000 Pa.

The main objective of this work is the development of a measurement system, which allows to characterize the different aspects of the interaction finger - contact surface, through the

measurement of the contact area and of the pressure distribution, both in static and dynamic conditions.

Many sensors based on different physical principles have been proposed for the measurement of pressure at contact surface between two rigid or flexible bodies. Some contact pressure measurement systems have been used for measuring pressure distribution at interfaces between objects, with application to comfort analysis and improvement of vehicle seats [3], for various biomedical applications such as measurement of contact pressure between hand and handle of a tool in order to analyze vibration transmission to the hand [4,5] or between foot and ground for plantar pressure analysis [6,7]. Many applications have been developed [8] also in other fields such as robot technology (tactile sensors), for contact force mapping of mechanical parts. The film sensors used for those applications are based on piezo-polymers, capacitive, conductive-ink or resistive polymers sensing elements. However, many metrological problems remain unresolved, due to non-linearity, reological behavior, mounting surface curvature and shape, dynamic characteristics, etc. Also frequency limitations can be due to the sensor itself or to the electronic processing and data acquisition system, when a matrix of many sensing elements is necessary. Piezo-polymers have probably the best metrological characteristic but cannot measure very slow fluctuations or static pressure components. Sensors based on conductive ink or resistive polymers showed from preliminary tests that metrological characteristics change with time and have large hysteresis. The capacitive sensing elements can be used to measure both dynamic and static pressure with acceptable linearity and hysteresis, but their sensitivity is low and they cannot measure very small pressures.

Here an optical measurement system based on light scattering is developed and analyzed.

The outline of this paper is as follows. First, the design of an optimized measurement system based on Frustrated Total Internal Reflection (FTIR) is described. Then the results of specific

tests performed on the measurement system are shown, to define its static and dynamic behavior and to evaluate if the proposed measurement technique can be effectively used to measure human fingertip mechanical properties in terms of contact area and pressure distribution.

## 2. Experimental background and setup

The principle of the measurement system is the light reflection/refraction at the interference between two transparent media. When the light passes through an interference between media of different refractive indices, the path of travel changes (Snell's Law).

Thus when a light source is installed at the edge of a thin glass plate and the incident angle  $\theta_1$  exceeds the critical angle  $\theta_{critical}$  (Fig.1a), the plate acts as a light guide. In this case (total internal reflection) the light cannot be seen when observing the plate from below the plate.

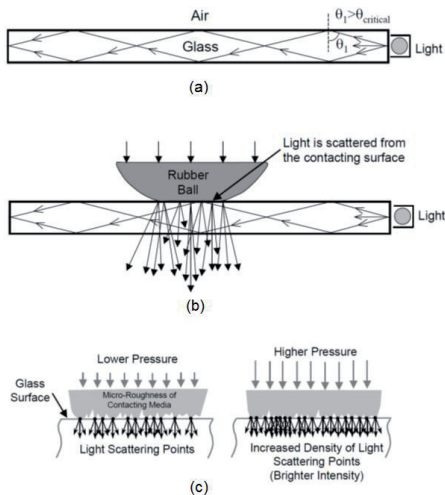


Fig. 1: Principle of measurement [9]

If a reflecting media is pressed against the plate, the surface of the media will scatter light in the contact surface, being the media with a refractive index different than the refractive index of the air (Fig.1b). By observing the light scattered, it is thus possible to view the shape of the contact surface. Depending on the roughness of the contact surface, the contact area will increase with the contact pressure, thus the light intensity can be used to measure the contact pressure between the two media (Fig. 1c).

Methods based on white light refraction are used for the measurement of normal contact stress

between 'soft' structures and a rigid planar surface, specifically for application to tire footprint analysis [9,10]. These systems are optimized to measure tire footprint pressures and are not suitable for the measurement of low pressures. The design of the proposed measurement system was developed to permit the measurement of low pressures that characterize human fingertip contact. The roughness and the mechanical characteristics of the contact surface are the most critical parameters for the realization of an effective pressure measurement system based on FTIR. These parameters must be carefully evaluated, because of their effects on the range and on the sensitivity of the measurement system.

The measurement system setup is shown in Figure 3: a sliding system realized through threaded rods permits to adjust the camera position depending on its optics; a 200 mm x 200 mm x 200 mm darkroom was realized to avoid the interference of light from external environment; a 150 mm x 150 mm x 10 mm glass plate was fixed on a square support with a green LED strip installed around the perimeter.

The main characteristics of the glass plate are shown in Table 1.

Chemical glass composition	(SiO <sub>2</sub> ) + oxides
Aspect	Transparent
Christallinity	Amorphous
Refractive index	1,458 ÷ 1,86
Nominal tensile strength	4 MPa
Nominal compression strength	1 GPa
Nominal bending strength	40 MPa

Table 1: Glass plate characteristics

## 3. System characterization

### 3.1. Static characterization

A first static analysis of the system was performed to characterize the behavior of the sensor when a constant pressure is applied on it. For this purpose, the glass plate was covered with a thin membrane and fixed on a square support with a green LED strip installed around the perimeter.

A Plexiglas frame was then realized to install the thin lattice membrane at the top of the glass plate: the membrane is stretched, thus there is a thin air gap (no contact) between the membrane and the glass plate in the starting configuration. The lattice membrane is talc-covered to increase the roughness of the contact surface and thus the sensitivity of the measurement system.

Figure 2 illustrates a typical result, from the literature, of the load-deformation curve for the latex membrane used.

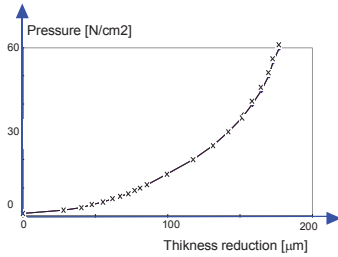


**Figure 2: Typical pressure - sensor thickness reduction curve [11]**

From this result it is possible to see, in general, the non-linear behavior of the latex membrane. However in the pressure range of interest (0 – 50000 Pa), as a first approximation, we can consider linear the curve pressure–thickness reduction.

For the static calibration, a reference pressure is applied to the sensor by the thin membrane, which is loaded by a constant pressure chamber, whose pressure is measured by a pressure sensor connected to a Scandura Pascal 100 system. In order to avoid pressure losses, the contact between the pressure chamber and the glass plate is realized through an O-Ring for pneumatic applications (Fig. 3).

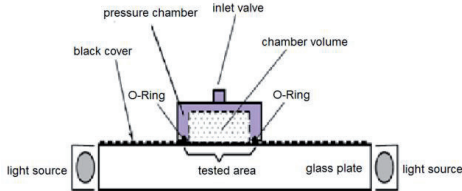


**Fig. 3: Test bed for static calibration**

The reference pressure varies from 0 Pa to 100000 Pa, that is the maximum pressure to avoid fracture of the glass plate.

A high performance reflex digital camera (Canon EOS 1100D, with a 12.2 megapixel CMOS sensor), was used to take high resolution grey-level images. The camera was equipped with a 18-55mm f/3.5-5.6 lens: the distance from the camera to the glass plate was adjusted depending on the focal length of the camera. The camera parameters (ISO settings, shutter speed, white balance) were adjusted to obtain maximum sensitivity for the specific setup (f-number = 5,6, exposure time = 1/8 s, ISO 400).

The raw images (4272 x 2848 pixels) were acquired with the software Canon Eos Utility, converted in .tiff format and thus post-processed with Matlab toolbox. Images were acquired for each pressure step (5000 Pa – 21 steps) in the calibration range.

For a given pressure, the grey level of each pixel varies depending on the pixel location and on the local characteristics of the contact surface (roughness). The uncertainty is less than 1% full scale. Figure 4 illustrates a typical static calibration diagram: abscissa refers to the reference pressure ( $q_i$  [Pa]); ordinate refers to the grey-level measured by the sensor ( $q_o$  [bar]). The calibration curve is obtained using the method of least squares.

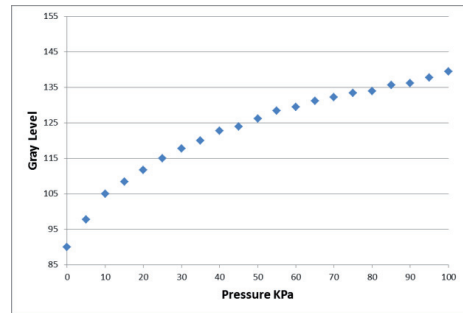


**Figure 4: Typical static calibration diagram for a pixel**

After these first measurements, a measurement area was defined to reduce the dispersion due to the localized imperfections of the contact surfaces (Fig. 5). This is the most effective sensor area both for static and dynamic measurements.

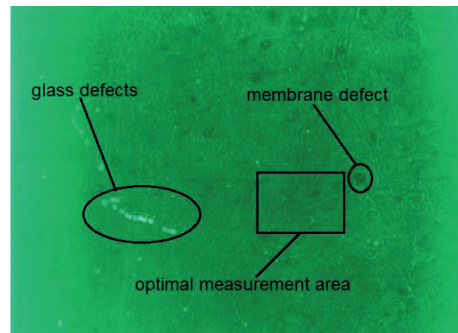


**Fig. 5: measurement area selection**



### 3.2. Preliminary dynamic characterization

Then a dynamic characterization was performed by loading the sensor with a sinusoidal excitation applied through a rigid feeler pin (Fig. 6). The compression force, generated by the electrodynamic exciter, is measured by a load cell.

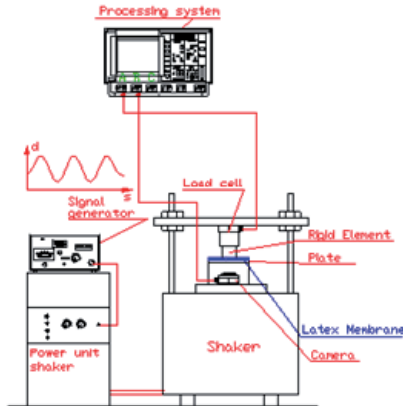


Fig. 6: test bench for dynamic characterization

Tests were performed using sine excitation: typical signals obtained are shown in Figure 7.

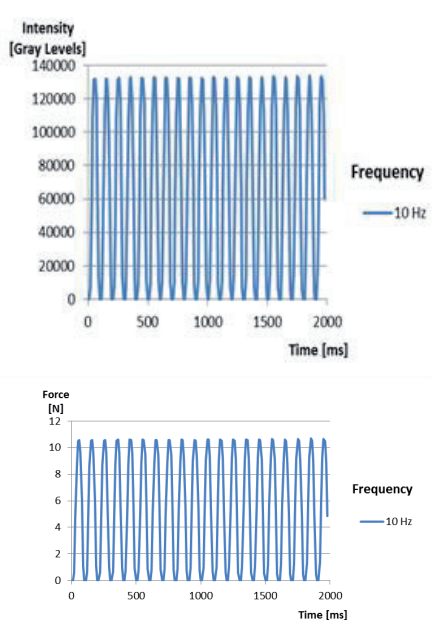


Figure 7: Time history output system and force.

For the images processing a specific software in Lab View has been developed (Fig. 8)

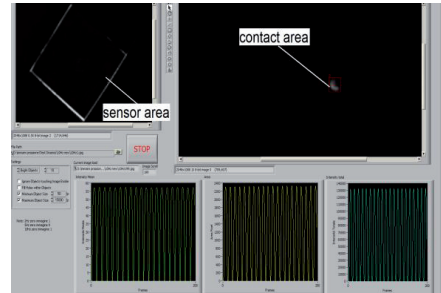


Fig. 8: image processing software interface

Changing excitation frequency keeping fixed the level of force the ratio between system output (gray level) and force amplitude vs frequency is plotted in Figure 9.

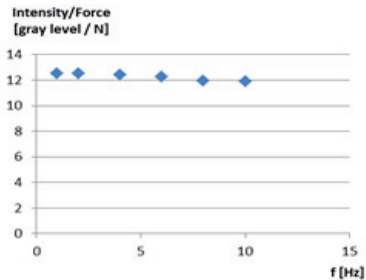


Figure 9: Time history output system and force.

These results allow establishing that a useful bandwidth is from 0 up to 10 Hz with tolerable response decrease lower than 5%.

### 4. Conclusions

The analysis of the contact pressure between the finger and a contact surface is of remarkable interest in the field of biomedical design, to characterize human fingertip mechanical properties in terms of contact area, deformation and pressure distribution.

In this work a measurement technique based on FTIR is proposed for the analysis of contact pressure between the finger and a flat contact surface (glass plate).

A FTIR measurement system was designed and tested to evaluate the feasibility and effectiveness of this measurement technique to measure the contact area and the pressure necessary for numerical fingertip model validation.

Results showed that there are good assumptions to use the sensor for the measurement of the

fingertip contact pressure both on static and dynamic conditions.

Consistency and repeatability observed at this first stage is very encouraging for the development of an effective fingertip pressure measurement system based on FTIR.

This will permit to analyze the behavior of the finger for different conditions, and thus to validate numerical models not only in contact area and force, but also in pressure, that is suitable for investigating the fingertip deformation in static and dynamic conditions.

Plans for future work are to further explore new materials for higher sensitivity, test different configurations with a complete set of loading conditions.

#### Bibliografia

- [1] J. Z. Wu, R. G. Dong, S. Rakheja, A. W. Schopper, and W. P. Smutz, "A structural fingertip model for simulating of the biomechanics of tactile sensation," *Med. Eng. Phys.*, Mar. 2004, vol. 26, no. 2, pp. 165–175,
- [2] S. Shimawaki, N. Sakai, "Quasi-static deformation analysis of a human finger using a three-dimensional Finite Element Model Constructed from CT Images", *Journal of Environment and Engineering*, 2007, Vol. 2, no. 1.
- [3] M. Shiratori, M. Ishida, "Development of body pressure distribution measurement device", *JSAE Review*, July 1992, Vol. 13 n. 3
- [4] R. Marsili, G.L. Rossi, "The measurement of contact and grip force as reference for human hand transmitted vibration evaluation by laser scanning vibrometers", *II Int. Conf. on Vibration Measurements by Laser Techniques*, 23-25 Sept. 1996, Ancona Italy, SPIE Vol. 2868
- [5] R. Gurram, G.J. Gouw, S. Rakheja, "Grip pressure distribution under static and dynamic loading", *Int. Jou. of Experimental Mechanics*
- [6] P. Sanfilippo, R. Stress, K. Moss. "Dynamic plantar pressure analysis", *Jou. of the American Pediatric Medical Associations*, 1992; Vol. 82 n. 10 pp 507-514
- [7] A. Mair, W. Diebschlag, O. Distl, H. Krausslich, "Measuring device for the analysis of pressure distribution on the foot soles of cattle", *J. Vet. Med*, 1988; A 35 pp 696-707
- [8] W. R. Iversen, "Tactile sensing, 1990s style", *Assembly*, Mar. 1993; pp 23-26
- [9] V. Roth, B. Moore, J. Turner, "An Optical Method for Normal Contact Stress Measurement with Applications to Tire-Road Interaction", *SEM X International Congress & Exposition on Experimental & Applied Mechanics*, 2004
- [10] A. N. Gent, J. D. Walter, "The Pneumatic Tire", *The National Highway Traffic Safety Administration, U.S. Department of Transportation, Washington DC 20590*, August 2005, pp 248-250
- [11] Matthew A. Hopcroft, Member, IEEE, William D. Nix, and Thomas W. Kenny, "What is the Young's Modulus of Silicon?" *Journal of microelectromechanical systems*, vol. 19, no. 2, april 2010

# ***A method to employ low-cost IR sensors for the indoor thermal comfort measurement***

## ***Application in a classroom***

*Gian Marco Revel\*, Marco Arnesano\*, Filippo Pietroni\**

*\* Università Politecnica delle Marche*

### **Abstract**

*An advanced measurement system has been developed to provide the real-time monitoring of indoor thermal comfort. The core device is a low-cost IR sensor assembled with two fixed-step motors, installed on the ceiling of the occupied room. The embedded tool performs the automatic scanning of each indoor surface to evaluate the temperature distribution. The mean radiant temperature ( $t_r$ ) and predictive mean vote (PMV) are computed for several positions in the environment and provided as output of the device through wireless or wired connection. The study presents the calibration of the IR sensor to allow the continuous measurement of the indoor surfaces temperature to retrieve the  $t_r$ . The results of the calibration procedure are used to employ and validate the IR-based system in a real environment, a classroom. The validation entails the comparison with a microclimate station and the subjective response of the occupants.*

### **1. Introduction**

According to the rational approach [1], the evaluation of thermal environments requires six quantities: two personal parameters (clothing thermal insulation and metabolic rate) and four physical parameters (air temperature, mean radiant temperature, air velocity and air humidity). These parameters have to be measured or estimated in order to derive the indoor thermal comfort by means of the PMV (Predicted Mean Vote) index [2]. As presented in [3], the mean radiant temperature  $t_r$  is a very significant factor in moderate environments, especially in buildings whose envelopes are exposed to a strong solar radiation [4]. A method based on the computation of angle factors, provided by ISO7726 [5], is capable of estimating the  $t_r$  with a good accuracy. However, it is complex because of the need of measuring all the surfaces temperature inside the room and the solar load with radiometers in case of transparent surfaces. For example, in [6] a

solution based on an infrared (IR) sensor is presented to estimate the thermal comfort of a subject in a vehicle in which the mean radiant temperature is not measured following the standard procedure in [3], but it is assumed to be equal to the measured local temperature. This paper presents an ad-hoc solution to provide the PMV index by means of continuous measurement of the indoor surfaces with an IR-based system and application of the angle factors methodology to calculate the  $t_r$ . Basics of the approach were presented by the authors in [7] with an initial validation to demonstrate its feasibility. The final system was presented with the description of the methodology and validation in a real office in [8] and [9]. In [10] a specific application of the system in AAL was illustrated. The complete description of the calibration procedure of the IR sensor was presented in [11].

This paper presents shortly the system and the calibration of the IR sensor to achieve the measuring performance required to allow its deployment. Then, the validation in a real classroom based on the comparison with a microclimate station and the subjective investigation about the thermal environment is for the first time illustrated to demonstrate the reliability of the solution proposed in a practical case currently of large interest. In fact, several studies concerning the methodology to assess the thermal comfort in public buildings are present in literature, such as sports and leisure facilities in [12], or, specifically for the classroom environment, in [13] [14]. The problem of how to accurately measure the thermal comfort in classrooms is thus a field of investigation where the solution proposed can address the issue of overcoming the traditional measurements performed with a thermostat or a temperature probe in the return air duct of the ventilation system.

The measurement system is now patent pending [15].

## 2. Assessment of the thermal comfort

### 2.1. Comfort model

According to ISO 7730 [2] "a human being's thermal sensation is mainly related to the thermal balance of his or her body as a whole. This balance is influenced by physical activity and clothing, as well as the environmental parameters: air temperature, mean radiant temperature, air velocity and air humidity". In a moderate environment, the human thermoregulatory system will automatically attempt to modify skin temperature and sweat secretion to maintain the heat balance. As the definition given in ISO 7730 implies, thermal comfort is a subjective sensation and it can be expressed with a mathematical model of PMV which is function of four environment parameters and two personal ones:

$$PMV = f(t_a, t_r, v_a, RH, I_{cl}, M) \quad Eq. 1$$

where  $t_a$  [°C] is the room air temperature,  $t_r$  [°C] is the mean radiant temperature,  $v_a$  [m/s] is the air velocity,  $RH$  [%] is the relative humidity,  $I_{cl}$  [m²K/W] is the clothing insulation and  $M$  [W/m²] is the metabolic rate. The PMV index predicts the mean value of the votes of a large group of persons with a 7-point thermal sensation scale (from -3, cold, to +3, hot) exposed to the same environment. The equation comes from the heat balance between the human body and the environment. The PPD (Percentage of People Dissatisfied) index is used to provide information on the thermal discomfort or thermal dissatisfaction predicting the percentage of people likely to feel too warm or too cool in a given environment. The PPD is calculated as function of the PMV:

$$PPD = 100 - 95 \cdot e^{-(0.03353PMV^4 + 0.2179PMV^2)} \quad Eq. 2$$

An environment is considered as very comfortable when the PMV varies between -0.5 and +0.5. It is considered as comfortable for values between -1.0 and +1.0. These cases lead to a PPD of 10% and 27% for  $-0.5 < PMV < +0.5$  and  $-1.0 < PMV < +1.0$  respectively. When PMV is zero, that is to say for the perfect case, the PPD is 5%.

### 2.2. Standardised measurement procedure

The measurement of comfort indexes is generally performed with a microclimate station. The station includes the probes needed to acquire the ambient parameters and a data logger. Then, a software provides the capability to apply the personal parameters and calculate the comfort

index in post-processing. This procedure is used for short period monitoring and not for real-time, continuous monitoring. The station used for this study is the "HD32.1". PMV and PPD indexes are calculated with DeltaLog 10 software. The metrological characteristics of the probes used are recapped in the Table 1. These characteristics can be considered representative of the standard measuring performances for standard comfort assessment according to the ISO 7726 [5].

**Table 1: Measurement characteristics of the microclimate station**

	Sensor	Range	Uncertainty
$t_a$	Pt100	-30°C + 100°C	± 0.1°C
$t_r$	Globe thermometer	-30°C + 120°C	± 0.2°C
$v_a$	Omni directional hot wire	0.05 - 5m/s	± 0.02m/s (0.05-1m/s) ± 0.1m/s (1-5m/s)
$RH$	Capacity	5 - 98 %	± 2.5

### 2.3. Subjective investigation

The subjective approach has the aim of investigating the perception of the thermal environment by means of judgment, preference and acceptability through surveys of the users. This was performed using questionnaires, that users were called to compile, elaborated from the model provided by ISO 10551 [16]. This method allows from one side the investigation of the occupants perception and from the other side to assess the capability of the measuring system to evaluate the comfort level and the typical constraints to apply a certain measurement methodology. An example of the subjective investigation is reported in [17].

There are a number of subjective judgment scales for thermal environments, which differ in whether emphasis is placed on some aspects of judgment: perceptual or affective (evaluative and preferential), global or localized, present or past, instantaneous or extended over a period of time. The survey drafted and used for this validation is shown in Fig. 1. The occupants were asked to provide general information (age, sex, kind of activity performed and clothing level), mark their position in the classroom and then indicate their thermal perception (point 6), thermal preference (point 7) and affective assessment (point 8).

The analysis of the thermal perception votes was performed according to standard [16]. It asserts that the only study devoted to the statistical characteristic of data distributions concerns those

obtained by applying the 7-degree scale, from -3 to +3. Degrees other than the two extreme ones are physiologically located at equivalent distances and may thus be treated as continuous data whose differences are defined numerically (interval scale); they approximate normal distributions, so it is quite legitimate to calculate the mean and standard deviation.

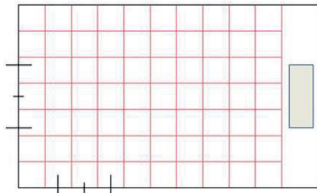
The degrees on the scales of perception proposed (thermal preference and affective assessment) are ranked as classes of observable data that correspond to a totally ordered finite mathematical set (ordinal data or scales). Therefore, the appropriate statistical tests of the null hypothesis are of the nonparametric type (e.g. sign test, median test or certain types of variance analysis).

The analysis presented in this paper focuses on the comparison between the thermal sensation and the PMV measured. Thus, the thermal preference and affective assessment are not considered for the comparison.

#### Survey on thermal environment – OCCUPANT

1. Age:
2. Sex: <input type="checkbox"/> M <input type="checkbox"/> F
3. Date:
4. Level of activity performed:
5. Clothes within the test (mark the most appropriate solution)
<input type="checkbox"/> Underwear, socks, tracksuit, t-shirt, shoes
<input type="checkbox"/> Underwear, shirt, trousers, socks, shoes
<input type="checkbox"/> Underwear, shirt, trousers, smock, socks, shoes
<input type="checkbox"/> Underwear, shirt, trousers, jacket, socks, shoes
<input type="checkbox"/> Underwear with long sleeves and legs, shirt, trousers, V-neck sweater, jacket, socks, shoes
<input type="checkbox"/> Other .....

#### Mark your position in the room



#### 6. How do you feel at the precise moment (mark appropriate box):

	Very hot	Hot	Warm	Slightly warm	Neither hot nor cold	Slightly cool	Cool	Cold	Very cold
Begin of lesson									
Break									
End of lesson									

#### 7. At this moment, would you prefer to be ... ?

	Much warmer	Warmer	Slightly warmer	Without change	Slightly cooler	Cooler	Much cooler
Begin of lesson							
Break							
End of lesson							

#### 8. At this moment, do you find this ...?

	Perfectly bearable	Slightly difficult to bear	Fairly difficult to bear	Unbearable
Begin of lesson				
Break				
End of lesson				

Fig. 1: Survey used to assess the thermal comfort by subjective judgements

## 3. System description and methodology

### 3.1. Methodology applied

The solution proposed is designed to provide the performances of a microclimate station, but in a manner suitable for the continuous real-time monitoring and for multiple positions. Fig. 2 represents the concept of the system. For this reason, the system is built with low cost components to measure all the needed ambient parameters. The capability to measure mean radiant temperatures with a spatial discretization and with a single sensor represents the main advance of the system. The specific design and calibration for this scope allows the employment of such solution in the field of the thermal comfort assessment.

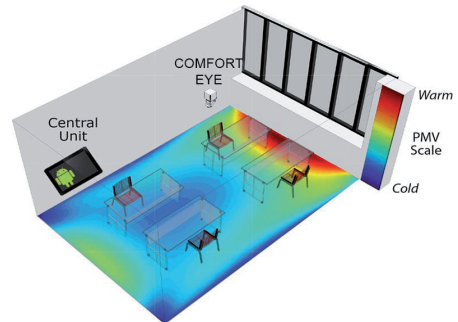


Fig. 2: Concept of the IR scanning system

The whole procedure to configure, control and acquire data is managed by a control unit. It is composed of a commercial board (Arduino Mega) and all the electronics needed for sensors integration and wired/wireless communication (i.e. Bluetooth for interaction with Android devices through a dedicated GUI). The inputs required to perform the algorithms embedded can be stored directly into the microcontroller EEPROM memory, or updated by the user and/or the technician.

The user can interact with the system through the terminal with the user interface implemented (PC or Android device) and is asked to provide the inputs required for the calculation of thermal comfort index (room geometry, subject positions and their personal parameters, metabolic activity and clothing thermal insulation). The microcontroller manages the automatic scanning of all the surfaces of the room, provides the needed measurements through integrated sensors and formulas implemented into the embedded C++ libraries and then sends the results back to



the device for the real-time monitoring and post-processing.

Next paragraphs describe in details the components used and the methodology applied to address the specific measurement requirements. Further details can be found in [11].

### 3.2. The IR scanning system

The concept relies on an IR scanning system to install on the ceiling of the room, that measures the indoor surface temperatures, and sends them to the control unit to calculate the mean radiant temperature  $t_r$  and PMV for several locations inside the room. The mean radiant temperature is derived for multiple positions of the subject inside the room according to the angle factors algorithm, as presented in the ISO 7726 [5]. The  $t_r$  is computed from the weighted average of the internal surface temperatures  $t_i$  and the respective view factor in relation to a subject,  $F_{s-i}$ , for  $N$  surfaces:

$$t_r^4 = \sum_{i=1}^N F_{s-i} T_i^4 \quad Eq. 3$$

A mathematical expression developed by Cannistraro et al. [18] was used to calculate the view factors between a subject and internal surfaces. This approach, turned into an algorithm, automatically computes the coefficients differentiating the kind of surface considered (vertical or horizontal).

The procedure to measure  $t_r$  requires the measurement of all the indoor surfaces temperature. Therefore, the core of the device consists of an array of thermopiles for non-contact IR temperature measurement and two servos to manage the orientation of the sensor ( $0^\circ$ - $180^\circ$  in both directions), as shown in Fig. 3. This device, installed on the ceiling of the room and possibly in the center, allows the continuous measurement of the indoor surface temperatures. Depending on the Field of View (FOV) of the sensor ( $5.12^\circ$  by  $6^\circ$  for each pixels in the row), an embedded algorithm was implemented into the microcontroller to manipulate the temperatures measured ( $T_{1(h,v)}, T_{2(h,v)}, \dots, T_{6(h,v)}$ ), where  $h$  and  $v$  represent the horizontal and vertical orientation of the sensor during the acquisition. The application of this algorithm provides low-resolution thermal images as output for each surface. The IR sensor is a commercial solution (array of eight thermopiles arranged in a row, built in electronics and a silicon lens), which provides a temperature measurement of eight consecutive points with a resolution of  $1^\circ\text{C}$  each. A methodology to correct the surface temperature, based on its emissivity

and environmental factors, is applied as part of the complete measurement process, as discussed above.

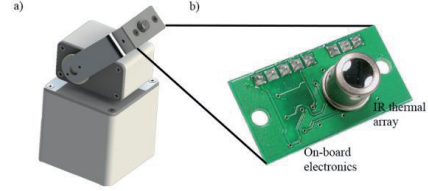


**Fig. 3: IR scanning system. a) Assembled device (IR sensor + servos); b) Detail of the thermopile array adopted**

The issue of correcting the infrared emissivity is addressed to reduce the measurement uncertainty. In fact, an on-board correction of the IR raw measurement is implemented by means of the following equation:

$$T_{obj}^4 = \frac{1}{\varepsilon\tau} T_{tot}^4 - \frac{1-\varepsilon}{\varepsilon} T_{refl}^4 - \frac{1-\tau}{\varepsilon\tau} T_{atm}^4 \quad Eq. 4$$

where  $\varepsilon$  is the surface average emissivity,  $\tau$  is the transmission coefficient of the atmosphere (assumed as a constant value of 0.99),  $T_{tot}$  is the total temperature (raw value) measured by the IR sensor,  $T_{refl}$  is the reflected temperature and  $T_{atm}$  is the temperature of the atmosphere (equals to indoor air temperature). The average emissivity of the surface has to be provided as input of the algorithm, while the reflected temperature is computed directly measuring the temperature of the opposite surface with an emissivity set to 1. Given that the IR sensor is installed on the ceiling, its inclination angle could affect the accuracy of the measuring procedure. However, the maximum angle of incidence of the IR ray is generally equal to  $25^\circ$ : according to the polar diagrams of the infrared emissivity of the material in consideration, as in [19], the emissivity can be assumed to be constant within certain limit values of the incidence angle. In any case, this effect was considered and assessed during the calibration procedure (paragraph 4).

### 3.3. Environmental sensors

The evaluation of PMV requires the measurement of air temperature, relative humidity and air velocity according to ISO 7726; for this reason, commercial low-cost solutions are adopted for the scope.

An integrated T/RH sensor allows the single-point measurement of the air temperature ( $t_a$ ) and relative humidity ( $RH$ ) parameters. It is based on DS18B20 1-Wire digital thermometer to measure the temperature and polymer humidity capacitor for  $RH$  and they are both connected to an 8-bit



single chip computer. The output is a calibrated digital signal that derives from a previous calibration and coefficients saved in the OTP memory.

A low-cost flow sensor (IST FS5), based on the thermal conductometric principle, has been adopted for single-point air velocity measurement. The sensor includes two platinum resistors in a chip and can be used as a constant temperature anemometer (CTA) through an electric circuit provided by the sensor manufacturer. An ad-hoc PCB was developed and integrated in the control unit to derive the air velocity, as a function of the bridge voltage measured by means of a 12-bit A/D Converter. The calibration curve has been found by means of a calibration conducted in the UNIVPM laboratory, with a reference anemometer (probe AP3203 of HD32.1 microclimate station). After calibration, the sensor presents an accuracy of  $\pm 0.06$  m/s in a range of  $0 \div 1$  m/s.

#### 4. IR system calibration

The IR system was calibrated and validated with experiments conducted in a test chamber [11]. The test room is a climatic chamber with two black-painted surfaces, which can be heated or cooled. Surface temperatures, together with environmental parameters, can be set according to the operative ranges. Four k-type thermocouples were placed on one of the heated surfaces (Fig. 4 a) and were used to calibrate the IR system.

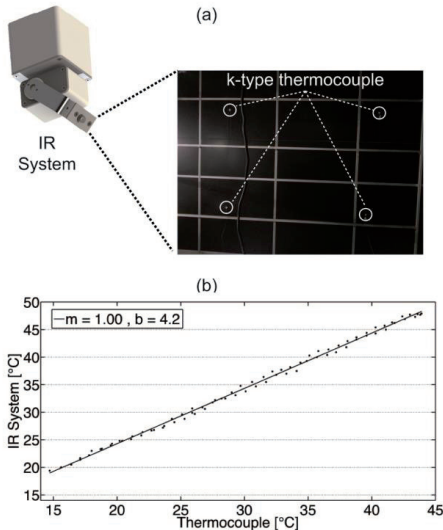


Fig. 4: Test chamber setup (a) and calibration curve of the IR system (b)

Depending on the FOV (Field Of View) of the IR sensor and its position within the test conducted, a matrix of  $5 \times 8$  samples was provided as final output for each acquisition, where each point is the IR temperature measurement in an area of  $20 \times 24$  cm. The calibration was performed comparing the values measured by the thermocouples with the mean value of four ROIs (region of interest). In particular, those four ROIs were identified, where the thermocouples were placed and the analysis was conducted for the average values of the ROIs. A previous analysis was conducted to determine the emissivity of the surface, which turned out to be 0.89. A test of 7 hours was conducted when the surface was heated up and cooled down, covering a range of  $15^\circ\text{C}$ - $45^\circ\text{C}$  which is typical of indoor environments.

The calibration (Fig. 4 b) revealed a sensitivity of 1.0, an offset of  $4.2^\circ\text{C}$  and an uncertainty of  $\pm 0.9^\circ\text{C}$  (coverage factor  $k=2$ ).

The calibration results were used to assess the overall measurement approach to derive the mean radiant temperature inside the test room. Two surfaces, S1 and S2, were heated and cooled following predefined profiles in order to simulate a real case situation, for example, the solar radiation that heats a wall exposed to the exterior. During the test, the IR sensor scanned all the six surfaces and the other sensors acquired the ambient parameters. Therefore, the real working operation was simulated in the controlled environment.

Table 2: Measurement of surfaces temperature: comparison with the reference

Parameter	IR system	
	Mean [°C]	STD [°C]
T (front surface) (S1)	-0.1	$\pm 0.8$
T (rear surface)	0.3	$\pm 0.4$
T (left surface)	-0.1	$\pm 0.9$
T (right surface) (S2)	0.1	$\pm 1.8$
T (floor)	0.1	$\pm 0.6$
T (ceiling)	-0.5	$\pm 0.4$

The measurement performance is recapped in Table 2. Using those temperatures the  $t_r$  was calculated and compared to the one measured at the same time with the globe-thermometer of the microclimate station.

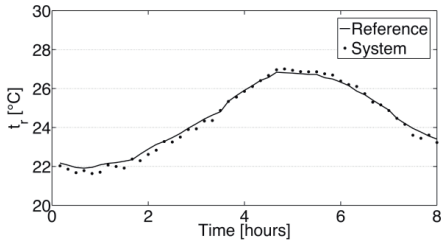


Fig. 5: IR system vs globe-thermometer during the test.

The metrological performances turned out to provide an average deviation of  $\pm 0.5^{\circ}\text{C}$  ( $k=2$ ) on the  $t_r$  with respect to the globe thermometer. This result confirms the capability of the solution proposed given that the ISO 7726 calls for a required accuracy of  $\pm 2^{\circ}\text{C}$  and a desirable accuracy of  $\pm 0.2^{\circ}\text{C}$ .

## 5. Validation in a classroom

Given the calibration results, the system has been tested in a real case to validate its functionality. The validation procedure consisted of a comparison with the microclimate station and the subjective investigation. The test was performed in a classroom at UNIVPM (10x9.2x3.4 m) during a regular lesson. The students attending the lesson were asked to compile an ad-hoc survey to express their thermal sensation and preference. The IR system was placed on the ceiling of the classroom, nearly in the centre and the control unit, with the other environmental sensors, positioned in a desk to provide the acquisition of the ambient parameters and data storing for post-processing. Data were compared to that monitored by HD32.1 microclimate station in two different positions, as shown in Fig. 6. Statistical analysis were carried out following guidelines provided by [16].

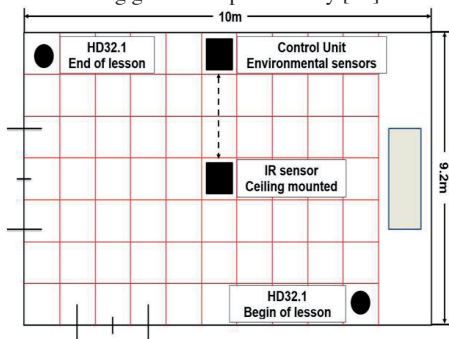


Fig. 6: Scheme of the microclimate station HD32.1 and the proposed solution during the validation in a classroom

### 5.1. Comparison with the reference system

The comparison of thermal comfort parameters retrieved from both the IR system and the microclimate station revealed discrepancies of  $\pm 0.5^{\circ}\text{C}$  for the mean radiant temperature and  $\pm 0.1$  for the PMV. Next two figures show the comparison between the IR system and the microclimate station.

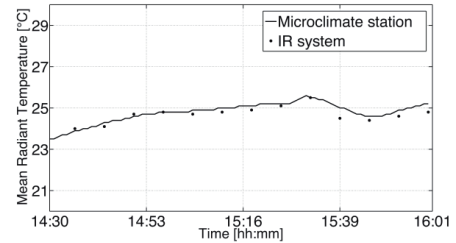


Fig. 7: Mean radiant temperature measured by the IR system compared with the reference measurement

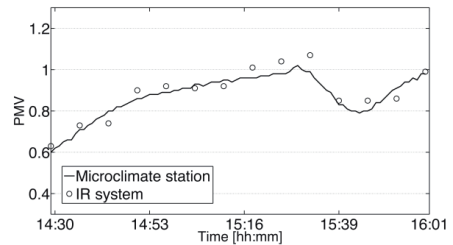


Fig. 8: PMV measured by the IR system compared with the reference measurement

The capability of the system to provide a spatial discretization is also assessed with the two graphs above. In fact, the curves compare from 14:30 to 15:16 the PMV estimated by the IR system in the position of the microclimate station at the beginning of the lesson (see Fig. 6) while from 15:16 to 16:01 in the position at the end of the lesson.

### 5.2. Comparison with subjective evaluation

During the lesson a total number of 40 students were analyzed (14 males and 26 females), with an average age of  $21 \pm 3$  years, a metabolic rate of 1.2 met (sedentary activity level) and a clothing level of  $1.2 \pm 0.3$  clo. Data related to thermal perception assessment are shown in Fig. 9. In all the cases people perceived a sensation of slight discomfort (average PMV of  $0.9 \pm 1.0$ ): the significance of the difference between observed values  $\bar{Y}$  to the neutrality level  $\bar{Y} = 0$  was verified by statistical

inference ( $t$  test for  $n < 60$ ). Results for all the cases are summarized in Table 3.

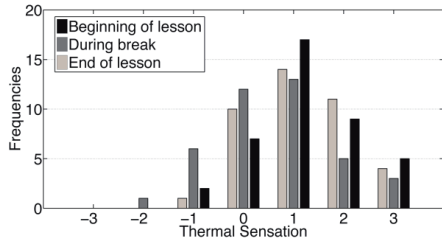


**Fig. 9: Thermal perception at beginning of the lesson, during the break and at the end of the lesson**

**Table 3: Statistics of thermal perception analysis**

Parameter	Begin of the lesson	Break	End of lesson
Mean	1.1	0.6	0.9
Standard deviation (K=2)	0.9	1.1	0.9
tn-1	7.7	3.4	6.3
p-value	< 0.0005	0.005 < p < 0.0005	< 0.0005

$p$ -values were under the admissible error threshold (0.05) in all the cases, so the slight discomfort perceived was statistically significant. The thermal sensation perceived was then compared to values provided by the monitoring systems as showed in Fig. 10. Confidence intervals were computed and compared to validate the comfort measurement system with respect to the subjective perception. As shown in Fig. 10, the subjective assessment revealed a higher discomfort level perceived with respect to that provided by both the measurement systems, but the differences were not statistically significant. This demonstrated that comfort measurements are comparable with the thermal perception. The IR system can provide information about indoor thermal comfort that is in agreement with persons perceived sensation. Fig. 11 shows the comparison in terms of PPD (Percentage of People Dissatisfied) index, which was computed by both measuring systems.

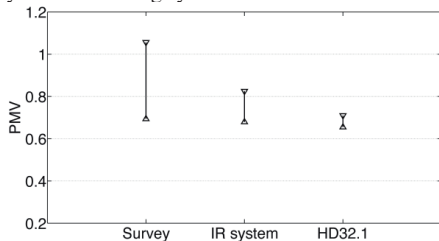


**Fig. 10: Comparison of the thermal sensation measured with the IR system, microclimate station and subjective survey**

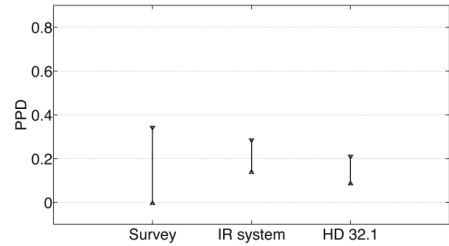


**Fig. 11: Comparison of the percentage of dissatisfied measured with the IR system, microclimate station and subjective survey**

## 6. Conclusions

The results show that the system proposed is able to provide the real-time measurement of surfaces temperature with enough accuracy to be employed for the methodology given by ISO7726. The system provides spatial information of the surface to measure the average surface temperature with an uncertainty of  $\pm 0.9^\circ\text{C}$  ( $k=2$ ) and derive the mean radiant temperature. In fact, the validation showed an uncertainty of  $\pm 0.5^\circ\text{C}$  ( $k=2$ ) on the  $t_r$  and the consequent uncertainty of  $\pm 0.1$  ( $k=2$ ) on the PMV with respect to commercial solutions (microclimate station). The uncertainty of the  $t_r$  obtained with the IR system is inside the accuracy required by the ISO 7726. The application in a classroom, which is a space larger than a typical office room, proved the capability of the system to provide a spatial information. In fact, the comparison with the microclimate station showed the same correspondence in two different positions. This is an important achievement given the relevance of the real-time monitoring of thermal comfort in schools. Moreover, the comparison with the subjective investigation proved the capability of the system to assess the thermal sensation of the occupants. The measurement system revealed and quantified the thermal discomfort perceived during the lesson with a degree comparable with the subjective sensation.

Thus, the solution proposed can be employed for the real-time and spatial monitoring to enhance the control of indoor environments.

## Acknowledgement

This work is co-funded by the European Commission within the FP7 European Project CETIEB (Cost – Effective Tools for Better Indoor Environment in Retrofitted Energy Efficient Buildings), Grant agreement no: 285623.

## Bibliografia

- [1] Fanger P.O., "Thermal comfort". Danish Technical Press, Copenhagen, 1970.
- [2] ISO, "7730. 2005. Ergonomics of the thermal environment - Analytical determination and interpretation of thermal comfort using calculation of the PMV and PPD indices and local thermal comfort criteria". International Standardization Organization, Geneva, 2005.
- [3] Alfano F.R., Dell'Isola M., Palella B.I., Riccio G., Russi A. "On the measurement of the mean radiant temperature and its influence on the indoor thermal environment assessment". *Building and Environment*, vol. 63, pagg. 79–88, 2013.
- [4] Atmaca I, Kaynakli O, Ygit A. "Effects of radiant temperature on thermal comfort". *Building and Environment*, vol. 42, pagg. 3210-20, 2007.
- [5] ISO, "7726. 2002. Ergonomics of the thermal environment - instruments for measuring physical quantities". International Standardization Organization, Geneva (Switzerland), 2002.
- [6] Mola S., Malvicino C. "System for controlling an air-conditioning system within an environment, in particular passenger compartment of a vehicle". US00793 1209B2, 2011.
- [7] Revel G.M., Sabbatini E., Arnesano M. "Development and experimental evaluation of a thermography measurement system for real-time monitoring of comfort and heat rate exchange in the built environment". *Measurement Science and Technology*, vol. 23(035005), 2012.
- [8] Revel G.M., Arnesano M., Pietroni F. "An Innovative Low Cost IR System for Real-Time Measurement of Human Thermal Comfort". *Proceedings of IAQ2013 conference, Vancouver (Canada)*, 2013.
- [9] Revel G.M., Arnesano M., Pietroni F. "Development and validation of a low-cost infrared measurement system for real-time monitoring of indoor thermal comfort". *Measurement Science and Technology*, vol. 25(085101), 2014.
- [10] Revel G.M., Arnesano M., Pietroni F. "A low-cost sensor for real-time monitoring of indoor thermal comfort for ambient assisted living". *Ambient Assisted Living - Italian Forum 2013* (Switzerland: Springer International Publishing).
- [11] Revel G.M., Arnesano M., Pietroni F., Schmidt M., Kaschtschejewa O. "Evaluation in a controlled environment of a low-cost IR sensor for indoor thermal comfort measurement". *Proceedings of QIRT2014 conference, Bordeaux (France)*, 2014.
- [12] Revel G.M., Arnesano M. "Measuring overall thermal comfort to balance energy use in sports facilities". *Measurement*, vol. 55, pagg. 382–393, 2014.
- [13] Alfano F.R., Ianniello M., Palella B.I. "PMV-PPD and acceptability in naturally ventilated schools". *Building and Environment*, vol. 67, pagg. 129–137, 2013.
- [14] Corgnati S.P., Ansal di R., Filippi M. "Thermal comfort in Italian classrooms under free running conditions during mid seasons: Assessment through objective and subjective approaches". *Building and Environment*, vol. 44, pagg. 785–792, 2009.
- [15] Revel G.M., Arnesano M., Pietroni F. "Sistema e metodo per il monitoraggio del comfort termico". MO2013A000279, 2013.
- [16] ISO, "10551. 2001. Ergonomics of the thermal environment – Assessment on the influence of the thermal environment using subjective judgement scales". International Standardization Organization, Geneva, 2005.
- [17] Revel G.M., Arnesano M. "Perception of the thermal environment in sports facilities through subjective approach". *Building and Environment*, vol. 77, pagg. 12–19, 2014.
- [18] Cannistraro G., Franzitta G., Giaconia C., Rizzo G. "Algorithms for the calculation of the view factors between human body and rectangular surfaces in arallelepid environments". *Energy and Buildings*, vol. 19, pagg. 51–57, 1992.
- [19] Maldague X.P.V., "Theory and Practice of Infrared Technology for Nondestructive Testing". Wiley-Interscience. 0471181900, 2001.

# ***Laser Ultrasonics for Train Wheel and Axle Diagnostics***

A. Cavuto\*, M. Martarelli\*\*, G. Pandarese \*, G.M. Revel\*, E.P. Tomasini\*

\* Università Politecnica delle Marche, Via Brecce Bianche, Ancona

\*\* Università degli Studi e-Campus, Via Isimbardi, Novedrate (CO)

## **Abstract**

*The present paper demonstrates the applicability of a laser-ultrasonics procedure to improve performances of train components ultrasonic inspection. The method, previously developed by the authors, exploits an air-coupled ultrasonic probe which detects ultrasonic waves generated by a high-energy pulsed laser. As a result the measurement chain is completely non-contact from the generation up to the detection, this letting speed up the inspection time and make the set-up more flexible. In this paper the technique developed has been applied to train component diagnostics, and specifically to wheels and high speed train hollow axles with variable section. In addition a sensitivity analysis to the surface conditions has been performed.*

## **1. Introduction**

Inspection of train components is a very important procedure which has to be periodically performed by train operators. Currently periodic inspection of axles and wheels is carried out by ultrasonic techniques using, for example, phased arrays [1] or in particular for hollow axle diagnostics a number of rotating contact probes or a bore probes [2].

Ultrasonic techniques, which are a long established method, have the disadvantage of requiring the probes to be in contact with the object to be investigated, which lengthens the inspection time necessary to prepare the object and apply the coupling medium. However, the typical problems of conventional techniques can be overcome by using a hybrid laser-ultrasonic system based on the detection of ultrasonic waves generated by a high-energy pulsed laser via air-coupled ultrasonic transducers [3, 4]. Air-coupled ultrasound inspection has already been successfully used in many industrial applications e.g. NDT on both thick [5] and thin [6] composites, NDT on light thin historical vaults

[7], density measurement of ceramic tiles [8], wood detection [9], and thin metallic laminated [10, 11].

The hybrid system proposed is completely non-invasive and it makes it possible to:

- overcome shape and accessibility problems,
- avoid the application of the coupling medium,
- shorten the inspection time for large surfaces.

Laser-ultrasonics has been applied in the aeronautical field for damage detection on thick composite materials [12] and honeycombs [13] and in the railway field for rail [14], rail wheels [15] and axle inspection [16]. Gonzales et al. [16] presented a Laser Air-Hybrid Ultrasonic Technique based on air coupled ultrasounds. The limits of the technique are that it is working in ablative regime and it exploits Rayleigh waves reflected by the crack. The necessity of working in ablative regime compromises the surface integrity and does not allow considering the technique as non-destructive. The use of Rayleigh wave reflection makes extremely difficult to work with complex geometry, as hollow axles with several section variations. In fact, the reflections due to the geometry can overlap with the one induced by the crack and thus the desired signal can be buried into the noise. The present paper shows the experimental application of laser ultrasonics to the inspection of a real high speed train axle and wheels provided by the Italian railway company (Trenitalia), where typical fatigue defects for the axle [17] and dominant wheel failure cracks for the wheels [18] have been expressly created according to defects occurring in real wheelset [19].

For the axles, it has been proved by the authors [20] that the technique can be applied also when the distance between laser source and ultrasound probe exceeds 200 mm. Consequently it is possible to apply it for the diagnostics of flaws located in the fretting surface by locating the laser source and the ultrasound probe at the opposite sides of the wheel press fitted area.

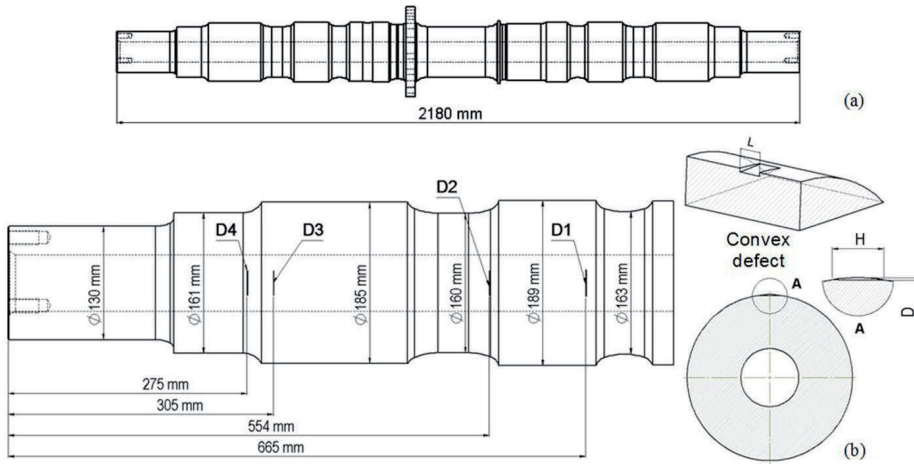


Fig. 1: Test item (a) and defect positions (b)

In [21] a model-assisted Probability of Detection curve has been derived for this technique, thus allowing to define the method reliability.

Here the attention is focused for the first time on the wheels, for which several configurations of the laser ultrasonics probes have been tested and two significant ones are reported. In the first configuration the ultrasound probe is located in the thread and works in transmission. In the second configuration, the harshest one, the laser source and the ultrasound probe are settled on the opposite sides of the wheel, thus allowing to detect the defect presence in the complete wheel profile.

The paper is structured in three Sections. Section 2 presents a feasibility study on a train hollow axle with section variation. Section 3 describes the application to the wheel test case. Finally a sensitivity analysis to the surface test item has been performed and its results illustrated in Section 4.

## 2. Experimental results on train axle

The application to a real train axle (Fig. 1a) where typical fatigue defects have been realized will be shown and results discussed. In practice four convex defects were machined on the external surface, see Fig. 1b, two of them in the wheel fitting area (D1 and D3) and the other two in the section transition (D2 and D4). The defect morphology is reported in Table 1.

In this paper only results corresponding to the D4 defect will be reported which is the most critical case it being located in the transition after

the wheel fitting area. For a complete analysis the reader can refer to [20].

Table 1 Defect morphology.

Defects	Size of defect		
	H (mm)	L (mm)	D Max depth (mm)
D1	31	1.1	1
D2	28	1.1	1
D3	28	1.1	1
D4	28	1.1	1

### 2.1 Test bench

The train axle was mounted on a support that made it possible to control its rotation, in order to be able to scan the axle surface along a circumference. The probes were installed on a frame where they could move along the axial direction. Therefore the complete lateral surface of the axle could be inspected by the laser ultrasonic system, see Fig. 2.

The laser ultrasonic system was made up of a pulsed laser source, a Nd-Yag IR laser (1064 nm), pulses of 12 ns duration and 82 mJ energy, from Continuum, and a 1 MHz air-coupled ultrasound piezoelectric probe from Ultrat Group (model NCT210, with 8 mm diameter of active area).

The ultrasound probe conditioning system was a DPR 300 Pulser/Receiver from JSR Ultrasonics.

The ultrasound signals were amplified with a gain level of 69 dB and acquired with a high speed Digitizer board NI PXI-5122 (100 MHz bandwidth). The laser beam was guided towards the axle under test by means of an arm connected to the pulsed laser cavity as shown in Fig. 2.



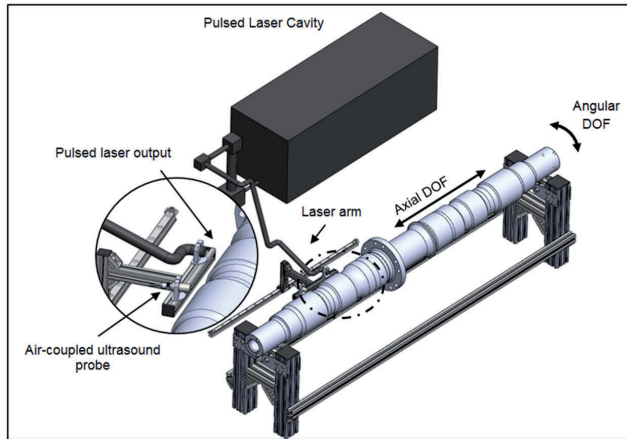


Fig. 2: Scheme of the laser-ultrasonic scanning system

The laser ultrasonics system was installed with the laser source and receiving probe far apart, in order to point outside the wheel fitting surface.

A collimated laser beam with a diameter of about 8.5 mm was used to keep the ultrasonic waves generation within a thermo-elastic regime. The air coupled ultrasound probe was inclined, with respect to the axle surface normal, of 8 deg in accordance to the Snell's Law. This inclination was optimized for the reception of surface Rayleigh waves, that are the most efficient for surface defect identification [20], in particular in case of complex geometry objects. The axle was made to rotate by an electric motor and the rotation angle measured by an integrated encoder. A circumferential scan has been performed along an angle of 93 deg with an angular resolution of 1.5 deg.

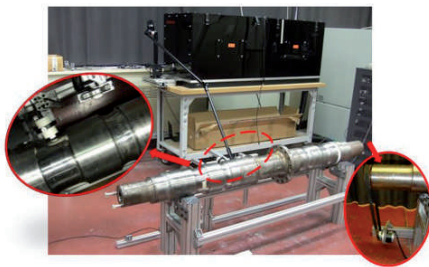


Fig. 3: The laser-ultrasonic scanning system

## 2.2 Analysis of results

For each configuration, a series of ultrasound time histories with a duration of 500  $\mu$ s was acquired at every scanning position along the arc considered.

The experimental set-up (i.e. laser and probe positions), the axle section tested and the defect location (D4) are shown in Fig. 4a. The time history acquired in the first scanning position and the B-scan, i.e. the waterfall plot collecting the time histories recorded at the different angular position on the axle circumference, are plotted in Fig. 4b and c, respectively. Both the time history and the B-scan evidence the Rayleigh wave arrival time at about 87  $\mu$ s. However, other waves are visible in the waveform which are reflections of longitudinal and shear waves due to the geometry complexity (section transitions). The B-scan close-up around the Rayleigh wave time of arrival is shown in Fig. 4d, evidencing the presence of the defect, which produces a strong attenuation of the Rayleigh wave itself.

The RMS plot over the time axis (abscissa) of the B-scan is shown in Fig. 5. This plot was normalized against the maximum RMS value. The contrast between the RMS in the damaged and in the undamaged areas is 5.1 dB, which was calculated considering the minimum values of the RMS (in the damaged area) and the floor values RMS (in the undamaged area).

## 3. Experimental results on train wheel

The laser ultrasonic technique has been applied to a train wheel where Shattered Rim Cracks (SRC), e.g. subsurface cracks parallel to the tread surface, have been created. Such kind of defect is one of the dominant wheel failure types and is the result of large fatigue cracks that propagate roughly parallel to the wheel tread surface, at a depth of about 12–20 mm beneath the thread. In

practice, the defect was simulated with a 7 mm diameter flat-bottom hole generated perpendicular to the rim face, to a depth of 90 mm and with the axis at a distance of 10 mm from the inside diameter of the rim.

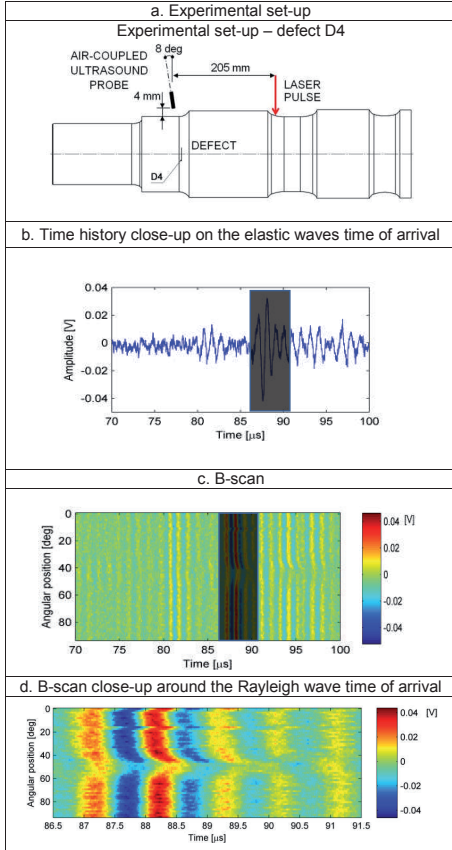


Fig. 4: Experimental set-up scheme (a), Time histories (b), B-scan (c) and (d)

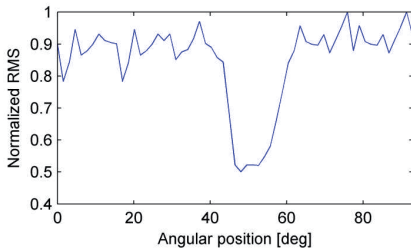


Fig. 5: Normalized RMS on D4 in function of the scanning angle

### 3.1 Test bench

The experimental set-up is shown in Fig. 6, for both the tested configurations. The pulsed laser for the ultrasound generation and the receiving probe were the same as the ones exploited for the train axle and described in Section 2.1.

The laser source was pointed on the outer edge of the wheel and the ultrasound probe was located on the thread, for the configuration C1, and on the inner edge, for the configuration C2, as shown in Fig. 6. In both configurations the system was working in transmission mode and the presence of the defect was detected from its interaction with the ultrasound bulk waves. The probe axis was tilted with respect to the surface normal of 6 deg. That angle was optimized for the detection of the transversal wave which resulted as the most efficient propagation wave in the wheel test case.

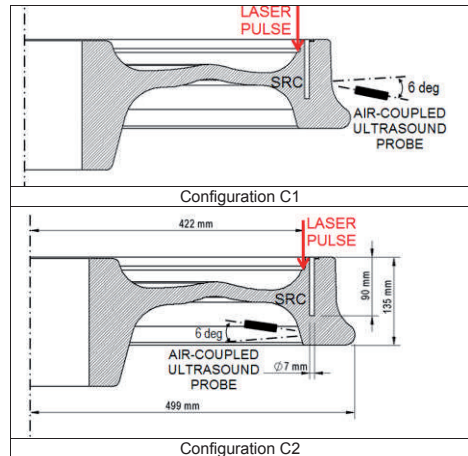


Fig. 6: Experimental set-up scheme for two measurement configurations

### 3.2 Analysis of results

The results obtained for the two configurations analyzed are reported hereafter. Fig. 7 shows the time history zoomed in the bulk waves time of arrival and the B-scan given in the same time span for configuration C1. The longitudinal and transversal wave time of arrival are 58 and 70 μs. The associated wave trains are visible in both the time history and the B-scan. Further propagation waves, related to reflection and scattering phenomena occurring in a complex geometry such as that of the wheel, are visible in the signal. The defect acts on the bulk waves as a strong attenuator due to the fact that the waves pass through a medium with different impedance.

The normalized RMS calculated over the time axis on a time window of 30  $\mu\text{s}$ , from 60 to 90  $\mu\text{s}$ , for all the angular positions is shown in Fig. 7c. The contrast between the RMS in the damaged and undamaged areas is 8.1 dB.

The results obtained in the configuration C2 are reported in Fig. 8 where the time history, the B-scan and the RMS plot are given. The defect is well evident in the B-scan and in the RMS plot, even though the attenuation is less (5.7 dB) than the one produced in the configuration C1 (8.1 dB). However, C2 would be a more suitable configuration for practical use.

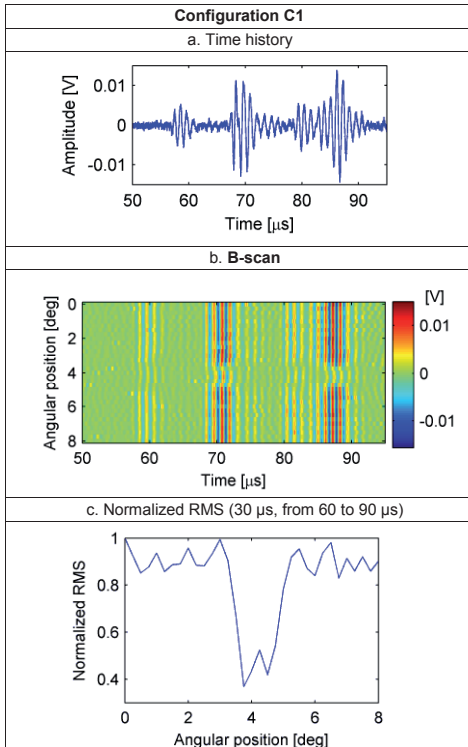


**Fig. 7: Ultrasound time history, B-scan close-up around the transversal wave time of arrival and RMS plot in function of the scanning angle – Configuration C1**

#### 4. Sensitivity analysis to surface conditions

When NDT methods based on laser ultrasonics are applied in field to working structures, the surface condition of the test item influences the diagnosis and it can produce false positive.

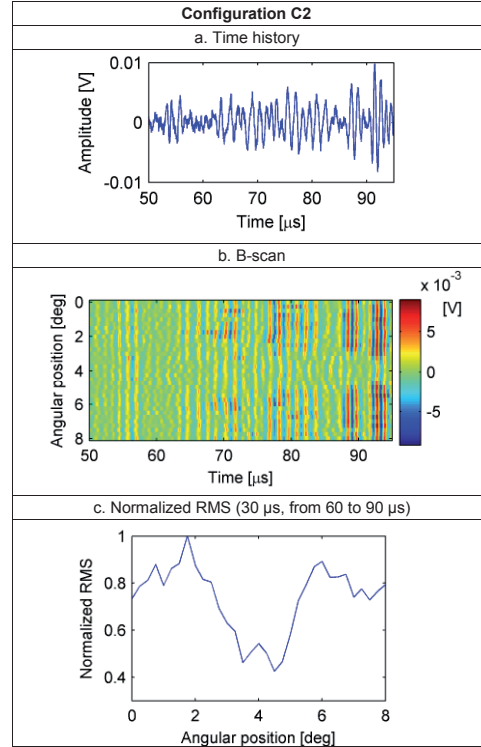


**Fig. 8: Ultrasound time history, B-scan close-up around the transversal wave time of arrival and RMS plot in function of the scanning angle – Configuration C2**

This may be particularly critical when Rayleigh wave propagation is exploited for damage detection, as it was done in the axle investigation reported in Section 2. In order to evaluate the interaction between the ultrasound propagation and the surface condition four different conditions have been considered:

- natural oxidized surface on the laser impinging area (thickness of about 35  $\mu\text{m}$ );
- areas with natural oxidation between the laser source and the receiving probe (extension of about 16 mm in the axial direction);
- painted surface on the laser impinging area (acrylic paint coating with thickness of about 45  $\mu\text{m}$ );
- painted areas between the laser source and the receiving probe (acrylic paint coating with extension of about 40 mm in the axial direction).

Those different configurations have been tested on the train axle described in Section 2 and the

experimental set-up is illustrated in Fig. 9a. The laser source and the receiving probe were installed at a distance of 136 mm. The ultrasound probe was fixed at a distance of 34 mm from the axle surface. The position of the laser source and the receiving probe were kept constant for all the configurations. The time histories recorded when the surface was clean, when the laser impinged on the painted surface and when painted areas were existing between the laser source and the probe are illustrated in Fig. 9b. It is evident the ultrasound is subject to an attenuation when the surface condition is not optimal. The attenuation of the RMS value is of 3.4 dB when the laser impinges on a painted surface and of 0.3 dB when the paint is in the surface path between the laser source and the probe.

Fig. 9c shows the time histories recorded when the surface was in good condition, when the laser was focused on an oxidized area and when the oxidation was present in between the laser source and the probe. The attenuation is evident again and it is of 4.6 dB when the laser interacts with the oxidized surface and 1.1 dB when the oxidation is in the path between the laser source and the probe.

The analysis brings to conclude the surface condition is an important parameter to design an optimal laser ultrasonics test, when considering the laser impinging area. On the other hand, the system is less sensitive to presence of oxidation or painted area in the propagation path.

## 5. Conclusions

The paper has shown the applicability of laser-ultrasonics, a non-destructive, non-contact technique, for the inspection of high speed train hollow axles and wheels. The main advantage of the proposed technique with respect to the state of the art is that it operates in thermo-elastic regime and therefore can be considered a non-destructive method. Furthermore, it is based on the fact that the defect produces an attenuation of the direct Rayleigh wave, when working in reflection mode, as for the axles, and of the bulk waves, mainly the transversal one, when working in transmission mode, as for the wheel. That effect, i.e. the attenuation of the propagating waves, can be therefore used as defect classification feature also with very complex geometry.

A convex defect typically generated by fatigue on the external surfaces of an axle has been investigated. Such crack has been identified by observing the Rayleigh wave propagation, it presenting an evident attenuation when passing

through the damaged area. The contrast between the undamaged area and the damaged one reached 6.5 dB and made it possible to identify the presence of the defect.

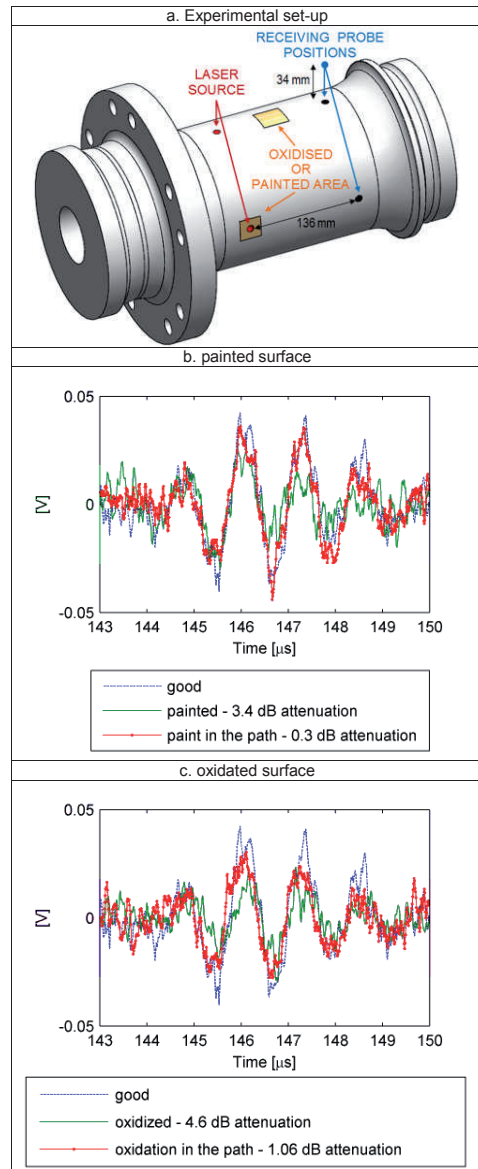


**Fig. 9: Experimental set-up scheme (a), Ultrasound time history for sensitivity analysis to the paint (b), Ultrasound time history for sensitivity analysis to the oxidation (c)**

On the wheel a Shattered Rim Crack has been created on purpose to reproduce typical subsurface defects that propagate roughly parallel to the wheel tread surface along the wheel tread. This defect acted as strong attenuator of the bulk waves and in particular of the transversal one, the technique working in thermo-elastic regime. The contrast between the damaged and undamaged area was between 5.7 and 8.1 dB depending on the laser ultrasonics configuration.

A sensitivity analysis to the surface condition has been also performed to consider the influence of oxidation and painting on the propagation of the Rayleigh wave and on the laser ultrasonics results. It has been shown that when the altered surface is located in the laser impinging area, the induced attenuation is relevant (3.4 dB for painted area, 4.6 dB for oxidized area) and can easily produce false positive in the diagnostic procedure.

### Acknowledgments

The authors wish to thank Trenitalia S.p.A. for their precious contributions and for providing of the train axle and wheel. The work has been partly funded by the National Ministry of the Instruction, University and Research within a National Project PRIN 2009PSJW8Z "Development of a laser-ultrasonics system for non-destructive testing aiming at improving railway safety".

### References

- [1] P N. Marty, "Latest Development in the UT inspection of train wheels and axles", *Proceedings of 18th World Conference on Nondestructive Testing*, 16-20 April 2012, Durban, South Africa.
- [2] S. Cantini, G. Patelli, S. Beretta, M. Carboni, Assessment of Safe Life Inspection Intervals for Forged Axles/Rotors: The Influence of In Service NDT Reliability (POD curve), *Proceedings of 7th European Congress of Joining Technology (Eurojoin7)*, (2009), Venice, Italy, CD-ROM (13 pages).
- [3] K. Gonzales, S. Kendarian, D. Carter, A Smith, R Morgan, "Non-contact interrogation of railroad axles using laser-based ultrasonic inspection", *Proceedings of JRC2005*, Pueblo, Colorado. DOI: 10.1109/RRCON.2005.186070.
- [4] S. Kenderian, D. Cerniglia, B. B. Djordjevic, G. Garcia, "Laser-air hybrid ultrasonic technique for dynamic railroad inspection applications", *Proceedings of 16th WCNDT 2004 - World Conference on NDT*, 2004, Montreal, Canada.
- [5] G.M. Revel, G. Pandarese, A. Cavuto, "Advanced ultrasonic non destructive testing for damage detection on thick and curved composite elements for constructions", *Journal of Sandwich structures and Material*, 15(1) (2013): 1-20, DOI 10.1177/1099636212456861.
- [6] P. Pietroni, G.M. Revel, "Non contact ultrasonic techniques for composite material diagnostics in aeronautics applications", *Proceedings of 9th European Conference on Non-Destructive Testing*, Berlin, 25-29 September 2006.
- [7] E. Quagliarini, G.M. Revel, S. Lenci, E. Seri, A. Cavuto, G. Pandarese, "Historical plasters on light thin vaults: State of conservation assessment by a Hybrid ultrasonic method", *Journal of Cultural Heritage*, 15 (2014) 104–111.
- [8] G.M. Revel, "Measurement of the apparent density of green ceramic tiles by a non-contact ultrasonic method", *Experimental Mechanics*, 47(5) (2007) 637-48.
- [9] M. R. Fleming, M. C. Bhardwaj, J. J. Janowiak, J.E. Shield, R. Roy, D.K. Agrawal, L. S. Bauer, D.L. Miller, K. Hoover, "Noncontact ultrasound detection of exotic insects in wood packing materials", *Forest Products Journal*, June 2005.
- [10] D.W. Schindel, "Air-coupled generation and detection of ultrasonic bulk waves in metals using micromachined capacitance transducers", *Ultrasonics* 35(2) (1997) 179-181.
- [11] W.M.D. Wright, D.A. Hutchins, "Air-coupled ultrasonic testing of metals using broadband pulses in through-

- transmission", *Ultrasonics* 37 (1999) 19–22.
- [12] Cerniglia, B.B. Djordjevic, V. Nigrelli, "Quantitative subsurface defect detection in composite materials using a non-contact ultrasonic system", *IEEE Ultrasonics Symposium*, (2001) 751-754.
- [13] C.Cosenza, D. Cerniglia, B.B. Djordjevic, "Non-contact ultrasonic inspection of skin/core bond in honeycomb with Lamb waves", *IEEE Ultrasonics Symposium*, Monaco (2002).
- [14] S. Kenderian, B.B. Djordjevic, Jr. R.E. Green, "Laser-based and air-coupled ultrasound as noncontact and remote techniques for testing railroad tracks", *Materials Evaluation* 60 (1) (2002) 65-70.
- [15] Kenderian, S., Djordjevic, B.B., Cerniglia, D., Garcia, G., "Dynamic railroad inspection using the laser-air hybrid ultrasonic technique", *Insight: Non-Destructive Testing and Condition Monitoring*, 48 (6) (2006), pp. 336-341.
- [16] K. Gonzales, S. Kendarian, D. Carter, A Smith, R Morgan, "Non-contact interrogation of railroad axles using laser-based ultrasonic inspection", *Proceedings of JRC2005*, Pueblo, Colorado.
- [17] M. Carboni, S. Cantini, "A new approach to the definition of "Probability of Detection" curves", *Proceedings of 10<sup>th</sup> European Conference on Non-Destructive Testing (ECNDT10)*, (2010), Moscow, Russia.
- [18] AAR Manual of Standards and Recommended Practices Wheels and Axles M-107/M-208.
- [19] Railway applications - In-service wheelset operation requirements - In-service and off-vehicle wheelset maintenance, in EN 15313.
- [20] A. Cavuto, M. Martarelli, G. Pandarese, G.M. Revel, E.P. Tomasini, "Experimental investigation by laser ultrasonics for high speed train axle diagnostics", *submitted to Ultrasonics*.
- [21] M. S. Malik, A. Cavuto, M. Martarelli, G. Pandarese, G. M. Revel, "Reliability Analysis of Laser Ultrasonics for Train Axle Diagnostics based on Model Assisted POD Curves", *Proceedings of 11th Int. Conference on Vibration Measurements by Laser and Noncontact Techniques & Short Course*, Ancona, Italy, 24 - 27 June 2014.



# Cross Correlation Method Enhancement for FBG Demodulation

Giuseppe Dinardo, Gaetano Vacca

Politecnico di Bari

## Abstract

*The purpose of the paper is to provide an analysis of the attitude exhibited by demodulation algorithms of Fiber Bragg Gratings (FBG) based on Cross Correlation methods. The Cross Correlation technique here considered is based on calculations performed in spectral domain. Its behavior against the peak-locking phenomenon has been analyzed and a way for attenuating it has been devised. The new Iterative Cross Correlation algorithm improves the FBG demodulation accuracy and precision, giving remarkably attenuated peak-locking amplitude.*

## 1. Introduction

The Fiber Bragg Gratings (FBGs) are optic fiber sensors used for local measurement of strain, temperature, and/or pressure. Its reflection spectrum exhibits a peak at the so-called Bragg wavelength, where the fiber shows the maximum reflectivity. When a FBG experiences a perturbation due to a measurand change, its reflection spectrum is subjected to a shift in the wavelength domain and a distortion.

An accurate and precise evaluation of such shift allows the calculation of the perturbing measurand changes.

Typically, a FBG spectrum is obtained by means of a static optical interrogator which is based on spectral reconstruction technique [2] [3] [5]. This type of configuration consists of a laser light source (characterized by a tunable wavelength), swept over the wavelength range (usually 1510 nm and 1590 nm), with a sampling resolution  $\Delta\lambda$ . This wavelength sampling resolution limits the FBG spectra peak tracking operation [4] [6].

The FBG spectrum is achieved once the synchronizazion between the back-reflected light and the swept laser source takes place.

Once the perturbed FBG spectra are acquired, a method for tracking the spectrum wavelength shift (which allows to determine the measurand change) is required. Typically such task is performed in the wavelength domain, and the spectrum wavelength shift is detected by means of a least-squares fit of the discretized spectrum in

such a way that an accurate and precise estimation of the Bragg wavelength shift occurring between two FBG spectra is achievable [6] [7] [10]. Such technique, among the others operating in the wavelength domain, are quite computationally efficient and lead to acceptable accuracies and precisions.

## 2. Cross Correlation Method (CC) for FBG demodulation based on spectral techniques

In this paper, a novel technique for FBG spectrum shift tracking based on Cross Correlation technique is devised.

There are several papers in the scientific literature dealing with and developing such tracking techniques [1] [8] [9].

The time consumption performance granted by the Cross Correlation method is comparable to the one of the standard methods operating in the wavelength domain and its strength is given by the remarkable performance in terms of accuracy and precision in the FBG wavelength shift detection [8].

In order to reduce the computational complexity characterizing such technique, the Cross Correlation calculation considered takes advantage of the *Cross Correlation Theorem* and the *Convolution Theorem*. They state that the *Fourier Transform* of the cross-correlation between two signals defined in their own physical domain equals the product of the individual *Fourier Transforms* of both signals, one of which is complex-conjugated [8]. Given  $N$  the length of the signals, the overall computational complexity is  $O[N \log N]$  instead of  $O[N^2]$ , typical of Cross-Correlation calculations based on the standard moving sliding-dot product.

The mathematical model used to represent the input FBG spectra (the reference spectrum and the shifted one because of an applied perturbation) is given by the following relations

$$\begin{aligned} x(\lambda) &= \rho(\lambda) + n_1(\lambda) \\ y(\lambda) &= \rho(\lambda + \Delta\lambda) + n_2(\lambda) \end{aligned} \quad \text{Eq. 1}$$

In the previous relations, the term  $\Delta\lambda$  refers to the Bragg wavelength shift, which allows the calculation of the perturbing measurand. The terms  $x(\lambda)$  and  $y(\lambda)$  refer to the reference and shifted FBG spectra, respectively. The term  $\rho$  is the un-noised component of the FBG spectra (reference and shifted ones), while the terms  $n_1(\lambda)$  and  $n_2(\lambda)$  refer to the noise components of both spectra.

The Cross Correlation function developed in [8], and computed in the *Fourier* domain, is given by Eq. 2.

$$\hat{R}_{xy}(\lambda) = \mathcal{F}^{-1} \left\{ \mathcal{F}[y(\lambda)] \cdot \mathcal{F}[x(\lambda)]^* \right\} \quad \text{Eq. 2}$$

In Eq.2 the *Fourier* and the *Inverse Fourier Transform* operators have been introduced.

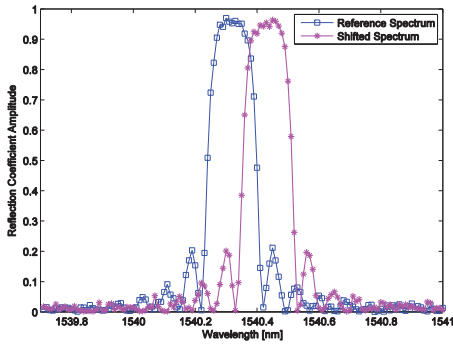


Fig. 1: Example of FBG reference and shifted spectra for a Bragg wavelength shift of ~114 pm.

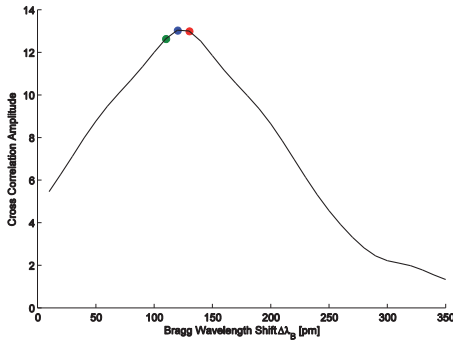


Fig. 2: Cross Correlation function of FBG spectra in fig. 1. The pictured points are subjected to the Gaussian fit for the determination of interpolated Cross Correlation peak x-position.

Fig. 2 shows the operations performed on the Cross Correlation function, in order to achieve the Bragg wavelength shift that is given by the Cross

Correlation function peak. Due to Cross Correlation function discrete nature, the peak interpolation carried out by means of 3-point Gaussian fit has been performed. The authors propose the implementation of such operation, in order to get better accuracies and avoid the FBG spectral resolution limitations.

## 2.1. Cross Correlation Performance Simulation through *Monte Carlo* Method

In order to evaluate the enhancements led by the described technique (mainly in terms of better accuracies and precisions) the authors, in a previous paper [8], applied the procedure to FBG spectra simulated by means of the *Transfer Matrix Method*, a powerful mathematical tool allowing the simulation of the FBG behavior under several strain conditions.

The physical properties of the FBG here considered are summarized in the following table.

Table I

Physical parameters of the simulated uniform fbg

Symbol	Description	Quantity
$L$	FBG total length	10 mm
$n_{core}$	core refractive index	1.46
$n_{cladding}$	cladding refractive index	1.44
$r_{core}$	core radius	4 $\mu\text{m}$
$r_{cladding}$	cladding radius	62.5 $\mu\text{m}$
$n_{eff}$	effective refractive index	1.46
$p_e, p_{11}, p_{12}$	photoelastic coefficients	0.26, 0.113, 0.252
$\nu$	Poisson ratio	0.17
$\Delta\lambda$	spectral resolution	10 pm
$\varepsilon_0$	applied strain coefficient	$10^{-4} \mu\epsilon$

The simulation produced a set of spectra which exhibit Bragg wavelength shifts from 2.34 pm up to 114 pm, with a FBG spectra resolution of 10 pm.

Fig. 3 shows the reflection spectra as the FBG is strained. The strain function considered is linearly-time varying.

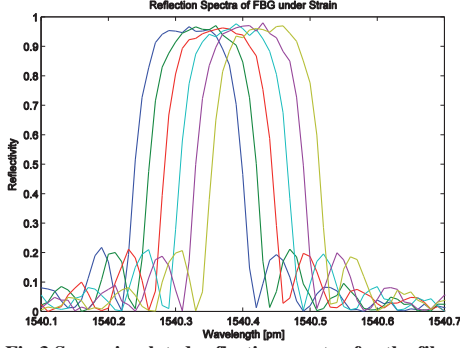


Fig.3 Some simulated reflection spectra for the fiber under consideration. The fiber considered experiences a linearly time varying strain.

In order to evaluate the Cross Correlation performance in noisy conditions (since the acquired spectra are actually affected by noise), the *Monte Carlo* method have been implemented. It allows the simulation of the FBG strain-shifted reflection spectra for several noise levels, expressed in terms of spectrum *Signal-to-Noise Ratio* (SNR). Thus, each shifted spectrum is considered white Gaussian noised with a SNR from 20 dB up to 60 dB with a 2 dB step. The *Monte Carlo* implementation has the purpose of evaluating each algorithm performances for several spectral noise levels.

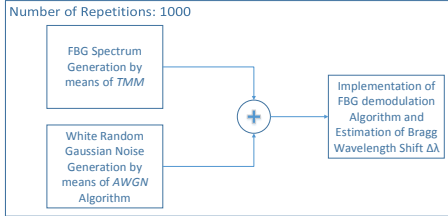


Fig.4 How the implemented *Monte Carlo* method works.

The paper [8] introduces a series of comparisons between the described Cross Correlation technique (see Eq. 2) and the usually employed FBG demodulation techniques operating in the wavelength domain (in particular, the paper considers the quadratic least-squares fit and the centroid algorithm, introduced by [4]).

The carried out performance analyses involve the time consumption, the accuracy and the precision indices. The accuracy and the precision indices are given by the following relations.

$$RMSE = \sqrt{\frac{1}{M} \sum_{i=1}^M (\Delta\lambda_{i,calculated} - \Delta\lambda_{i,effective})^2}$$

Eq. 3

$$StDev = \sqrt{\frac{1}{M} \sum_{i=1}^M (\Delta\lambda_{i,calculated} - \Delta\bar{\lambda}_{i,calculated})^2}$$

Eq. 4

The *Root Mean Squared Error* and the *Standard Deviation* values are calculated for each sample (containing  $M=1000$  simulated spectra) and for each SNR considered.

Figs.5 and 6 show the *RMSE* comparison between the Cross Correlation method described and the other standard FBG demodulation techniques.

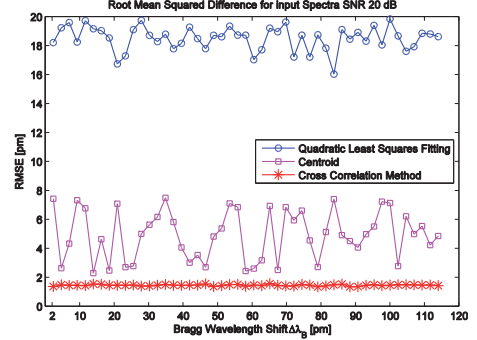


Fig. 5 *RMSE* trend for the three methods vs the Effective Bragg wavelength shift.

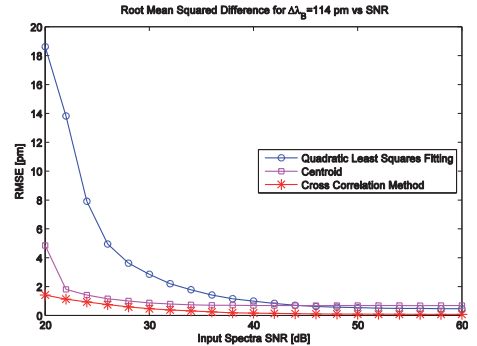


Fig. 6 *RMSE* comparisons for an effective Bragg wavelength shift ~114 pm vs spectra SNRs.

The pictures show that for a given SNR the Cross Correlation algorithm perform better and for a given Bragg wavelength shift the *RMSE* granted by the Cross Correlation method is always less than the other two methods, regardless of the noise.

The following table shows a computational time comparison. These comparisons have been performed on an 8 Gb memory *Intel® Core i7™* 3632QM (2.20 GHz) computer.

TABLE II  
Average computation time required by each method

Method	Average Time Required
Quadratic Least- Squares Fit	$1.5 \cdot 10^{-3}$ s
Centroid Algorithm	$7.2 \cdot 10^{-4}$ s
Proposed Spectral Cross Correlation	$1.6 \cdot 10^{-4}$ s

As can be noted, the Cross Correlation method offers also the best time consumption performance.

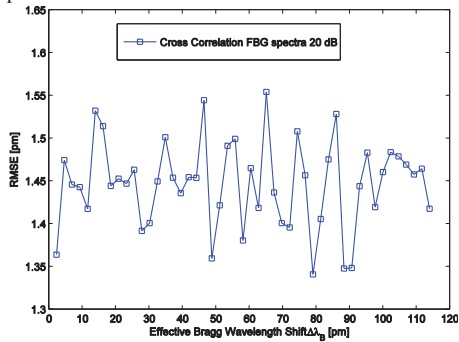


Fig. 7 RMSE trend for Cross Correlation method vs effective Bragg wavelength shift for SNR=20 dB revealing the *peak-locking* phenomenon.

Despite the excellent performance typical of the Cross Correlation method, the oscillatory trend exhibited by the *RMSE* index (as the effective Bragg wavelength changes) could lead to inaccurate  $\Delta\lambda_{Bragg}$  evaluation. The minimum error is located at integer multiples of sampling spectral resolution (10 pm in this case). The calculated  $\Delta\lambda_{Bragg}$  then drifts away from the actual one following an oscillatory trend with a period equaling the spectral resolution.

This particular trend resembles the one occurring in *Particle Image Velocimetry* (PIV), as described by [11] [12].

This phenomenon is due to the inability showed by the FBG demodulation technique, to resolve the effective  $\Delta\lambda_{Bragg}$  whenever it is less than one sampling spectral resolution. This inability is accentuated by larger sampling spectral resolutions and is influenced by the 3-point peak fit of the Cross Correlation function (with a Gaussian fit as considered in this paper). Thus, the *peak-locking* effect (definition actually borrowed from PIV) can be considered as a bias

towards integer values of sampling spectral resolution.

### 3. Iterative Cross Correlation Method (ICC)

In order to reduce the  $\Delta\lambda_{Bragg}$  evaluation inaccuracies due to the *peak-locking* effect, the authors investigate the enhancement of the described Cross Correlation algorithm, by performing it iteratively.

The proposed improvement is going to be discussed later.

#### 3.1. Further Considerations on *Peak-Locking* Effect

This paragraph is aimed to provide further insight about *peak-locking* effect.

As previously said, the accuracy parameter *RMSE* reveals a quasi-periodic trend that should be considered as a biasing phenomenon induced by the sampling spectral resolution and the interpolation operations based on peak-fit performed on the Cross Correlation function.

Such phenomenon is due to the relative inability of the demodulation techniques based on FFT-based Cross Correlation function, to correctly detect the Bragg wavelength shifts at sub-resolution extent [8]

Indeed, the CC function has the resolution of the input spectra. Therefore, the ability of accurately finding the CC function peak is limited by its own resolution. This inability is partially overcome by the 3-point peak fit operation.

Furthermore, if the defined effective  $\Delta\lambda_{Bragg}$  is an entire multiple of resolution, the 3-point Cross Correlation peak fit returns a peak point whose abscissa remains mostly constant (as the added random Gaussian noise superimposed to both spectra changes during the *Monte Carlo* iterations) and it accurately represents the effective Bragg wavelength.

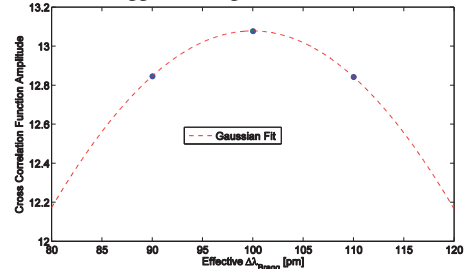
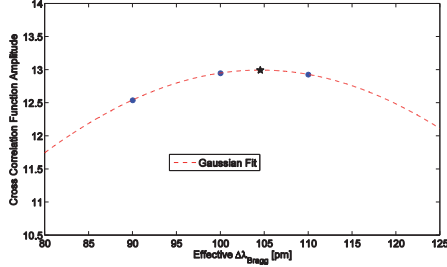


Fig. 8 Cross Correlation peak interpolation for an effective  $\Delta\lambda_{Bragg} = 100$  pm. Here the interpolated peak is coincident to the peak value of discrete Cross Correlation function

Fig. 9 shows the peak fit process when the effective  $\Delta\lambda_{Bragg}$  is not equal to an entire multiple of spectral resolution (105 pm in this case)



**Fig. 9 Cross Correlation peak interpolation for an effective  $\Delta\lambda_{Bragg} = 105$  pm. The star indicates the peak of the Gaussian fit.**

As the *Monte Carlo* iterations evolve, the peak of the discretized Cross Correlation function and the peak of the gaussian fit are not coincident and their mutual position randomly changes during the *Monte Carlo* iterations. This behavior is mainly responsible for the *RMSE* relatively high values for effective  $\Delta\lambda_{Bragg}$  not equal to a multiple integer of resolution.

In order to provide a quantitative estimator of such phenomenon, the authors implement a series of statistical considerations on the already defined *RMSE* accuracy index.

The overall accuracy of calculated Bragg wavelength displacement is a combination of various aspects, and it can be explained (for a specified SNR) by means of the following relation.

$$\Delta\lambda_i = \Delta\lambda_{eff} + \beta + \varepsilon_i \quad Eq. 5$$

In the Eq. 5, the term  $\Delta\lambda_i$  is each of the calculated Bragg wavelength shift in each sample generated by *Monte Carlo* simulation for a constant SNR (sample that contains  $M=1000$  simulated FBG spectra),  $\Delta\lambda_{eff}$  is the effective Bragg wavelength shift, the term  $\beta$  refers to the bias error and  $\varepsilon_i$  is the random error with zero mean. Each sample (for each effective Bragg wavelength displacement and SNR and containing  $M$  generated spectra) is such that the average of the random error is null and the bias error,  $\beta$ , is constant.

Therefore, the average value of the calculated Bragg wavelength shift for each *Monte Carlo* generated sample can be calculated as follows.

$$\overline{\Delta\lambda} = \frac{1}{M} \sum_{i=1}^M \Delta\lambda_i = \Delta\lambda_{eff} + \beta + \frac{1}{M} \sum_{i=1}^M \varepsilon_i = \Delta\lambda_{eff} + \beta \quad Eq. 6$$

The random error level is evaluable by means of the root mean squared fluctuation of the calculated values around the mean value.

$$\begin{aligned} \sigma &= \sqrt{\frac{1}{M} \sum_{i=1}^M (\Delta\lambda_i - \overline{\Delta\lambda})^2} = \\ &= \sqrt{\frac{1}{M} \sum_{i=1}^M (\Delta\lambda_{eff} + \beta + \varepsilon_i - \Delta\lambda_{eff} - \beta)^2} = \\ &= \sqrt{\frac{1}{M} \sum_{i=1}^M \varepsilon_i^2} \quad Eq. 7 \end{aligned}$$

Let us recall the *RMSE* value (Eq.3).

$$\begin{aligned} RMSE &= \sqrt{\frac{1}{M} \sum_{i=1}^M (\Delta\lambda_i - \Delta\lambda_{eff})^2} = \sqrt{\frac{1}{M} \sum_{i=1}^M (\beta + \varepsilon_i)^2} = \\ &\cong \sqrt{\frac{1}{M} \sum_{i=1}^M (\beta^2 + \varepsilon_i^2)} = \sqrt{\beta^2 + \sigma^2} \quad Eq. 8 \end{aligned}$$

By means of Eq. 8, the bias term  $\beta$ , representative of the *peak-locking* phenomenon can be calculated.

### 3.2. Description of the ICC Method

In order to attenuate the oscillatory trend exhibited by the *RMSE* index as the  $\Delta\lambda_{Bragg}$  varies, the author propose an iteratively performed Cross Correlation method.

The peak position (whose abscissa indicates the computed  $\Delta\lambda_{Bragg}$ ) is up to date at each iteration. The peak position detected in the latter iteration is used as one of the three-interpolation point taken close to the peak position detected in the current loop.

At the first step, a 3-point peak gaussian fit of the discretized Cross Correlation function is performed. Once the peak of the interpolating function is calculated, its x-value is used for the calculation of the renewed Cross Correlation peak amplitude from the Fourier coefficients.

The iterations stop until the error function (calculated as the absolute value of the difference between the last two calculated Cross Correlation peak amplitudes) reaches a desired value.

This method is more time consuming depending on the desired accuracy level, but it allows the achievement of better accuracy and precision performance.

The following flow chart shows the several calculations involved in the proposed method.

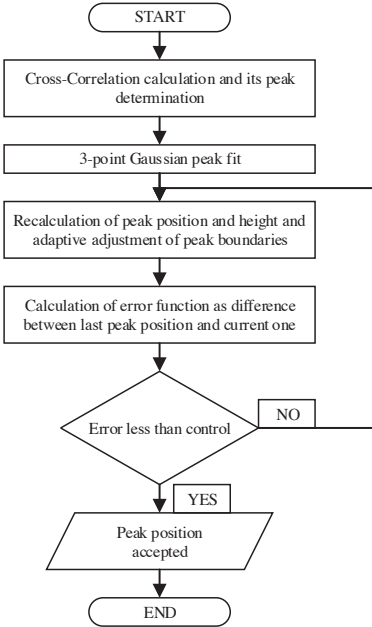


Fig. 10 Proposed Iterative Cross Correlation method flow chart.

#### 4. Performance Comparisons between proposed ICC and the CC Methods

The following picture shows the *bias error* trend against the effective Bragg wavelength shift for CC and ICC methods.

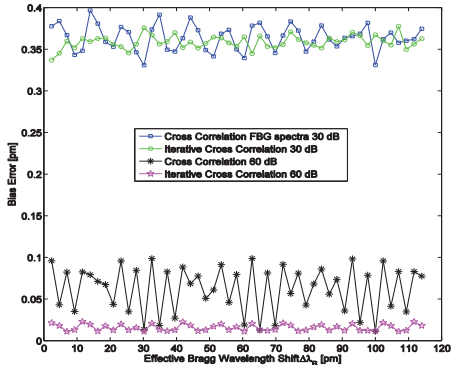


Fig. 11: Bias comparison between the Cross Correlation and the Iterative Cross Correlation methods for input FBG spectra with SNR 30 dB and 60 dB.

By means of an iteratively performed Cross Correlation algorithm, a significant reduction of the oscillatory trend is obtained. This

improvement is more evident for low and very low SNRs, where the best oscillatory trend reduction could reach values up to 80%.

The following table reports the average peak-to-peak values of the *bias error* index (whose trend is considered a waveform) for both methods under comparison and for several SNRs.

Table III  
Average Peak-to-Peak values for both methods [pm]

Method	20 dB	30 dB	60 dB
CC	0.18	0.04	0.07
ICC	0.11	0.01	0.006

The table, as Fig. 11, shows a significant decrease of the peak-to-peak value of the waveform associated to the *bias error* trend as the noise level decreases. The efficacy of the proposed Iterative Cross Correlation method become, thus, more robust with high FBG spectra SNRs.

#### 5. Some Comments about *Peak-Locking* in PIV

In the PIV technique, several physical parameters contribute to the *peak-locking* effect. In this case, the average seeding particle diameter plays a crucial role. Indeed, when the seeding particle diameter becomes significantly small, the detected displacement between two time-consecutive frames is biased towards integer values (especially when the particles are smaller than the interrogation pixel dimension).

The effect exacerbates when a gaussian sub-pixel peak estimator is employed.

In the case of 1-D signals, (such as the ones contemplated in this paper and relative to the FBG reflection spectra) the 3-point gaussian peak fit has an improving effect (since it allows overcoming the limitation due to not fine sampling spectral resolutions). In 2-D signal, in imagery and PIV imagery, the concomitance of pixel discretization, limited by seeding particle diameters, seeding particles density and gaussian peak fit accentuate the *peak-locking* trend.

In addition, the biasing phenomenon characterizing the PIV techniques is exacerbated by the FFT-based Cross Correlation calculation, which can be described by the following block diagram.



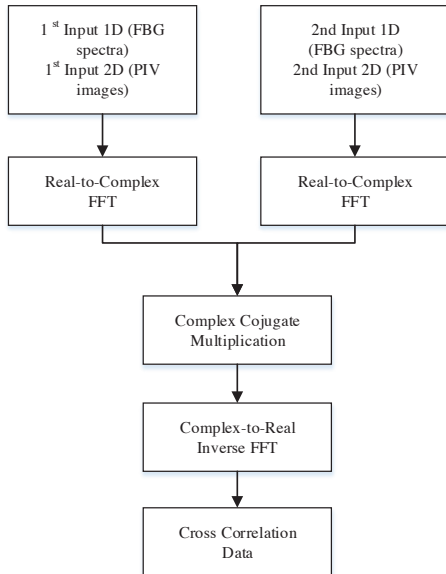


**Fig. 12: Block Diagram relative to CC calculation for both 1D signals (i.e. FBG spectra) and 2D PIV images.**

Although the CC computation is relatively easy to perform in the *Fourier* domain (with the main advantage of significantly reducing computational complexity), the pixel discretization in PIV field and the resolution limitation for FBG signals, in addition to finite interrogation window length, introduces errors within the estimation of the spectra content, inhibiting the performance of the *Fourier*-based calculations. Furthermore, the periodicity of the assumed signal boundaries implies aliasing effects, affecting negatively the ability of the demodulation method to accurately detect shifts not equal to integer multiples.

In PIV applications two possible stages of operation have been introduced, [11] [12]. The first one deals with the pre-processing of the images under analysis. The operations involved in this step are image windowing and zero-padding. The higher level of operation involves an iteratively performed CC calculation on input images that are manipulated in order to obtain (at the end of each iteration) successive displacements tending to sub-pixel levels. Thus, in the PIV technique, the joint implementation of an iteratively performed CC calculation and an adequate manipulation of the input images under analysis, successfully leads to a sensible attenuation of the bias error characterizing the *peak-locking* effect.

## 6. Conclusion

In this paper, the authors set the purpose of enhancing the Cross Correlation function (addressed to FBG signals demodulation for determining  $\Delta\lambda_{Bragg}$ ), which is calculated by means of the *Fast Fourier Transform* tool, according to the *Convolution Theorem*. In particular, the proposed enhancement has the aim of reducing the so-called *peak-locking* effect. This term, borrowed from the *Particle Image Velocimetry*, refers to a biasing phenomenon, which leads to Bragg wavelength shift evaluations inaccuracies.

The physical and mathematical causes implying such behavior have been explained, for the FBG spectra.

The authors show that an iterative execution of the Cross Correlation algorithm (in conjunction with the determination of  $\Delta\lambda_{Bragg}$  at sub-resolution extent by means of 3-point peak gaussian fit) leads to more accurate  $\Delta\lambda_{Bragg}$  evaluations, especially for effective Bragg wavelength shifts not equal to entire multiples of the FBG sampling spectral resolution.

Several FBG reflection spectra have been generated by means of the *Transfer Matrix Method*, in order to simulate the fiber behavior under an applied strain. Therefore, in order to take into account the noise (inevitably characterizing the effective sampled spectra), some white gaussian noise have been added and the efficacy of the proposed algorithm is then tested on a series of FBG spectra, generated by means of *Monte Carlo* method.

The overall results, in terms of accuracy and precision of the detected  $\Delta\lambda_{Bragg}$ , have been compared with those relative to the Cross Correlation technique applied once.

The comparisons between the ICC and the CC show a remarkable improvement of the accuracy, precision and a significant reduction of the fluctuations exhibited by the accuracy index, symptom of the *peak-locking* effect.

## Bibliography

- [1] D. Tosi, M. Olivero e G. Perrone, «Performance Analysis of Peak Tracking Techniques for Fiber Bragg Grating Interrogation Systems,» *Journal of Microwaves, Optoelectronics and Electromagnetic Applications*, vol. 11, n. 2, pp. 252-262, 2012.

- [2] Y.-J. Rao, «In-fibre Bragg Grating Sensors,» *Measurement Science and Technology*, vol. 1997, pp. 355-375, 1997.
- [3] Y. J. Rao, «Recent Progress in Applications of in-Fibre Bragg Grating Sensors,» *Optics and Lasers in Engineering*, vol. 31, pp. 297-324, 1999.
- [4] L. Negri, A. Nied, H. Kalinowski, A. Paterno, «Benchmark for Peak Detection Algorithms in Fiber Bragg Grating Interrogation and a New Neural Network for its Performance Improvement,» *Sensors (Basel)*, vol. 11, n. 4, p. 3466–3482, 2011.
- [5] A. D. Kersey, D. M., H. J. Patrick, M. LeBlanc, K. P. Koo, C. G. Askins, P. M. A., E. J. Friebele, «Fiber Grating Sensors,» *Journal of Lightwave Technology*, vol. 15, pp. 1442-1463, 1997.
- [6] T. Erdogan, «Fiber Grating Spectra,» *Journal of Lightwave Technology*, vol. 15, n. 8, pp. 1277-1294, 1997.
- [7] S. D. Dyer, P. A. Williams, R. J. Espejo, J. D. Kofler, S. M. Etzel, «Fundamental Limits in fiber Bragg Grating Peak Wavelength Measurements,» *Proceedings SPIE*, vol. 5855, 2005.
- [8] G. Dinardo, «Optical Measurements of Rotating Blade Vibrations», Ph. D. Dissertation, Bari, 2014
- [9] C. Caucheteur, K. Chah, F. Lhomme, M. Blondel, P. Megret, «Autocorrelation Demodulation Technique for Fiber Bragg Grating Sensor,» *IEEE Photonics Technology Letters*, pp. 2320-2322, 2004.
- [10] K. Kalli, *Fiber Bragg Gratings: Fundamentals and Applications in Telecommunications and Sensing*, 1999, pp. 301-389.
- [11] M. Raffel, C. Willert, S. Wereley e J. Kompenhans, «Particle Image Velocimetry: A Practical Guide», New York: Springer, 2007.
- [12] U. Ullum, Ph.D. Disseration «*Imaging Techniques for Planar Velocity and Concentration Measurements*», Lyngby, Denmark, 1999.

# Proposal of a Simpler Procedure for Flow Rate Estimation in Square Cross Section Ducts

Giuseppe Dinardo, Laura Fabbiano, Gaetano Vacca  
Politecnico di Bari

## Abstract

*Focus of the present work is the evaluation of the air flow rate in a pipe of squared cross section through the direct measurement of the mean velocity at a fixed location of the section. To this aim, an extension of the methodology already utilized for circular section pipes is here proposed. The method simplifies and improves the procedure suggested by the technical standard EN 12599. Specifically, it has been possible to state a geometrical position in the cross section where to straight measure the mean flow velocity in order to evaluate the flow rate. Here, it is shown that the proposed methodology allows the estimation of the flow rate with higher accuracy than the normed one does, estimating errors less than those accepted in common practice.*

## 1. Introduction

The measure of the flow rate is very important in scientific, industrial and economic fields; in particular, the measure of the air flow rate and the evaluation of the leakages in piping networks could be important for the energy efficiency of the complete air conditioning system when trying to improve energy conservation. For several constructional reasons, this type of installations have, normally, a rectangular/squared sections.

The most straightforward method for measuring the flow rate is based on its definition and consists in measuring the volume or mass of the fluid flowing in steady conditions in a given time interval. This method is very time consuming and laborious (it has in fact no industrial applications; is used, for example, in the process of primary calibration of instruments), so the flow rate must be evaluated by measuring the local velocity (or the average one), knowing the appropriate cross-section. Usually, the measure of local velocity of the fluid in pipes is obtained by means of Pitot Static Tube, wire anemometer, and so on, while the measure of the average velocity of the flow is obtained by the using throttling devices, rotameter, electromagnetic flow meter, turbine meter, ultrasonic meter, etc.

In literature there are many papers dealing with the problem of measuring the flow of fluids [1]-[4]; in [5] it is experimentally shown that, for turbulent flows and circular ducts, the ratio between the punctual speed measured at approximately  $\frac{3}{4}$  of the radius of the duct from its axis and the average speed in the section is, at different values of the Reynolds number, approximately unitary. This leads to the conclusion that it would be enough to measure the velocity right at a point in an opportune cross-section of the pipe (punctual speed) to obtain from that the average speed, and then the flow rate. Starting from these considerations, the authors derive empirically a similar relationship between the punctual speed and the average speed of a turbulent flow in ducts with squared cross-section exploiting the concept of equivalent circular cross section.

In this work experimental results are presented relatively to flow rate measurements in a square cross-section tube; in particular, the authors evaluate the flow rates from velocity measurements (acquired by LDA instrumentation) according to the EN 12599 Standard guidelines and derive an empirical formula suitable to obtain the position in the section where directly measuring the flow rate velocity.

The results obtained show that the proposed method provides a low measurement uncertainty for flow rate evaluations in turbulent regime and may be applied to air conditioning systems as well as, more generally, to installations using ducts of squared cross-section.

## 2. Empirical model

### 2.1. Background: Circular cross section ducts

It is known that for all continuous fluids the velocity at the wall of the duct is stationary relative to it (no slip condition).

The velocity then increases by moving toward the axis of the duct, both for laminar and turbulent flow, Fig. 1.

In laminar case and for fully developed profile, the mean velocity of the flow in a circular cross section pipe is given by

$$\bar{V} = \frac{V_0}{\pi R^2} \int_0^R 2\pi \left\{ 1 - \left( \frac{r}{R} \right)^2 \right\} dr = \frac{V_0}{2} \quad \text{Eq. 1}$$

where  $R$  is the cross section radius and

$$V_0 = \frac{1 \Delta p R^2}{4 \mu l} \quad \text{Eq. 2}$$

If the flow is turbulent, Eq.1 is no more valid and it has been proved that the local flow velocity can be evaluated by the empirical formula

$$\frac{V}{V_0} = \left( 1 - \frac{r}{R} \right)^{\frac{1}{n}} \quad \text{Eq. 3}$$

where  $n$  is linked to the *Reynolds number* from experimental data [5] and here reported in Table 1

**Table 1 Reynolds number versus  $n$**

$Re$	$4.0 \cdot 10^3$	$2.3 \cdot 10^4$	$1.1 \cdot 10^5$	$1.1 \cdot 10^6$	$2.0 \cdot 10^6$ to $3.2 \cdot 10^6$
$n$	6.0	6.6	7.0	8.8	10.0

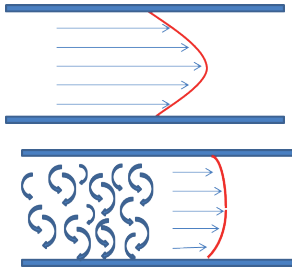


**Fig. 1: Laminar and turbulent pipe velocity profiles**

In such condition, the mean flow velocity is measurable at about  $3/4$  of  $R$  from the axis (i.e., see Preston device) and then,

$$r \cong \frac{3}{4}R \rightarrow \frac{V}{\bar{V}} \approx 1 \quad \text{Eq. 4}$$

Integrating Eq.3, the mean velocity can be expressed by:

$$\frac{\bar{V}}{V_0} = \frac{2n^2}{(n+1)(2n+1)} \quad \text{Eq. 5}$$

or

$$\frac{V}{\bar{V}} = \frac{(n+1)(2n+1)}{2n^2} \left( 1 - \frac{r}{R} \right)^{\frac{1}{n}} \quad \text{Eq. 6}$$

Combining these last two equations, the velocity profile descends as given by Eq. 3.

Experimental data show that  $V \cong \bar{V}$  at  $r = 0.758R$  for turbulent flow.

## 2.2. Squared cross-section ducts

In the case of turbulent flows, it is possible to extend the previous model to squared cross section pipes in the form:

$$\frac{V}{V_0} = \left( 1 - \frac{2x}{l} \right)^{\frac{1}{n}} \quad \text{Eq. 7}$$

being  $x$  the distance from the axis of a generic point in the pipe cross-section and  $l$  is the side of the squared section considered. This empirical formula in some way descends from the Eq. 3, by suitably rearranging the quantities there present for similarity.

By considering the equivalent circular section draining the same volumetric flow rate, such as:

$$\bar{V} S_r = \bar{V} S_{eq.c} \quad \text{Eq. 8}$$

where  $S_r$  and  $S_{eq.c}$  are the squared and the equivalent circular cross-sections respectively, the radius of the latter is given by

$$R_{eq.c} = \sqrt{\frac{l^2}{\pi}} \quad \text{Eq. 9}$$

where  $l$  is the side of the squared cross-section.

The direct proportionality between  $R_{eq.c}$  and  $l$  clarifies the proposed formula where the coefficient 2 approximates the square root of  $\pi$ . Eq. 9 then allows to apply the original model for the equivalent circular cross-section to the actual squared one and to find the appropriate location  $x$  in the squared section area where to measure the expected mean velocity for the flow rate evaluation. The use of  $\sqrt{\pi}$  instead of 2 multiplier in Eq. 7 gives more accurate results, of course, but the discrepancy is very insignificant in the frame of the practically used uncertainties.

## 3. Experimental tests

The experimental tests have been carry out to prove the reliability of the proposed model for locating the right position in a squared section where to measure the mean velocity and so evaluating the volumetric flow rate flowing inside the duct.

### 3.1. Experimental setup and instrumentation

A small subsonic wind tunnel has been arranged whose test section has been properly designed, Fig. 2.

The tunnel is an open circuit, in which a maximum air velocity of 32 m/s has been measured along the axis of the test section.

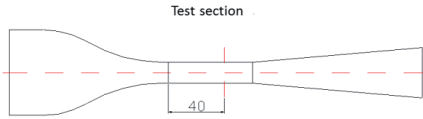


**Fig. 2: Test section in the subsonic wind tunnel**

The inlet nozzle, 1.125 m long, has a contraction ratio of 4:1 (in terms of section sides ratio), while the test volume is 0.600 m long having a squared transversal section with side of 0.153 m. Its walls have been realized by plexiglass except that one crossed by the laser beam, a glass plate 4 mm thick, in order to limit diffraction phenomena across it. The diffuser, 1.200 m long, has a squared inlet section and a circular outlet section ( $\phi = 0.355$  m). At the exit of the diffuser an axial fan is connected driven by a three-phase asynchronous electrical engine (2900 rpm nominal speed), whose round speed is controlled by inverter. The test section has been chosen at 0.400 m from the nozzle exit with the optical access for the LDA device used to measure the flow velocity profile on it, Fig. 3.

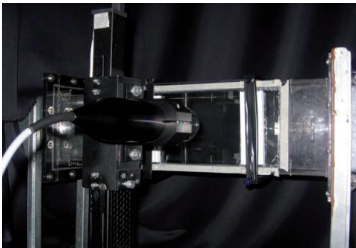


**Fig. 3: Wind tunnel optical access for the LDA device.**

### 3.1.1. LDA and moving system

A LDA anemometer, FlowLite 2D System by Dantec Dynamics, [6] (Fig. 4) has been employed having blue (Laser Sapphire,  $\lambda = 488$  nm) and green (Laser Yag,  $\lambda = 532$  nm) beams combinations, for a power of 200 mW and 2.2 mm beam diameter.



**Fig. 4: Flowlite LDA System**

The laser probe moves along two binaries allowing  $4.5 \pm 0.1$  mm horizontal and/or vertical displacement steps. The probe optical lens has  $\phi = 60$  mm and  $f = 160$  mm. The signal processor of the LDA is the BSA F60 – Dantec Dynamics.

### 3.1.2. Seeding generators

The pneumatic seeding generator here utilized was fed by air extracted downstream of a pressure controller and located upstream of the inlet section of the nozzle, in axial position.

The seeding was constituted by a 3% solution of ethylene and paraffinic oil in order to guarantee a better diffraction of light from the seeding particles and so a better SNR. Its flow rate was regulated through the air pressure feeding the generator.

## 3.2. The EN 12599 procedure

A short description of the normed procedure regarding the evaluation of the flow rate of a fluid, is described as reported in EN 12599. The efficiency of the proposed procedure is attested by the computation of discrepancies between the measured velocities and their theoretical values coming from the model.

In the technical standard EN 12599:2012 [7], titled “Ventilation for buildings - Test procedures and measurement methods to hand over air conditioning and ventilation systems”, is illustrated the method for evaluating the air flow rate in rectangular ducts (see Annex D), and, specifically, the measuring methods and devices.

In Annex D is specified that the measurement cross-section of rectangular ducts should be divided into  $i$  elements of  $S_i$  equivalent area as shown in Fig. 5

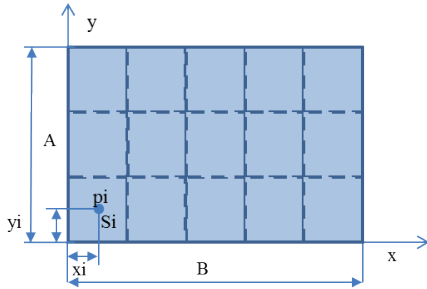


**Fig. 5:** Areas of equal size where  $p_i$  is the measuring point of the area  $S_i$

The mean velocity is obtained as the arithmetic mean of the punctual velocity measured at the centroids of the sub-areas  $S_i$ ; but there is also written that “the number of measurement point depends not only on the geometrical size of the cross section but also and decisively on the velocity profile. In case of large velocity differences, the distance between measurement points should be smaller and the measurements should be appropriately differently evaluated”.

According to this advice, the authors have divided the squared cross-section under investigation in analogy to the partitions of circular sections and fixed the points of measure, as illustrated in Fig. 6, as example.

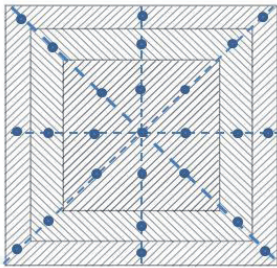


**Fig. 6:** partition of the test section in areas of equal size with indication of the measuring points.

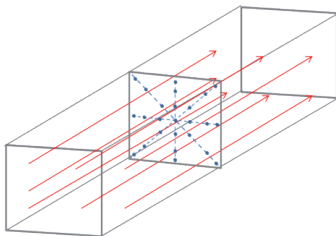


**Fig. 7:** Perspective view of the control volume

### 3.3. Test procedure

The measuring points are numbered as shown in Fig. 8 so indicating the path followed by the moving system of the laser probe, and whose coordinates are reported in Table 2.

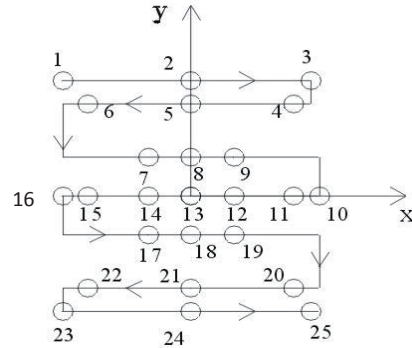


**Fig. 8:** path of the probe into the test section

**Table 2** Cartesian coordinates related to the measurement points,  $p_i$

$p_i$	1	2	3	4	5
X (mm)	-67.5	0	63	54	0
Y (mm)	67.5	67.5	67.5	54	54
$p_i$	6	7	8	9	10
X (mm)	-54	-22.5	0	22.5	67.5
Y (mm)	54	22.5	22.5	22.5	0
$p_i$	11	12	13	14	15
X (mm)	54	22.5	0	-22.5	-54
Y (mm)	0	0	0	0	0
$p_i$	16	17	18	19	20
X (mm)	-67.5	-22.5	0	22.5	54
Y (mm)	0	-22.5	-22.5	-22.5	-54
$p_i$	21	22	23	24	25
X (mm)	0	-54	-67.5	0	63
Y (mm)	-54	-54	-67.5	-67.5	-67.5

The measurements have been carried out for three different values of flow rate (3 different revolution frequencies controlled by the inverter, 10, 25 and 40 Hz); further, at each point five measures of velocity have been taken every 60 minutes and each of these measurements has been replicated for 5 consecutive days. For each acquisition the number of samples has been about  $N=1000$  and the acquisition time  $T_s$  equal to 10 s. The acquisitions have been carried out in burst mode.



## 4. Results and comments

### 4.1. Velocity profiles

The averaged velocity profiles are reported below for the 3 different revolution regimes, obtained by taking the mean values of those measured at the correspondent points on the four reference lines (2 axes and 2 diagonals) of the cross section.

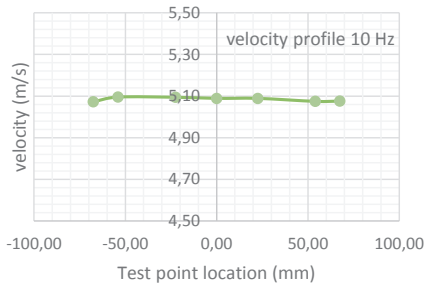


**Fig. 9:** averaged velocity profile obtained at 10 Hz revolution regime

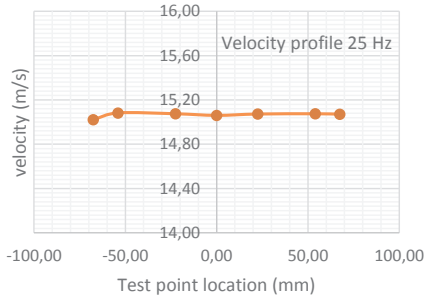


**Fig. 10:** averaged velocity profile obtained at 25 Hz revolution regime

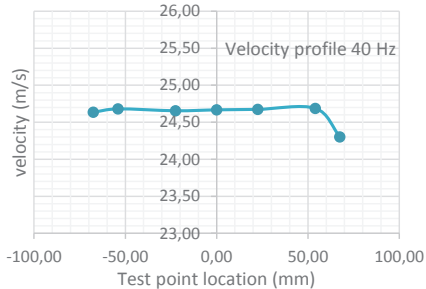


**Fig. 11:** averaged velocity profile obtained at 40 Hz revolution regime

### 4.2. Theoretical velocity profiles evaluation

The test section is squared with side  $l = 153,0 \text{ mm}$ , which corresponds to a radius of the equivalent circular cross-section, by using Eq. 9, equal to:

$$R_{eq.c} = \sqrt{\frac{l^2}{\pi}} = 86.3 \text{ mm}$$

Calculating the theoretical profile for the case 10 Hz by Eq. 7 with values of  $n$  as reported in the text, [5], and here in Tab. 1, it appears as in Fig. 12 where it is compared with the experimental one.

This result leads to the consideration that  $n$  might depend not only on Reynolds number but also on the geometric form of the pipe cross-section.

theoretical profile vs experimental profile, 10 Hz

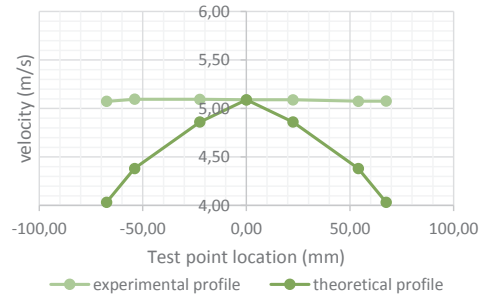


**Fig. 12:** experimental averaged velocity profile compared with theoretical profile obtained using the values of  $n$  as reported in [5].

Then, new values of  $n$  have been calculated by Eq. 3 rewritten as:

$$\ln\left(\frac{V(r)}{V_0}\right) = \frac{1}{n} \ln\left(1 - \frac{x}{R_{eq}}\right) \quad \text{Eq. 10}$$

and using the mean experimental velocity profile values for  $V(r)$ , for each revolution regime: the slope of the straight line, then, obtained from a least squares regression is the best estimation of  $1/n$ , and therefore for  $n$ .

The values of  $n$  obtained are reported in Table 3

**Table 3** new value of  $n$

	10 Hz	25 Hz	40 Hz
$Re$	56943	169535	278957
$n$	457	1317	2740

where the Reynolds number is calculated from

$$Re = \frac{\rho V_{mean} D_{eq}}{\mu} \quad Eq. 11$$

and  $\rho = 1.206 \frac{kg}{m^3}$ ,  $\mu = 18.24 \cdot 10^{-6} Pa \cdot s$ , for  $T_{env} = 20,0^\circ C$  and  $p_{env} = 100 kPa$ .

The mean theoretical velocity profiles for each flow rate investigated have been then estimated by Eq. 7 by means of the new values of  $n$  and plotted in Fig. 13, Fig. 14 and Fig. 15, where they are compared with the experimental ones.

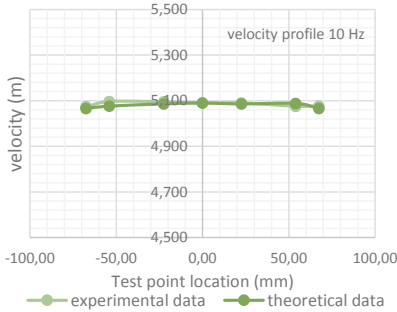


**Fig. 13: comparison between experimental and theoretical averaged velocity profile at 10 Hz.**

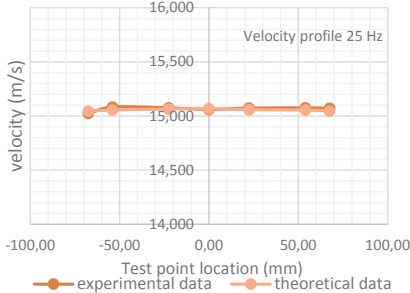


**Fig. 14: comparison between experimental and theoretical averaged velocity profile at 25 Hz.**

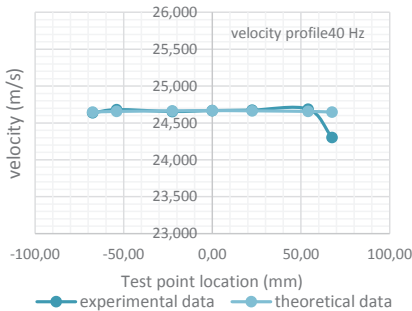


**Fig. 15: comparison between experimental and theoretical averaged velocity profile at 40 Hz.**

As shown in the graphs, the theoretical and experimental profiles match very well.

For each one of the revolution regimes, the experimental mean velocity is obtained as the average value of the 25 test points ones, as:

$$V_{mean,exp} = \frac{1}{25} \sum_{i=1}^{25} V_i \quad Eq. 12$$

where  $V_i$ 's are the mean weighted experimental values of the local velocities obtained by the measurements. Its standard deviation is simply calculated by the law of propagation of uncertainty,  $\delta V_{mean}$ .

The mean velocity values with their standard deviations for each regime are reported in Table 4

**Table 4 flow rate velocities**

	10 Hz	25 Hz	40 Hz
$V_{mean,exp} (m/s)$	4.95	14.73	24.24
$\delta V_{mean} (m/s)$	0.07	0.11	0.18

Thus, the location  $x$  correspondent to the mean velocity of the flux can be now estimated from Eq. 7.

For all the 3 fluxes experimented the ratio  $\frac{2x_{mean}}{l}$  has resulted equal to  $\sim 0.776$ , compared with  $\sim 0.758$  for circular cross-section.

#### 4.3. Evaluation of measurement uncertainty of the proposed method

The followings Table 5 contains the deviations between experimental velocities and theoretical ones for each flow rate.

The maximum relative deviation estimated is 0.01%.

##### 4.3.1. Theoretical mean velocity evaluation at 0.776 $l/2$

The theoretical mean velocity has been estimated, for each one of the rotational regimes considered, from the empirical model stated (Eq. 7) and compared with the experimental correspondent value calculated by means of Eq. 12, as shown in Table 6. There, the discrepancies between the homologous velocity values and relative errors are also present.

The error estimated appears to be less than 3%, so validating the hypothesis of obtaining the flow velocity for the estimation of the flow rate directly from a unique measurement at a chosen position even in the squared cross-section pipe as well as in circular cross-section ones.

**Table 5 Comparison between experimental and theoretical velocity averaged profiles****10 Hz**

	$V_{experimental}$ [m/s]	$V_{theoretical}$ [m/s]	$\Delta V$ [m/s]	$\Delta V/V_{experimental}$ %
-67.50	5.074	5.066	0.008	0.2
-54.00	5.096	5.076	0.020	0.4
-22.50	5.095	5.086	0.009	0.2
0.00	5.090	5.090	0.000	0.0
22.50	5.090	5.086	0.004	0.1
54.00	5.075	5.088	-0.008	-0.2
67.50	5.076	5.066	0.010	0.2

**25 Hz**

Test point locations [mm]	$V_{experimental}$ [m/s]	$V_{theoretical}$ [m/s]	$\Delta V$ [m/s]	$\Delta V/V_{experimental}$ %
-67.50	15.023	15.044	-0.021	-0.1
-54.00	15.083	15.054	0.029	0.2
-22.50	15.075	15.064	0.009	0.1
0.00	15.060	15.068	-0.008	-0.1
22.50	15.072	15.057	0.015	0.1
54.00	15.075	15.054	0.021	0.1
67.50	15.071	15.044	0.027	0.2

**40 Hz**

Test point locations [mm]	$V_{experimental}$ [m/s]	$V_{theoretical}$ [m/s]	$\Delta V$ [m/s]	$\Delta V/V_{experimental}$ %
-67.50	24.635	24.647	-0.012	-0.0
-54.00	24.679	24.655	0.024	0.1
-22.50	24.654	24.663	-0.009	-0.0
0.00	24.667	24.666	0.001	0.0
22.50	24.673	24.663	0.010	0.0
54.00	24.686	24.655	0.031	0.1
67.50	24.303	24.647	-0.344	-1.4

**Table 6 Comparison between experimental and theoretical mean velocity values**

	$V_{mean,th}$ [m/s]	$V_{mean,exp}$ [m/s]	$ \Delta V $	$ \Delta V\% $
<b>10 Hz</b>	5.07	4.95	0.12	2.42
<b>25Hz</b>	15.05	14.73	0.32	2.17
<b>40 Hz</b>	24.65	24.24	0.41	1.69

The error estimated appears to be less than 3%, so validating the hypothesis of obtaining the flow velocity for the estimation of the flow rate directly from a unique measurement at a chosen position even in the squared cross-section pipe as well as in circular cross-section ones.

The estimated position has resulted equal to about 0.78 of the half transversal dimension of the pipe. It is presumable that similar empirical model could be set even for rectangular cross-

section pipes provided that its aspect ratio would not differ so much from unity.

## 5. Conclusions

An innovative empirical model has been set up for evaluating the suitable position where to measure the velocity of turbulent flow allowing to directly calculate the volumetric flow rate flowing in pipes with squared cross-section. The solving formula arises from the analogy to the circular

cross sections, for which the standard EN 12599 estimate such position at  $\frac{3}{4}R$ ,  $R$  being the radius of the section.

The model has been validated by measurements taken in a small subsonic wind tunnel whose test section has been properly designed. A laser Doppler anemometer has been utilized to measure the local velocities in the test section over a grid of points suitably chosen.

The comparisons between calculations and measurements have shown discrepancies of order of 3% at most for the mean velocity and then for the volumetric flow rate, if the uncertainties on the section dimensions are neglected. Such discrepancies are much lesser than the errors accepted in common practice.

### Bibliography

- [1] Cushing, M., "The future of flow measurement, Flow Control", January 2000.
- [2] Eren, H., "Flowmeters, in Survey of Instrumentation and Measurement", S.A. Dyer, Ed., John Wiley & Sons, New York, 2001, 568 – 580
- [3] Baker, R. C., "Flow Measurement Handbook: Industrial Designs, Operating Principles, Performance, and Applications". Cambridge University Press. 2005
- [4] Spitzer, David W., "Flow measurement: practical guides for measurement and control". Isa, 1991.
- [5] Baker, R. C. "An Introductory Guide to Industrial Flow. Mechanical Engineering" Publications Limited, London. 1996
- [6] <http://www.dantecdynamics.com/flowlite-lda-systems> [Accessed: 25 March 2014]
- [7] "DIN EN 12599 - Ventilation for buildings - Test procedures and measurement methods to hand over air conditioning and ventilation systems." [Online]. Available: <http://www.techstreet.com/products/1849254>. [Accessed: 25 March 2014].

# Lower limb strength measurements by Hand Held Dynamometer assisted by optoelectronic system.

A. Ancillao<sup>1</sup>, F. Patanè<sup>1</sup>, S. Rossi<sup>2</sup>, A. Pacilli<sup>1</sup> & P. Cappa<sup>1</sup>

<sup>1</sup>Dep. Of Mechanical and Aerospace Engineering, Sapienza University of Rome, Roma, IT

<sup>2</sup>Dep. of Economics and Management – Industrial Engineering, University of Tuscia, Viterbo, IT

## Abstract

*Strength measurements on the lower limb muscles are popular in the medical practice to evaluate the health status and effectiveness of training programs. Quality of strength measures obtained by Hand Held Dynamometer (HDD) is anyway under discussion, as reliability depends on operator as well as testing conditions. In this work the authors used an optoelectronic system to assist HDD measurements in order to check quality and to propose a method to reduce interval of uncertainties due to HDD method.*

## 1. Introduction

Very often, in the medical practice and in rehabilitation programs, strength measurements are performed to evaluate the health status of patients and effectiveness of training programs. The force measurements by Hand Held Dynamometer (HDD) are also used to assess muscle strength in children with developmental disabilities, such as cerebral palsy (CP) [1].

The use of HDD is very popular because the device is inexpensive, easy to use and does not require specific patient preparation; in fact, the patient has just to assume the position defined by the protocol, e.g. sitting on a bench for knee flexion/extension trials, while the therapist applies the HDD on the leg and asks the patient to push against the HDD. At the end the therapist simply reads the force value on the display of the device. On the other side, HDD measures are affected by errors due to the operator and patient positioning.

Studies were already conducted on the inter-tester reliability of the method and concluded that the method is questionable since due to the low reproducibility among trial repetitions [1], [2].

The reproducibility increases when the test is conducted by a trained clinician, but quality of measurements depends on application and positioning of the HDD [2].

The aim of this work is to conduct strength measurements while tracking position of the HDD with respect to the limb. Position and 3D

orientation are recorded by an optoelectronic system. This will allow to quantify the error due to positioning, orientation and rotation of the HDD and to develop a method to correct the measurement.

## 2. Methods

### 2.1. Equipment

Measures took place in the Motion Analysis and Robotics Laboratory at Ospedale Pediatrico Bambino Gesù, where a Vicon MX (Oxford, UK) motion capture system (8-camera-workstation, Nexus 1.7 software, 200 Hz, PlugInGait marker set based on the Davis protocol) is installed.

A MicroFet™ dynamometer (Hoggan Scientific, Salt Lake City, UT) was equipped with four passive markers as shown in Fig. 1. Markers were placed on sticks fixed to the HDD in order to improve the visibility by the Vicon system.

The central marker was used only for the static trial, to find the sensing HDD axis, and it was removed for the dynamic trials.



**Fig. 1: HDD Dynamometer equipped with passive markers.**

The Vicon system allowed to reconstruct the position of the subject and the HDD (Fig. 2) with an overall inaccuracy of 0.5 mm. Thus, the method proposed here allowed to compute the direction, orientation and application axis of the force measured by the HDD.

## 2.2. Subjects and Trials

Two adult healthy subjects were recruited for the tests. Knee extension trials were recorded with the subject sitting on a medical bench. Knee extension force was measured by applying the HDD on the shank, at  $\approx 50$  mm from the ankle (Fig. 2).

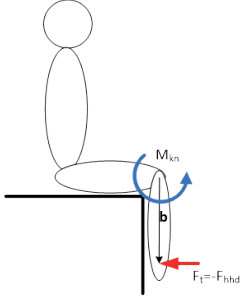


Fig. 2: Measured force, lever arm and knee torque.

The subjects were requested to extend the knee against the dynamometer with as much force as they could, for  $\approx 5$  s. The therapist had to push back in order to keep the shank still [1]. The test was repeated three times. Maximum force measured was recorded. The nominal moment was computed by multiplying the maximum force and the length of the shank, obtaining a constant value. Instead, the actual applied moment was computed by reconstructing the orientation of the HDD with respect to the subject. Knee extension moment was computed along the three anatomical axes: flex/extension, ab/adduction and intra/extra rotation obtaining a track for each axis, representing how the component changed during the trial.

The angular range of motion of the knee was also measured, to ensure that the knee maintained the requested position during the trial.

## 3. Results

The time-histories of force and torques, determined in one of the performed trial, are depicted in Fig. 3 and 4. As expected, the main component of the force was in the antero-posterior direction ( $x$ -axis). The other components were lower ( $\approx 1.5\%$  and  $\approx 30\%$ ). For the knee moment, the main component was along the  $z$ -axis (flex/ext  $\approx 40$  Nm). Other components were lower ( $\approx 0\%$  and  $\approx 30\%$ ). The dotted line in Fig. 4 is the nominal moment ( $\approx 43$  Nm). The black line is the intensity of moment vector.

## 4. Conclusion

The preliminary results showed that the average torque in the principal direction was compatible with the respective nominal value. The difference was  $\approx 3$  Nm. The other components were lower. In case of erroneous application of HDD, the undesired components would increase.

Further study and trial acquisition is required to define threshold values that may represent a numerical index to characterize the quality of a strength measurement.

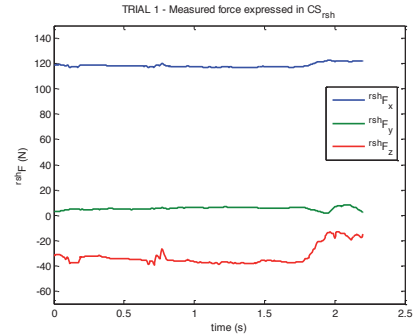


Fig. 3: Subject No.1, test: right knee ext, repetition 1: Components of measured force vector.

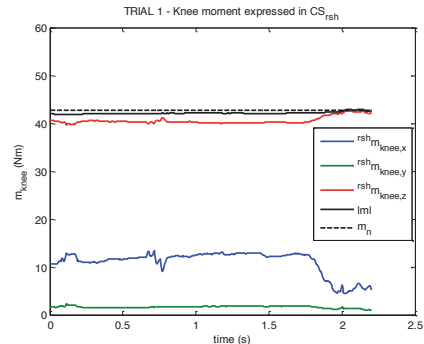


Fig. 4: Subject No.1, test: right knee ext, repetition 1: components of knee moment vector.

## References

- [1] O. Verschuren, M. Ketelaar, T. Takken, M. Van Brussel, P. Helders, and J. Gorter, "Reliability of hand-held dynamometry and functional strength tests for the lower extremity in children with cerebral palsy," *Disabil. Rehabil.*, vol. 30, no. 18, pp. 1358–1366, 2008.
- [2] K. Mahony, A. Hunt, D. Daley, S. Sims, and R. Adams, "Inter-tester reliability and precision of manual muscle testing and hand-held dynamometry in lower limb muscles of children with spina bifida," *Phys. Occup. Ther. Pediatr.*, vol. 29, no. 1, pp. 44–59, 2009.



# Metrological Characterization of an Hexapod-Shaped Multicomponent Force Transducer

Gianfranco Genta<sup>1</sup>, Alessandro Germak<sup>2</sup>

<sup>1</sup> DIGEP, Politecnico di Torino, Corso Duca degli Abruzzi 24, 10129 Torino, Italy, [gianfranco.genta@polito.it](mailto:gianfranco.genta@polito.it)

<sup>2</sup> Istituto Nazionale di Ricerca Metrologica (INRiM), Strada delle Cacce 91, 10135 Torino, Italy, [a.germak@inrim.it](mailto:a.germak@inrim.it)

## Abstract

*A Multicomponent Force Transducer (MFT) was devised by INRiM for a specific request in railway industry of measuring two force components (transversal and axial force). The measurement of the two transversal components was not required, but it was helpful for the practical use. INRiM, basing on its experience, developed and calibrated a full six-components hexapod-design prototype of MFT. Linear regression analysis was applied to get an empirical mathematical model linking the applied components to the MFT outputs. Best Subset Regression was adopted to identify parsimonious models by considering all possible combinations of predictor variables. Finally, the uncertainty associated to the values of transversal and axial force was evaluated.*

## 1. Introduction

The present work was originated by a specific industrial request, i.e. the determination of “Chasse” (orthogonality error under load) generated by the transversal force due to compression on springs used in railway carriage suspension. The target uncertainties required by this application are 1% on the measurement of transversal force and class 1 of ISO 7500-1:2004 [1] for axial force. Typical capacity being up to a few hundreds of kilonewtons, a Multicomponent Force Transducer (MFT) was devised ad hoc, on the basis of sizable experience in this field acquired at INRiM by developing several multicomponent measurement and calibration systems [2,3]. MFTs developed at INRiM found application in the characterization of primary force standard machines, e.g. control of parasitic components [4], as well as in such areas as robotics [5] and verification of material testing machines [6]. Both range (from a few newtons to hundreds of kilonewtons) and type (compound elements or monolithic) of MFTs developed cover a broad spectrum of applications.

While measurement of main axial and transversal force magnitudes were mainly required, the direction of transversal force had

also to be estimated, the direction of main axial force being the longitudinal axis of the spring. A three-component force transducer was therefore required. In addition, advantages coming from an even rough information on the applied moments allow a better identification of the calibration equations. Therefore, a full six-components hexapod-design prototype of MFT was developed. This design is typical of six degrees of freedom displacement measuring devices (Stewart platforms). It has been used till now in the field of MFTs mainly for low-force transducers such as those for application in robotics [7,8,9]; for the specific application an high load capacity MFT was developed in cooperation between INRiM and a company in the field of mechanical testing.

## 2. Description of the MFT

The MFT has an axial force capacity of 200 kN and of 30 kN for transversal force. Its built-up design is made up by six Uniaxial Force Transducers (UFTs) decoupled by elastic hinges (Fig. 1), substantially eliminating spurious components, which might otherwise affect single UFT measurements [10].

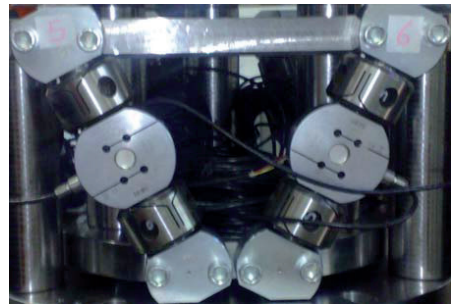


**Fig. 1: Two of the six Uniaxial Force Transducers (UFTs) decoupled by elastic hinges at both ends.**

Such a structure (Fig. 2) enables measuring three force components (transversal,  $F_x$  and  $F_y$ , and axial,  $F_z$ ), and three moment components, (bending,  $M_x$  and  $M_y$ , and torsion,  $M_z$ ).

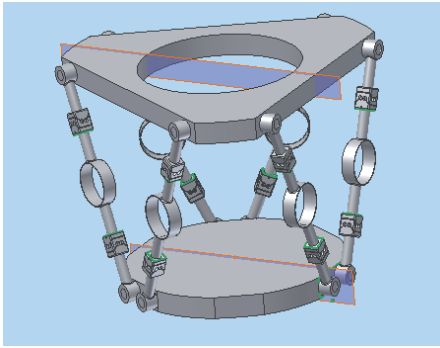


**Fig. 2: Layout of the hexapod-shaped Multicomponent Force Transducer (MFT).**

A two-step spring test procedure applies first axial force,  $F_z$ , and measures the two components of the transversal force ( $F_x$  and  $F_y$ ), enabling estimation of transversal force direction. The second step implies rotation of the spring in order to align transversal force with the  $x$ -axis, and applications of the axial force, iterating as required the rotation until a correct alignment is obtained (typically, no more than two iterations).

### 3. Calibration of the MFT

An important aspect which was considered for the choice of type of transducer design was the possibility of calibration, both initial and for maintenance over time.

The main advantage of this type of MFT is that all the UFTs are subject to a tensile stress, greater or lower depending on the applied forces and moments. The first calibration is useful to determine both the effects of the geometry of the structure and the sensitivities of the UFTs. Since the MFT, installed in a spring testing machine (Fig. 3), is not moved over time, the geometry is not subject to significant changes. Thus, the subsequent calibrations can be restricted only to the evaluation of the variation over time of sensitivities of the UFTs by applying known values of vertical components  $F_z$ .

INRiM was tasked with the first calibration of the MFT in order to have traceable measurements, i.e. with an uncertainty evaluation [11]. A well-established metrological approach [2] asserts that known forces must be applied both independently and in combination to assess cross sensitivity among output channels (if any). Testing procedure strictly requires only calibration for  $F_x$  and  $F_z$ .

Calibration for  $F_z$  was performed on the primary INRiM deadweights standard machine with a

capacity of 1 MN, following the international calibration procedure; results showed the MFT being in class 00 according to ISO 376:2011 [12]. Calibration of  $F_x$  was instead performed right on the spring testing machine, evaluating the all-important cross sensitivity with  $F_z$ . The latter was generated using deadweights, transversal force being applied by mechanical devices and measured with a calibrated UFT (Fig. 3).



**Fig. 3: Calibration set-up on the spring testing machine.**

### 4. Analysis of calibration results

Using the described calibration set-up (Fig. 3), transversal forces and axial forces were applied. Given the target of uncertainties (mentioned in section 1), and in the light of results obtained in preliminary tests, an abridged experimental plan with only two levels of  $F_z$  and few levels of  $F_x$  was deemed adequate and performed accordingly.

According to the availability of deadweights in the site of calibration, the selected levels of  $F_z$  were about 14 kN and 23 kN. With these levels of force, values of  $F_x$  ranging up to 3 kN and 5 kN respectively have been chosen in order to apply only tensional stress to the single UFTs. By applying component  $F_x$  an associated bending moment  $M_y$  is also generated. The zero condition is obtained with the MFT in the minimum preloading condition. Applied components, corresponding force outputs and moment outputs are shown, respectively, in Table 1, 2 and 3.

**Table 1. Applied components.**

n.	$F_x/\text{kN}$	$F_z/\text{kN}$	$M_y/\text{N}\cdot\text{m}$
1	0.000	0.000	0.0
2	0.000	-22.969	0.0
3	0.563	-22.969	-281.6
4	1.050	-22.969	-524.8
5	2.019	-22.969	-1009.5
6	4.045	-22.969	-2022.4
7	4.992	-22.969	-2495.9
8	0.000	-14.066	0.0
9	0.528	-14.066	-264.1
10	0.996	-14.066	-498.2
11	2.028	-14.066	-1014.2
12	3.006	-14.066	-1503.0

**Table 2. Force outputs corresponding to the applied components shown in Table 1.**

n.	$U_x/\text{kN}$	$U_y/\text{kN}$	$U_z/\text{kN}$
1	0.000	0.000	0.000
2	0.000	0.000	-22.969
3	0.520	0.001	-22.959
4	0.962	0.004	-22.959
5	1.850	0.016	-22.952
6	3.699	0.049	-22.931
7	4.563	0.070	-22.937
8	0.000	0.000	-14.066
9	0.483	0.041	-14.134
10	0.914	0.044	-14.134
11	1.862	0.059	-14.121
12	2.759	0.075	-14.111

**Table 3. Moment outputs corresponding to the applied components shown in Table 1.**

n.	$U_{mx}/\text{N}\cdot\text{m}$	$U_{my}/\text{N}\cdot\text{m}$	$U_{mz}/\text{N}\cdot\text{m}$
1	0.0	0.0	0.0
2	0.0	0.0	0.0
3	76.7	-279.4	-0.4
4	69.7	-517.7	0.4
5	52.9	-995.7	-0.4
6	4.5	-1996.3	-0.4
7	-33.0	-2465.2	-4.7
8	0.0	0.0	0.0
9	-11.7	-244.6	7.7
10	-16.3	-474.5	8.4
11	-38.7	-982.4	7.7
12	-62.8	-1462.2	5.1

While  $F_x$  is expected to be related mainly to the output  $U_x$ , and  $F_z$  to the output  $U_z$ , owing to cross-sensitivity the presence of other terms was anticipated. Linear regression analysis [13] was applied to get an empirical mathematical model linking the applied components to the MFT outputs. In particular, Best Subset Regression [14]

was adopted to identify parsimonious models for  $F_x$  and  $F_z$  by considering all possible combinations of predictor variables ( $U_x$ ,  $U_y$ ,  $U_z$ ,  $U_{mx}$ ,  $U_{my}$  and  $U_{mz}$ ). The limited number of experiments allowed only to consider models up to first order with interactions. This is acceptable considering the linearity characteristic of the UFTs. For the transversal force, it is obtained:

$$F_x = a \cdot U_x + b \cdot U_{mx} + c \cdot U_x \cdot U_z \quad \text{Eq. 1}$$

where  $a = 1.08$ ,  $b = -6.16 \times 10^{-2} \text{ m}^{-1}$  and  $c = -6.04 \times 10^{-4} \text{ kN}^{-1}$ .

Instead, for the axial force, it is obtained:

$$F_z = d \cdot U_x + e \cdot U_y + f \cdot U_z \quad \text{Eq. 2}$$

where  $d = -3.90 \times 10^{-2}$ ,  $e = 2.00$  and  $f = 1.00$ .

The models include as significant terms for  $F_x$  besides  $U_x$ , also  $U_{mx}$  and the interaction term  $U_x \cdot U_z$  (Eq. 1), while the corresponding model for  $F_z$  includes, besides  $U_z$ , also  $U_x$  and  $U_y$  (Eq. 2). The significant contribution of the interaction  $U_x \cdot U_z$  in Eq. 1 underlines the advantages of exploiting a full six-components MFT even when measurement of only two components is required.

Once estimated the mathematical models, it was evaluated the expanded uncertainty associated to the values of  $F_x$  and  $F_z$  [15,16]. For all the equation coefficients, the relevant standard uncertainty was evaluated as the corresponding standard deviation obtained in the performed linear regression (Table 4). For the MFT outputs, the relevant standard uncertainty was evaluated considering the metrological characteristics of the UFTs and the geometry of the MFT (Table 5).

**Table 4. Standard deviations of equation coefficients.**

Coefficient	Std. dev.
$a$	$7.56 \times 10^{-4}$
$b$	$6.73 \times 10^{-3} \text{ m}^{-1}$
$c$	$3.52 \times 10^{-3} \text{ kN}^{-1}$
$d$	$2.65 \times 10^{-3}$
$e$	$1.19 \times 10^{-1}$
$f$	$1.82 \times 10^{-4}$

**Table 5. Relative standard uncertainties of MFT outputs.**

MFT output	Relative std. unc.
$U_x$	0.5%
$U_y$	0.5%
$U_z$	0.025%
$U_{mx}$	5.9%
$U_{my}$	2.9%
$U_{mz}$	2.1%

The uncertainty evaluation according to GUM [11] and PUMA method (described in ISO 14253-2:2011 [17]) may be properly organized in a tabular format, with reference to EA-4/02 M:2013 [18]. A small modification from this format has been introduced by substituting standard deviations with variances; it has the advantage to manage additive quantities which can be compared more easily. In this way, individual contributions to variance of output quantity  $F_x$  are shown for a specific working condition in Table 6.

**Table 6. Uncertainty table for the transversal force  $F_x$  (expressed in kilonewton).**

$x_j$		$u(x_j)$	$c_j$	$u_j^2(F_x)$	$v_j$	$u_j^4(F_x)/v_j$
Symbol	Value					
$a$	1.08	$7.6 \times 10^{-4}$	3.0	$5.1 \times 10^{-6}$	9	$2.9 \times 10^{-12}$
$b$	$-6.16 \times 10^{-2}$	$6.7 \times 10^{-3}$	$1.0 \times 10^{-1}$	$4.5 \times 10^{-7}$	9	$2.3 \times 10^{-14}$
$c$	$-6.04 \times 10^{-4}$	$3.5 \times 10^{-5}$	-42.0	$2.2 \times 10^{-6}$	9	$5.3 \times 10^{-13}$
$U_x$	3.00	$1.5 \times 10^{-2}$	1.1	$2.7 \times 10^{-4}$	61	$1.2 \times 10^{-9}$
$U_{mx}$	$1.00 \times 10^{-1}$	$5.9 \times 10^{-3}$	$-6.2 \times 10^{-2}$	$1.3 \times 10^{-7}$	40	$4.5 \times 10^{-16}$
$U_z$	-14.00	$3.5 \times 10^{-3}$	$-1.8 \times 10^{-3}$	$4.1 \times 10^{-11}$	100	$1.7 \times 10^{-23}$
$F_x$	3.26		$u^2(F_x)$	$2.7 \times 10^{-4}$	$\Sigma$	$1.2 \times 10^{-9}$
			$u(F_x)$	$1.7 \times 10^{-2}$	$v_{F_x}$	64
			$p$	95%		
			$t_p(v_{F_x})$	2.0		
			$U(F_x)$	$3.3 \times 10^{-2}$		
			$W(F_x)$	1.0%		

The same type of calculation was performed for  $F_z$ . Therefore, it is obtained a relative expanded uncertainty of 1.0% for  $F_x$  and 0.15% for  $F_z$ . These values resulted to be nearly constant in all the working conditions.

## 5. Conclusion

A Multicomponent Force Transducer (MFT) was devised by INRiM for a specific request in railway industry. Even if the testing procedure strictly required only calibration for  $F_x$  and  $F_z$ , the INRiM experience suggested to develop a full six-components hexapod-design prototype of MFT. In fact, the analysis of calibration results showed that the measurement of  $F_x$  is not only affected by the value of  $U_x$ , but also by  $U_{mx}$  and the interaction term  $U_x \cdot U_z$ .

Besides, the uncertainty associated to the values of transversal and axial force was evaluated. The applied calibration method allowed to keep these uncertainty values within the targets required by the customer. In particular, it is obtained a relative expanded uncertainty of 1.0% for transversal

Symbols of independent variables appearing in the mathematical model and their values are written down in column  $x_j$ . Entries in column  $u(x_j)$  are the standard uncertainties for each contribution, while values in column  $v_j$  represent the degrees of freedom. Coefficients of sensitivity  $c_j$  may be evaluated either by partial derivation, or numerically, and eventually contributions  $u_j^2(F_x)$  of variance of dependent variable  $F_x$  can be calculated. By taking into account all these information, it is possible to get the expanded uncertainty  $U(F_x)$ .

force and 0.15% for axial force, much better than the required class 1 of ISO 7500-1:2004.

## Acknowledgments

The authors wish to thank Professors Giulio Barbato and Raffaello Levi who gave a scientific guidance to the present work through fruitful discussions.

## References

- [1] ISO 7500-1:2004, "Metallic materials -- Verification of static uniaxial testing machines -- Part 1: Tension/compression testing machines -- Verification and calibration of the force-measuring system".
- [2] A. Bray, G. Barbato, R. Levi, "Theory and Practice of Force Measurement", Academic Press, London, 1989.
- [3] G. Barbato, S. Desogus, A. Germak, "Calibration system for multicomponent force and moment transducers", *Experimental Mechanics*, pp. 341-352, 1992.

- [4] C. Ferrero, A. Bray, R. Levi, C. Marinari, "An investigation on parasitic effects on force standard machines", In: VDI Berichte, vol. 312, 1978.
- [5] G. Barbato, S. Desogus, A. Germak, "Multicomponent force sensors for robotics", In: Proceedings of the First International Symposium on Measurement and Control in Robotics, Houston, Texas, USA, June 1990.
- [6] G. Barbato, A. Bray, A. Germak, R. Levi, "Calibration and verification of multicomponent dynamometers in the meganewton range", In: Proceedings of the 11th International Conference on Measurement of Force and Mass, Amsterdam, The Netherlands, May 1986.
- [7] M. Sorli, S. Pastorelli, "Six-axis reticulated structure force/torque sensor with adaptable performances", Mechatronics, vol. 5, no. 6, pp. 585-601, 1995.
- [8] U. Seibold, B. Kubler, G. Hirzinger, "Prototype of instrument for minimally invasive surgery with 6-axis force sensing capability", In: Proceedings of the 2005 IEEE International Conference on Robotics and Automation, Barcelona, Spain, April 2005.
- [9] Y. Hou, J. Yao, L. Lu, Y. Zhao, "Performance analysis and comprehensive index optimization of a new configuration of Stewart six-component force sensor", Mechanism and Machine Theory, vol. 44, pp. 359-368, 2009.
- [10] S. Desogus, A. Germak, F. Mazzoleni, D. Quagliotti, G. Barbato, A. Barbieri, G. Bigolin, C. Bin, "Developing multicomponent force transducers at INRiM", In: Proceedings of the IMEKO 2010 TC3, TC5 and TC22 Conferences, Metrology in Modern Context, Pattaya, Chonburi, Thailand, November 2010.
- [11] JCGM 100:2008, "Evaluation of measurement data - Guide to the expression of uncertainty in measurement (GUM)".
- [12] ISO 376:2011, "Metallic materials -- Calibration of force-proving instruments used for the verification of uniaxial testing machines".
- [13] N. R. Draper, H. Smith, "Applied Regression Analysis", 2nd ed., Wiley, New York, 1981.
- [14] R. R. Hocking, "The analysis and selection of variables in linear regression", Biometrics, vol. 32, pp. 1-49, 1976.
- [15] G. Genta, "Methods for uncertainty evaluation in measurement", VDM Verlag, Saarbrücken, 2010.
- [16] G. Barbato, A. Germak, G. Genta, "Measurements for decision making", Società Editrice Esculapio, Bologna, 2013.
- [17] ISO 14253-2:2011, "Geometrical product specifications (GPS) -- Inspection by measurement of workpieces and measuring equipment -- Part 2: Guidance for the estimation of uncertainty in GPS measurement, in calibration of measuring equipment and in product verification".
- [18] EA-4/02 M:2013, "Evaluation of the Uncertainty of Measurement in Calibration".